Summer 8-15-2022

Dynamics of Spatiotemporal Heterogeneities in Particulate Intercalation Electrodes

Shubham Agrawal
Washington University in St. Louis

Recommended Citation

Agrawal, Shubham, "Dynamics of Spatiotemporal Heterogeneities in Particulate Intercalation Electrodes" (2022). *McKelvey School of Engineering Theses & Dissertations*. 774.
https://openscholarship.wustl.edu/eng_etds/774

WASHINGTON UNIVERSITY IN ST. LOUIS

McKelvey School of Engineering
Department of Energy, Environmental and Chemical Engineering

Dissertation Examination Committee:
Peng Bai, Chair
Pratim Biswas
Rohan Mishra
Vijay Ramani
Elijah Thimsen

Dynamics of Spatiotemporal Heterogeneities in Particulate Intercalation Electrodes

by
Shubham Agrawal

A dissertation presented to
the McKelvey School of Engineering
of Washington University in
partial fulfillment of the
requirements for the degree
of Doctor of Philosophy

August 2022
St. Louis, Missouri

Table of Contents

List of Figures

List of Tables

Acknowledgments

Writing the acknowledgement, I look back to the long journey of my PhD and recall the names of the individuals who provided assistance, encouragement and guidance, and without whom I would not have succeeded. I am very grateful to those people who have givem me so much of their time, love, and energy.

The first person I want to acknowledge is my advisor Dr. Peng Bai. I was fascinated by his research aptitude and mindset in our first meeting itself and made up my mind to join his lab. I am truly grateful to him for he took a leap of faith with me as his first student even without doing a research rotation with him. Dr. Bai has been supportive and patient with me throughout these five years. I cannot have imagined a better Ph.D. advisor than him and I can never forget the exciting and enriching experience under his guidance.

I would also like to thank my committee members, Dr. Pratim Biswas for his support and guidance, Dr. Rohan Mishra for introducing me to the concepts of atomistic modeling, Dr. Vijay Ramani for his constant motivation, and Dr. Elijah Thimsen for an amazing experience as his assistant in his course. I would also like to thank Dr. Daniel Giammar for inviting me to the fun social events in his group and for countless constructive discussions.

I must express my sincere gratitude to Dr. Sanmathi Chavalmane at Nano Research and Environmental Facility and to Dr. Huafang Li and Dr. Tyrone Daulton at Institute of Materials Science and Engineering, for training me on the sophisticated instruments. I would also like to thank the administrative staff at EECE for taking care of all the administrative requirements and documentation related to graduate studies and finances. They did a commendable job for the department, especially during the COVID-19 outbreak.

Being a graduate student during COVID-19 period, the sudden lockdown made this journey difficult at times. Thus, I sincerely thank my small group of friends Yashika, Sukrant, Priya, Girish, Nishit and Piyush, who were always there for me during tough times. I would always cherish the weekend game nights and potlucks with them.

A positive working environment makes the job easier. I thank my labmates and friends Bingyuan, Youngju, Poom, Rajeev and He, for maintaining a positive work attitude and for their constant motivation. They always cared for my well-being and were always eager for discussions. I loved talking to them about their amazing culture and foods. I will always be grateful for this lifelong friendship.

At the end, I would like to thank my parents and siblings for their continuous love and support. They always believed in me in every phase of my life.

Finally, a very special thanks to my wife Neha for her unconditional love and support. She ensured that I keep moving forward throughout all the ups and downs during my Ph.D. degree. I cannot imagine walking this journey without her.

Shubham Agrawal

Washington University in St. Louis

August 2022

Dedicated to my family

ABSTRACT OF THE DISSERTATION

Dynamics Of Spatiotemporal Heterogeneities In Particulate Intercalation Electrodes

by

Shubham Agrawal

Doctor of Philosophy in Energy, Environmental and Chemical Engineering

Washington University in St. Louis, 2022

Professor Peng Bai, Chair

Electrochemical energy systems rely on particulate porous electrodes to store or convert energies. While the three-dimensional porous structures of the electrodes were introduced to maximize the interfacial area for better overall performance of the system, spatiotemporal heterogeneities arising from materials thermodynamics localize the charge transfer processes onto a limited portion of the available interfaces. These reaction heterogeneities may cause local hot and cold spots, and early battery failures. This dissertation focuses on the following three aspects of the dynamic reaction heterogeneities in the particulate cathodes and anodes in the lithium-ion batteries: (i) the real-time evolution of reaction heterogeneities in graphite anodes, (ii) the origin of reaction heterogeneities and their interplay with the phase transformation mechanisms in graphite anodes, and (iii) the quantification method of reaction heterogeneities in solid-solution cathodes. The dissertation also discusses the systematic electrochemical investigation of the graphite cathodes in aluminum-ion batteries for their coherent design.

A simple but precision method has been developed that can directly track and analyze the *operando* (i.e. local and reacting) interfaces at the mesoscale in a practical graphite porous electrode to obtain the true local current density. The seemingly random reaction heterogeneities are actually controlled by the interplay between the non-equilibrium material thermodynamics and the electrochemical kinetics. The combined theoretical and experimental analyses revealed that unlike other phase-transforming porous electrodes, not all phase separation processes in graphite electrodes can be suppressed by high currents. The results shed light on the long-standing discrepancies in kinetics parameters derived from electroanalytical measurements and from first principles predictions, and highlight the necessity to examine the concentration-dependent exchange current density for intercalation electrodes undergoing complex phase transformation processes.

While optical microscopy revealed the subtleties of spatiotemporal heterogeneities in graphite electrodes, their identification in solid-solution materials posed challenges. A Raman spectroscopy tool has been developed to map and quantify the spatiotemporal heterogeneities in Ni-rich layered oxide cathode materials (NMC532). The results revealed a significantly high true current densities than the widely-accepted globally-averaged one. Incorporating nonequilibrium thermodynamics into classical electrochemical models and electroanalytical techniques will ensure self-consistent understandings of practical porous electrodes toward precision design and management.

Lithium-ion batteries rule the energy storage market owing to their overall high performance, which, however, deteriorate severely at temperatures below -10°C. Emerging aluminum-ion batteries (AIBs) can deliver higher reversible capacities at low temperatures down to even -30°C. A systematic electrochemical characterization of the AIBs using classical electroanalytical methods at five temperatures selected between -20°C and room temperature, has been performed to assess the fundamental kinetics. The temperature-insensitive fast kinetics could be attributed to the high availability and easy access of active species at the inner Helmholtz plane near the electrode surface. The results revealed the governing mechanisms facilitating the high performance of AIBs in a wide temperature range and demonstrated the necessity of electrolyte optimization with a focus on the inner Helmholtz plane of the electric double layer structure to ensure high-rate electrode performance at low temperatures.

Chapter 1: Introduction

1.1 Background

Advanced rechargeable/secondary batteries are imperative for the industrial revolution towards a more sustainable society.[1–5] These batteries play a pivotal role in the electrified world and are a key to decarbonization in mobility and energy generation.[6] In the last decade, lithium-ion batteries (LIBs) have brought a paradigm shift in the key modern-life necessities such as personal electronics, stationary energy storage, communication, and mobility.

Conventional lithium-ion batteries, also known as “rocking-chair” or “shuttlecock” cells work on a to and fro movement of Li ions between transition metal oxide cathodes and graphite anodes. These transition metal oxides have high theoretical specific and volumetric capacities, low self-discharge, high discharge voltage and good cycling performance which makes them best suited for energy storage.[4] While a variety of cathode materials are available (**Figure 1.1**), graphite acts as a versatile anode material for LIBs owing to its low cost, high abundance, low delithiation potential vs Li, high Li diffusivity, high electrical conductivity, and relatively low volume change during lithiation/delithiation.[7–12] These active materials are broadly classified into two categories, phase transforming and solid solution, based on the intercalation mechanisms.

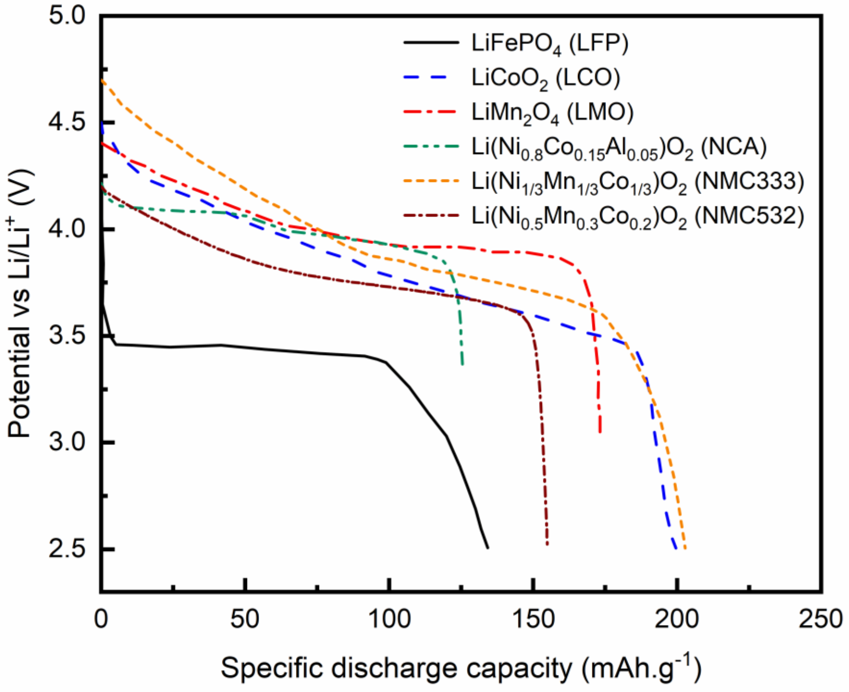

Figure 1.1: Popular cathode materials in LIBs. Discharge curves of common cathodes used in LIBs. Among them, LFP is a phase transforming material while the remaining are solid-solution materials.

Despite LIBs being the most dominant energy conversion and storage technology in the last decade, a truly sustainable energy industry necessitates the diversification of the storage chemistries. The concept of graphite cathodes for DIBs has existed for a long time, however, there is limited research on the intercalation mechanisms of anions into carbon materials.[13] Dual-ion batteries (DIBs) with graphite as cathodes have recently gained attention owing to their low cost, relatively high energy densities, and cycling stability.[14] Aluminum-ion batteries (AIBs) are particularly encouraging owing to their exceptional performance at temperatures as low as -30°C, ideal for cold weather conditions.[15] AIBs use ionic liquids as electrolytes and operate on the fast and reversible intercalation of aluminum-based bulky anions between the graphene layers. The development of such reliable and cost-effective alternate chemistries can help fulfill the rising energy demands.

1.2 Motivation

Despite the success of LIBs, they face scrutiny over the incidents of random and elusive safety accidents including life-threatening fires and explosions.[16–18] Like all engineered materials, the macroscopic failures in LIBs originate from the microscopic inhomogeneities in the electrode materials.[19] The cathode and anode materials are typically combined with carbon black (to create an electron-conductive network) and binder material to form porous electrodes for LIBs. Both the phase transforming,[20–28] and solid solution[29–33] electrodes exhibit state-of-charge (SOC) heterogeneities (**Figure 1.2**) due to a non-uniform distribution of electrochemical reactions enabled by either the thermodynamics of the active material[34,35] or the heterogeneous microstructure of the composite porous electrodes,[33,36] respectively. The solid solution material may also undergo “fictitious” phase separation, causing further heterogeneous charge distribution.[37] Thus, a much smaller area compared to the total particles’ area is active at any instant[38] or, possibly leading to hot and cold spots, and early battery failures. The heterogeneous Li ions distribution may cause faster localized degradation[24], ultimately leading to fatal phenomena such as Li plating and thermal runaways.[39] While advanced imaging techniques including sophisticated X-ray[24,26,27,29,31,33,34,40] and lasers[30,32] have enabled the identification and quantification of the spatial heterogeneities, their real-time examination in realistic surroundings is challenging and critical to understanding the true local electrochemical kinetics that dictates the dynamic charge-transfer process. New horizons to elucidate the role of spatiotemporal heterogeneities under realistic conditions can be obtained by coupling the theory and modeling with advanced experimental techniques and methods.

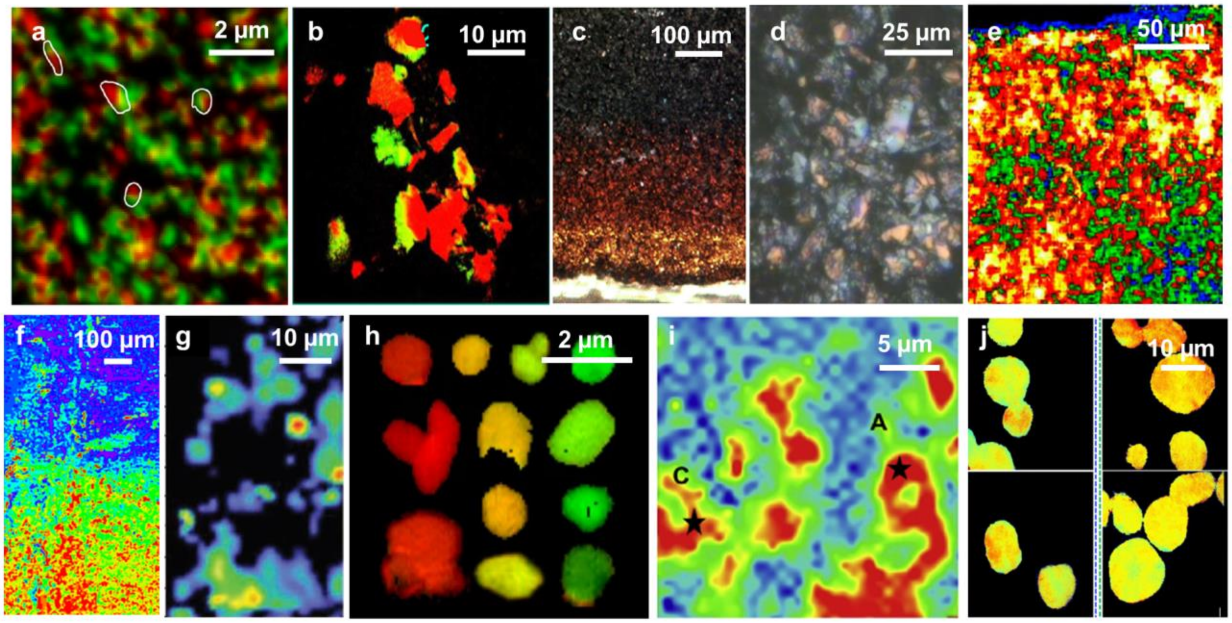

Figure 1.2: Spatial reaction heterogeneities in particulate porous LIB electrodes. Reaction heterogeneities are observed in phase transforming materials such as a) $LiFePO_4$ using scanning transmission X-ray microscopy (STXM),[34] b) $LiFePO_4$ using X-ray absorption near-edge spectroscopy (XANES),[27] c) mesocarbon microbeads (MCMB) using optical microscope (OM),[80] d) graphite flakes using OM,[22] and e) synthetic graphite using High-resolution transmission electron microscopy (HR-TEM).[135] Reaction heterogeneities are also observed in solid-solution materials such as f) $LiCoO_2$ using X-ray absorption spectroscopy (XAS),[31] g) NCA using Raman mapping,[33] h) NMC333 using STXM,[37] i) NMC532 using Raman mapping,[32] and j) NMC622 using Full-field (FF) TXM.[101] The blue, red and gold colors in the graphite electrodes in panels c) and d) indicate 21%, 50% and 100% SOCs, respectively. The bright yellow and blue colors in panel e) indicate 100% and 0% SOCs, respectively. The red color indicates 0% SOC while blue color indicates 100% SOC for NMC622 in panel j). Red color signifies 100% SOC in the remaining panels.

The direct consequence of the spatiotemporal heterogeneities in the porous electrodes is that the active reaction area at any instant is a small fraction of the total available surface area. Since the classical electroanalytical techniques,[41–45] shown in **Table 1.1**, rely on the true current density (total current $I(t)$ divided by the active reaction area S) to estimate the solid-state diffusion coefficients D_A^{chem}, the inability to quantify the SOC heterogeneities may result in misinterpretation of the fundamental kinetic parameters. The diffusion coefficients of the widely studied phase transforming materials, lithium iron phosphate (LFP)[46,47,56,57,48–55] and graphite,[9,38,58–65] estimated using the classical electroanalytical techniques vary by 8 orders of magnitude in the existing literature. The solid-solution material such as $Li_x(Ni_{0.5}Mn_{0.3}Co_{0.2})O_2$ (NMC532) also suffers from a three-orders-of-magnitude variation in the estimated diffusion coefficients.[66–68] These discrepancies in the kinetic parameters raise important concerns about the rate-determining phenomena, and thus the effectiveness of the design strategies of the porous electrodes. Thus, a deeper understanding of these microscopic heterogeneities and their interactions on the battery level is necessary to elucidate the cause of the arbitrary accidents.[69]

Table 1.1: Classical Electroanalytical Techniques. GITT: Galvanostatic Intermittent Titration Technique; PITT: Potentiostatic Intermittent Titration Technique; EIS: Electrochemical Impedance Spectroscopy; CV: Cyclic Voltammetry

Method	$\mathbf{t \ll L^2/D_A^{chem}}$	$\mathbf{t \gg L^2/D_A^{chem}}$
GITT[41]	$\frac{\mathrm{I}}{\mathrm{S}} = \frac{z_A F}{2V_M}\left[\frac{dE(t)}{d\sqrt{t}} / \frac{dE(\delta)}{d\delta}\right]\sqrt{\pi \mathrm{D}_\mathrm{A}^\mathrm{chem}}$	$\frac{\mathrm{I}}{\mathrm{S}} = \frac{3z_A F}{V_M L}\frac{E(t)\|_{t=0} - E(t=0)}{dE(\delta)/d\delta}\mathrm{D}_\mathrm{A}^\mathrm{chem}$
PITT[42]	$\frac{\mathrm{I(t)}}{\mathrm{S}} = \frac{z_A F}{V_M L}\frac{\Delta E}{dE(\delta)/d\delta}\sqrt{\mathrm{D}_\mathrm{A}^\mathrm{chem}/\pi t}$	$\frac{\mathrm{I(t)}}{\mathrm{S}} = \frac{2z_A F \mathrm{D}_\mathrm{A}^\mathrm{Chem}}{V_M L^2}\frac{\Delta E}{dE(\delta)/d\delta}\exp\left\{-\frac{\pi^2 \mathrm{D}_\mathrm{A}^\mathrm{Chem} t}{4L^2}\right\}$
EIS[44]	$Z_W^0 = \frac{1}{\mathrm{S}}\frac{V_M}{z_A F}\frac{dE(\delta)}{d\delta} \Big/ \sqrt{2\mathrm{D}_\mathrm{A}^\mathrm{Chem}}$	$\mathrm{Re}(Z_\mathrm{lim}) = \frac{1}{\mathrm{S}} \cdot \frac{V_M}{z_A F}\frac{dE(\delta)}{d\delta}\frac{L}{3\mathrm{D}_\mathrm{A}^\mathrm{Chem}}$
CV[43]	$\frac{\mathrm{I_p}}{\mathrm{S}} = 0.4463 z_A F c_A \sqrt{z_A F \nu \mathrm{D}_\mathrm{A}^\mathrm{Chem}/RT}$	

D_A^{chem}: Diffusivity of intercalant ion A into the host; I: Applied current; $I(t)$: Transient current during a voltage step; ΔE: Magnitude of the voltage step; L: Diffusion length; I_p: Peak current; $E(\delta)$: Equilibrium voltage as a function of mole fraction δ; $E(t)$: Transient voltage response; S: Reacting surface area; z_A: Charge number of the ion A; V_M: Molar volume of the host material; F: Faraday constant; Z_W^0: Warburg factor; c_A: Equilibrium concentration of A; v: Scan rate; R: Gas constant; T: Temperature

Graphite, one of the most widely used electrodes for non-aqueous[15,22] and aqueous batteries,[70] undergo multiple phase transformations during Li ion intercalation.[71] These stable phases, also known as the ordered stages, display different colors under visible light.[20,72] Thus, optical microscope can track the phase transformations in hundreds of graphite particles in realistic surroundings and in real-time. Similarly, Raman spectroscopy enables fast acquisition of the Li ion concentration in the active materials which cannot be differentiated visually.[30,32] Such accessible and versatile techniques can easily identify the spatiotemporal heterogeneities in the LIB electrodes and provide accurate kinetic parameters. The inclusion of the population dynamics acquired from such useful techniques can bridge the gaps between the single-particle models and the multiscale commercial battery models.[73]

While LIBs have widespread applications, they have a relatively small optimal temperature range of 10°C – 60°C,[74–77] making them infeasible for colder areas in the world. AIBs have recently gained popularity as they exhibit high performance over a wider temperature range than LIBs. Moreover, their low cost, rich abundance and processing safety support further development. With extensive research towards their cell construction, a systematic investigation of the electrochemical kinetics in the AIBs is also necessary. The realization of alternate chemistries for energy storage relies on the appropriate electrochemical characterization, which is critical for optimized batteries.[78]

1.3 Research Objectives

Broadly, the dissertation will provide a detailed understanding of the origin and impact of reaction heterogeneities in the porous particulate electrodes in LIBs and suggest electrochemical characterization strategies in AIBs required for their optimal design. For this purpose, the dissertation is divided into three main objectives schematically described in **Figure 1.3**.

Objective 1: Theoretical understanding of reaction heterogeneities in particulate graphite electrodes in LIBs

1A. Quantification of dynamic charge heterogeneities in porous graphite electrodes

The objective was to observe the spatiotemporal heterogeneities during Li ion intercalation in the graphite electrode on the mesoscale. We employed an optical microscopy setup to provide an accurate understanding of the dynamic intercalation process under realistic surroundings. We determined that only a limited fraction of the area is active at any instant, which can be used to accurately estimate the fundamental kinetic parameters and the rate-determining mechanisms.

1B. Interplay between spatiotemporal heterogeneities and phase transformations in porous graphite electrode

The objective was to understand the relationship between the dynamic spatiotemporal heterogeneities and the phase transformation mechanisms during Li ion transfer within graphite electrodes. We observed that the seemingly random mesoscale spatiotemporal heterogeneities in the graphite electrode were actually caused due to their inherent thermodynamics. The mechanism of phase transformation on the particle-scale controlled the population dynamics in the particulate electrode and hence, the true electrochemical kinetics. We concluded that all the phase transformations in graphite cannot be suppressed using high currents, unlike the general assumption.

Objective 2: Quantification of *in situ* spatial reaction heterogeneities in porous NMC532 electrodes

The objective was to develop a method to observe and quantify spatial reaction heterogeneities in the particulate electrodes without visual characteristics to differentiate ion concentrations. Raman spectroscopy was an apt non-destructive technique for such purposes. We confirmed the occurrence of severe reaction heterogeneities during Li ion intercalation in the particulate NMC532 electrodes. We concluded that only the partially-lithiated areas were active and governed the true electrochemical kinetics.

Objective 3: Investigation of temperature-dependent electrochemical kinetics in the graphite cathodes in AIBs

The objective was to estimate the fundamental kinetic parameters and determine the rate-limiting mechanism of the graphite cathodes at different temperatures during the charge and discharge of AIBs. We discovered that the charge transfer in AIBs was mildly affected by reducing the temperature from ambient to -20°C, unlike LIBs. We observed that the use of solvent-free ionic electrolytes in AIBs facilitated fast charge transfer even at low temperatures, which could make them a viable option for mobility applications in colder areas.

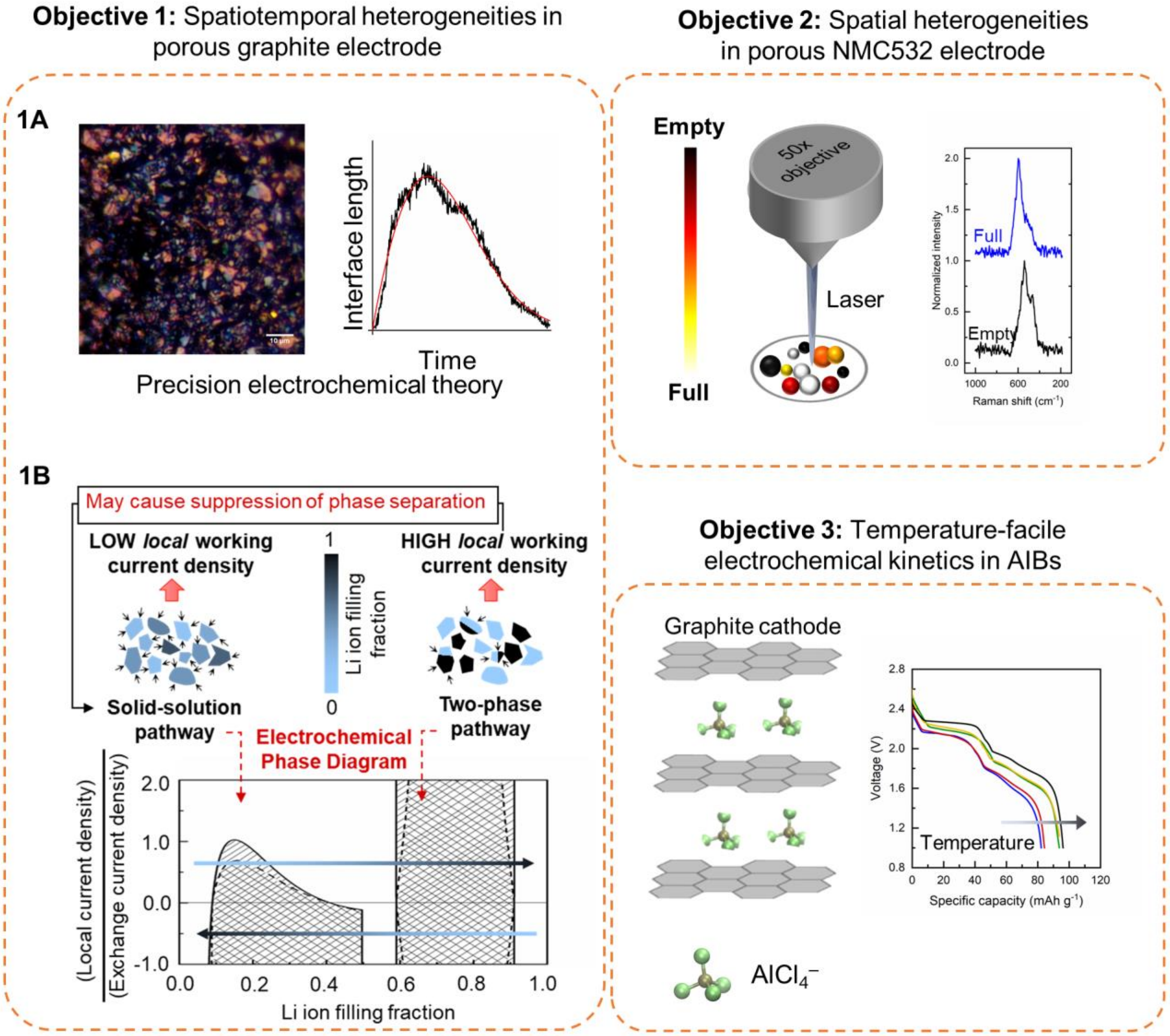

Figure 1.3: Research objectives of the dissertation

1.4 Dissertation outline

The dissertation will illustrate ways to quantify and understand the fundamental mechanism of dynamic reaction heterogeneities in the porous LIB electrodes and perform a systematic characterization of the electrochemical kinetics in AIBs to assist in the development of new energy storage technologies. The following six chapters would describe the tasks performed towards achieving the objectives of the dissertation. Each chapter is self-contained containing introduction, methodology, results, discussion, and conclusion sections. **Chapters 2 and 3** provide systematic studies to understand the origin and impact of the less investigated spatiotemporal heterogeneities in the porous graphite electrodes to determine the true electrochemical kinetics. **Chapter 4** offers the methods to identify and quantify the electrochemically active regions in the particulate NMC532 electrodes using Raman spectroscopy. **Chapter 5** describes the subtleties of the electrochemical kinetics in graphite cathodes in the AIBs, at five temperatures selected between -20°C and room temperature. Chapter 6 provides the future scope and direction for the scientific community to gather more understanding towards the development of better batteries. The above five chapters are followed by a list of all the references cited in the dissertation.

There are five appendices attached in the dissertation. **Appendices A – D** contain the supplementary information of Chapters 2 – 5, respectively, followed by **Appendix E** including my curriculum vitae.

Chapter 2: *Operando* Electrochemical Kinetics in Particulate Graphite Electrodes

The results reported in this chapter have been published in – Agrawal, S., & Bai, P. (2021). "Operando Electrochemical Kinetics in Particulate Porous Electrodes by Quantifying the Mesoscale Spatiotemporal Heterogeneities." Advanced Energy Materials, 11(12), 2003344.

2.1 Introduction

Electrochemical energy storage and conversion systems are critical for a sustainable future.[79] Lithium-ion batteries (LIBs) that offer the highest energy density have revolutionized electronic devices, portable power tools and electric cars.[1–3] But their further advancements have been impaired by the random occurrences of elusive safety accidents,[16,39] which are believed to originate from microscopic heterogeneities in the particulate porous electrodes.[19] State-of-charge (SOC) heterogeneities have recently been identified in both the solid-solution[29–33] and phase-transforming electrodes,[20–26,80] as a direct result of non-uniform distribution of electrochemical reactions due to either the structures of the composite porous electrodes[33,36] or the thermodynamics of the active materials.[34,35] While the nanoscale heterogeneities in individual particles detected by synchrotron X-ray provide deep insights on the possible degradation mechanisms, the evolutions of the heterogeneities among hundreds of particles sitting in realistic surroundings are critical for the understanding of the true local electrochemical kinetics that dictate the real-time performance. Recent breakthroughs in a few synchrotron facilities have enabled *in situ* imaging of large number of particles in realistic battery electrodes.[24,25,40,81–83]

However, achieving very high spatial and temporal resolutions at the same time is still very challenging. Yet more accessible testing platforms that can enable the economical and systematic verifications of new mathematical models to achieve the comprehensive understanding of dynamic heterogeneities in relevant electrochemical systems are critically needed.

The immediate consequence of the spatiotemporal heterogeneities is that the actual reacting interfacial area at any instant, i.e. area of the *operando* (local and working) electrochemical interface, is only a small portion of the total available interfacial area usually obtained from the Brunauer-Emmett-Teller (BET) method. Given that existing electroanalytical techniques[45,84] rely on the square-law scaling $D_{Li} \sim [I(t)/S]^2$ to extract the diffusion coefficient D_{Li} from the total current $I(t)$ and the assumed *constant total* interfacial area S, the electrochemical kinetics in systems with strong heterogeneities may have been misinterpreted due to the smaller *operando* interfacial area.

As one of the most widely used electrodes for both the nonaqueous[15,22] and aqueous[70] batteries, graphite electrodes are known to have strong reaction heterogeneities[22,80] reflected by its particle-by-particle reaction mechanism,[22,34] during the phase transformation between ordered stages[71] upon ion intercalation. Depending on the choices of electrode area, e.g. BET or geometric, the lithium-ion diffusion coefficient in graphite (D_{Li}) extracted by the classic electroanalytical methods varies by about 8 orders of magnitude in the literature.[8,9,38,58,60,63–65] Still, D_{Li} obtained for SOC ranges with phase transformation were always about 2 orders of magnitude lower than the average.[9,38] The discrepancy has long been doubted as the inaccuracy of the interfacial area,[62] but conclusive evidence is still missing. Similar orders-of-magnitude discrepancies also exist in other porous electrodes composed of phase-transforming[45] or solid-solution particles,[66–68] missing satisfactory explanations. The discrepancies in the kinetic parameters directly affect the determination of the rate-limiting step, and thereafter the validity of traditional electroanalytical techniques and the effectiveness of the predicted rational design strategies.

Here, we use graphite as a model system to demonstrate the direct quantification of the true local current densities for precision electrochemical kinetics. The unique color changing property during graphite lithiation[22,85] allows us to develop economical *operando* platform with optical microscope (**Figure A-1**) to investigate the dynamics of the heterogeneities at high speed and at the mesoscale (imaging hundreds of particles simultaneously every two seconds). Our study reveals that the state of charge (SOC) heterogeneities are indeed the result of reaction heterogeneities, which lead to the localization of the reaction flux onto a limited number of particles in the electrode. Using the moving phase boundaries between different stages (phases) of lithiated graphite to approximate the *operando* electrochemical interfacial area, the true local current density was determined to be as least 2 orders of magnitude higher than the averaged current density over the adjusted BET surface area. The insights gathered from the interface area and the true local current density suggest that, once the heterogeneities emerge, the *operando* (i.e. local and working) electrochemical kinetics of the porous electrode is not diffusion limited. This study highlights the need of tracking the phase boundaries to resolve the long-standing huge discrepancies between experiments and theoretical predictions.

2.2 Results

2.2.1 Spatiotemporal heterogeneities

We conducted three sets of potentiostatic intermittent titration technique (PITT) experiment with 10 mV, 100 mV and 200 mV steps, respectively. **Figure 2.1(a)-(c)** demonstrates the color evolution in the thin graphite electrode with thickness of 5 μm (**Figure A-2**) during the 10 mV PITT experiment, with a threshold current of C/20. The entire lithiation process can be divided into three segments based on the colors of the lithiated graphite (**Figure A-3**). In segment (I) all empty particles (dark grey) reacted concurrently regardless of their morphology and size to become blue (Stage 3). At this point, the blue particles accommodated 23% of the total capacity supplied in the entire PITT discharge and brought down the cell voltage from 275 mV to 85 mV. Since, at this moment (t = 0 s shown in Figure 2.1(a)), all the particles were in Stage 3 (blue), the SOC associated with Stage 3 was determined to be the global SOC of the electrode, i.e., x_B = 23%, slightly higher than the values adopted in earlier works.[22,72]

In segment (II), a few blue particles began to turn red at the onset of the PITT voltage stepping from 85 mV to 75 mV. The localized red (Stage 2) regions always coexisted with the blue (Stage 3) regions within the same particle. The evolving boundaries between the red and blue regions clearly reveal the phase transformation process. Upon careful visual inspection, we observed that the Li^+ ion flux prefers to go into particles with phase boundaries. The remaining blue (Stage 3) particles will begin receiving Li^+ ion flux only after existing boundary-containing phase-transforming particles become completely red. The red particles then remain idle, waiting for all the other particles to reach the same stage. This process is consistent with not only the sequential reaction front in thick graphite electrode,[26] but also the particle-by-particle reaction mechanism of $LiFePO_4$ electrodes at low current densities.[34] Similarly, we determine the SOC associated with Stage 2 (x_R) to be 55%, which is the global SOC when all particles turned red. In segment (III), while the cell is still under the same voltage held at 75 mV, the red particles start a similar particle-by-particle phase transformation process to turn gold (Stage 1). The SOC associated with Stage 1 (x_G) is calibrated to 100%. The phase transformation process from Stage

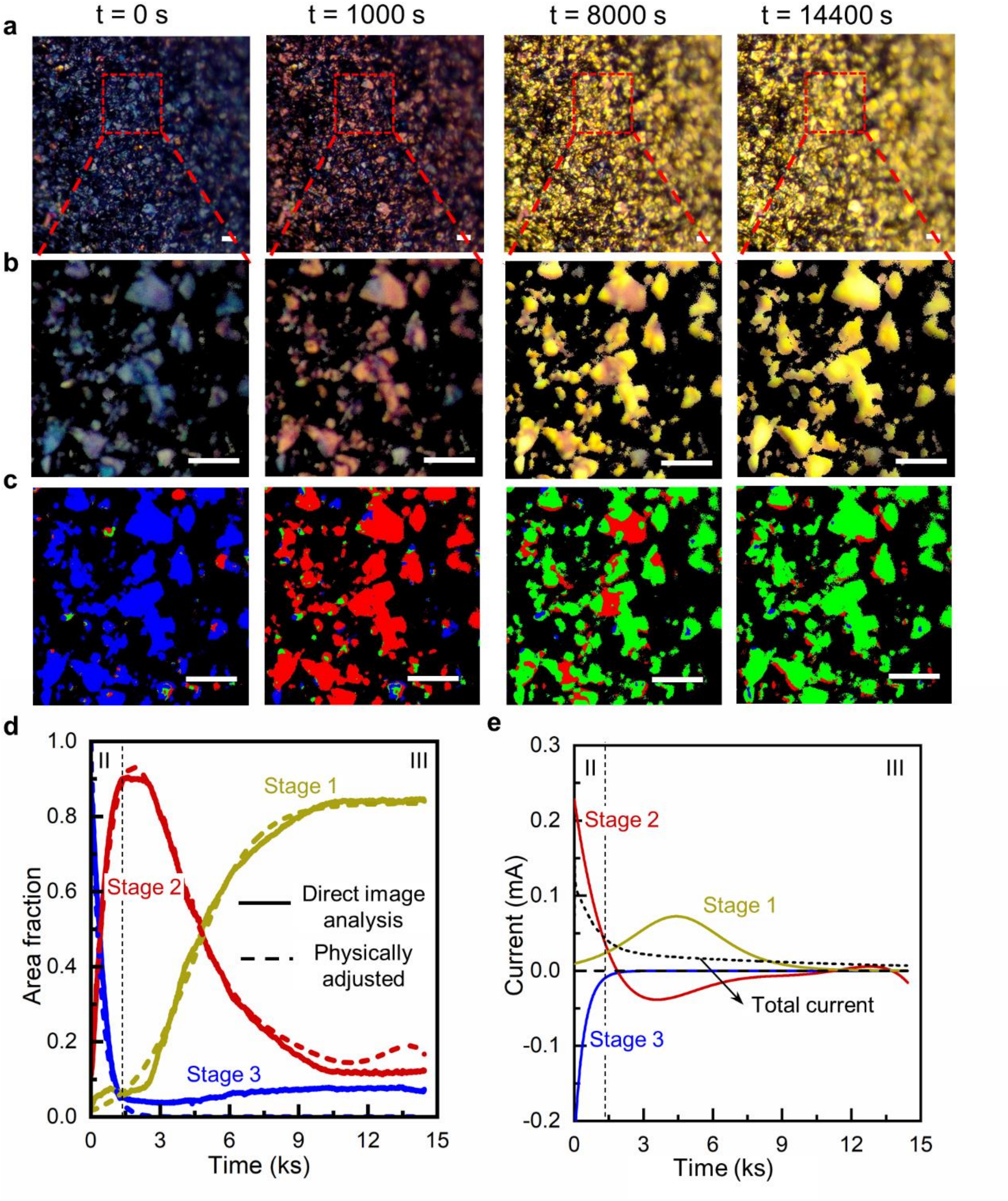

Figure 2.1: Evolution of stages during Li$^+$ ion intercalation during the voltage stepping from 85 mV to 75 mV vs Li/Li$^+$. a) Snapshots of the entire viewing area under the optical microscope with the 50x objective, at four times: t = 0 s, 1000 s, 8000 s and 14400 s. b) Magnified photos highlighting the coexistence of different stages intra- and inter- particles. c) The converted RGB images showing the actual area fraction quantification by ImageJ. The observed blue, red and gold colors were converted to standard blue, red and green colors, respectively. d) The evolution curves of the colored areas during the voltage stepping, obtained from the direct image analysis along with the physically adjusted analytical

curves (refer **Appendix A.5** for the fitting parameters). e) The derived phase currents based on the time-derivative of the physically adjusted area evolution curves. *Scale bar: 10 µm*

3 to Stage 1 is shown in Figure A-4. By converting the color into standard RGB map (Figure 2.1(c)), we were able to exclude the all-time inactive region and accurately quantify the areas covered by the three colors (Stages) in thousands of operando snapshots. The sequential reaction process is quantitatively reflected by the evolution curves of the area fractions for the colors, shown in Figure 2.1(d).

2.2.2 Currents carried by individual colors (phases)

With the SOCs for each color determined above, i.e. $x_B = 23\%$, $x_R = 55\%$. $x_G = 100\%$, the area fraction evolution curves can be converted into capacity evolution curves (**Figure A-5**), by $Q_i = x_i a_i(t) q_o A_T$. Here, i represents Blue, Red, and Gold colors, Q_i and a_i re the capacity and the area fraction of color i. q_o is the areal capacity of the entire electrode, and A_T is the total area of particles accounted in the image analysis. The capacity curves directly converted from experimental data were physically adjusted based on charge conservation, to exclude possible system and sampling errors. By further taking the first order time derivative of the charge associated with each color, the phase current can be obtained,

$$I_i(t) = \frac{dQ_i}{dt} = x_i q_o A_T \left(\frac{da_i}{dt}\right) \tag{1}$$

Figure 2.1(d) of the derived phase currents suggests that the stable phases grow/diminish faster than the rate of charge addition (total current), which points towards the direction that the local kinetic rate reflected by the phase boundary propagation is much higher than the electrochemical reaction rate estimated by using the total current. Since Li^+ ions insert into graphite particles through the edge planes, not the basal plane that reveal the colors, the area of the phase boundary, i.e. length of the phase boundary times the thickness of the particle, needs to be determined to quantify the true local current density for more accurate analysis of the kinetics. **Figure A-6** shows the area evolution and phase currents during 100 mV and 200 mV PITT experiments.

2.2.3 *Operando* interfacial current densities

In principle, Li^+ ions can intercalate into graphite particles from anywhere on the edge plane to form a shrinking-core type pattern, as observed in a 50-μm graphite disk[86] and 400-um graphite flake.[87] For our graphite particles with a mean particle size of 8.13 μm (**Figure A-7**), however, ion intercalations appear to occur only on a limited portion of the particle perimeter. The phase boundary, originated from the edge, appears to straighten itself to form an intercalation wave propagating through the remaining body of the particle (**Figure 2.2(a)**). Since we only observe color change at the phase boundaries and not in the stable regions during Li^+ ion intercalation, the net flux within any color is conserved. Therefore, the flux that leads to the movement of phase boundary is identical to the reaction flux at the particle edges. Based on this observation, we propose to use the mathematical product of the total length of the phase boundaries and the thickness of the graphite particles to evaluate the true *operando* interfacial area within the porous electrodes (see 2.5Experimental Section). With proper Boolean operations (see Experimental Section and **Figure A-8**), the length of the phase boundaries can be determined (**Figure A-9**). As shown in Figure 2.2(b), the total length of the Blue-Red (L_{BR}) boundaries increased at the beginning of the voltage stepping from 85 mV to 75 mV, then decreased toward zero in a time span of 1250 s. While the total length of the Red-Gold boundaries (L_{RG}) slightly increased at the onset of voltage stepping, it remained relatively constant at a value close to zero. The trend is consistent with the decaying of the global total current. At the moment L_{BR} decayed to nearly zero and stopped changing, a rapid increase in L_{RG}

was observed, corresponding to the onset of phase transformation from Red (Stage 2) to Gold (Stage 1), while the global total current was still decreasing, indicating a dramatic change of the true local (*operando*) interfacial current density. Similar to L_{BR}, L_{RG} decayed after reaching its peak value but with a much slower rate in accordance with the slow decaying rate of the total current during the Red-to-Gold phase transition.

The growth periods of the three stable phases are mutually exclusive, suggesting that the entire global current at any time is carried only by one phase. Hence, by using the global current and the *operando* interfacial area calculated above, the *operando* interfacial current density, i.e., the truly working local current density, can be estimated. As shown in Figure 2.2(c), the *operando* interfacial current densities are more than two orders of magnitude higher than the average current density calculated using the BET area ($9.424\ m^2 \cdot g^{-1}$). This two-orders-of-magnitude discrepancy will be amplified to a four-orders of magnitude difference in the derived diffusion coefficients, via the square-law scaling of traditional electroanalytical methods.[45,84] This discrepancy questions the prevailing belief that the rate-limiting step of Li^+ ion intercalation in graphite is the bulk solid-state diffusion.

2.2.4 Physical interpretation of the evolving phase boundaries

As suggested above, the color change only occurs at the phase boundaries during lithiation, which implies that their movement should be equivalent to the net reaction flux. At the same time, multiple nucleation and growths can emerge within a single particle (Figure 2.2(a)), followed by impingements between the growing domains. The observation is consistent with the classic recrystallization process that can be analyzed by the Kolmogorov-Johnson-Mehl-Avrami (KJMA) theory.[73,88–91] As shown in **Figure 2.3(a)** schematically, KJMA theory assumes that the ratio between the normalized *actual* incremental area of the new phase (dA) and the normalized “*extended*” incremental area (dA_{ext}) is always equal to the fraction of the untransformed area, $dA/dA_{ext} = (1 - f)$, where f is the fraction of the transformed area, identical to A. The differential equation can be solved (see the complete derivation in **Appendix A.10**) to obtain the normalized transformed area as $A = f = 1 - \exp(-A_{ext})$, and further develop into the final Avrami kinetic equation by incorporating the growth rate and dimensions for the ideal A_{ext}. However, the challenge for electrochemical phase transformation in our graphite electrode is to quantify the evolution dynamics of the total length of the phase boundaries, instead of the area.

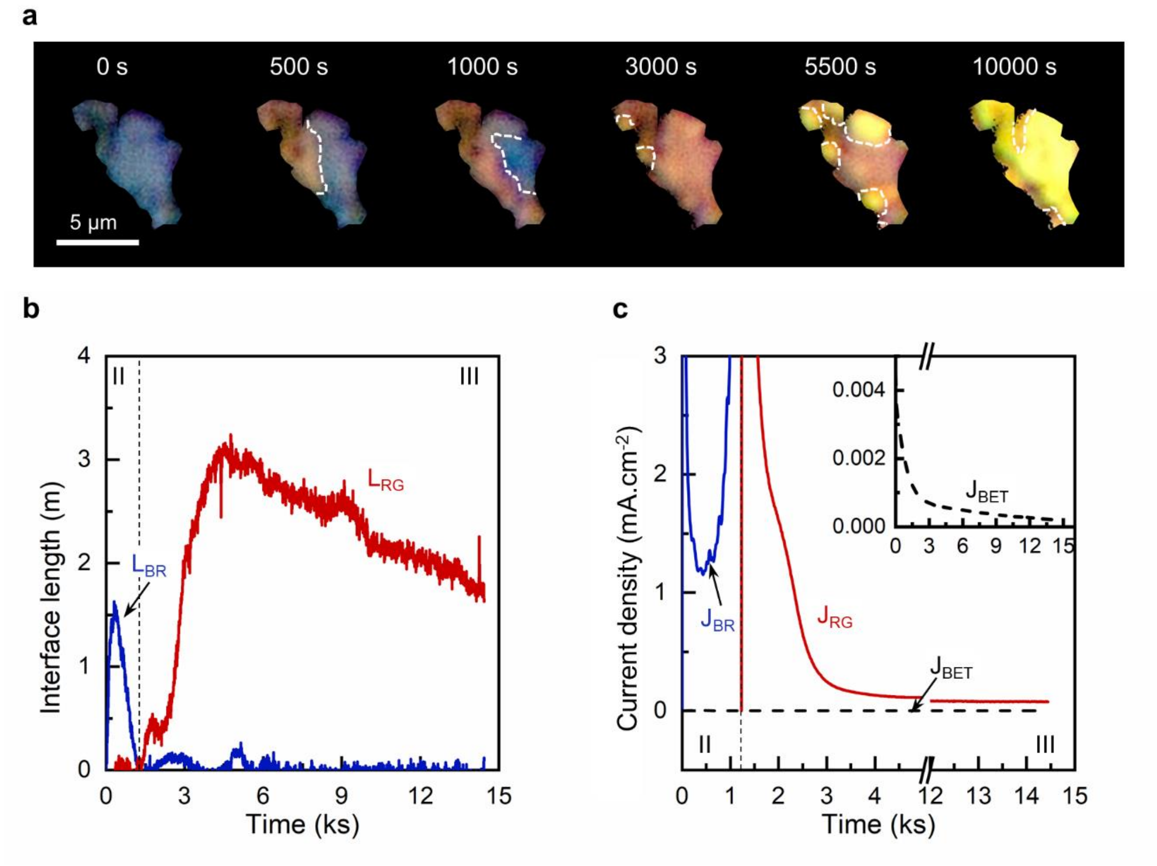

Figure 2.2: Evolution of the total lengths of phase boundaries and the associated true local current densities. a) Moving phase boundaries (white dotted lines) within a typical graphite particle during the 85 mV – 75 mV voltage stepping. b) Evolutions of the total lengths of interfaces between blue and red regions and between red and gold regions during the voltage step, determined from the direct image analysis of the viewing area of the electrode. c) The current density calculated based on the effective *operando* interfacial area. Inset shows the globally average current density based on the BET surface area.

The time axis has been shrunk for improved viewing of the *operando* interfacial current density during Blue-Red transition, since it is almost constant during the Red-Gold transition.

The key question is how much of the phase boundary associated with the ideal “extended” incremental growth dA_{ext}, designated as l_{ext}, will lie in the transformed region that cannot be accounted for the total length of the *actual* phase boundary l, as shown in Figure 2.3(a). Following the same strategy of KJMA, we propose that $l/l_{ext} = (1-f) = \exp(-A_{ext})$. Further considering the shape factor S, the dimension of growth n, and the growth velocity k, we obtained the final kinetic equation for phase boundary evolution as,

$$l = nS(kt)^{n-1}\exp[-(Skt)^n] \tag{2}$$

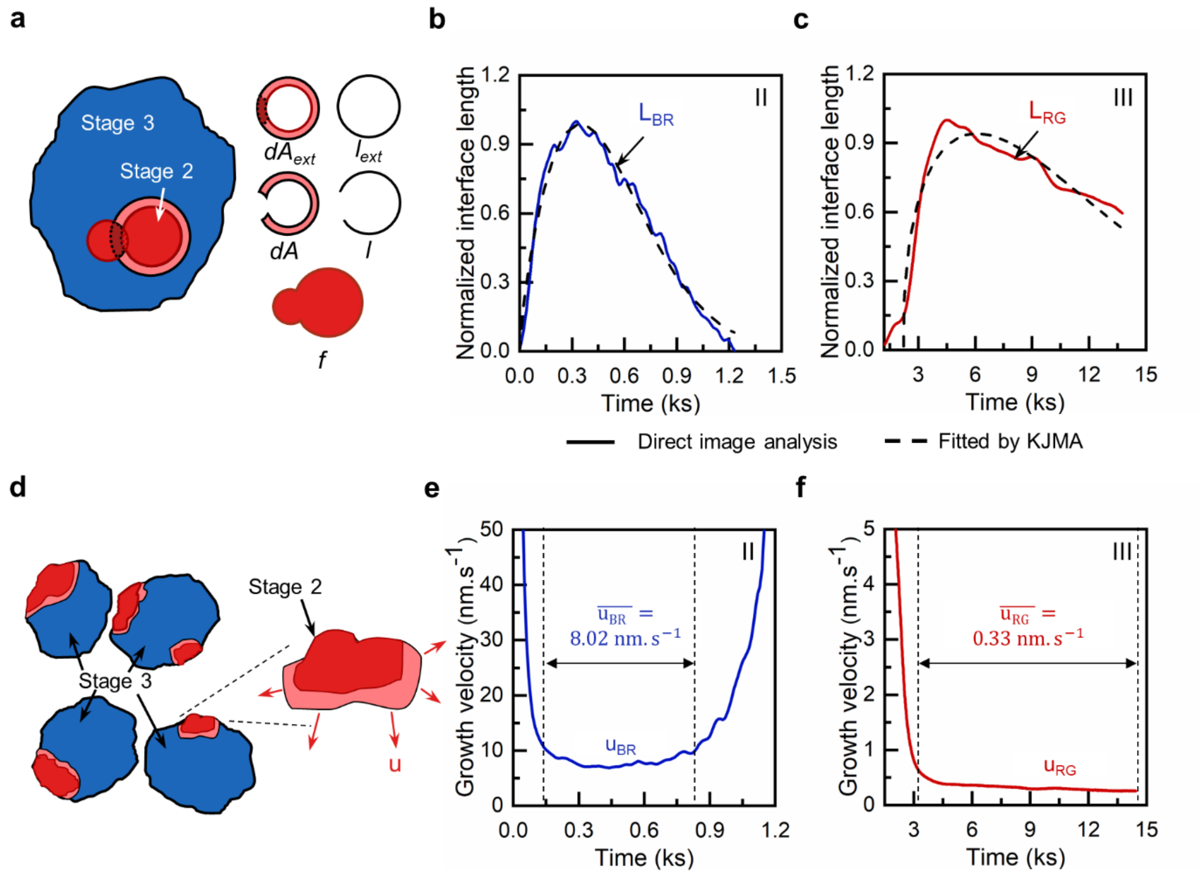

Figure 2.3: **Estimation of growth velocity of the stable phases using the proposed models.** a) Schematic representation of growth of Red phase onto the Blue phase explained using KJMA theory. b)

The normalized total length of interface between blue and red regions and c) between red and gold regions fitted using Equation 2 to estimate the dimension of growth *n*, shape factor *S* and growth velocity *k*, during the 85 – 75mV voltage stepping. The legend on panel c) applies to panel b) as well. d) Schematic representation of growth of Red phase from the Blue phase in multiple particles where its growth can be tracked using the *operando* interfacial current density. e) The growth velocity during Blue-Red transition and f) Red-Gold transition, calculated from the operando interfacial current density, during the 85 – 75mV step. The marked region between the dashed vertical lines indicate the region chosen to estimate the growth velocity.

Interestingly, Equation (2) is essentially the first-order time derivative of the classic KJMA equation.

As shown in Figures 2.3(b-c), our Equation (2) fit the normalized length of phase boundary very well, especially for the boundary between the blue and red regions Figure 2.3(b). While for an ideal 2-dimensional growth problem, the dimension exponent *n* should be 2, and the shape factor S should be $\sqrt{\pi} \approx 1.77$ for an isotropic circular growth, as can be seen in the **Appendix A.10**, here we relaxed the constraints during the fitting to keep the analysis general. As can be seen in **Table 1**, the fitted dimension exponent *n*'s are indeed close to 2, especially for the blue-red phase boundary for all three sets of the *operando* PITT experiments (**Figure 2.4**), which indicate that the new phase growth through plate-like graphite particles in our thin-layer porous electrode is indeed two dimensional. The fitted shape factor *S* is close to but not equal to the value of $\sqrt{\pi}$, indicating that the growth is not ideally isotropic as a shrinking-core process.

The third parameter in Equation (2) also has clear physical meaning. It represents the rate of growth of the new phases, i.e. the propagation velocity of the phase boundary, which is a direct result of the net reaction flux and can be quantified from the *operando* experiments by using mass conservation.

$$u(t) = j^{int} \frac{V_m}{F} \tag{3}$$

u(*t*) is the *effective* one-dimensional growth velocity of the new phase at time *t*, j^{int} is the interfacial current density of the corresponding phase calculated by dividing the global current *I(t)* with the *operando* interface area *A(t)*. V_m is the molar volume of that particular phase of the lithiated graphite, and *F* is the Faraday constant. Figure 2.3(d) schematically shows the growth of the new phase. The complete derivation can be found in the **Appendix A.11**).

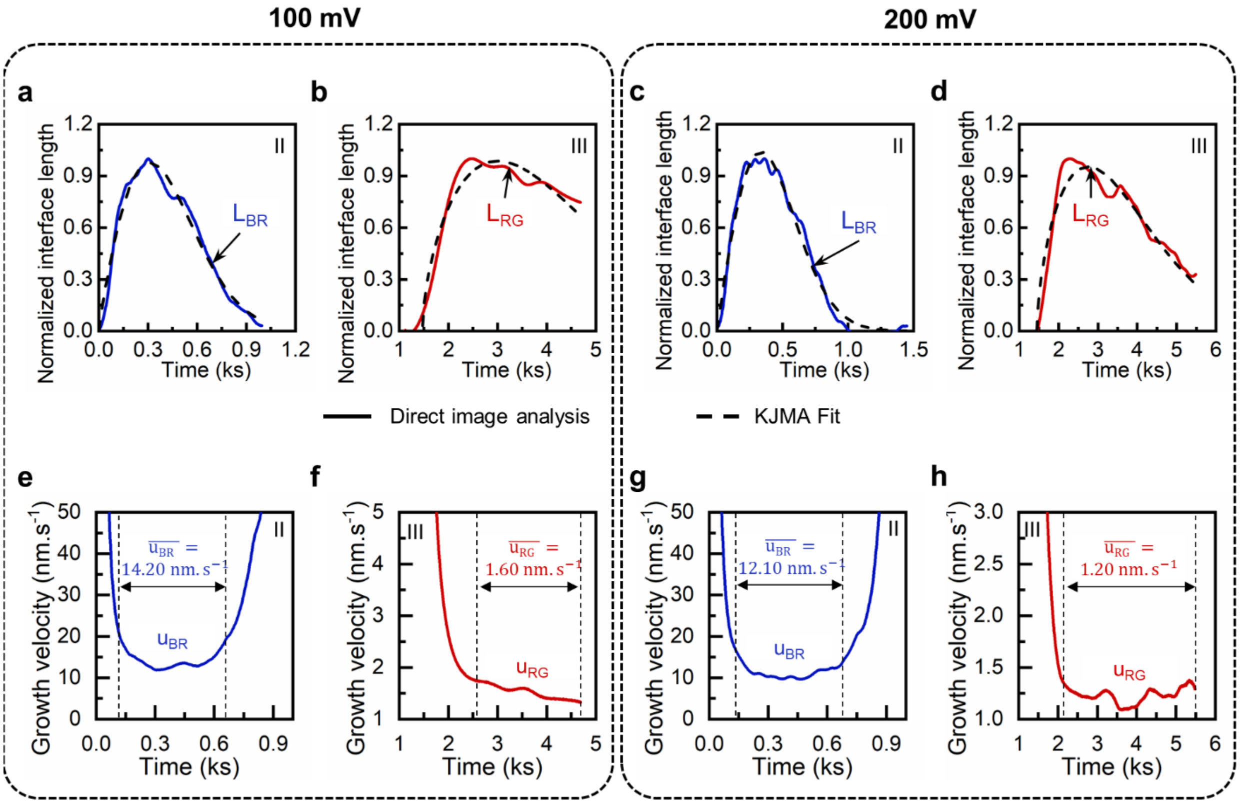

Figure 2.4: Growth velocity from operando observations during phase transition induced by 100 mV and 200 mV steps. Replication of *operando* interface length with KJMA equation during a) Blue-Red transition and b) Red-Gold transition in 100 mV case, and c) Blue-Red transition and d) Red-Gold transition in 200 mV case. Average growth velocity estimated from operando interfacial current density during e) Blue-Red transition and f) Red-Gold transition in 100 mV case, and g) Blue-Red transition and h) Red-Gold transition in 200 mV case.

Equation (3) shows that the growth velocity can be directly estimated from the *operando* interfacial current density. Since the *operando* interfacial current densities are relatively stable for the major portion of the corresponding phase transformation segments, despite spikes at the beginning and/or the end, an averaged growth velocity ($\bar{u}$) can be calculated (**Figures 2.3(e-f), and Figures 2.4(e-h)**). Table 1 lists the fitting parameters obtained from Equation (2) for all three cases, along with the averaged growth velocities obtained by using *operando* interfacial current densities. It is noteworthy that Equation (2) returns the growth velocity *k* with the units of s^{-1}. To find the actual growth velocity, we solved for Equation (2) with actual dimensions shown in the **Appendix A.10**. Equation (2) that fits the transient total length of the phase boundary, and Equation (3) that derived from the ratio between the transient total current and the transient phase boundary, independently explain the same phenomena from different perspective, but surprisingly obtain almost the same growth (i.e. interface propagation) velocity in the units of nm · s^{-1}. The self-consistent results not only validate our new model on the kinetics of the phase boundary evolution, but also indicate that the dynamic is controlled by the *operando* (i.e. local and working) electrochemical reaction flux, not solid-state diffusion.

Table 2.1: Parameters obtained from fittings the *operando* interface lengths with Equation (2) and the averaged growth velocity calculated from *operando* interfacial current densities

		10 mV	**100mV**	**200 mV**
Blue-Red	**n**	1.75	1.90	1.98
	S	1.48	1.36	1.48
	k_{fit} (nm·s^{-1})	13.4	11.6	15.8
	$k_{exp} = \bar{u}$ (nm·s^{-1})	8.02	14.20	12.10
Red-Gold	**n**	1.39	1.58	1.60
	S	1.41	1.52	1.43
	k_{fit} (nm·s^{-1})	0.5	1.5	2.2
	$k_{exp} = \bar{u}$ (nm·s^{-1})	0.33	1.62	1.24

2.2.5 Determination of the diffusion coefficients

The direct correlation between the growth velocity and the *operando* interfacial current density revealed above raises the question whether the solid-state diffusion coefficient can still be reliably extracted from the standard PITT experiment originally established specifically for the evaluation of solid-state diffusion.[42] As can be seen in **Figure 2.5(a-c)**, the lack of straight lines (predicted by the classic Cottrell equation) suggests that the processes are likely not diffusion-limited. As our first attempt, we adopted the modified PITT (mPITT) model,[92,93] without the presumption of the rate-limiting step, to fit the *operando* interfacial current densities. Both the diffusion coefficient D_{Li} and the electrochemical Biot number B, can be obtained by minimizing the least squares. Good agreements can be found for the solid solution processes (**Figure 2.5(a)**), but not for the Blue-Red phase transformation (**Figure 2.5(b)**). Interestingly, the mPITT model (Equation (S7a) in **Appendix A.12**) can fit the *operando* interfacial current density for the Red-Gold phase transformation in the $t << l^2/D_{Li}$ regime fairly well, especially in the PITT experiments with 10 mV and 200 mV steps. It's worth noting that, among all the recorded phase transformation processes, only the Red to Gold transformation was long enough to enter in the regime of $t >> l^2/D_{Li}$, but cannot be fitted by the mPITT model for $t >> l^2/D_{Li}$, i.e. Equation (S7b) in **Appendix A.12**, as the *operando* interfacial current densities remain relatively constant. Although the mPITT model does not specifically take into account the phase transformation processes, it holds the generality from its origin of direct mathematical approximations to the battery voltage and current. Therefore, the fittings for the Red-Gold phase transformation process may still provide insights from the apparent good agreements. A critical feature of the mPITT model is that the apparent two independent fitting parameters are actually constrained by the system-specific exchange current density (j_0) via the definition of Biot number, $B = -j0l(\partial U/\partial C)/(DLiRT)$. Here, $\partial U/\partial C$ is the derivative of the open-circuit voltage (OCV) with respect to the solid-state Li^+ ion concentration, R is the gas constant and T is the temperature. Again, the model becomes inapplicable in the “ideal” phase-transformation regimes due to $\partial U/\partial C$ being zero leaving j_0 impossible to identify. Nevertheless, the application of a modified PITT (mPITT) model[92,93] without presumption of the rate-limiting step can give a rough estimate of the diffusion coefficients of Li^+ ions into graphite. The Li^+ ion diffusion coefficients, extracted from fitting the mPITT model on the *operando* interfacial current density during the solid-solution lithiation (Segment (I)), lies between $1.35 \times 10^{-11} – 3.27 \times 10^{-10}$ $cm^2 \cdot s^{-1}$, consistent with the reported values.[8,9,58,60,63,64] The corresponding electrochemical Biot numbers (B) shown in Figure 2.5(d) suggest a diffusion-limited process. On the other hand, the diffusion coefficients for the Red-Gold phase transformation processes lying in the range 1.98×10^{-8} – 1.31×10^{-7} $cm^2 \cdot s^{-1}$ across the three sets of experiments, which are in very good agreements not only with the Cahn-Hilliard phase field simulation of a 50-um graphite disk,[86] but also the first principles calculations.[62] Such a fast diffusion means a very low diffusion time constant, $\tau_D = L^2/D_{Li} = 1 – 8$ s where L is the diffusion length, set to be one half of the dimension of basal plane,[9] i.e. 4 µm for our case. **Figure A-10** shows consistent interpretation for the responses in other PITT voltage steps during solid-solution intercalation. Our results provide a straightforward evidence that once the spatiotemporal heterogeneities emerge, the process is no longer diffusion-limited, consistent with a recent scaling analysis.[87]

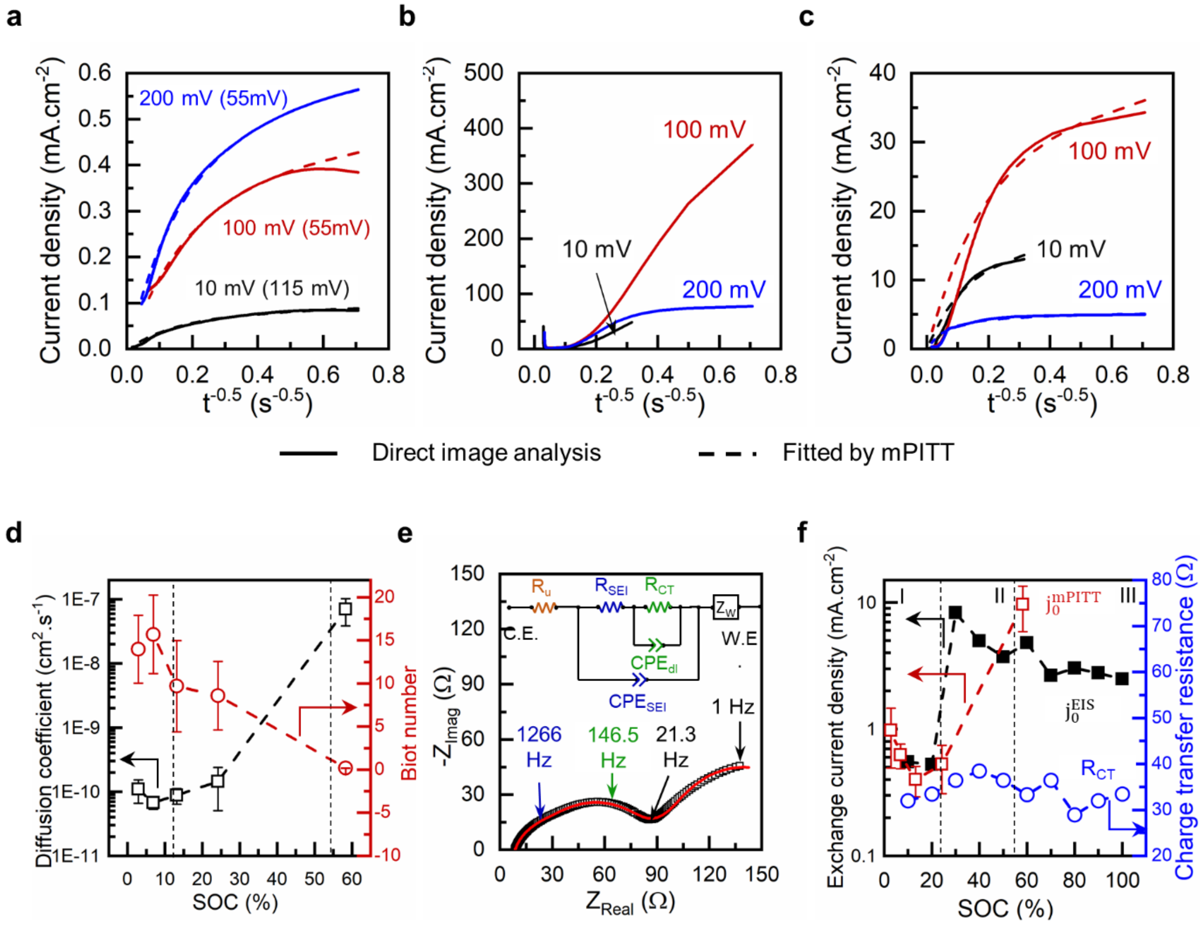

Figure 2.5: Independent experiments to estimate the kinetic parameters. a) The fitting of representative *operando* interfacial current density during solid-solution processes in all the three sets of experiments with the modified PITT model to extract the Li$^+$ ion diffusion coefficient into graphite. The voltage mentioned in brackets are the voltage step during the corresponding PITT experiment. b) The *operando* interfacial current density during Blue-Red phase transformation in all the three sets of experiments. They could not be fitted with the modified PITT model owing to their highly non-monotonic nature. c) The fitting of *operando* interfacial current density during Red-Gold phase transformation in all the three sets of experiments with the modified PITT model to extract the Li$^+$ ion diffusion coefficient into graphite. d) Extracted D_{Li} and B from the fitting the operando interfacial current densities in panel (a) and (c) with the mPITT model. The vertical dashed lines separate the entire region into diffusion-controlled, mixed control and reaction-controlled regimes. e) Fitting of experimental EIS data with the specified equivalent circuit model composed of two RC circuits and a porous-bounded Warburg impedance. The blue and red semi-circles are the individual contribution of the two RC circuits with the frequencies of the respective peaks being ω_{SEI} and ω_{dl}. Here, R_{SEI} and R_{CT} are the charge-transfer resistances of the SEI and double layer, CPE_{SEI} and CPE_{dl} are the constant phase elements of SEI and double layer, and Z_W is the porous-bounded Warburg impedance. f) Exchange current density estimated from the EIS using *operando* interface area and that from mPITT averaged over three sets of experiments

along with its close agreement with the exchange current densities calculated from D_{Li} and B using mPITT model.

2.2.6 Impedance analysis for the *operando* exchange current densities

While the mPITT method itself allows the evaluation of $j0$, independent electrochemical impedance spectroscopy (EIS) experiments were performed on the same *operando* cells to assess the interfacial reaction kinetics during Li^+ ion intercalation. **Figure 2.5(e)** shows the Nyquist plot of a typical EIS spectra, which appears to have two partially merged semicircles followed by a Warburg tail. While the Warburg tail can be attributed to the solid diffusion in graphite particles, the two semicircles need careful examination of their physical basis. Based on the consensus that the charge transfer reaction occurs on the surface of graphite particles, but beneath the solid electrolyte interphase (SEI) layer, we hypothesize that (i) the electrical double layer capacitance associated with the charge transfer will form within the SEI; and (ii) the charges at the electrolyte|SEI interface and those at the SEI|graphite interface will form a double-plate capacitor filled with the SEI layer. To test the hypothesis, the EIS spectra was fitted with the equivalent circuit model shown in **Figure 2.5(e)** to obtain the two resistances (R_{SEI} = 38.4 Ω and R_{CT} = 32.0 Ω), which were then use to calculate the capacitances from the two characteristic frequencies (ω_{SEI} = 1266 Hz and ω_{CT} = 146.5 Hz) labeled in Figure 2.5(e), via the general formula $\omega = (RC)^{-1}$. The calculated capacitances (C_{SEI} = 20.5 μF and C_{CT} = 21.4 μF) were then used to determine the associated dielectric constants via $C = \varepsilon_r\varepsilon_0 A_{\mathrm{edge}}/d$, where A_{edge} = 1.459 cm^2 is the total area of the edge planes, d is the thickness of the respective capacitors (assuming 10 nm for the SEI layer and 1 nm for the electrical double layer), ε_0 is the absolute permittivity of vacuum and ε_r is the dielectric constant. The resulting dielectric constants (161.2 and 167.5) are surprisingly very close to each other, but much higher than the dielectric constants for liquid electrolyte (<90) we used in the *operando* cells,[94] yet consistent with the reported values for the solid electrolyte interphase[95] and solid polymer electrolytes.[96] This quantitative physical confirmation validates our hypothesis on the microstructure of the equivalent circuit model. All the parameters obtained from the fittings of the equivalent circuit model at 10% - 100% SOCs are displayed in **Table A-3** in **Section 13**. The charge-transfer resistance (R_{CT}) thus obtained were used to calculate both the exchange current density via[90] $j_0 = RT/(FR_{\mathrm{CT}}\ A_{int})$ as shown in Figure 2.5(f), and the reaction time constant $\tau_R = Q/j_0A_{int} = (QFR_{CT})/(RT)$. Here, A_{int} is again the *operando* interfacial area, Q is the total charge transferred to the electrode, R is the gas constant and F is the Faraday constant. These values of j_0 are in good agreement with those obtained from mPITT fitting at selected SOCs. The reaction time constant τ_R calculated from the maximum capacity of the electrode lies between 488 and 680 s for the three sets of experiments. These maximum possible values of τ_R is almost half of the Blue-Red transition time (1000 – 1250 s), and 7 – 20 times lower than the Red-Gold transition time (5000 – 13000 s). While this comparison between time constants seems to suggest that the process is not limited by reaction, it is the actual *operando* interfacial current density, not the exchange current density or the exchange reaction rate that plays the role in the actual process, which was also pointed out by Fraggedakis et al.[87]

2.3 Discussion

From analyzing the dynamics of phase boundary evolution by using Equation (2) and evaluating the true local exchange current density by using the physics-based equivalent circuit model, our results clearly suggest that the electrochemical lithiation process of particulate graphite electrode is not diffusion-limited. Therefore, classic electroanalytical methods based on the diffusion-limited assumption are not appropriate for determining the diffusion coefficient, even if the true local current density can be accurately determined. This is particularly important for phase-transformation electrodes, for which the classic methods require the term *dU/dC* that becomes zero at the phase-transformation plateau, making other physical quantities impossible to identify. This is also the reason that the Warburg fittings from our physics-based EIS analysis cannot be used to determine the diffusion coefficient, as the *dU/dC* term is again required for the Huggins equation to convert the Warburg factor.[44] From a deeper perspective, the original derivation[60] of now the widely used Warburg impedance did not take into account any phase transformation processes. Even if one can get around the *dU/dC* term,[97] the obtained the diffusion coefficients are still several orders of magnitude lower (**Table A-5**), by which a Cottrell-type diffusion-limited process is dictated but does not exist in all our experiments. The only reliable electrochemical method of obtaining the diffusion coefficient in phase transformation materials appears to be modeling the transients from a single particle with precise *operando* current density.[86]

Regarding the rate-limiting step of electrochemical processes in particulate phase transformation electrodes, our results rejects the simple yet convenient terms of diffusion-limited or reaction-limited. It should rather be designated as phase-transformation controlled for two reasons at two different scales. First, at the single particle scale, the reaction rate is controlled externally by electrochemical driving force. Therefore, whether the entire process is diffusion-limited or reaction-limited is extrinsic. Unless the local current density for the single particle can be exclusively and precisely determined and controlled, determining the rate-limiting step and the kinetic parameters would remain very challenging. Second, at the mesoscale with at least hundreds of particles, while one can precisely determine and control the *total* current, the self-adapted local driving force would activate different numbers of particles[73] to share the total current, leading to unexpected *operando* (local and working) current density. As can be seen in

Figure 2.5(b-c), the *operando* interfacial current densities from 200 mV PITT experiments are surprisingly and significantly lower than those from 10 mV and 100 mV PITT experiments, which are the exact results of that the higher driving force (200 mV versus 100 mV and 10 mV) promoted more phase transforming particles with longer total phase boundaries. This observation is consistent with a recent study on thick graphite electrodes using XRD-CT, in which the phase transformation from stage II (red) to stage I (gold) requires higher local overpotentials to initiate and move the reaction front.[26] It is the phase transformation dynamics that controls how many particles and how much interfacial area will be activated for working, and it is still the phase transformation dynamics that controls the evolution of phase boundaries within each particle. Therefore, it should be recognized that the phase-transformation control mechanisms at both scales induce the spatiotemporal heterogeneities and limit the overall performance of the electrode.

Our results also raise a fundamental question: whether the electrochemical response from electrode under small excitations (e.g., low total current) can be considered from quasi- or near-equilibrium physical processes. It is apparent now that the electrochemical responses of the electrode (total current and terminal voltage) are collective behaviors of *far-from-equilibrium* dynamics contributed only from a small portion of the electrodes. The insights from this study stress the necessity of careful examination of the local electrochemical activities.

The accuracy of our image analysis is largely dependent on the color segmentation process, as described in the Experimental Section. The color segmentation process is susceptible to human error, and careful multi-point calibrations must be implemented. We also performed a necessary sensitivity analysis on the choices of thresholding criteria extracted from the benchmark images (**Figure A-8**). The results suggest only minor variations in the extracted areas

(**Figure A-13**), which must be further verified by charge conservation (**Figure A-5**). Due to the brightness changes of different colors under the visible light microscope, it is necessary to exclude some very small particles that can only be clearly revealed when they are gold. The application of a black mask on all the digital images ensures the consistency for all cases. Despite being an area approximation method, the systematic calibration and validation ensure the fidelity of our method to be a simple yet effective way to study the dynamic heterogeneities in thin electrodes.

Our method, with an ability to clearly identify particles as small as ~2 μm and phase boundaries (color interfaces) as thin as ~ 0.1 μm, is not limited to the PITT technique. Revealing the mesoscale spatiotemporal heterogeneities under other types of electrochemical excitations (e.g. galvanostatic cycling, cyclic voltammetry, etc.) will lead to critical refinements to existing understandings of the electrochemical kinetics and rate-limiting steps. The study of spatiotemporal heterogeneities should only be performed on thin electrodes to dampen them along the electrode thickness[19,26], as ensured in our case to be 5 μm. For electrode materials without this unique visible color-changing property, our setup may be combined with other imaging techniques such as Raman spectroscopy and X-ray diffraction computed tomography to achieve more accurate heterogeneity maps with enriched physical information,[26,40,98] which can be further analyzed following our methods to obtain the *operando* interfacial kinetics.

2.4 Conclusion

By exploiting the colorimetric behavior of lithiated graphite, we have demonstrated a direct, simple, yet precision method to monitor and quantify the spatiotemporal heterogeneities in particulate porous electrodes. The true local current density, i.e. the *operando* interfacial current density by our definition, obtained from direct image analysis is ~100 times higher than the BET-average current density. Although all the particles in the porous electrodes are electrochemically active and eventually get fully intercalated with the Li^+ ions, at any time instant, only a limited number of particles and limited portion of the total available area receive the ionic flux. Our *operando* monitoring clearly revealed that once a successful nucleation event occurs and phase boundaries start to form in a randomly chosen particle, it is preferred for further intercalation irrespective of its shape and size. Since the Li^+ intercalation into graphite particles is not diffusion-limited, smaller particles do not necessarily provide a substantial improvement in the high-rate performance. However, reducing particle size may help eliminate the reaction heterogeneities by altering the nucleation barrier for solid-state phase transformation in individual particles, such that the concurrent reaction pathway become thermodynamically favorable.

2.5 Experimental Section

Thin electrode preparation: Graphite flakes (7-10 µm, 99%, Alfa-Aesar), PVdF binder (>99.5%, MTI Corp) and conductive acetylene black powder (35-40 nm, MTI Corp) were mixed in the ratio 88:10:2 and dissolved in 1-methyl-2-pyrrolidone (NMP, 99.5%, Sigma Aldrich) to form a homogeneous slurry. To ensure the best imaging quality, the slurry was coated onto separator film by the doctor-blade method. The electrodes were dried at 60°C to remove the NMP. Φ8 mm electrodes were punched out and were kept under vacuum at 70°C for 12 hours to remove the residual moisture. The active material loading, and electrode thickness were 0.7 mg cm^{-2} and 5 µm, respectively. The SEM images of the electrode are shown in the **Figure A-1**.

***Operando* setup and experiments.** A half-cell using the thin graphite electrode, a Li anode, a glass-fiber separator, and 1M $LiPF_6$ in EC:DMC (50:50 v/v) in a standard 2032 coin cell with a 2 mm hole on the top, was assembled in an Ar-filled glovebox. A 5 x 5 mm glass window was attached using epoxy to seal the cell and view the graphite flakes under the optical microscope. The coin cell was placed on a stage of the Olympus BX53M microscope under objective 50x for *operando* observation. The cell was cycled at C/4 current five times between cut-off voltages 1.5V and 0.4 mV, to form a stable SEI. We then, performed a three PITT discharge experiments from 245 mV to 0.1 mV, varying the voltage steps and C/20 threshold current: 1), with 10 mV, 2) 100 mV, and 3) 200 mV step sizes, while capturing the time frames every 10s. All the acquired digital photos were processed using ImageJ to quantify the colored regions. The detailed description of the procedures is mentioned below. See **Appendix A.3-A.9** for more details.

An Electrochemical Impedance Spectroscopy (EIS) was conducted at intervals of 10% SOC from 10% to 100% SOCs. The cells were discharged at 0.1C current to the relevant SOC and relaxed for 2h to reach equilibrium before taking the EIS measurements. All the EIS measurements were taken at 10 mV amplitude in the frequency range 1 MHz – 1 Hz. The obtained Nyquist plots were fitted using the equivalent circuit model, shown in Figure 2.5(a).

Color thresholds for area quantification. The built-in Hue-Saturation-Brightness threshold method of ImageJ was used to identify the blue, red and gold colors in the photos captured in the *operando* PITT experiment. ImageJ auto-selects the brightness to accommodate all the non-black regions/graphite flakes. Due to the difference in the brightness of blue, red and gold colors, some smaller particles (~ 2 μm), which were not clearly visible when they were blue or red, got illuminated upon turning into gold color. This illumination caused the auto-select feature of

ImageJ to select more area when the particles entered Segment III (or Stage I). The maximum difference in the selected area across all the images was < 10%, but still resulted in slight inconsistency while calculating the area fraction of different phases. To avoid this inconsistency, the same sampling region was defined based on the images at 55% SOC while converting the surrounding areas black (i.e. excluding voids, in which there could be small blue and red particles that are not clearly visible). Note that at 100% SOC, all active particles should appear bright gold. The unreacted regions (in the saturation range between 0 and 40) were selected and converted into black. The final black mask was applied to all the images. Within the sampling regions, a fixed range of hue was used to select similar colored regions (Red: 0 – 24, Gold: 24 – 44, and Blue: 44 – 255) while maintaining the same range of saturation (40 – 255) and brightness. The criteria were selected based on the low current discharge (C/72) when all the particles are in a particular phase as shown in **Figure A-8**. The above criteria were applied to all the digital images with the help of an ImageJ script. A variation of ±10% in the selected thresholds results in a deviation of only ±0% – 5% in the selected areas of blue, red and gold as shown in the **Figure A-13**.

Charge conservation calibration. The area evolution curve in Figure 2.1(c) was investigated to understand how the stable phases change, which is responsible for the surface reaction, by applying the charge conservation within the electrode, $\sum_i q_i A_i(t) = q_T(t) A_T$, where i represents Blue, Red, and Gold, q_i is the areal capacity of the i^{th} color and can be calculated from the SOC of the i^{th} color (estimated above) and the theoretical areal capacity of the material (q_o), $q_i = x_i q_o$, A_i is the area covered by i^{th} color, q_T is the areal capacity of the electrode and A_T is the total surface area of particles in the electrode. The above equation can, then be transformed into $\sum_i x_i a_i(t) = x_T(t)$ where a_i is the area fraction of the i^{th} color, and x_T is the global SOC of the electrode. For known area fractions of stable phases, a phase-transforming material should inherently follow this equation. Since we only observed a 100 × 100μm window under the optical microscope, the validity of the above equation for the observed region confirms that the analysis can be confidently extrapolated to the entire electrode (**Appendix A.5**).

Curve validation and physical adjustment. The capacity carried by each stage during the PITT discharge was calculated using $Q_i = q_i A_i(t) = x_i q_o a_i(t) A_T$, as explained in the main text. The equation is valid because the intercalation process satisfied the equation $\sum_i x_i a_i(t) = x_T(t)$ during the entire PITT (**Appendix A.5**). The individual capacity contribution follows the same trend as the area fraction evolution curve in Figure 2.1(c). They were individually represented by analytical expressions, for instance, Stage 3 by an exponential curve, Stage 2 by a 6th order polynomial equation and Stage 1 by a logistic S-shaped curve. A detailed description with fitting parameters is provided in the **Appendix A.5**. The phase currents were calculated by taking a 1st order time derivative of the obtained analytical expressions (Equation 1).

Small noises were observed while estimating the length of interface using ImageJ (Figure 2.2(a)) due to errors arising in the pixel-by-pixel measurement. We removed this noise by applying a quadratic regression method in MATLAB, enabling us to obtain smooth interfacial current densities.

Determination of the effective interfacial area: For a shape with two colors, ImageJ can be used to find the perimeter covered by each color, and the outer perimeter of the shape, which together can be solved for the length of the interface. In our case, particles existed in three different states at a time. To calculate the length of the interface, for instance, the Blue – Red interface, we relied on the fact that the phase transformation in graphite can only occur in one order: Stage 3 to Stage 2 to Stage 1. We converted all the green regions in the transformed RGB images, to the standard red color, thus eliminating all Red – Gold interfaces. This enabled us to find the length of the Blue – Red interface using the above methodology from the following equation, $L_{BR} = (l_{Blue} + l_{Red} - l_{particles})/2$. Similarly, we calculated the length of the Red – Gold interface by converting all the blue regions to the standard red and applying following equation, $L_{RG} = (l_{Red} + l_{Gold} - l_{particles})/2$ where L_{BR} and L_{RG} are the lengths of Blue – Red and Red – Gold interfaces respectively, l_{Blue}, l_{Red} and l_{Gold} are the perimeters of the blue, red and gold regions in the corresponding transformed images, and $l_{particles}$ is the outer perimeter of all the particles within the viewing frame.

Considering disc-shaped flakes with an average diameter 8µm and thickness 0.5 µm, our ~5 µm thick electrode constituted ~10^7 particles with 10 layers stacked over each other. On making a statistical assumption that all layers were similar, we calculated the active area by multiplying the total length of phase boundaries with the electrode thickness.

Chapter 3: Dynamic Interplay between Phase Transformation Instabilities and Spatiotemporal Heterogeneities in Particulate Graphite Electrodes

The results reported in this chapter have been published in – Agrawal, S., & Bai, P. (2022). "Dynamic interplay between phase transformation instabilities and reaction heterogeneities in particulate intercalation electrodes." Cell Reports Physical Science, 100854.

3.1 Introduction

The great success of lithium-ion batteries (LIBs) has allowed them to penetrate the markets of consumer electronics and electric vehicles.[1–3] The dynamic performance, cycle life, and safety of LIBs are directly dependent on the microscopic heterogeneities arisen from multiple fully-coupled electrochemical dynamic processes, which however are still not completely understood.[99,100] The state-of-charge (SOC) heterogeneities or non-uniform distribution of charge in both the phase-transforming[20,21,23,80] and solid solution[29,31–33,101] materials occur due to either the far-from-equilibrium thermodynamics of the active material or the heterogeneous microstructure of the composite electrode. In solid-solution cathode materials, in particular,[24,29,32] SOC heterogeneities were commonly attributed to structural heterogeneities, such as the non-uniform distributions of conductive additives, electrolyte, etc., but the actual root cause is worth careful examination, as the well-known solid-solution materials may exhibit "fictitious phase transformation" only under dynamic conditions that require *operando* characterizations.[37] The SOC heterogeneities in battery electrodes influence the accurate estimation of battery SOC in the battery management systems (BMS) which are responsible for their safe and reliable operation, prevention of physical damages, and handling of thermal degradation and cell unbalancing.[102–104] Sophisticated *operando* techniques employing synchrotron-based X-ray,[24,26,27,29,31,34,40,105] lasers[32,101] and visible light,[80,106–109] have been developed to generate valuable insights and obtain quantitative understandings about the effect of reaction heterogeneities on the intercalation mechanism and degradation behavior in the battery materials. Among them, the *operando* characterization using economical benchtop optical microscopes have demonstrated a well-rounded balance of large field of view with hundreds of particles, sub-micron resolution, fast imaging rate, and accurate interpretation of the electrochemical response.[32,101,106,108,109]

Graphite is one of the most studied carbon materials and is the dominant anode material for lithium-ion batteries, yet can be used as cathode in other battery systems.[110–113] Unlike other reversible electrode materials, graphite experiences multiple phase transformation steps upon ion intercalations, also known as ordered stages.[114–116] During lithiation into graphite, the optical characterization of phase transformation reveals three major stages visible as blue (Stage 3), red (Stage 2), and gold (Stage 1) colors.[109,117] However, the widely accepted theory that the phase transformations can be suppressed[118] has not been rigorously tested in graphite,[86,117] due to the lack of cohesive combination of *operando* characterization tools and mathematical analyses. The complex phase transformation mechanisms in graphite affect its rate capability and cycle life and need a careful inspection to ensure improved performance.

Here, we use our benchtop *operando* platform to observe the reaction pathway of graphite (de)lithiation in real-time under both slow and fast galvanostatic conditions. Despite the 10 times difference in the applied total currents, direct image analyses reveals that the true local current densities are very similar. The phase transform dynamics appear to modulate both the numbers of reacting particles in the electrode and the propagation of phase boundaries in individual particles autonomously to achieve the most "comfortable" local current density for the composing particles. Our linear stability analysis based on the non-equilibrium thermodynamics provides the predictive explanations to the suppression or persistence of phase separation in these graphite particles. With the confirmation from phase-field simulations of 200 particles, the insights obtained from this study not only complement other advanced *operando* characterizations including those based on synchrotron X-ray, but also can help understand the effects of operation protocols of battery charging and discharging to minimize the dynamic heterogeneities toward longer battery cycle life.

3.2 Results

3.2.1 Phase transformations in galvanostatic cycling

Our simple optical method has demonstrated the capability to reveal the subtleties of Li^+ ion (de)intercalation into practical graphite electrode under constant-voltage conditions, allowing the development of the boundary-length evolution kinetic model to understand the local electrochemical kinetics.[28] Here, under the practical constant-current conditions, the seemingly random phase transformation dynamics is found to be governed by the interplay between the non-equilibrium thermodynamics of the material and the true local current densities. We first evaluated the transition of colors in graphite particles (**Table A-3**) from grey (Empty) to blue

(Stage 3), to red (Stage 2) and to gold (Stage 1), under slow (0.1 C) and fast (1 C) galvanostatic conditions between 0.0004 V and 1.5 V vs Li/Li^+ in Li-graphite half cells (**Figure 3.1 and Figure B-2**). The applied currents of 0.1 C and 1 C correspond to 0.034 $mA.cm^{-2}$ and 0.34 $mA.cm^{-2}$, respectively, based on the geometric area of the electrode. At the critical SOCs shown in **Figure 3.1(a)**, all particles in the porous electrode appeared the same color, indicating the same stage, but the dynamic phase transformation processes between the critical stages were highly heterogeneous. The entire lithiation process followed a sequential phase transformation from empty to stage 3 (grey to blue, Step I), stage 3 to stage 2 (blue to red, Step II), and stage 2 to stage 1 (red to gold, Step III), which was reversed during delithiation. An accurate identification of the three stages via their respective colors in all the captured snapshots on the electrode-scale, serves as the backbone of the data analysis presented in this study. The consistency between net electrode capacity calculated from the image analysis (**See Experimental Section**) and the electrochemical measurements in **Figure B-4**, confirms the accuracy of the image analysis. Hence, the evolution of the stable phases (**Figure B-3**) and the length of the phase boundaries (**Figure B-5**) in the entire electrode were estimated from the image analysis during the galvanostatic experiments. The initial grey to blue transition always follows a solid-solution reaction pathway, during which all particles react concurrently. To examine the intricacies of the two phase-transformation steps (II and III) closely, we selected five representative particles, P1 – P5, highlighted in **Figure 3.1(a)** and magnified in **Figure 3.1(b-d)**. We chose these five particles P1 – P5 randomly from the entire field of view based on their different shapes and sizes, as marked on the particle size distribution curve (**Figure B-14**) obtained using ImageJ from the view under optical microscope. Such a selection would exclude any bias introduced while comparing particle-level phenomenon to the electrode-level phenomenon.

During 0.1 C lithiation, the new phases in both phase transformation steps always nucleate at the particle edge to create sharp phase boundaries, which sweep across the particle to complete the phase transformation. However, at a large scale, the intra-particle blue-red transformation is associated with a highly random and selective inter-particle dynamics. Like the particle-by-particle intercalation in $LiFePO_4$ electrode at a low current,[34] the red phase nucleated in particle P3 first, followed by P1. Particles P2, P4, and P5 remained idle (blue) until P3 and P1 became completely red (**Figure 3.1(b)**). Moments later, the red phase nucleated in particle P2 and took nearly an hour to complete the transformation, whereas the smaller particles P4 and P5 easily transformed into red color, successively, due to smaller volume. A similar sequential blue-red transformation occurred in all the other particles, suggesting that only a limited fraction of the electrode was "active" at any instant. The red-to-gold phase transformation at 0.1 C current, however, started simultaneously in most of the particles, within which sharp phase boundaries between the red (Stage 2) and gold (Stage 1) colors were still clearly visible. More obvious than in the blue-to-red transformation, smaller particles such as P4 and P5 incubated successful nucleations much sooner and got fully-filled much earlier than larger particles. The delithiation process at 0.1 C current triggered the random nucleations of the red phase (Stage 2) in most gold particles, essentially reversed the lithiation process until SOC reaches 55%, as shown in **Figure 3.1(c)**. The red-to-blue (Stage 2 to 3) phase transformation reflected by the particles in the last four columns of **Figure 3.1(c)**, however, did not follow the reversed pathway of particle-by-particle lithiation. Instead, it behaved more like the gold-to-red (Stage 1 to 2) transformation with most particles experiencing the phase transformation concurrently. Despite the subtle differences, it is evident that the phase transformations in Steps II and III occur through clear phase separation at slow galvanostatic condition during both lithiation and delithiation.

During the lithiation at 1 C current, the blue-to-red (Stage 3 to 2) transformation appeared more homogeneous than in the case of 0.1 C current, showing smeared phase boundaries and cloudy domains and thus, resembling a solid-solution mechanism, as visible in 22% - 39% SOCs in **Figure 3.1(d)**. This observation is consistent with the suppression of phase separation predicted[118] and confirmed[34,119] in $LiFePO_4$ electrodes. However, the red-to-gold (Stage 2 to 1) transformation remained unaffected by the elevated current density, random nucleations of the gold phase (Stage 1) at the edges of multiple particles generated sharp phase boundaries that swept across the particles to complete the phase transformation, just like what we observed at 0.1 C current. The high reaction overpotential at 1 C current, shown in **Figure B-1**, resulted in only 65% of the total capacity at the cut-off voltage, leaving a few particles partially lithiated, still with clear red-gold phase boundaries. These active phase boundaries within partially lithiated particles, may recede to disappear via inter-particle exchanges during a long time relaxation.[119] In our experiments, they started to move with newly nucleated phase boundary during the subsequent delithiation at 1C current, until all particles turned red (Stage 2). Unlike the rather homogeneous blue-to-red (Stage 3 to 2) lithiation at 1 C current, the red-to-blue (Stage 2 to 3) delithiation process at 1C always induced random nucleations and two-phase coexistence, as can be seen in the last four columns of **Figure 3.1(d)**.

The above features of phase transformation in individual particles may differ from cycle to cycle. Since the graphite particles expand and contract repeatedly upon Li ion intercalation and deintercalation, the surface imperfections may slightly change and alter the surface energy. Thus, the nucleation of the stable phases could start at different spots on the particle edges in different cycles and the phase boundaries may evolve slightly differently. In addition, the nucleation in single particle may be influenced by the particle curvature as it affects the surface energy and may lead to easier nucleation due to surface wetting.[118,120] However, we focus on the less investigated spatiotemporal heterogeneities on the mesoscale and their impact on the local phase transformation dynamics. Despite these changes across different cycles, the charge and flux balances and the phase transformation mechanisms would remain same due to the inherent thermodynamics as discussed in the later sections.

The above observation raises two intriguing questions: (i) Why does the highly reversible graphite electrode show asymmetrical dynamics of phase transformation during lithiation and delithiation? (ii) Why the high current can suppress the phase separation in the blue-to-red transformation, but not the red-to-gold transformation?

3.2.2 True local electrochemical driving force

The surprising high resolution of the distinct colors in micron-sized particles allows determination of the local SOC by converting the color to the standard capacity associated with the color (stage). The calibration method of our analysis is explained in **Experimental Section** and **Figure B-4**. Following the same principle validated at the larger scale, we further calculated the capacity evolution curves within the selected particles P1 – P5, as shown in **Figure B-5**. In the solid-solution regimes, the capacities increased/decreased linearly in each particle, yielding low constant currents. However, in the phase-separation regimes, the total capacity within a particle was the net capacity contributed by each color. The total capacity remained constant when the particle was idling. We obtained the temporal variation of the current carried by each particle by taking the numerical first-order time-derivative of the capacity evolution curves, shown in **Figure B-5**. These local “working” currents represent the true electrochemical conditions experienced by each particle, under the global slow and fast galvanostatic conditions.

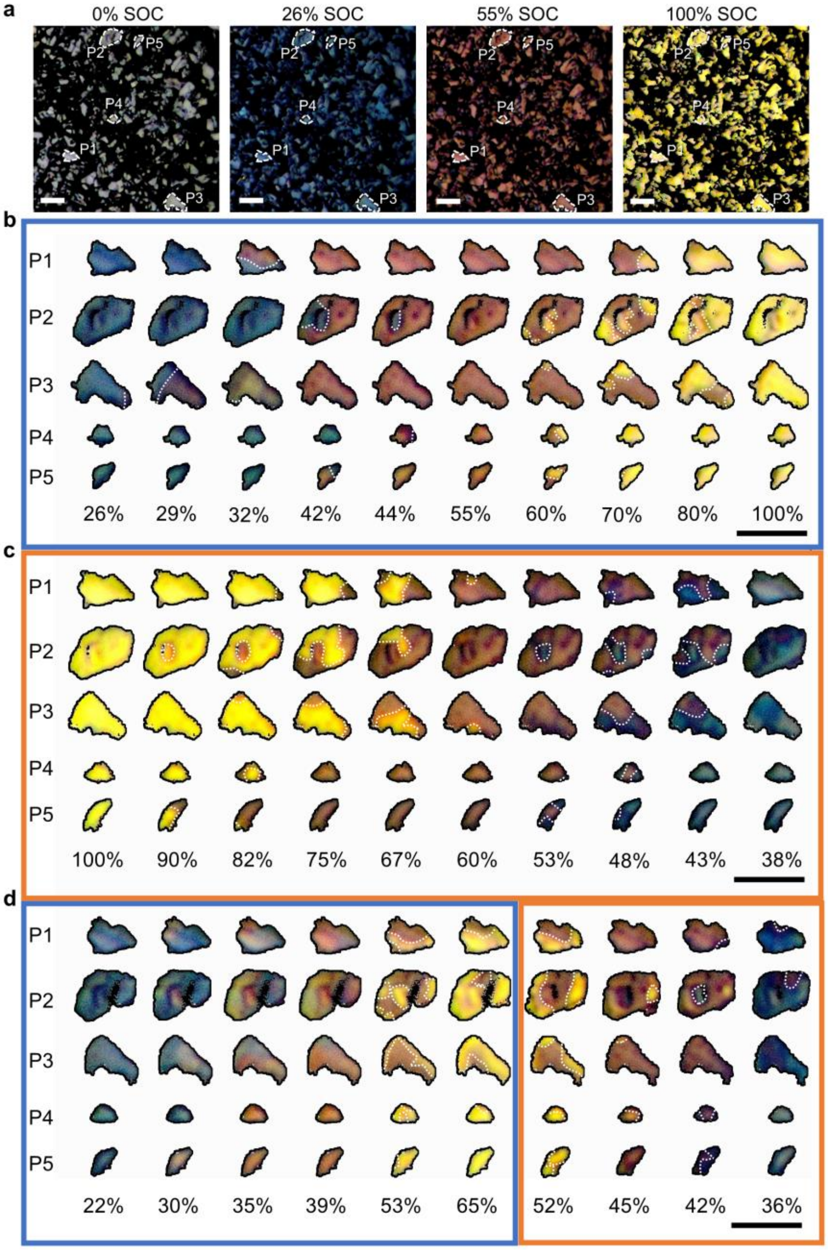

Figure 3.1: Phase-transformation during (de)lithiation in graphite particles under constant current. a) The entire view of graphite electrode under the optical microscope in the empty state (grey), and stages 3 (blue), 2 (red), and 1 (gold). These frames are obtained at very low current (C/72) and are used as the calibration frames for the estimation of the SOCs of each stable phase. The white dashed outlines in these snapshots are the five selected particles (P1 – P5) for intra-particle inspection. b) Lithiation process of the

selected five particles at 0.1 C current. c) Delithiation of the selected five particles at 0.1 C current. d) Lithiation and delithiation of the selected five particles at 1 C current. The blue rectangle indicates lithiation while the orange rectangle denotes delithiation. The white dotted lines in the panels (b-d) indicate the phase boundaries generated during the phase transformations. The lithiation and delithiation processes at 0.1 C current show the phase transformations along the generated phase boundaries while the lithiation process at 1 C from 22% - 39% SOCs shows smeared phase boundaries and cloudy domains, resembling a solid solution mechanism. *Scale bar: 10 µm.*

To determine the local working *current density* for consistent transport analysis in each particle, the active reaction interfaces need to be identified in addition to the current. In general, Li^+ ions intercalate through all edge planes of the graphite particle and not the basal planes, as shown in the schematic in **Figure B-17(a)**. The active reaction area is the product of the length of the perimeter and the thickness of the particle. This is true for the cases of the solid-solution pathway. However, in the cases of phase separation, almost all Li^+ ions quickly equilibrate within the stable phase domains and only make concentration jumps at the phase boundary between the two phases (colors), which is confirmed by the *operando* observations that the net Li^+ ion flux through the edges concentrates at the phase boundaries without causing any color change in the stable domains. In another word, Li^+ ion reaction flux at the particle edges is equivalent to the internal Li^+ ion flux at the phase boundary that makes the phase boundary move. If the internal phase boundary does not move, no net electrochemical current will be seen on the edges of the particles. For consistent transport analysis, the flux that is normal to the particle edge but tangent to the phase boundary is less responsible for the movement of the phase boundary. Therefore, only the edges that are nearly parallel to the internal phase boundary should be counted as the effective reaction interface. We calculated the local working current densities or the interfacial current densities within each selected particle by dividing the local current with the associated active area, either the entire edge area for the solid-solution cases, or the phase boundary area for the phase-separation cases, as shown in **Figure 3.2(a-d)**.

As shown by the schematic highlight in **Figure 3.2(e)**, the single-particle level solid-solution behavior tends to induce concurrent reactions of all particles at the many-particle level. On the other hand, the single-particle level two-phase dynamics tends to activate just a few particles at a time[73,121], resulting in sequential reactions, which in turn yield a very high local working current density that can enable a solid-solution dynamics at the single-particle level. It is then not unexpected to discover that the true local current densities during phase separation are much higher than those in the solid-solution step (**Figures 3.2(a-d)**). More specifically, nucleation events of a new phase that led to the emergence of phase boundaries always caused sudden current density spikes. The positions of these spikes during lithiation at 0.1 C current in **Figure 3.2(a)** correspond to the particle-by-particle activation process. During the red-to-gold (Stage 2 to 1) lithiation at 0.1 C current, more active phase-separating particles lowered the absolute current shared by each particle and therefore lowered the true local current densities ($0.1 – 0.2\ mA\ cm^{-2}$) in individual particles shown in **Figure 3.2(a)**. The overlapping current densities are consistent with the relatively concurrent reaction among particles. During delithiation at 0.1C current, the obtained true local current densities are similar to those during the lithiation, only that the SOC ranges changed due to hysteresis between lithiation and delithiation.[122,123] In the case of 1 C current in **Figure 3.2(c)**, the solid-solution-like blue-to-red (Stage 3 to 2) lithiation makes the quantification of phase boundary improbable. Only the red-to-gold (Stage 2 to 1) lithiation exhibits phase-boundary-based high local current densities. True local current densities for the delithiation process consistently reflect the existence of phase boundaries and the sequential reaction process.

It is evident from the above observations that, while the solid-solution mechanism led to a homogeneous distribution of the external driving conditions on the entire domain, the phase-separation caused higher working current densities on a limited number of reacting particles. These findings are consistent with the widely recognized theory that the nucleation a new phase via phase separation requires higher driving force than solid solution in the intercalation materials.[120,124] These interfacial current densities were 2-3 orders of magnitude higher than the average current density calculated using the BET surface area ($9.424\ m^2\ g^{-1}$). Surprisingly, a ten-fold increase in the external total current from 0.1 C to 1 C increased the actual working current densities by only up to five times. The high working current densities in the studied cases of phase transformation suggest a far-from-equilibrium (de)intercalation dynamics at both slow and fast galvanostatic conditions. These understandings also indicate that the process is not diffusion-limited,[109] and requires innovative theoretical analyses to uncover the underlying mechanisms.

3.2.3 Non-equilibrium thermodynamics of graphite

The thermodynamic origin of the electrochemical phase transformation has been well explained by the balance between the non-monotonic diffusional chemical potential and the applied electrochemical overpotential,[118,125] based on which it was predicted and verified in $LiFePO_4$ single particles[123] that phase separation, therefore the coexistence of two stable phases, can be suppressed by an external electrochemical driving force. Graphite, as another well-known phase separating material, has not been examined rigorously over the possibility of suppression of phase separation, despite a few attempts to explain the evolution of phase separation.[115,126,127]

Here, we performed a linear stability analysis[118] of the electrochemical phase transformation in a single graphite particle, by evaluating the dynamics of a linear perturbation, superimposed over a reaction-limited homogeneous system, but under various constant-current working conditions. An experimentally verified bilayer regular solution model[114,128] (not to be confused by the electrical double layer in a liquid solution) was adopted here to investigate the stabilities. The bilayer regular solution model allows the filling fraction $\tilde{c_1}$ to vary between 0 and 1 while $\tilde{c_2}$ ~ *0* for blue-red (Stage 3 to 2) phase transformation; once $\tilde{c_1}$ ~ *1*, the second filling fraction $\tilde{c_2}$ starts to increase during red-gold (Stage 2 to 1) phase transformation. As presented in **Appendix B.7**, our theoretical analysis provides the normalized growth speed of the perturbation with wave number k for the blue-red transformation,

$$\tilde{s_1}(\tilde{k},\tilde{c_1},\tilde{J}) = \left[2\tilde{\Omega}_a + 2\tilde{\Omega}_c\tilde{c_2}(1-\tilde{c_2}) - \frac{1}{\tilde{c_1}(1-\tilde{c_1})} - \tilde{K}\tilde{k}^2\right]\sqrt{\frac{\tilde{J}^2}{4} + [F(\tilde{c_1})]^2} + \left(\frac{F'(\tilde{c_1})}{F(\tilde{c_1})} + \frac{1}{2}\tilde{K}\tilde{k}^2\right)\tilde{J} \quad (1)$$

where $\tilde{\Omega}_a$ and $\tilde{\Omega}_c$ represents the regular solution coefficients for the intra-layer and inter-layer particle-vacancy interactions respectively; $\tilde{K} = V_S K/k_B T L^2$ is the dimensionless gradient penalty parameter dependent on the volume per intercalation site V_S, diffusion length L, Boltzmann constant k_B, and the room temperature T taken as 298 K. Following a similar strategy, the stability equation of the growth speed during red-gold phase transformation is slightly different,

$$\tilde{s_2}(\tilde{k},\tilde{c_2},\tilde{J}) = \left[2\tilde{\Omega}_a + 2\tilde{\Omega}_c\tilde{c_1}(1-\tilde{c_1}) - \frac{1}{\tilde{c_2}(1-\tilde{c_2})} - \tilde{K}\tilde{k}^2\right]\sqrt{\frac{\tilde{J}^2}{4} + 1} + \left(\frac{1}{2}\tilde{K}\tilde{k}^2\right)\tilde{J} \quad (2)$$

Apparently, the growth speeds s_1 and s_2 depend on $\tilde{J}$, which is the local interfacial current density J scaled to the concentration-dependent exchange current density in the homogeneous state $J_0(\tilde{c_i}) = k_0 F(\tilde{c_i})$ with k_0 being the rate constant and $F(\tilde{c_i})$ being the normalized exchange current density function for respective phase transformations. The complete derivation of Equations (1) and (2) can be found in **Appendix B.7**. It is important to note that the local exchange current density is an intrinsic interfacial property and needs to be determined experimentally in a self-consistent manner using the area of the active sites, instead of the total

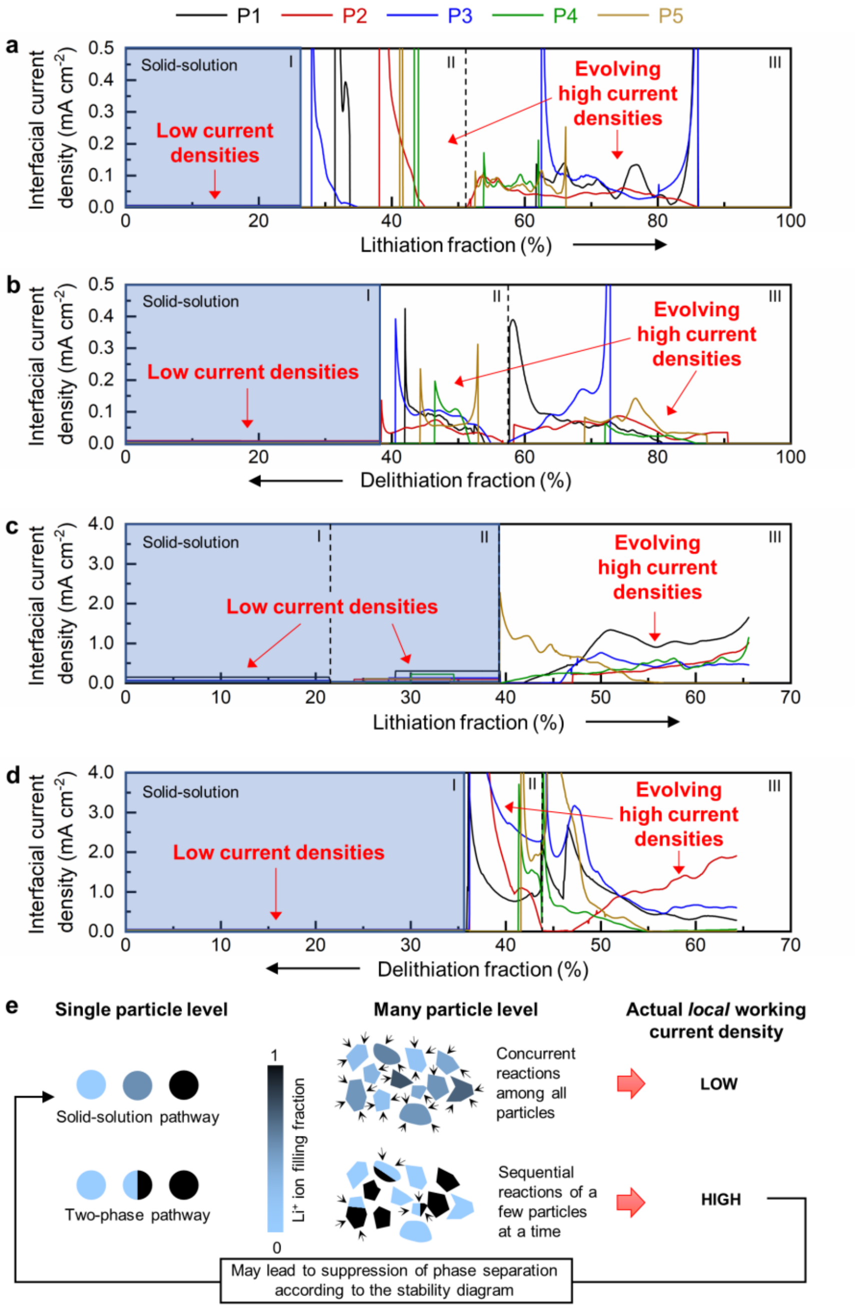

Figure 3.2: Local working interfacial current densities during (de)lithiation in graphite under constant currents. a) Lithiation at 0.1 C current, b) delithiation at 0.1 C current, c) lithiation at 1 C current, and d) delithiation at 1 C current. The solid-solution regions in these four panels (shaded in light blue in Step I and with the additional Step II for panel (c) yielded low *local* interfacial current densities, while the two-phase regions yielded evolving but high local current densities. The distinct positions of the sharp peaks in Step II during lithiation at 0.1 C current indicate a particle-by-particle mechanism. The almost overlapping current density regions in the remaining phase-separation regimes show that the phase boundaries emerge simultaneously within these particles. e) Schematic comparison of solid-solution

pathway vs two-phase pathway at the single-particle level and many-particle levels, yielding different actual local current densities due to population of active particles[73] that in turn influence the single-particle dynamics.

or apparent area. Based on our *operando* observations, image analyses, and impedance diagnosis,[109] the intrinsic exchange current densities for particles in the solid-solution and red-gold (Stage 2 to 1) phase transformation states are relatively independent of the Li^+ ion filling fraction as $0.5\ mA\ cm^{-2}$ and $3\ mA\ cm^{-2}$. The exchange current density for particles in the blue-red (Stage 3 to 2) phase transformation, however, is sensitive to the filling fraction and appears as a skewed non-monotonic curve in **Figure B-8**.

With the consistent exchange current densities and the regular solution coefficients, we plotted in **Figure 3.3** the neutral and driven linear stability boundaries, $\tilde{s}_{max}\left(\tilde{k},\tilde{c_1},\tilde{J}\right) = 0$ and $\tilde{s}_{max}(2\pi,\tilde{c_1},\tilde{J}) = |\tilde{J}|$, using the most unstable mode $\tilde{k} = 2\pi$. The regular solution coefficients govern the nucleation barrier of the respective phase transformations. The shape of the stability boundaries is thus dictated by both the regular solution coefficients and the exchange current densities due to their ability to affect the growth speeds, as shown in Equations (1) and (2). The stability boundary for the blue-red (Stage 3 to 2) phase transformation in **Figure 3.3(a)** has a maximum, resembling the diagram for $LiFePO_4$.[118,123] The relatively constant exchange current density for the red-gold (Stage 2 to 1) phase transformation, however, leads to different stability boundaries that do not close to reaching a maximum, as shown in **Figure 3.3(b)**.

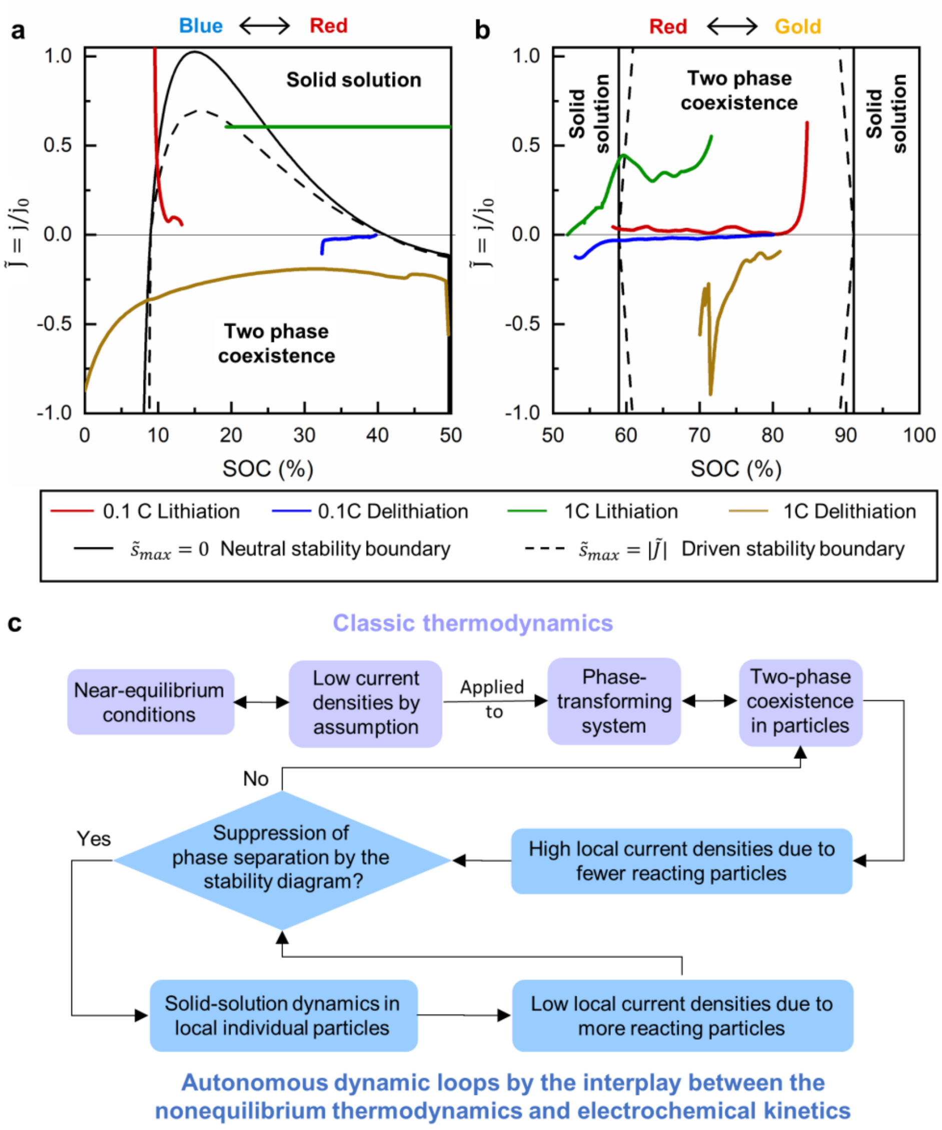

Figure 3.3: Comparison of *operando* current densities and the linear stability diagram for graphite single particles. Linear stability diagram for a) blue to red (Stage 3 to 2), and b) red to gold (Stage 2 to 1) phase transformations during both lithiation and delithiation at both the galvanostatic conditions. The experimental *operando* current densities (Steps II and III) lie within the domains of two-phase coexistence in all the cases except the blue-red (Stage 3 to 2) lithiation process at 1 C current (green solid curve in the SOC range of 20% to 50% in panel (a). This observation is consistent with the visual examination of the (de)lithiation process shown in Figure 3.1. Current density data displayed here are from particle P1. c) The dynamic interplay between the nonequilibrium thermodynamics and electrochemical kinetics reveals the autonomous dynamic loops regarding the intra- and inter-particle behaviors, as depicted in the flowchart.

The linear stability diagram acts as a “nonequilibrium electrochemical phase diagram” generated from the interplay between the nonequilibrium thermodynamics of the materials and the exchange current densities at the materials interface. The stability diagram is a rigorous quantitative summary of the dynamic interplay. As shown in the flowchart (Figure 3.3(c)), conventional understandings following the classic thermodynamics would consider that a near-equilibrium excitation will only induce near-equilibrium dynamics. Therefore, a low current applied to phase-transforming electrodes would induce two-phase coexistence in every single particle. However, as we proved here in complex phase-transforming electrodes like graphite, phase separation will lead to highly localized current density, that may lead to the suppression of phase separation and thereafter the solid-solution dynamics, but only if an SOC-dependent non-monotonic exchange current density is in place. As discussed above, the phase separation can then be suppressed only in the blue-red (Stage 3 to 2) phase transformation regime, owing to a skewed concentration-dependent exchange current density. Due to the non-monotonic stability curves for the blue-red (Stage 3 to 2) phase transformation during the lithiation process, there exist critical current density $\tilde{J}_{BR}^{c}$ ~ 1.02 beyond which the phase transformation would occur via the solid-solution pathway. On the other hand, the diverging unstable region for the red-gold (Stage 2 to 1) phase transformation during both the lithiation process and the delithiation process suggests that the respective phase separations will always be triggered, irrespective of the current densities. Take particle P1 as an example, we overlay the *operando* interfacial current densities from **Figure 3.2** on the stability diagram **Figure 3.3**, and observed that only the blue-red (Stage 3 to 2) transformation during lithiation at 1 C current lied close to the critical current density $\tilde{J}_{BR}^{c}$, where a dynamic solid-solution pathway becomes possible. The *operando* current densities during the other phase transformation processes, however, lied within the phase-separation domains for all the phase transformations. Similar results were obtained for the other four particles and are shown in **Figure B-9**. It should be noted that the regular solution model spans across the entire SOC range from 0%, to 100% SOCs, while the actual phase-transformation in our electrodes occurs within different SOC ranges shown in **Table B-1**. To better compare them, the *operando* interfacial current densities have been scaled (only horizontally along the SOC axis) to match the phase-transformation SOC ranges of the regular solution model. This theoretical understanding offers a consistent explanation of the visually obtained local current densities during phase transformations and indicates that the dynamics is indeed controlled by the *operando* electrochemical flux, and not the solid-state diffusion.

3.2.4 Simulations of mesoscale many-particle dynamics

The single-particle analyses necessitate the incorporation of non-equilibrium materials thermodynamics into electrochemical models[118,125,129] toward the holistic design of battery materials and electrodes. Here, we adopt the multiphase porous electrode theory (MPET) developed by the Bazant group,[130] which not only incorporates materials thermodynamics for phase transformation, but also can predict the transport processes through the electrode that can also be modeled by the classic porous electrode theory pioneered by J. Newman.[131,132] With the consistent kinetic parameters, i.e., Li$^+$ ion diffusion coefficient D_{Li} and exchange current density j_0, now extracted from our *operando* experiments, we modeled 200 thin flake-like square graphite particles to simulate the many-particle dynamics in practical surroundings. The cluster of particles has a fixed thickness (*0.5 mm*) with both the length and width dimensions (same for square particles) lognormally distributed with a mean and standard deviation of *8.13 mm* and *2.61 μm*, respectively (same as experiments). The model framework adopts a two-parameter Cahn-Hilliard reaction theory where the equilibrium voltage curve is represented by a periodic bi-layer regular solution model.[114] The regular solution model implicitly controls the nucleation barrier of individual phase transformation via the regular solution coefficients, as shown in Equation (S1). The reduced 1D simulation with surface reaction boundary condition applied on both ends of the particle was performed. Thus, the Li^+ ions can enter the graphite particles only from the two opposite ends, as schematically shown in **Figure B-17(b)**. To replicate the true local dynamics, we employ the values of the Li^+ ion diffusion coefficient in graphite D_{Li} (9×10^{-8} $cm^2\ s^{-1}$) and the rate constant k_0 ($8.3\ mA\ cm^{-2}$) evaluated from the *operando* interfacial current densities in our recent work,[109] with the Cahn-Hilliard gradient penalty parameter K required in the equilibrium voltage calculation as $5\times10^{-7}\ J/m$ for the phase transformations.[86] The details of the MPET model can be found in multiple reports by Bazant and collaborators.[114,117,130,133] The key governing equations used in the model are presented in **Appendix B.9**.

As suggested in earlier section, we studied the phase transformation by evaluating the progression of the area fractions of the stable phases in the lognormally distributed particles. With the particle size sorted in ascending order and assigned respective numerical IDs as shown in **Figure 3.4**, we identified the phases based on the concentration gradient at the phase boundaries, similar to **Figure B-10** for Particle ID #100. Here, the solid-solution processes, which include both the empty (grey) to Stage 3 (blue) and Stage 3 (blue) to Stage 2 (red) lithiation at 1C (but not at 0.1C), would appear blue. In cases of phase separation, the vertical line/region corresponding to each particle ID will show the coexistence of the two colors in accordance with the respective phases. The lithiation at 0.1 C current (**Figures 3.4(a-d)**) began with homogeneous intercalation within all particles until the battery voltage reaches the spinodal point (~4% SOC), which triggered the blue-red (Stage 3 to 2) transformation.[118] The smaller particles showed the blue-red phase boundaries first and became completely red before inducing the phase transformation in new particles. This particle-by-particle filling mechanism continued in the electrode without any appearance of the gold color, except in a small overlapping SOC range of 50% - 60%. Multiple particles activated during the red-gold (Stage 2 to 1) phase transformation and possessed phase boundaries simultaneously. But the smaller particles tend to completely transform into gold earlier than the larger ones. The lithiation at 1 C current (**Figures 3.4(c-h)**), however, mapped blue color in all the particles up to ~34% SOC, indicating that the blue-red (Stage 3 to 2) phase transformation continued the solid-solution behavior even after all the particles reached stage 3. While some smaller particles exhibited the blue-red phase boundaries, the gold (Stage 1) color appeared at ~37% SOC. The red-gold (Stage 2 to 1) phase transformation then continued similar to the lithiation at 0.1 C current with significant remaining phase boundaries at the end, due to a reduced electrode capacity at the cut-off voltage (~65%). The delithiation process at both 0.1 C and 1 C currents, however, exhibited gold-red (Stage 1 to 2) and red-blue (Stage 2 to 3) phase transformations via the respective phase boundaries, as shown in **Figure B-11**. The model response was consistent with the experimental *operando* observations, confirming its validity. The accurate prediction of the phase transformation pathways at both low and high currents provides a validation of the kinetic parameters and also demonstrates the predictive capability of MPET to understand the dynamics of the battery materials.

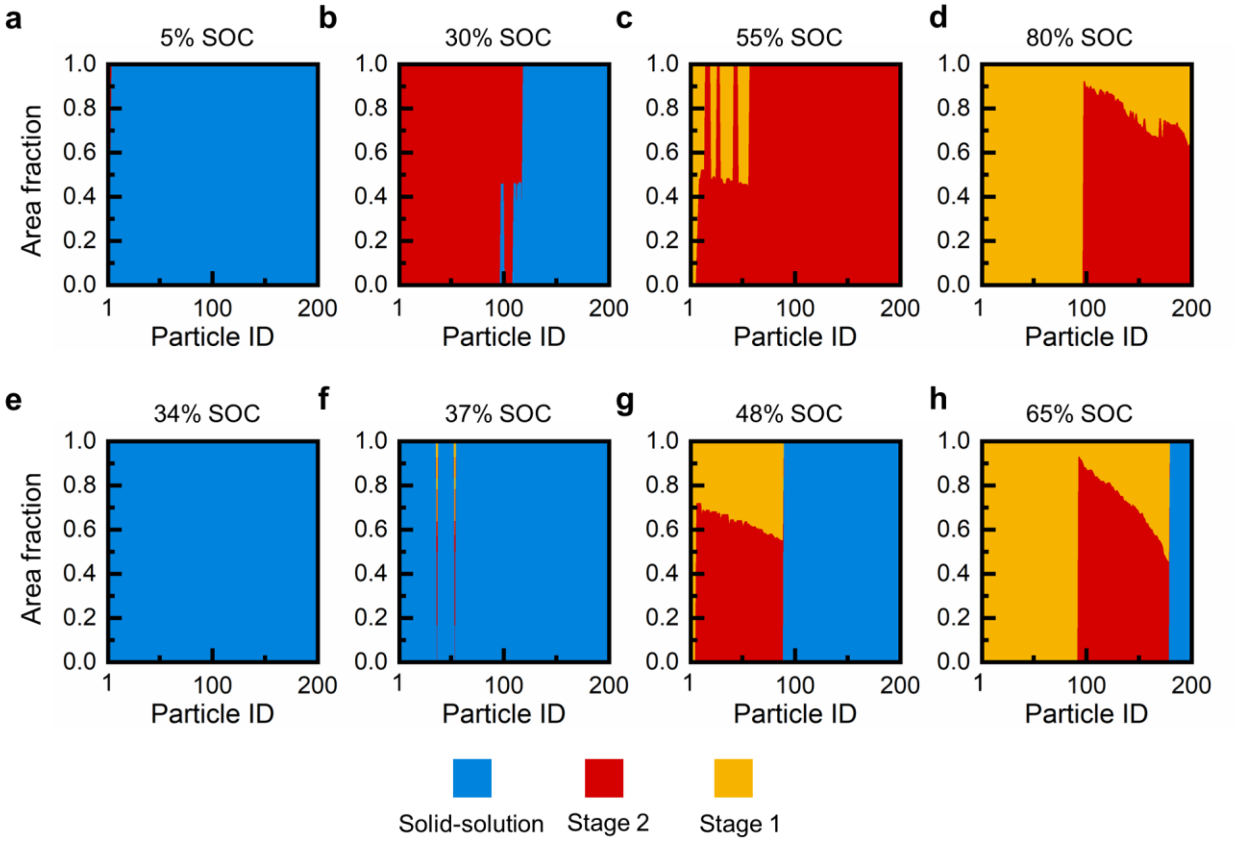

Figure 3.4: Theoretical predictions of area fraction of the stable phases using MPET with 200 lognormally distributed particles. Area fraction of stages 3, 2 and 1 at four global SOCs at (a-d) 0.1 C current, and (e-h) 1C current. The increasing particle IDs signify increasing particle lengths. At 0.1 C current, the blue-red phase boundaries appear initially in smaller particles. The new phase boundaries begin only when the phase transformation in the earlier particles is finished. For example, at 5% SOC (panel (a)), particles #01 - #04 show coexistence of Stages 3 and 2. At 55% SOC (panel (c)), particles #08 - #60 except #16, #18, #27, #46 and #47, show coexistence of Stages 2 and 1. On the other hand, the solid solution behavior continues up to ~34% at 1 C current which means that the blue-red (Stage 3 to 2) phase transformation also occurs almost via the solid-solution mechanism. Once almost all particles are in stage 2, the red-gold (Stage 2 to 1) transformation occurs along the phase boundaries at both currents.

In addition to the qualitative consistency, the simulations allow evaluation of the instantaneous total interface length within the simplified ideal rectangular particles, using the concentration gradient at the phase boundaries. Based on the 1D simulation, the phase boundaries emerged parallel to the active dimension of the particles. Thus, the total length of the phase boundaries was equal to the collective size of the active particles and could be extrapolated to the total volume of the graphite electrode used in the experiments. These simulated spatiotemporal responses of phase boundaries in the considered galvanostatic conditions, during both lithiation and delithiation, despite notable deviations, were in the same orders of magnitude with the *operando* observations, as shown in **Figure 3.5(a-b)** and **Figure B-12**, respectively. The widened curves and shifted peaks in the simulated lengths of the phase boundaries, as compared to the image analyses, are mainly due to the inconsistency introduced by the simple 1D particles, in which the ideal 1D phase boundaries cannot reflect the 2D results perfectly. While the numerical challenges in simulating hundreds of realistic 2D particles will be addressed in our future works, the comparison shown in **Figure 3.5** is still deemed meaningful, as it closes the loop of our analysis: using kinetic parameters (D_{Li} and k_0) extracted from true local electrochemical processes and incorporating nonequilibrium materials thermodynamics enable mathematical simulations that can capture the spatiotemporal heterogeneities at multiple scales in complex phase-transforming electrodes.

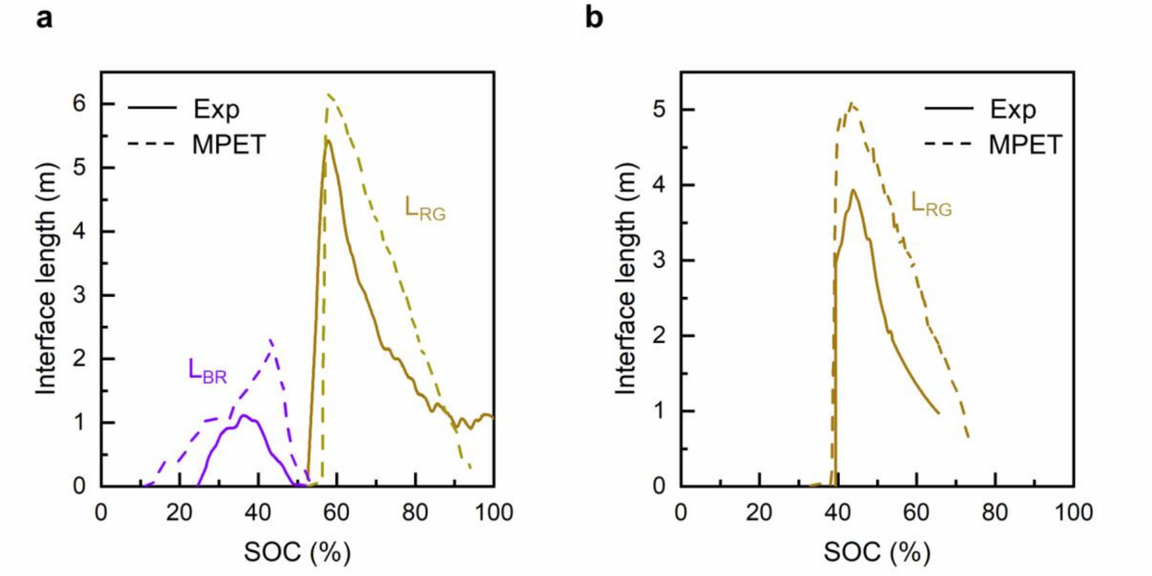

Figure 3.5: Physical Interpretation of phase boundary evolutions. Comparison between lengths of phase boundaries extracted from direct image analysis (solid lines) and that simulated using MPET

(dashed lines) at a) 0.1C current, and b) 1C current. The blue-red (Stage 3 to 2) transformation begins earlier in the simulation than in experiments because the simulation triggers phase-transformation when the Li^+ ion concentration reaches a spinodal point (~4% SOC) in the regular solution equilibrium voltage curve.

3.3 Discussion

Quantifications of the phase boundaries and hence the *operando* interfacial current densities provide a consistent understanding of the active reaction fronts and the local electrochemical activity in the phase-transforming porous electrodes. A three-orders-of-magnitude higher interfacial current density than the averaged one, at a low current of 0.1 C, suggests a far-from-equilibrium dynamics as opposed to widely known near-equilibrium process, and necessitates special attention in interpreting experimental data. Moreover, a comparable magnitude of interfacial current densities at 0.1 C and 1 C currents highlights that the local reaction flux remains almost unchanged on increasing the total current, as the interfacial reaction appears to be autonomously coordinated and modulated by the phase transformation dynamics among many particles. Despite the similar orders of magnitude of the interfacial current densities at low and high currents, the intercalation mechanism may be different, owing to the intrinsic exchange current density affected by the local filling fraction.[109] The electrochemical stability diagram (**Figure 3.3)** obtained from the linear stability analysis with the constant-current integral constraint shows that only the blue-red (Stage 3 to 2) phase transformation during the lithiation process can be suppressed at a high current, while red-gold (Stage 2 to 1) phase transformation would always occur via a two-phase coexistence, consistent with the visual observations. However, our *operando* experiments at 1.5 C and 2 C currents show that in real battery operation, the much larger overpotential resulted in the incomplete charge/discharge at the cut-off voltages, that the capacity obtained at such high currents would be insufficient to start the red-gold (Stage 2 to 1) transformation, as shown in **Figure B-1**. Therefore, the spatiotemporal heterogeneities seem to dampen at high currents in our thin graphite electrodes shown in **Figure B-13**.

There are two experimental aspects pertinent to this study, enabling the successful analysis of the spatiotemporal heterogeneities. Firstly, we ensured a low thickness of the electrode (~ 5 µm) to avoid the occurrence of the reaction heterogeneities in the thickness direction due to the concentration gradient in the electrolyte.[24,26,80] A consistent comparison between the total capacities obtained from the electrochemical experiments and the direct image analyses, confirms a similar level of reaction heterogeneities in the entire electrode. Secondly, we used flake-type graphite particles to allow easy in-focus imaging of hundreds of particles with high resolution at the single-particle level. While the natural graphite flakes are susceptible to the stacking defects due to polycrystalline nature, the degree of defects depend on the size of the flakes.[134] The flakes with average size of 8 µm used in this study, have less stacking defects. Thus, the layers can be considered parallelly stacked and suitable for Li ion intercalation. The absence of such defects and crystalline domains within a particle is further justified by the nucleation of phases only at the particles' edges and not internally. Hence, the light color patches seldomly appearing in the low Li content images are probably due to the surface roughness of the particles and are accounted for using a range of Hue for each stable phase during image segmentation (**See Experimental Section and Figure B-15**). These structural imperfections can also affect the direction of phase boundaries within the particles. The many-particle MPET simulation represents an ideal system with square-shaped single-domain particles. The 200 particles/domains in the MPET simulation are arranged parallelly with each other and can statistically represent the entire electrode. The conclusions, based on the fundamental material properties, apply to other types of graphite such as mesocarbon microbeads (MCMB) and synthetic graphite, in which phase transformation and reaction heterogeneities were already observed.[80,135]

A recent scaling analysis suggests that the Li^+ ion intercalation in large graphite particles of 50 mm[86] and 400 mm[87] is diffusion-controlled, but according to our latest observations,[109] the intercalation process in our graphite flakes (< 10 mm) at mesoscale is not diffusion-controlled, but rather governed by phase-transformation that determines both the number of reacting particles (therefore the true local current density) and the evolution of the phase boundaries in individual particles. For this reason, the classical electroanalytical methods developed under the assumption of diffusion-controlled scenario may not be used without careful examination to extract the kinetic parameters, i.e. D_{Li} and j_0.[92,93,109] To fully understand the autonomous dynamic loops (**Figure 3.3(c)**), it is necessary to incorporate electrochemical phase-field models for single particles with porous electrodes theories for the electrode, like the MPET model we used here. In this study, we considered lognormally distributed square-shaped particles with intercalation only along one dimension. Although rectangular particles with fixed width and lognormally distributed length dimension would represent actual graphite particles more accurately, it may cause theoretical inconsistency in a 1D simulation. Our 1D simulation lacks the feature to choose the direction of intercalation based on surface energy which may contradict that the phase boundaries align preferentially towards the shorter dimension. Further improvements of the code, by using consistent particles shapes and performing 2D or 3D simulations, would enable more accurate agreement with the experimental true local current densities and the intra- and inter-particle dynamics.

Although the current study focuses on the intercalation mechanisms in flake-like graphite particles, the methodology can be translated to the other varieties of graphite due to the common phase transformation behavior. In graphite such mesocarbon microbeads[80] and synthetic graphite,[135] different surface energy can affect the nucleation barrier and the reaction sequence of the particles but they still show phase transformation dynamics and severe reaction heterogeneities. With accurate regular solution coefficients and exchange current densities, the stability diagram similar to Figure 3.3 can be obtained for other graphite types with the aid of proper image analysis, to evaluate the phase transformation dynamics.

3.4 Conclusion

We have utilized a simple benchtop *operando* setup to observe the spatiotemporal heterogeneities in practical graphite electrodes under various constant current densities. Unlike other well-known phase-transforming battery materials, not all phase separation processes in graphite can be suppressed by a high current. By comparing the true local current density of a single particle from direct image analysis with the linear stability diagram of electrochemical phase transformation, it is now clear that whether an ion-intercalation-induced phase transformation can be suppressed or not, depends on the dynamic interplay via the interfacial kinetics. An SOC-dependent (concentration-dependent) non-monotonic exchange current density is the premise for the suppression of phase separation, via the autoinhibitory pathway.[136] Beyond the consistent single particle analysis, a many-particle model was developed to understand the mesoscale behavior of the electrode, by using the MPET code. The results reveal a good agreement between the phase boundaries identified from direct image analysis and from simulation, which valid our self-consistent close-loop analysis for more effective battery design strategies.

3.5 Experimental Section

Thin electrode preparation: We formed a homogeneous graphite slurry by dissolving graphite flakes (7-10 µm, 99%, Alfa-Aesar), PVdF binder (>99.5%, MTI Corp) and conductive acetylene black powder (35-40 nm, MTI Corp) in the ratio 88:10:2, in 1-methyl-2-pyrrolidone (NMP, 99.5%, Sigma Aldrich). This slurry was coated onto separator film by the doctor-blade method. We, then, dried the electrodes at 60°C to remove the NMP, punched out Φ8 mm electrodes and kept them under vacuum at 70°C for 12 hours to remove the residual moisture. The active material loading, and electrode thickness were 0.7 mg cm^{-2} and 5 µm, respectively, shown in **Figure B-13**.

***Operando* setup and experiments:** We assembled a graphite half-cell with a Li anode, a glass-fiber separator, and 1M $LiPF_6$ in EC:DMC (50:50 v/v) in a standard 2032 coin cell with a Φ2 mm hole on the top, in an Ar-filled glovebox. We sealed the viewing hole with a 5 x 5 mm glass window using epoxy to seal the cell to view the graphite flakes under the optical microscope Olympus BX53M microscope with objective 50x for *operando* observation. We ran five formation cycles at 0.25 C between cut-off voltages 1.5V and 0.4 mV. We then, performed a galvanostatic charge and discharge at 0.1 C and 1 C currents, and captured the frames every 20s and 2s time intervals, respectively. All the acquired digital photos were processed using ImageJ to quantify the colored regions. The detailed description of the procedures is mentioned below.

Color thresholds for area quantification: We used the built-in color threshold method of ImageJ identify the blue (Stage 3), red (Stage 2) and gold (Stage 1) colors based on the Hue, Saturation and Brightness in the frames captured in the *operando* galvanostatic experiments. The brightness difference of blue, red and gold colors caused some smaller particles (< 2 µm), which were not clearly visible when they were blue or red, to get illuminated upon turning into gold color. Since ImageJ auto-selects all the non-black regions/graphite flakes according to the brightness, this illumination resulted to select more area when the particles entered Step III (or Stage 1). The difference in the selected area across all the images was always under 10%, resulting in slight inconsistency while calculating the area fraction of different phases. To avoid this inconsistency, the same sampling region was defined based on the images with all red-colored particles while converting the surrounding areas black. The black mask constituted all the non-particles regions and the unreacted regions obtained from 100% SOC image. This final black mask was applied to all the images. Within the sampling regions, a fixed range of hue was used to select similar colored regions (Red: 0 – 24, Gold: 24 – 44, and Blue: 44 – 255) while maintaining the same range of saturation and brightness. The above criteria were applied to all the digital images with the help of an ImageJ script. The conversion of three representative images is shown in **Figure B-15**. A variation of ±10% in the selected thresholds results in a deviation of only ±0% – 5% in the selected areas of blue, red and gold.

Charge conservation calibration: We first converted the blue, red, and gold colors into the standard RGB colors using our segmentation algorithm in ImageJ, explained above, and determined the evolution of area fractions (a_i) of these colors in the overall view (**Figure B-3**). Since these colors represent stable phases of the lithiated graphite, they have a fixed SOC with respect to the total electrode capacity, associated with them. During phase transformation at near-equilibrium conditions, the transformed particles wait until the entire electrode reaches the same state, making the SOC of that particular state same as the global SOC. Hence, we determined the SOCs of the blue (x_B), red (x_R) and gold (x_G) colors as 26%, 55% and 100% under low galvanostatic conditions (C/72 current). We used these SOC values for the validation of our color segmentation algorithm with the electrochemical response, via charge conservation within the electrode, $\sum_i q_i A_i(t) = q_T(t) A_T$, where i represents Blue, Red, and Gold, q_i is the areal capacity of the i^{th} color and can be calculated from the SOC of the i^{th} color (estimated above) and the theoretical areal capacity of the material (q_o), $q_i = x_i q_o$, A_i is the area covered by i^{th} color, q_T is the areal capacity of the electrode and A_T is the total surface area of particles in the electrode. The above equation can, then be transformed into $\sum_i x_i a_i(t) = x_T(t)$ where a_i is the area fraction of the i^{th} color, and x_T is the global SOC of the electrode. For known area fractions of stable phases, a phase-transforming material should inherently follow this equation. Since we only observed a 100 × 100μm window under the optical microscope, the validity of the above equation for the observed region confirms that the analysis can be confidently extrapolated to the entire electrode (**Figure B-4**).

Determination of the effective interfacial area: For a shape with two colors, we used ImageJ to find the perimeter covered by each color, and the outer perimeter of the shape, which together can be solved for the length of the interface. In our case, particles existed in three different states at a time. To calculate the length of the interface (**Figure B-6**), for instance, the Blue – Red interface, we relied on the fact that the phase transformation in graphite can only occur in one order: Stage 3 to Stage 2 to Stage 1. We converted all the green regions in the transformed RGB images, to the standard red color, thus eliminating all Red – Gold interfaces. This enabled us to find the length of the Blue – Red interface using the above methodology from the following equation, $L_{BR} = (l_{Blue} + l_{Red} - l_{particles})/2$. Similarly, we calculated the length of the

Red – Gold interface by converting all the blue regions to the standard red and applying following equation, $L_{RG} = (l_{Red} + l_{Gold} - l_{particles})/2$ where L_{BR} and L_{RG} are the lengths of Blue – Red and Red – Gold interfaces respectively, l_{Blue}, l_{Red} and l_{Gold} are the perimeters of the blue, red and gold regions in the corresponding transformed images, and $l_{particles}$ is the outer perimeter of all the particles within the viewing frame. The representative image conversion to calculate the interface lengths in particle P1 is shown in **Figure B-16**.

Considering disc-shaped flakes with an average diameter 8μm and thickness 0.5 μm, our ~5 μm thick electrode constituted ~10^7 particles with 10 layers stacked over each other. On making a statistical assumption that all layers were similar, we calculated the active area by multiplying the total length of phase boundaries with the electrode thickness.

Chapter 4: Spatial Heterogeneities in Nickel-rich Layered Oxide Cathodes

4.1 Introduction

Lithium-ion batteries (LIBs) are ubiquitous in the energy storage and conversion industry.[2] The particulate porous electrodes enable them with high energy densities and dynamic performance capabilities, however, LIBs suffer from random failures and safety-related accidents.[1,3] Such arbitrary incidents arising from the random spatiotemporal charge heterogeneities in the porous electrodes,[99,100] can lead to local hot and cold spots and escalate detrimental processes such as metal dissolution, electrolyte decomposition and oxygen release from the active materials.[101,137,138] While phase-transforming materials are susceptible to severe charge heterogeneities owing to their thermodynamics,[21,34,80,109,139] the solid-solution materials also exhibit heterogeneous charge distribution due to structural nonuniformities.[29,31,32,101,105,140] An occurrence of "fictitious" phase separation[37] under dynamic conditions may also lead to charge heterogeneities in the solid-solution materials. Quantification of the charge heterogeneities is necessary to assess their impact on the overall performance of the LIBs. Although the sophisticated X-ray techniques can identify these charge heterogeneities in the electrode materials,[24,26,27,29,31,34,40,105] they are difficult to capture the dynamic process and may cause damage to the samples. Not to mention, these techniques are not readily available. Simpler techniques employing visible light[80,106–109,139] and lasers[32,101,140–143] have enabled the imaging of the dynamic charge transfer process via fast acquisition on the many-particle scale in the porous electrodes. These versatile techniques combined with quantitative methods need to be promoted to acquire high quality *in situ* data on a wide range of electrode materials.

Nickel-rich layered oxides such as Li(Ni, Mn, Co)O_2 (NMC) are the most popular cathode materials in the LIBs.[144–146] These solid-solution materials should ideally exhibit a homogeneous Li ion transfer in the porous electrode, unlike phase transforming materials. However, multiple reports suggest the occurrence of severe charge heterogeneities in the electrode arising either structurally or mechanistically. Raman spectroscopy has proved to be a fast and non-invasive technique to characterize the charge heterogeneities in the solid-solution materials.[32,101] Being a quantitative method, Raman spectroscopy can provide vital information about the charge distribution in the solid-solution materials for their improved performance.

Here, we use NMC532 as a model system to demonstrate the direct quantification of the true local current densities using *in situ* Raman spectroscopy. The ability of Raman spectroscopy to distinguish the vibrational modes of NMC532 with varying Li ion concentration, allows us to use our optical coin cell setup to investigate the dynamics of the heterogeneities at the mesoscale. Our results reveal that the mapped regions may contain empty and completely-filled areas at intermediate state-of-charges (SOCs) under galvanostatic conditions. Thus, only a fraction of the particle may be active at any instant. On a global scale, less than 50% of the total particle area is active leading to higher local current densities than the globally-averaged ones. The methods developed in this study are critical to estimating the kinetic parameters using true electrochemical responses and further aid in the design of the particulate porous electrodes.

4.2 Results

4.2.1 Performance of optical cell and Reference Raman spectra

We fabricated thin NMC532 electrode on the ceramic-coated separator (**Figure C-1**) to avoid any lateral charge heterogeneities during electrochemical experiments. We, then, characterized the electrochemical performance of the optical coin cell setup (**Figure 4.1(a)**) using constant current charge (delithiation) and discharge (lithiation) at 0.25 C current between 2.5 – 4.2 V. We obtained the typical voltage profiles of NMC532 with specific capacity ~155 mAh.g^{-1} as shown in **Figure 4.1(b)** and the cell exhibited >90% capacity retention over 100 cycles with ~100% Coulombic efficiency (**Figure C-2**). Due to the spherical shape of the particles and high surface roughness (**Figure C-1**), the particles are not easily distinguishable under the optical microscope even after coating on Al current collector, as shown in **Figure 4.1(c)**.

We obtained the reference Raman spectra on a grid of 30 µm × 30 µm with 3 µm steps, at five points selected in the entire SOC range during lithiation by reaching the desired voltage at 0.25 C current followed by a voltage hold until the current drops to 0.1 C. Using this protocol, we obtained two sharp and consistent Raman peaks (A_{1g} and E_g) at each location on the grid (wherever the active material was present). Thus, this protocol ensured that all the particles would reach the desired SOC. We observed the rise in the frequencies of both A_{1g} and E_g peaks with increased lithiation in the active material, consistent with the reports.[32,147] Moreover, the A_{1g} peak intensified and became sharper while the E_g peak became broader with increasing SOC and almost vanished at 100% SOC (2.5 V). After the noise and baseline removal, we identified the A_{1g} and E_g peaks of 0% SOC (4.2 V) at 540.6 cm^{-1} and 468.0 cm^{-1} respectively with corresponding full-width half-maximum (FWHM) as 115.3 cm^{-1} and 40.6 cm^{-1}. Similarly, the

A_{1g} peak at 100% SOC (2.5 V) was present at 599.9 cm^{-1} with FWHM as 63.3 cm^{-1} while the E_g peak was negligible in intensity. The corrected Raman spectra of empty and full states during lithiation of NMC532 are shown in **Figure 4.1(d)**. The remaining three points of the reference spectra are shown in the **Figure C-2**. The positions and intensities of the A_{1g} and E_g peaks at intermediate SOCs lied between those of the two extreme states. Any broader Raman spectrum would be a linear combination of the above reference spectra suggesting the presence of multiple states.

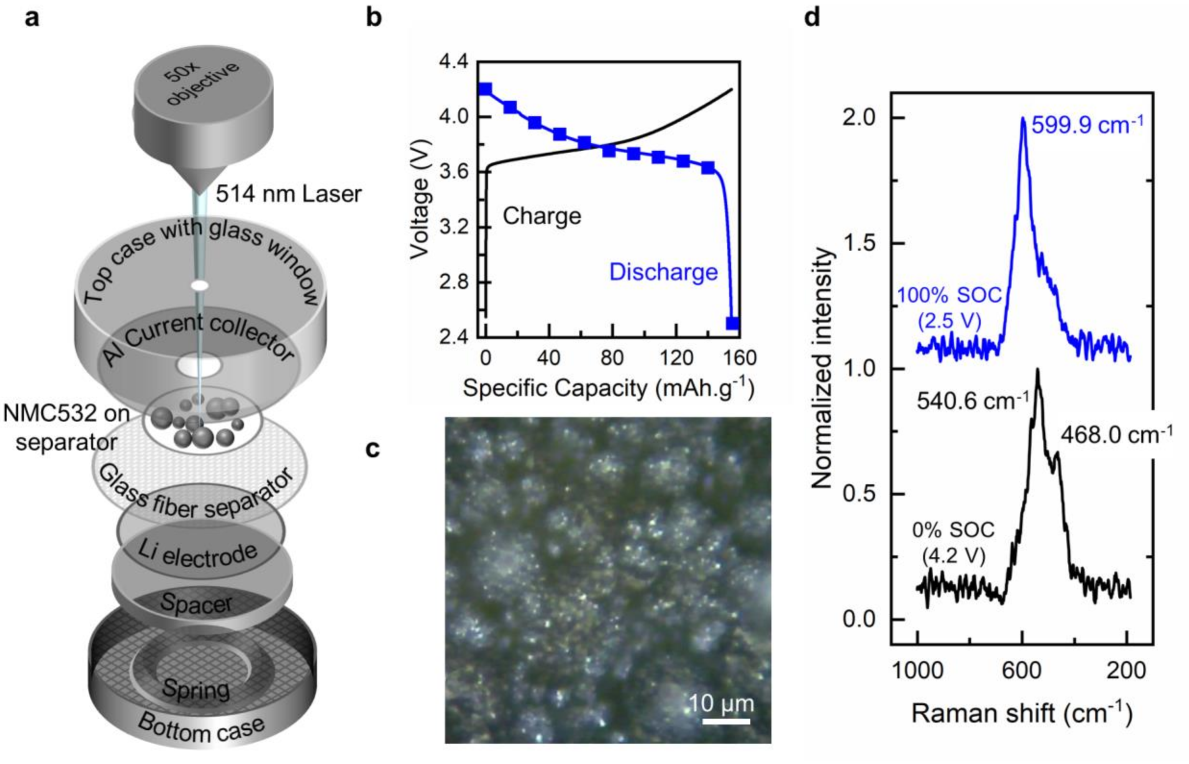

Figure 4.1: Electrochemical performance of the optical cell and Reference Raman spectra. (a) Schematic of the optical cell setup under Raman microscope. (b) Charge and discharge voltage curve of the optical cell. The markers on the discharge curve indicate the 11 points selected at equal intervals between 0% - 100% SOC for Raman mapping. (c) Particulate NMC532 electrode on Al foil under optical microscope. (d) Reference spectra of 0% and 100% SOCs obtained after voltage hold at 4.2 V and 2.5 V

respectively. The 0% SOC shows two sharp peaks at 540.6 cm^{-1} (A_{1g}) and 468.0 cm^{-1} (E_g) while the 100% SOC shows only 1 peak at 599.9 cm^{-1} (A_{1g}). These peaks have fixed FWHM, mentioned in the main text.

4.2.2 Local and global active regions under galvanostatic conditions

The presence of severe charge heterogeneities in NMC532 suggests that the local SOC can be much different from the global SOC of the electrode. Since the laser spot size of the Raman spectroscopy is much larger than the host active sites, each grid location may contain multiple states under constant current conditions. We used 0.1 C current discharge (0.034 mA.cm^{-2}) between 4.2 V and 2.5 V and obtained Raman spectra at each location on the same 30 µm × 30 µm grid (**Figure 4.2(b)-(l)**) at eleven SOCs. As suggested for graphite in recent studies, the areas with stable states are inactive for the surface reaction.[109,139] Thus, the empty and fully-lithiated regions in NMC532 should be inactive and any intermediate state should be considered as active regions. With this analogy, we deconvoluted the obtained spectrum at each location into three components: empty, full and active states, as shown in **Figure 4.2(a)**. Since each state is expressed by two signature peaks (A_{1g} and E_g), except for the full state, we deconvoluted the entire spectrum into five peaks using linear combination of fitting. The two peaks of the intermediate state contained the lumped contribution from all the local SOCs other than 0% and 100% SOCs. We also observed and fitted an additional at ~1100 cm^{-1} indicating the presence of carbon black in the electrode. Similar deconvolution was performed at each location with the active material for all the eleven SOCs during constant current discharge. Some of the examples of deconvolution are shown in the **Figure C-3**. Raman spectroscopy being a quantitative tool, the area fraction under each peak corresponds to the area fraction of the respective state. Thus, the maps of active area fractions can be obtained for each global SOC, as shown in **Figure 4.2**.

Li ions, after intercalation into the host, can arrange themselves to minimize surface energy. This energy can be governed by several factors such as crystal alignment, surface reaction rate and diffusion rate. Thus, the fractions of empty and fully-lithiated states, as well as active region can vary substantially with the addition of each Li ion. Each color map in Figure 2 shows severe heterogeneous distribution of charge and high variation in the local active regions, in the porous NMC532 electrode. The black regions in the color map showed no or faint peaks as there was no active material at those points in the topmost layer (**Figure C-4**). Since the particles' shape and size could not be clearly identified under the optical microscope, the estimation of local current was difficult. Hence, we could not calculate the local current densities in this case. However, if the particles can be distinguished clearly, the methods recently developed for graphite are applicable to estimate the local electrochemical properties.[109,139]

Using the local active area fractions, the average global active area fraction can be calculated at each selected SOC, as shown in **Figure 4.3(a)**. Nearly 50% of the total area was active 4.2 V (0% SOC) after the formation cycles. The global active area fraction dropped gradually on Li ion intercalation and saturates to around ~20% of the total particle area. The fraction fully-lithiated areas increase with the degree of lithiation in the NMC532 electrode. Since the total current was known, the true current densities were 2 – 5 times higher than the average current density estimated using the Branauer-Emmett-Teller (BET) specific surface area (average 0.3 $m^2.g^{-1}$, see Methods section), as shown in **Figure 4.3(b)**.

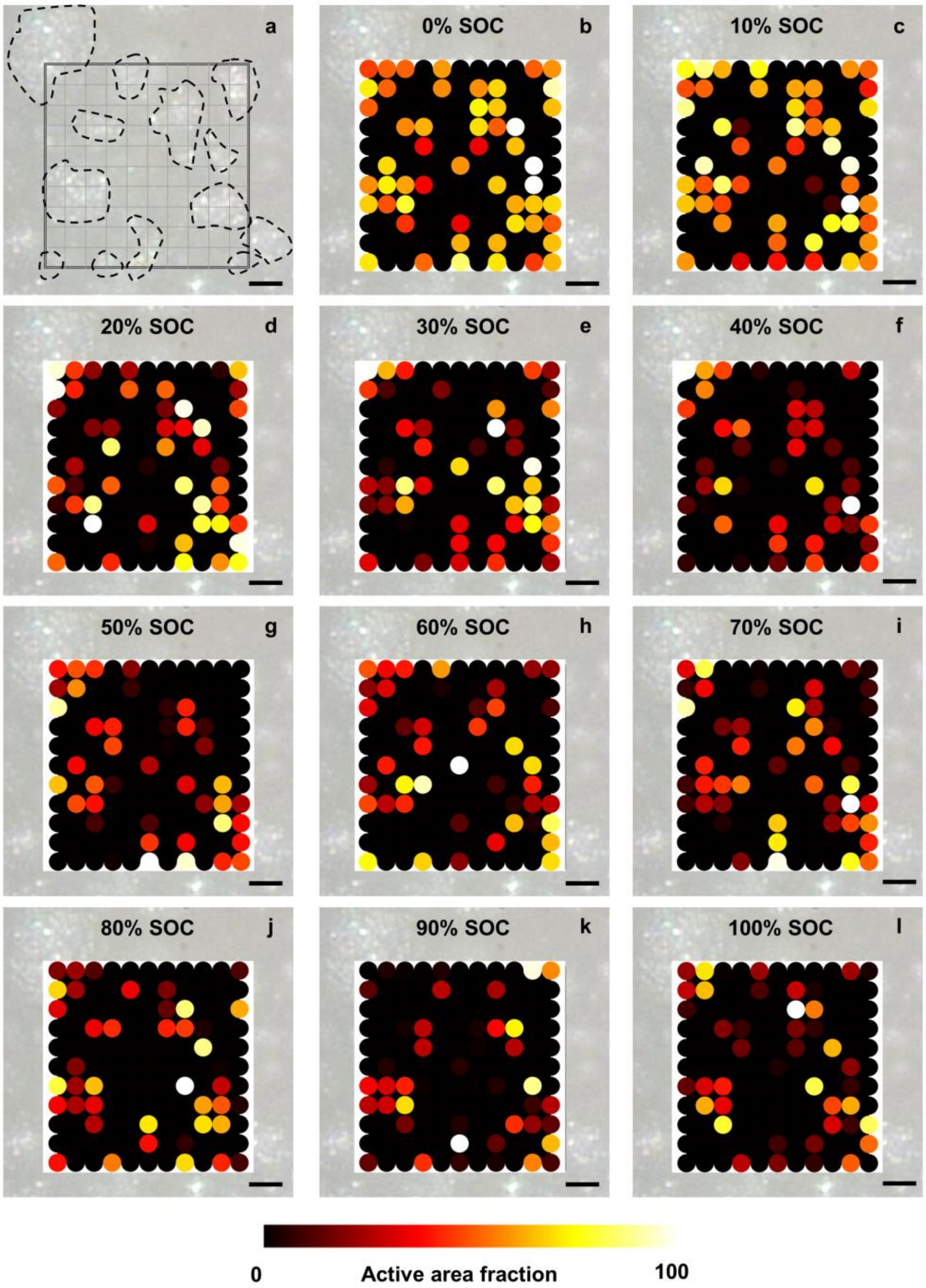

Figure 4.2: Mapping of spatiotemporal heterogeneities using Raman spectroscopy. (a) View under Raman microscope showing multiple particles. The identified particles are marked with the black dashed boundary. The Raman spectra were obtained at each node on the grid. (b)-(l) Map of active area fractions at each location on the grid at SOCs ranging from 0% - 100% at equal intervals. Here, white indicates the fully-lithiated regions while black represents empty regions and the regions with faint signals. The intermediate colors represent the active area within the particles. *Scale bar: 5 µm*

The true current densities on the electrode-scale are much higher than the globally-averaged current densities, suggesting far-from-equilibrium dynamics at low currents. However, the local true current densities can be either orders-of-magnitude higher than the averaged values or negligible. This is because the local current is governed by the rate of change of capacity in the localized region. The severe charge heterogeneities may lead to a drastic/negligible change in the local capacity, leading to hot/cold spots locally. Thus, the quantification and interpretation of the charge heterogeneities is necessary in the electrode materials to understand their detailed implications.

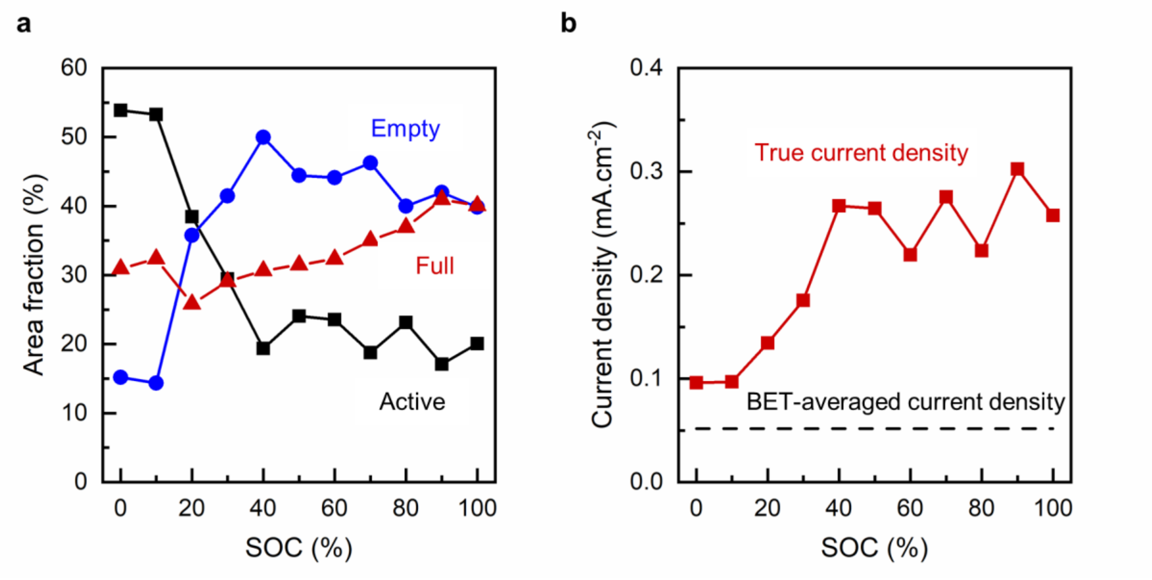

Figure 4.3: True electrochemical response on the electrode scale. (a) Fractions of empty, fully-lithiated and active regions. Over 50% of the total area is active initially and saturates at ~20% at higher SOCs. The fully-lithiated region increases gradually with SOC. (b) True current density estimated from the active area in the electrode. This transient current density is 2-5 times higher than the BET-averaged current density.

4.3 Discussion

In situ determination and quantification of the spatiotemporal heterogeneities in the electrode materials are necessary to facilitate the enhanced performance of the LIBs. A 2-5 times higher true current density as compared to the averaged one, even at a low current of 0.1 C, suggests a far-from-equilibrium dynamics as opposed to a widely accepted near-equilibrium process. These higher current densities would lead to a better estimation of the fundamental kinetic parameters such as diffusion coefficients and exchange current densities, resulting in a clearer understanding of the rate-limiting processes.[109] While the process of Li ion transfer within NMC532 is known to be solid-solution mechanism, the appearance of “fictitious” phase separation generates new possibilities.[37] As shown recently for graphite, the active area determination for the solid-solution and phase separation mechanisms is entirely different. During solid-solution mechanism, the active area is estimated by the entire particle surface accepting the Li ions, but the phase boundaries between the stable phases form the active area in phase separation mechanisms.[139] The mechanism of phase transformation affects the true current density severely and thus, is necessary to comprehend for a better electrode design.

The analysis of spatiotemporal heterogeneities relies on two important aspects in this study. First, the low electrode thickness (~10 µm) ensures no reaction heterogeneities along the lateral direction due to concentration polarization in the electrolyte. Moreover, electrochemical experiments with low excitations would further avoid lateral heterogeneities. Second, we use spherical secondary particles with average diameter as 10 µm in this study, sufficient for many-particle observation under optical microscope. While Raman spectroscopy is unaffected by the particle morphology, optical microscope poses challenges in imaging spherical particles due to curvature and surface imperfections. Plate-like particles can be observed very well under optical microscope, as proved for graphite flakes.[106,109] A combination of visual observation and quantitative analysis via Raman spectroscopy can provide a complete understanding of the spatiotemporal heterogeneities in NMC532 electrodes.

While the observation and quantification of spatiotemporal heterogeneities is important for the estimation of fundamental parameters, the real-use implications can be vastly different. LIB electrodes, especially phase transforming electrodes, are susceptible to memory effect, a degradation mechanism arising due to cycling history.[121,148] Solid-solution materials such as NMC and NCA also exhibit change in interfacial kinetics and degradation based on their cycling history.[24,93] Thus, it is evident that the degree of spatiotemporal charge heterogeneities would also be affected by the ageing of the electrodes. Again, optical microscopy coupled with quantitative techniques can be used to develop theoretical models to capture the effect of heterogeneous charge distribution. These models can be combined with the thermodynamic phase-field simulations to provide the mesoscale kinetics in the porous electrodes. The inclusion of such population dynamics model in the LIBs can provide better prediction of the battery life and degradation.

4.4 Conclusion

We have used an optical setup with Raman spectroscopy for *in situ* quantification of the spatiotemporal heterogeneities in the practical NMC532 electrode under slow galvanostatic condition. We have proposed a method to identify and quantify the active reaction area under dynamic conditions for accurate estimation of the fundamental kinetic parameters. The high true current densities at expected near-equilibrium conditions demands attention towards the rate-controlling mechanism on the electrode scale. Similar strategies adopted over multiple cycles and their consideration in the thermodynamic models can improve their accuracy and propose better electrode design approaches.

4.5 Experimental Section

Thin electrode preparation: NMC powder (MTI Corp, Specific surface area obtained from BET Analyzer: 0.2 – 0.4 $m^2.g^{-1}$), PVdF binder (>99.5%, MTI Corp) and conductive acetylene black powder (35-40 nm, MTI Corp) were mixed in the ratio 92.5:5:2.5 and dissolved in 1-methyl-2-pyrrolidone (NMP, 99.5%, Sigma Aldrich) to form a homogeneous slurry. To ensure the best imaging quality, the slurry was coated onto separator film by the doctor-blade method. The electrodes were dried at 60°C to remove the NMP. Φ8 mm electrodes were punched out and were kept under vacuum at 70°C for 12 hours to remove the residual moisture. The active material loading and electrode thickness were 2.23 mg cm^{-2} and 10 µm, respectively. The SEM images of the electrode are shown in **Figure C-1**, Supporting Information.

***In situ* setup and experiments.** A half-cell using the thin NMC532 electrode, a Li anode, a glass-fiber separator, and 1M $LiPF_6$ in EC:DMC (50:50 v/v) in a standard 2032 coin cell with a 2 mm hole on the top, was assembled in an Ar-filled glovebox. A 5 x 5 mm glass window was attached using epoxy to seal the cell. The optical coin cell was placed on a stage of the Raman microscope under objective 50x for *operando* observation. The cell was cycled at C/10 current five times between cut-off voltages 2.5V and 4.2V, to form a stable SEI. We then, discharged the cell up to the desired SOCs and rest them for 2 hours before taking the Raman spectra. We obtained such Raman spectra at 11 SOCs selected at regular intervals during discharge (lithiation), as shown in Figure 1. All the Raman spectra were taken in the same 30µm × 30µm grid and were processed using OriginLab Origin 2018 to quantify the active regions. The detailed description of the procedures is mentioned below.

Raman spectra acquisition: We performed the laser calibration using Si wafer to ensure consistent peak intensity as ~24000, before Raman measurement at each SOC. We selected the same 30µm × 30µm grid with 3µm steps to obtain Raman spectra at 121 points using Renishaw InVia confocal Raman spectrometer coupled to a Leica microscope. We used laser with wavelength 514 nm, chose static mode and obtained 10 accumulations with 10% laser power at each point on the grid. Each spectra takes 3s, thus, requiring 1 hour for the entire grid.

Raman spectra analysis: Each Raman spectrum were analyzed using the following steps: Smoothing, Baseline correction, and Deconvolution. All the above tasks were performed with Origin 2018 software. We used “Locally weighted least-squares” (Loess) method with span of 0.1 for smoothing. After default baseline correction, we selected five peaks for deconvolution. The position and FWHM of three out of five peaks were fixed to values shown in Section 2.2. The area under the peak denoted the area fraction of the corresponding phase. All the spectra with undetected or small peaks were discarded.

Chapter 5: Anion Intercalation Kinetics in Graphite Cathodes for Aluminum-ion Batteries

5.1 Introduction

Efficient electrical energy conversion and storage systems are increasingly needed to fulfill future energy demands.[1–3] Lithium-ion batteries (LIBs), while being the most mature portable power sources for both small-scale and large-scale applications, are evolving to become cost-effective, reliably safe, and environmentally friendly. LIBs are known to suffer from quick performance deterioration at low temperatures. At temperatures below -10°C, LIBs are prone to lithium plating on graphite anodes, raising the unpredictable high risk of fire and explosion.[75,76] The compromised performance at low temperatures has been attributed to the following factors: (i) lower ionic conductivity of the electrolyte, (ii) reduced Li-ion diffusion into graphite electrodes, and (iii) significantly increased charge-transfer resistance at the electrode|electrolyte interface with complications from the solid-electrolyte interphase (SEI).[149] Unlike LIBs, aluminum-ion batteries (AIBs), enabled by room-temperature ionic liquid electrolytes, exhibit remarkable high-rate cycling performance at temperatures as low as -30°C, making them an attractive option for cold-weather conditions.[150] The aluminum metal anode also appears particularly promising, owing to its low cost, rich abundance, and processing safety.[151–154] To the best of our knowledge, systematic investigations of the electrochemical kinetics in this AIB system, other than the ionic conductivity of the electrolyte, are yet to be performed to achieve a comprehensive understanding of the coupled interfacial charge transfer and bulk phase transformation dynamics.

Carbon materials, such as natural graphite,[110] amorphous carbon,[155] and graphene microflakes composites,[156] have been successfully demonstrated as a host for the reversible intercalation of the chloroaluminate ($AlCl_4^-$) ions. At room temperature, the Al vs. graphite system with the aluminum chloride:1-ethyl-3-methylimidazolium ($AlCl_3$:[EMIm]Cl = 1.7:1 mole ratio) ionic liquid electrolyte can provide a reversible capacity of 80 mAh g^{-1} at 1C rate with an average cell voltage of 2V.[150] At temperatures lower than -10 °C, not only could the system still function, it even provides a higher capacity due to the emergence of the third intercalation voltage plateau,[150] yet at relatively high C-rates. This phenomenon is in stark contrast to the sluggish Li intercalation into graphite electrodes, given that the intercalant in the AIBs is the much larger $AlCl_4^-$ anion. While there have been many first-principles studies investigating the diffusion mechanism of $AlCl_4^-$ anion in graphite, no conclusive agreement has been reached. The reported diffusion coefficients vary from 10^{-4} *to* 10^{-9} cm^2 s^{-1}.[157–159] On the other hand, the diffusion coefficients obtained from traditional electroanalytical techniques lie between 10^{-10} and 10^{-15} cm^2 s^{-1}.[160] The large variation in these values, and the discrepancies between the theory and experiments, demand a careful examination of the diffusion coefficients and the performance-limiting factors at various temperatures.

In this study, we perform diagnostic measurements of the reaction kinetics in the AIBs at several temperatures ranging from -20°C to room temperature (RT). The constant-current charge and discharge voltage curves along with the cyclic voltammogram reveal the subtle differences in the intercalation and deintercalation behavior at different temperatures. We further use the potentiostatic intermittent titration technique (PITT) and electrochemical impedance spectroscopy (EIS) to understand the fast reaction kinetics at various temperatures. Our results highlight that interfacial intercalation kinetics must be decoupled from the bulk diffusion to resolve the discrepancies in the kinetic parameters between experiments and theoretical predictions.

5.2 Results

5.2.1 Cycling at different temperatures

We performed galvanostatic cycling of the AIB pouch cells (see Experimental Section) under 0.5 C current within the voltage range 1 V – 2.5 V at five different temperatures between -20°C and RT (~21°C). Unlike LIBs showing a huge capacity drop on reducing the temperature from RT to -10°C, the AIBs only had a reduction in specific discharge capacity from 96 mAh.g^{-1} at RT to 82 mAh.g^{-1} at -20°C, as shown in **Figure 5.1(a)**. The two voltage plateaus observed during both charge and discharge have been identified as stable stages of graphite, suggesting a phase separation mechanism during (de)intercalation. While the RT discharge displayed these two characteristic voltage plateaus at 1.80 V and 2.25 V, the discharge at -20°C exhibited the same plateaus at lower voltages of 1.60 V and 2.10 V. This difference is due to the fact that the reaction rate is reduced upon lowering the temperature, thus requiring a higher overpotential to overcome the activation barrier for reaction. A similar difference in the voltage plateaus was observed to occur during charging at different temperatures. Near the upper cutoff voltage, a third voltage plateau around 2.5V was observed, which in our cells did not contribute toward the discharging capacity. This irreversible plateau is attributable to potential side reactions between the electrolyte with the current collector,[161–164] as also seen in the charging voltage curves at 0°C, 10°C, and RT. The additional voltage plateau becomes more prominent as the upper cutoff voltage is slightly increased (**Figure D-1**). Side reactions can reduce Coulombic efficiency at higher temperatures, as hinted in earlier reports,[150] highlighting the importance of the choice of upper cutoff voltage in the cell design. While better choices of the current collector can mitigate the side reaction and enable a reversible third intercalation plateau, the present work focuses on the fundamental intercalation and deintercalation mechanism of the $AlCl_4^-$ anion into graphite in the range of the two main voltage plateaus.

We tested the AIB pouch cells by cyclic voltammetry (CV) between 1 V and 2.5 V, with a scan rate of $10\ mV\ s^{-1}$, at five different temperatures. As the temperature increases from -20°C to RT, the positions of the respective charging peaks move forward while those during discharging move backward, consistent with the shifting of voltage plateaus we mentioned above. In addition, the absolute current density of the redox peaks in **Figure 5.1(b)** decreases with lowering temperatures, confirming that the reaction rate is affected by temperature.

5.2.2 Determination of diffusion coefficients

We used the potentiostatic intermittent titration technique (PITT) between 1 V and 2.2 V during charging and between 2.5 V and 1 V during discharging, with *10 mV* potential steps at all the selected temperatures to extract the different diffusion coefficient of $AlCl_4^-$ ion into graphite cathode ($D_{AlCl_4^-}$). The threshold currents of our PITT experiments are 0.05 C for temperatures ≤ 0°C and 0.1 C for 10°C and RT. We carefully selected the aforementioned upper cutoff voltage during charging and different threshold currents at higher temperatures to avoid the side reaction observed during galvanostatic cycling. The unwanted chemical reaction, if occurring, could hamper the accurate estimation of the diffusion coefficients.

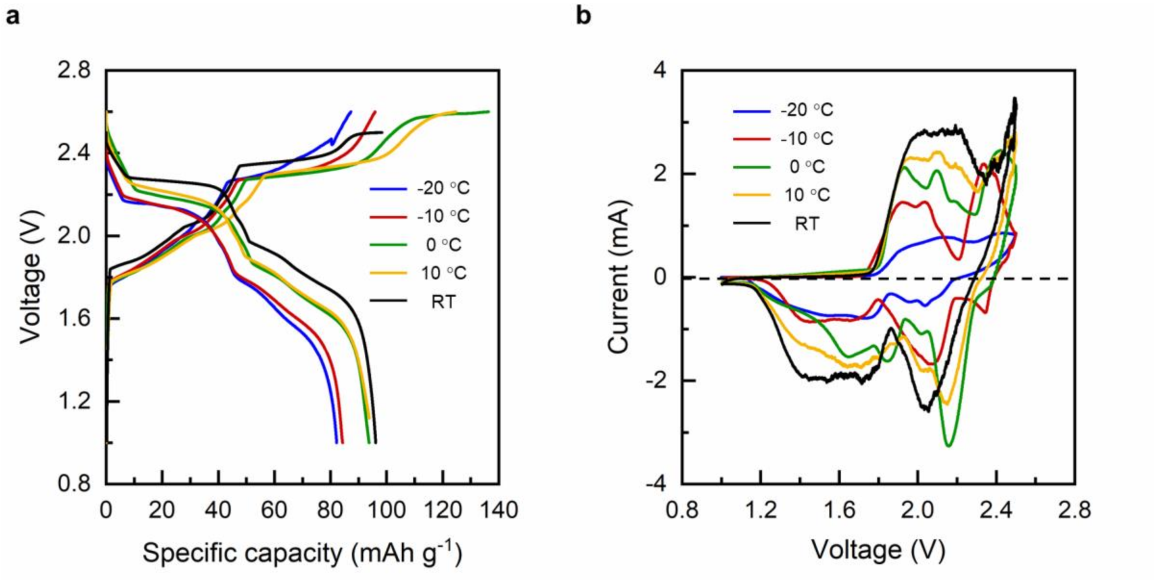

Figure 5.1: (a) Galvanostatic cyclic and (b) cyclic voltammetry of the AIB pouch cells. The capacity during galvanostatic discharge increased with temperature while the charging suffered from a side reaction at high voltages, leading to a ~70% Coulombic efficiency. The cyclic voltammogram showed higher peak currents at higher temperatures, confirming faster reactions at higher temperatures.

The Cottrell equation is the standard model for analyzing the transient current in response to the voltage steps in the PITT experiments, which assumes a diffusion-limited mechanism, reflected by a straight line in the Cottrell plots. However, results from our AIBs cells, like those from particulate porous electrodes for LIBs,[109,165] always show nonlinear data in the Cottrell plots, as shown in **Figures S2 – S11**, which suggest a possible mix-control mechanism. The modified PITT (mPITT) method has been successfully applied in LIBs and can provide a more comprehensive understanding of the processes,[92,93,109] via the electrochemical Biot number that relates rates between the solid-state diffusion and the surface reaction. By this definition, the "electrochemical Biot number" originally proposed by Li et al.[92,166] may be called the Damköhler number to avoid possible confusions with the classic Biot number that compares heat transfer resistance in the bulk and at the interface.

In general, the mPITT model separates the entire voltage step into two regimes: (i) short-time: $t << l^2/D_{AlCl_4^-}$ and (ii) long-time: $t >> l^2/D_{AlCl_4^-}$. We chose the transient current data within the initial 15% of the estimated diffusion time ($l^2/D_{AlCl_4^-}$) for the short-time fitting (Figures S2 – S11). Only a few voltage steps among the recorded ones generated long enough transient current to enter the long-time regime, where satisfactory fittings with the mPITT model were challenging, due to the lack of feasible *operando* characterization method to confirm the actual reacting area. According to the lithium-intercalation-induced population dynamics in similar particulate graphite,[109] the limited number of reacting particles at any time instant justify a limited reacting area much smaller than the total available interfacial area. This true reacting area is close to the apparent geometric area of the electrode.[109] We, therefore, adopted the geometric area for the data fitting.

The diffusion coefficients obtained by fitting the discharging transient currents with the mPITT model fell in the range of $10^{-9} – 10^{-7}\ cm^2\ s^{-1}$ for all cases, as shown in **Figure 5.2(a)-(e)**. On the other hand, the obtained Damköhler number *Da* showed a large variance at lower temperatures than higher temperatures. For instance, the B values ranged from 3 to 64 at -20°C, suggesting a transition from a diffusion-limited regime to a mixed-control regime. The B values of 1.14 – 2.25 for the RT case indicate the mixed-control mechanism. This result further confirmed that directly using the Cottrell equation to extract the diffusion coefficient based on the diffusion-limited assumption is not strictly valid, although practically an approximation of the curved data with a straight Cottrell line may yield similar diffusion coefficients (**Figure 5.2**).

The physical insights provided by the Damköhler number, however, are necessary, as they are critical for determining whether modifying the particle size or morphology will enable better (de)intercalation dynamics. The average value of $D_{AlCl_4^-}$ increased with increasing temperature, as shown in **Figure 5.2(f)**.

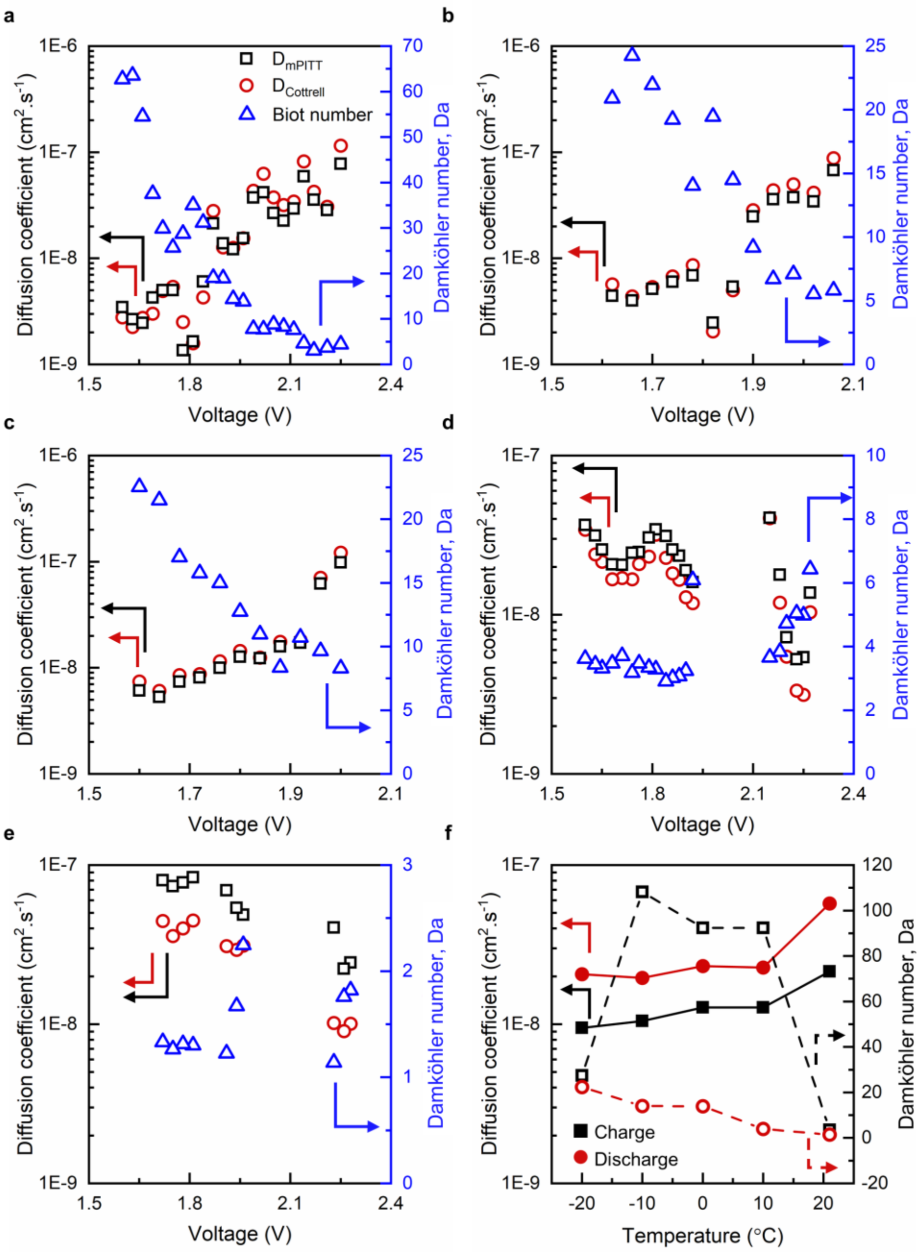

Figure 5.2: Potentiostatic titration intermittent technique (PITT) at different temperatures. The solid-state diffusion coefficients (black rectangle) and Damköhler number (blue triangle) are obtained

during discharging from the mPITT method at (a) -20°C, (b) -10°C, (c) 0°C, (d) 10°C, and (e) RT. The panels (a)-(e) also show the diffusion coefficients obtained using the Cottrell equation for comparison. (f) Average diffusion coefficients and Damköhler numbers during charge and discharge. The average diffusion coefficients increase with temperature during both charge and discharge. The Damköhler numbers indicate that the process is diffusion-limited at -20°C but becomes mixed-control at RT.

5.2.3 Temperature-insensitive Kinetics Revealed by Impedance Analysis

While the mPITT model is self-sufficient for the evaluation of the exchange current density j_0 via the expression $B = -j_0(\partial U/\partial C)/(D_{AlCl_4^-}RT)$, where $\partial U/\partial C$ is the derivative of the open-circuit voltage with respect to the anion concentration in the solid-state, R is the gas constant and T is the temperature,[92] its evaluation for the ideal phase transformation materials is impossible due to $\partial U/\partial C$ being zero. Hence, we performed electrochemical impedance spectroscopy (EIS) for an independent evaluation of j_0. We obtained the impedance spectra of the AIBs at several state-of-charges (SOCs) between 0% and 100% during both charging and discharging at all the five selected temperatures, with 0% SOC indicating empty graphite while 100% SOC indicating the highest intercalated state. **Figure D-22** shows the fitting of all the impedance spectra along with the fitting values in **Appendix D.6.2**. We charge or discharge the battery at a current of 0.5 C to the desired SOC and provide relaxation of 2 hours to achieve equilibrium before running an EIS. The Nyquist plots exhibited two semicircles followed by a straight line, modeled by the equivalent circuit displayed in **Figure 5.3(a)-(b)**. Here, the Warburg tail represents the solid-state diffusion in the graphite particles,[167] and the charge-transfer resistance can be calculated by measuring the diameter of the second semicircle. Generally, charge-transfer resistance governs the reaction kinetics, and its higher value represents a sluggish reaction. The initial charge-transfer resistance at -20°C was 7-folds higher than RT but was less than 4.4 times the RT charge transfer resistance at other SOCs. Moreover, the charge-transfer resistance only reaches a maximum of twice the RT value for higher temperatures as shown in **Figure 5.3(a)-(b)**. This trend is in contrast with the LIBs where the charge-transfer resistance increases drastically and becomes nearly 15 times of the RT at -10°C. Such a drastic increase slows the reaction rate in LIBs at low temperatures causing poor performance. In the case of AIBs, since the increase in charge-transfer resistance is not as severe as LIBs, they can provide a substantial capacity at lower temperatures, demonstrating their potential viability for low-temperature climates.

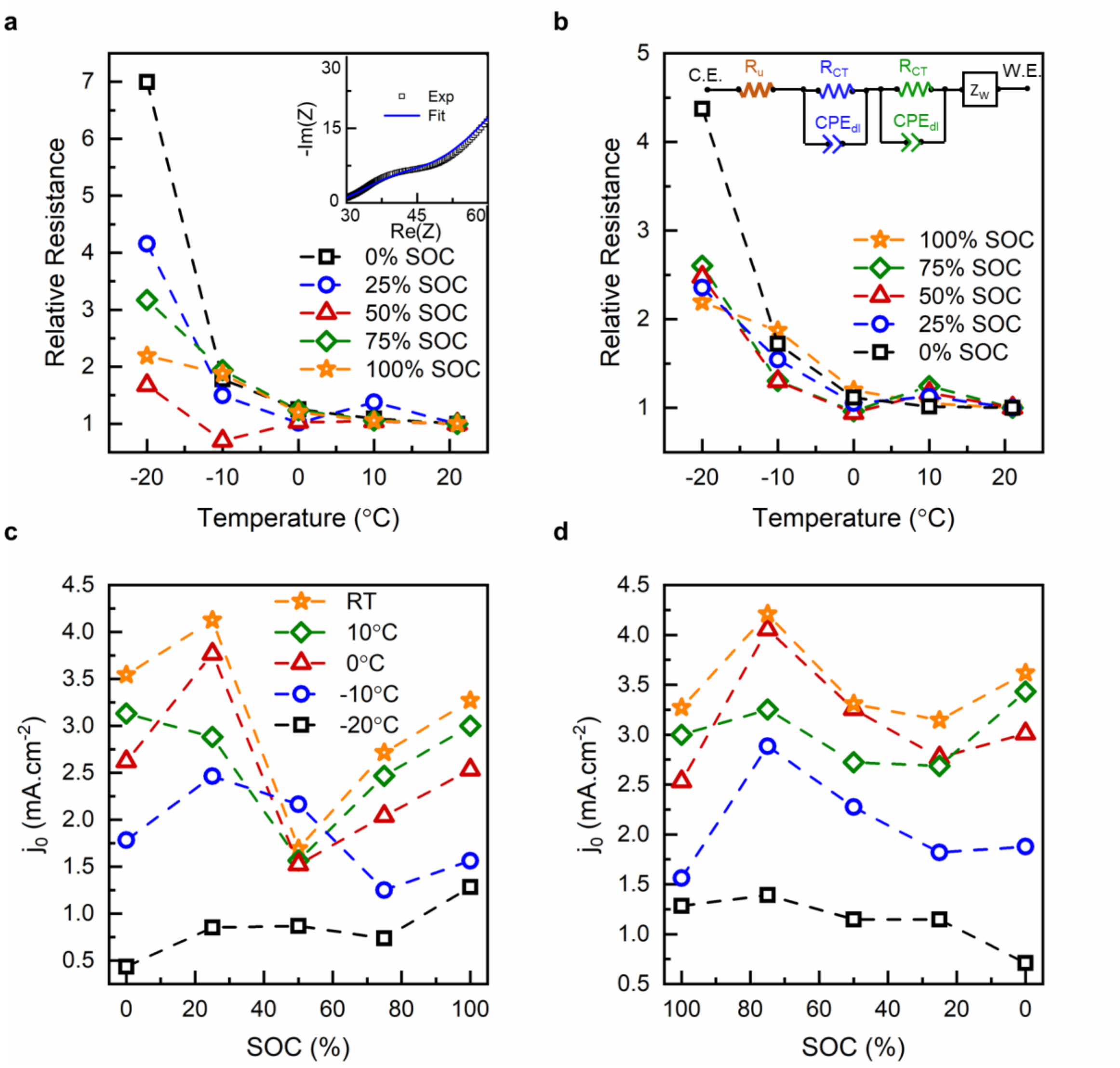

Figure 5.3: Temperature-dependent properties of AIBs revealed by impedance analysis. Charge-transfer resistance relative to the RT at the five temperatures at the selected SOCs during (a) charge, and (b) discharge. Inset in panel (a) shows a typical Nyquist plot showing two semicircles followed by a Warburg tail. Panel (b) also shows the equivalent circuit used to fit all the Nyquist plots. Exchange

current density obtained from the charge-transfer resistances at the five temperatures during (c) charge, and (d) discharge. The charge-transfer resistances reduce with increasing temperature, leading to faster reactions but the decay is much smaller as compared to the LIBs. The fastest reaction at RT results in the highest exchange current densities. The hysteresis in the exchange current densities arises due to an assumption of the constant active area in the estimation.

Exchange current density is a material property that characterizes the surface reaction at the electrode-electrolyte interface, often calculated using the Butler-Volmer equation.[131] At low overpotentials, the Butler-Volmer equation for j_0 simplifies to $j_0 = RT/(FAR_{CT})$, where R_{CT} is the charge-transfer resistance and A is the active area for reaction, assumed as the geometric area for simplification.[93] As shown in **Figure 5.3(c)-(d)**, our experiments confirmed that the j_0 for the surface reaction was between 0.5 and $1.4\ mA\ cm^{-2}$ at -20°C and as high as $4.2\ mA\ cm^{-2}$ at RT. In addition to the temperature dependence, the exchange current density for our system was highly SOC-dependent, as is the case for many other electrochemical systems.[131,168] Comparing **Figures 5.3(c) and 5.3(d)** reveals the existence of a slight hysteresis in j_0 between charge and discharge. Charging-discharging hysteresis has been observed in many battery cathode materials, including $LiFePO_4$, NMC, and NCA in LIBs, potentially attributable to phase transformation,[122] or crack formation,[93] both of which would affect the actual reacting area, hence affect the overpotential. As shown in a recent study for the graphite electrodes for lithium intercalation, the actual reacting area of the porous electrode is highly dependent on both the applied current and the exchange current density.[165] In the present study, we exploit our experience with lithium intercalation in graphite and extracted the SOC-dependent j_0 for anion intercalation in graphite at various temperatures for the first time.

5.2.4 Ionic Species in the Electrical double layer structure

The surprisingly fast low-temperature kinetics of graphite in AIBs may be explained by the temperature-insensitive supply of active species within the electrical double layer (EDL) structure, due to the lack of inactive but indispensable polar solvent molecules, e.g., ethylene carbonate (EC) that stabilizes carbonaceous anodes for LIBs, that may crowd into the inner Helmholtz layer. Here in AIBs, the ionic liquid consists of two salts without any solvent molecules, allowing a high concentration of active species without a blocking layer of inactive solvent molecules at the electrode surface to impede the charge transfer reaction.[169] The EDL structure was simulated via classical molecular dynamics (cMD) by applying surface charges to a Cu current collector as a proxy for the graphite electrode surface during operation.[170] As the surface charge is set to ±0.1 $C.m^{-2}$ at RT, the aluminum anode as represented by the negatively charged Cu was crowded by the $[EMIm]^+$ ions in the inner Helmholtz plane of the EDL to screen the surface charge, followed by a layer of the $AlCl_4^-$ ions to maintain the local neutrality (**Figure 5.4(a)**). At the cathode side with a positive surface charge, we see a much lower concentration of the $[EMIm]^+$ ions near the electrode surface, and the $AlCl_4^-$ anions can easily reach the electrode surface to complete the fast reaction. Based on the averaged concentration from the last 2 ns of the simulation, the EDL structure shows alternating layers of cations (**Figure 5.4(b)**), with little influence from the low temperature. Our MD simulations at -20°C, shown in **Figure D-23**, showed similarity in the distribution of ions in the electric double layers at both the electrodes, compared to RT. We observed almost no change in the average ion concentrations in the double layers when the temperature dropped from RT to -20°C. The enriched but oscillating concentrations of active species damp to their bulk concentrations at around 20 Å. Moreover, the bulky anions with a diameter of 10.70 Å are in close contact with the cathode surface, as indicated by the length of horizontal error bars in **Figure 5.4(b)**. Increasing the surface charge linearly decreases the concentration of $[EMIm]^+$ in the EDL while that of $AlCl_4^-$ remains relatively constant and fluctuates between 1.0 – 3.5 M (**Figure 5.4(c)**). Such temperature-insensitive distributions support the easy accessibility of the $AlCl_4^-$ anions for fast intercalation at the graphite surface, even at low temperatures such as -20°C, yielding a smaller difference in the charge-transfer resistances between -20°C and RT.

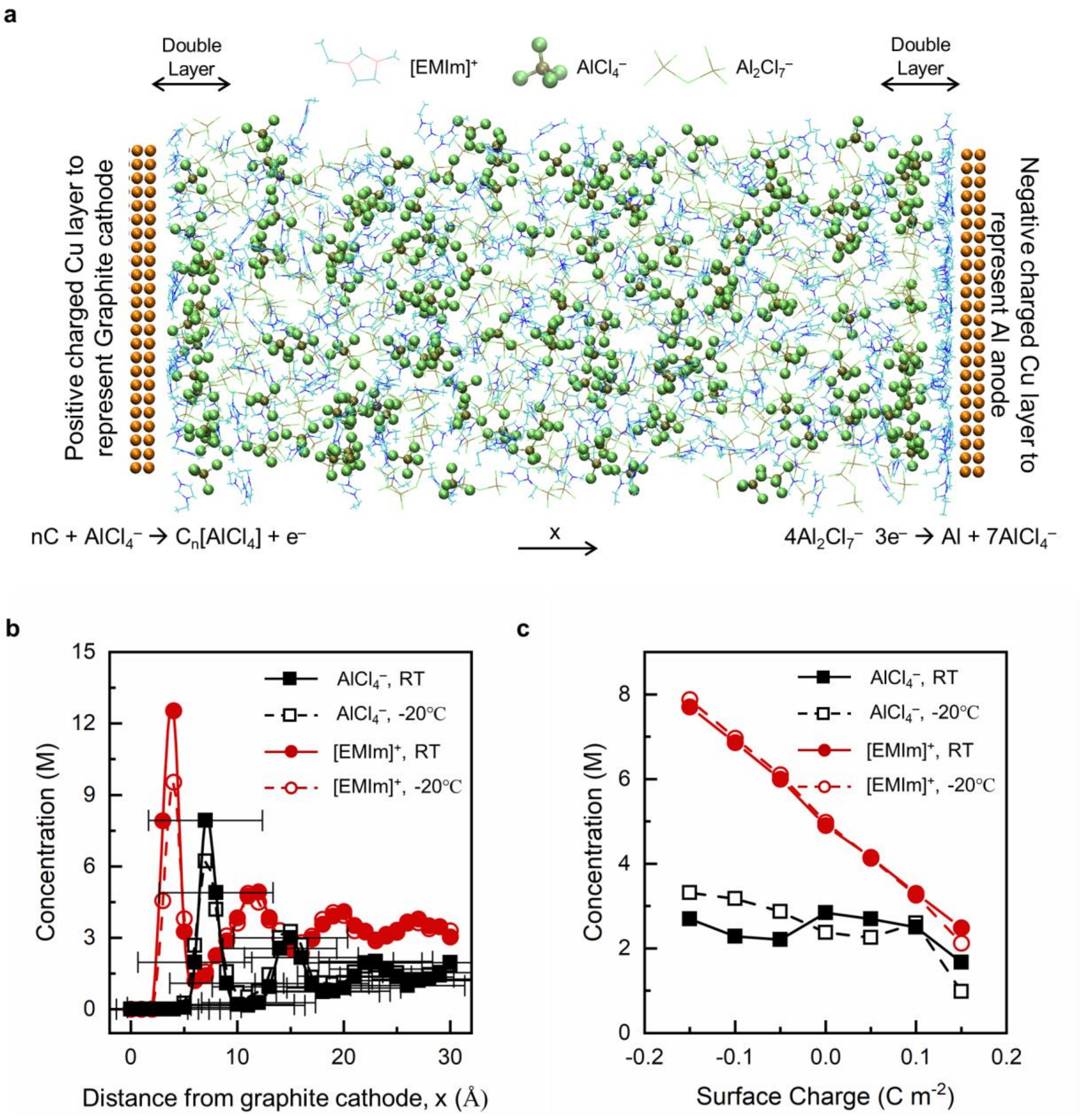

Figure 5.4: Molecular Dynamics simulation of AIB at RT and -20°C. (a) Structure of the electric double layer near the cathode and anode with the surface charge of ±0.1 C m^{-2}, along with the bulk at RT obtained from MD simulation. The electrodes are represented by positive and negative charged Cu layers. The MD simulation shows a high concentration of $AlCl_4^-$ anions at the cathode at RT. (b) Absolute concentrations of $[EMIm]^+$ and $AlCl_4^-$ ions within 30 Å from the graphite cathode with surface charge 0.1

C m^{-2}. The profile is obtained from averaging the final 2 ns of the simulation. The horizontal error bars on the concentration of $AlCl_4^-$ ions indicate their diameter, suggesting that they are already close to the charged electrode surface. (c) Average concentrations of [EMIm]$^+$ and $AlCl_4^-$ ions in the double layer at surface charges 0, ± 0.05, ± 0.1, and ± 0.15 C m^{-2}, at RT and -20°C temperatures.

5.3 Discussion

The galvanostatic cycling, along with CV, PITT, and EIS, provided valuable insights into the reaction kinetics governing the anion intercalation and deintercalation into the graphite cathodes in AIBs. In addition to the higher activation barrier for the surface reaction at low temperatures, the increased (decreased) operating voltage during galvanostatic charge (discharge) has been ascribed to a rise in electric polarization caused by decreased ionic conductivities of both the electrolyte and the SEI.[75] This effect appears less severe in AIBs than in LIBs, owing to the smaller drop in the ionic conductivity of the ionic liquid[171] from *15 mS.cm*$^{-1}$ at RT to *9 mS.cm*$^{-1}$ at -20°C, in stark contrast to the reported three-times drop in LIB from *9 mS.cm*$^{-1}$ at RT.[75] Although the increased overpotentials at lower temperatures would reduce the total capacities, the galvanostatic cycling and CV alone did not allow the rigorous investigation of the fundamental governing mechanisms. Combined with the independent EIS, the mPITT method provided a more detailed understanding of the reaction mechanisms in the AIBs. Our modeling suggested that both the diffusion (derived from $D_{AlCl_4^-}$) and surface reaction (derived from j_0) slowed down with decreasing temperature from RT to -20°C. However, the charge transfer mechanism shifted from mixed control at RT to diffusion control at -20°C. Assuming diffusion limitation from the Cottrell method, reducing the particle size would enhance the diffusion and the overall charge transfer. But, according to the insights from mPITT fitting, smaller particles would help the charge transfer at low temperatures to overcome the diffusion limitation, while higher surface area would enable faster surface reaction and avoid reaction limitation at higher temperatures. Thus, a robust electrode design for AIB would require an optimal particle size and surface morphology for better performance to operate under a relatively wide range of weather conditions.

The study confirms a mild increase in the charge-transfer resistance with decreasing temperature in AIBs, owing to the high availability of active species in the electric double layer even at low temperatures. In addition to the structures and local concentrations obtained from MD simulations, explicitly including the EDL contribution in the Butler-Volmer equation, e.g., via a modified Frumkin-Butler-Volmer equation[172], may further improve the mPITT method. Adopting the microscopic Marcus theory[173,174] and connecting the desolvation energy of active species at the inner Helmholtz plane with the reorganization energy[175,176] may provide quantitative explanations of the charge transfer resistance and the exchange current density, without using free fitting parameters. Since the ionic liquids exhibit different EDL structures than the polar solvent electrolytes,[169,177] the inclusion of EDL effects in the reaction kinetics especially becomes necessary for ionic liquids.

The understanding of the rate-governing mechanisms in the particulate phase-transforming electrodes is a multi-faceted multi-scale problem. While in the present study, we investigated the two important kinetic parameters, and their competing characteristics at various conditions, the anion-intercalation-induced phase-transformation dynamics at the single-particle level and the porous electrode level are important. Single-particle observations will aid in a deeper examination of the fundamental solid-state nucleation process. Mesoscale *operando* experiments at the electrode level will also be beneficial for a complete diagnosis of the population dynamics to facilitate the electrode design, as performed recently for LIBs.[109,165] The combined understanding coupled with a consistent thermodynamic model would be essential in determining the phase transformation mechanisms, crucial for the long-term performance of the AIBs.

5.4 Conclusion

We have performed a systematic electrochemical characterization, at five different temperatures, to assess the high-rate bulky anion intercalation in graphite electrodes of the AIBs invented by Dai et al.[15,110,178]. We adopted the modified PITT (mPITT) method and EIS to estimate the kinetic parameters and gauge the rate-limiting steps. Without the assumption of the diffusion limitation as in the Cottrell method, self-consistent diffusion coefficients ($10^{-9} – 10^{-7}$ cm^2 s^{-1}) and the exchange current densities ($0.5 – 4.2$ mA cm^{-2}) were obtained, both of which increase with increasing temperature, but the governing process changes from mixed control at RT to diffusion control at -20°C, as revealed by the Damköhler number. In stark contrast to LIBs that suffer from a 40-times increase of charge transfer resistance[75] upon decreasing the temperature from on reducing the temperature from RT to -20°C, the charge transfer resistance for the intercalation of much bulkier anion into similar graphite electrodes only increases up to five times. Our analysis suggested that the synergy of fast diffusion, low interfacial resistance, and high availability of the active species in the double layer enabled the surprising high-rate performance at low temperatures. Future research of incorporating explicitly the dielectric and concentration characteristics of the electrical double layer structure into charge transfer kinetics may enable more accurate quantitative understandings of the interfacial processes and help translate the insight from AIBs to low-temperature LIBs.

5.5 Experimental Section

Preparation of graphite electrode: We formed a homogeneous graphite slurry by dispersing SP-1 graphite powder (TED PELLA, Inc.) and PVdF binder (>99.5%, MTI Corp) in the ratio 90:10, in 1-methyl-2-pyrrolidone (NMP, 99.5%, Sigma Aldrich). This slurry was coated onto Cu foil by the doctor-blade method. We, then, dried the electrodes at 60°C to remove the NMP and punched out Φ8 mm electrodes. The Cu foil was then etched by immersing the punched electrodes into 2.5M iron chloride (Sigma Aldrich, 97%) solution to form free-standing graphite film. Finally, these graphite films were rinsed with deionized water to remove the residual $FeCl_3$ and dried at 70°C for 12 hours to obtain the graphite electrode for AIB.

Preparation of ionic liquid electrolyte: We formed the ionic liquid electrolyte for AIB by mixing 1-Ethyl-3-methylimidazolium chloride ([EMIm]Cl) (Sigma Aldrich, 98%) and anhydrous $AlCl_3$ (Alfa Aesar, 99%). [EMIm]Cl was dried at 70°C under vacuum for 24 hours to remove residual water. The ionic liquid was prepared by mixing $AlCl_3$ with dried [EMIm]Cl in the molar ratio 1.7:1 in an Ar-filled glove box. After stirring for 15 minutes, we obtained a light-yellow, transparent liquid.

mPITT method: Adopting the method developed by Li et al.[92], the analytical solution of $AlCl_4^-$ ion diffusion in graphite particles is

$$\frac{C(x,t) - C_0}{C_S - C_0} = 1 - 2Da \sum_{n=1}^{\infty} \frac{\cos\left[\lambda_n \left(1 - \frac{x}{l}\right)\right]}{(\lambda_n^2 + Da^2 + Da)\cos\lambda_n} \exp\left(-\lambda_n^2 \frac{D_{AlCl_4^-} t}{l^2}\right)$$

where $Da = -\frac{l(j_0|_S)(\partial U/\partial C|_S)}{D_{AlCl_4^-} RT}$ is the dimensionless Damköhler number, a ratio of the diffusion resistance and the resistance due to surface reaction. λ_1 is the 1st positive root of equation $\lambda_1 \tan \lambda_1$

= *Da*. For our systems, the term $(C_S - C_0)$ can be replaced with the total charge transferred in the applied potential step using Faraday's law as $Q_T = zFSl(C_S - C_0)$, where S is the geometric area of the electrode and l is the diffusion length. Neglecting higher order terms, the transient current can be written as Equation (1) for $t << l^2/D_{Li}$ and as Equation (2) for $t >> l^2/D_{Li}$

$$I(t) = \frac{D_{AlCl_4^-}Q}{l^2} Da \exp\left(Da^2 \frac{D_{AlCl_4^-}t}{l^2}\right) erfc\left(Da\sqrt{\frac{D_{AlCl_4^-}t}{l^2}}\right) \tag{1}$$

$$\ln[I(t)] = -\lambda_1^2\left(\frac{D_{AlCl_4^-}t}{l^2}\right) + \ln\left[\frac{2QD_{AlCl_4^-}}{l^2}\frac{Da^2}{(\lambda_1^2 + Da^2 + Da)}\right] \tag{2}$$

Both Da and $D_{AlCl_4^-}$ were estimated by fitting the experimental transient currents with the above analytical expressions by minimizing least squares using MATLAB.

MD simulation: The classical MD simulation was performed at constant volume and temperature (NVT) to the electrolyte-electrode nano-slit geometry[170] with two 40×40×20 $Å^3$ Cu electrodes in an FCC lattice sandwiching the 40×40×100 $Å^3$ electrolyte. According to the corresponding product stoichiometry of $AlCl_3$:[EMIm]Cl as 1.7:1,[179] the simulation box contains 351 $[EMIm]^+$, 140 $AlCl_4^-$, and 176 $Al_2Cl_7^-$. The model was constructed using the all-atom force field developed by Lopes et al.[180] for imidazolium cation and parameters developed by Mains et al. for anions[181] with geometric combination rules for the Lennard-Jones parameters between different atom types. Surface charge was applied by placing partial charge on the first layer of Cu atoms. Equilibration was performed at 1 fs time step for 10 ns without surface charge, followed by 20 ns simulation for each surface charge ramping continuously from ±0.05 to ±0.15 $C.m^2$. The final 2 ns of each surface charge was used for data collection. The initial configuration was generated by the open-source software Moltemplate and PACKMOL.[182,183] RDF analysis and visualization were performed using VMD.[184]

Chapter 6: Conclusions and Future Outlook

6.1 Conclusion

This dissertation explored the reliable and self-consistent ways to interpret million-particles electrode dynamics to the single-particle dynamics and further correlate with the atomic scale properties, and also paves the path for the systematic development of the anion intercalation-based chemistries for energy storage. For this purpose, we developed simple, yet precision techniques to identify and quantify the spatiotemporal heterogeneities in the particulate porous electrodes in realistic surroundings. We exploited the colorimetric behavior of lithiated graphite using optical microscope to monitor hundreds of particles along with fast acquisition rate of 0.5 fps, to capture the dynamic true electrochemical kinetics. With a new kinetic theory for the dynamics of phase evolution, we obtained a self-consistent precision understanding of the true electrochemical kinetics in phase transforming materials such as graphite, which have long been inferred by globally-averaged electrode responses. The kinetic parameters, such as the solid-state diffusion coefficients, estimated using the instantaneous electrochemical response were close to the *ab initio* calculations.[185] Thus, we achieved a consistent connection between the mesoscale and atomic scale predictions in the lithiated graphite through this research, for the first time. Contrary to the popular belief, the electrochemical dynamics in graphite is not controlled by solid-state diffusion process once the spatiotemporal heterogeneities emerge. Moreover, not all the phase separation processes in graphite can be suppressed by a high current, unlike other well-known phase transforming battery materials.[118]

To understand the phase transformation instability under the influence of reaction heterogeneities, we implemented the one-of-a-kind linear stability analysis to obtain an electrochemical phase diagram. This analysis was governed by the SOC-dependent non-monotonic intrinsic exchange current density, determined from the direct image analysis. The results revealed that the suppression of phase separation is determined by the interplay between the non-equilibrium thermodynamics of the materials and the intrinsic exchange current density at the interfaces. Thus, we performed a closed-loop analysis with a many-particle simulation based on the kinetic and thermodynamic properties established from the image analysis, for consistent predictions of the spatiotemporal heterogeneities in the particulate graphite electrode.

While the visual properties of lithiated graphite enabled a thorough examinations, there were challenges to monitor and quantify the reaction heterogeneities in particulate electrodes without colorimetric differentiation, such as NMC532 cathodes. For this purpose, we employed *in situ* Raman spectroscopy as a non-invasive and quantifiable technique to differentiate the regions based on the concentration of Li ions. Severe spatial heterogeneities existed at the particle-scale in the solid-solution material NMC532, even at low galvanostatic conditions. The true local current densities on the mesoscale under near-equilibrium conditions were 2-5 times of the globally-averaged ones, which would drastically affect the estimation of the fundamental kinetic parameters.

The dissertation also investigated the subtleties of the electrochemical kinetics during the anion intercalation into graphite cathodes in AIBs, at different temperatures between -20°C and ambient. We applied an elaborate analytical method to understand the transient current responses during the PITT experiments to reveal the rate-limiting mechanisms, unlike the Cottrell's method which assumes a diffusion limitation. This method complemented and cross-validated by other electroanalytical techniques including electrochemical impedance spectroscopy (EIS), galvanostatic cycling, and cyclic voltammetry (CV), provided a comprehensive understanding of the electrochemical behavior of graphite cathodes in AIBs. We revealed that the anion intercalation changed from a diffusion-controlled process at -20°C to a mixed-controlled process at ambient temperature. The use of solvent-free ionic electrolyte facilitated the fast kinetics at all the selected temperatures in AIBs.

6.2 Futue Outlook

Significant advances in the design of LIBs in the last decade have opened several avenues for their application, but the accurate predictions of the battery performance still pose challenges due to the nature of complexity involved in the extrapolation of the mesoscale response from the microscopic behavior. Such estimations are necessary for further revolutions of LIBs.

As a first step, the development of more imaging techniques is required to understand the dynamic process in the functioning materials under realistic surroundings, in real time and on the nano- to mesoscale.[32,108] These generalized techniques coupled with elegant theoretical analyses can reveal more accurate heterogeneity maps with enriched physical information. Further, the classical electroanalytical methods based on diffusion-limited assumption should be used carefully for estimating the solid-state diffusion coefficients, even if the true local current densities are accurately determined. The high local current densities even under low excitations suggest a far-from-equilibrium dynamics and requires the use of generalized models for the estimation of the kinetic parameters. Moreover, the inclusion of population dynamics is required to understand the mesoscale behavior since the self-adapted local driving force controls the activation of particles in the particulate electrodes.

While the observation and quantification of spatiotemporal heterogeneities are important for the estimation of fundamental parameters, the practical implications can be vastly different. LIB electrodes, especially phase transforming electrodes, are susceptible to memory effect, a degradation mechanism arising due to cycling history.[121,148] Solid-solution materials such as NMC and NCA also exhibit changes in interfacial kinetics and degradation based on their cycling history.[24,93] Thus, the degree of spatiotemporal charge heterogeneities would also be affected by the aging of the electrodes. The fast imaging techniques coupled with quantitative techniques suggested in this dissertation can be used to understand the interplay between the battery life and the heterogeneous charge distribution. These models can be combined with the thermodynamic phase-field simulations to provide the mesoscale kinetics in the porous electrodes. The inclusion of such comprehensive models can provide a better prediction of the life and degradation of the LIBs.

AIBs are one of the most promising emerging energy storage technologies that can operate in relatively wider range of weather conditions than LIBs. Their successful development relies on a methodical electrochemical characterization of the graphite cathodes along with an optimal cell design. The understanding of the rate-governing mechanisms in the particulate phase-transforming electrodes is a multi-faceted multi-scale problem. In addition to the estimation of the kinetic parameters and their competing characteristics at various conditions, the investigation of anion-intercalation-induced phase-transformation dynamics at the single-particle level and the porous electrode level are important. Single-particle observations will aid in a deeper examination of the fundamental solid-state nucleation process. Mesoscale *operando* experiments at the electrode level will also be beneficial for a complete diagnosis of the population dynamics to facilitate the electrode design, as performed for LIBs in this dissertation.[109,165] The combined understanding coupled with a consistent thermodynamic model would be essential in determining the phase transformation mechanisms, crucial for the long-term performance of the AIBs.

References

1. Tarascon, J.M., and Armand, M. (2001). Issues and challenges facing rechargeable lithium batteries. Nature *414*, 359–367.

2. Choi, J.W., and Aurbach, D. (2016). Promise and reality of post-lithium-ion batteries with high energy densities. Nat. Rev. Mater. *1*.

3. Goodenough, J.B., and Kim, Y. (2010). Challenges for rechargeable Li batteries. Chem. Mater. *22*, 587–603.

4. Nitta, N., Wu, F., Lee, J.T., and Yushin, G. (2015). Li-ion battery materials: Present and future. Mater. Today *18*, 252–264.

5. Kim, T., Song, W., Son, D.-Y., Ono, L.K., and Qi, Y. (2019). Lithium-ion batteries: outlook on present, future, and hybridized technologies Taehoon. J. Mater. Chem. A *7*, 2942–2964.

6. Pacala, S., and Socolow, R. (2004). Stabilization wedges: Solving the climate problem for the next 50 years with current technologies. Science (80-.). *305*, 968–972.

7. Levi, M.D., and Aurbach, D. (1997). The mechanism of lithium intercalation in graphite film electrodes in aprotic media. Part 1. High resolution slow scan rate cyclic voltammetric studies and modeling. J. Electroanal. Chem. *421*, 79–88.

8. Levi, M.D., and Aurbach, D. (1997). Diffusion coefficients of lithium ions during intercalation into graphite derived from the simultaneous measurements and modeling of electrochemical impedance and potentiostatic intermittent titration characteristics of thin graphite electrodes. J. Phys. Chem. B *101*, 4641–4647.

9. Markevich, E., Levi, M.D., and Aurbach, D. (2005). Comparison between potentiostatic and galvanostatic intermittent titration techniques for determination of chemical diffusion coefficients in ion-insertion electrodes. J. Electroanal. Chem. *580*, 231–237.

10. Kaskhedikar, N.A., and Maier, J. (2009). Lithium storage in carbon nanostructures. Adv. Mater. *21*, 2664–2680.

11. Persson, K., Sethuraman, V.A., Hardwick, L.J., Hinuma, Y., Meng, Y.S., Van Der Ven, A., Srinivasan, V., Kostecki, R., and Ceder, G. (2010). Lithium diffusion in graphitic carbon. J. Phys. Chem. Lett. *1*, 1176–1180.

12. Qi, Y., Guo, H., Hector, L.G., and Timmons, A. (2010). Threefold increase in the young’s modulus of graphite negative electrode during lithium intercalation. J. Electrochem. Soc. *157*, 558–566.

13. McCullough, F.P., Levine, C.A., and Snelgrove, R. V. (1989). Secondary Batteries.

14. Wang, G., Yu, M., Wang, J., Li, D., Tan, D., Löffler, M., Zhuang, X., Müllen, K., and Feng, X. (2018). Self-Activating, Capacitive Anion Intercalation Enables High-Power Graphite Cathodes. Adv. Mater. *30*.

15. Pan, C.J., Yuan, C., Zhu, G., Zhang, Q., Huang, C.J., Lin, M.C., Angell, M., Hwang, B.J., Kaghazchi, P., and Dai, H. (2018). An operando X-ray diffraction study of chloroaluminate anion-graphite intercalation in aluminum batteries. Proc. Natl. Acad. Sci. U. S. A. *115*, 5670–5675.

16. Williard, N., He, W., Hendricks, C., and Pecht, M. (2013). Lessons learned from the 787 dreamliner issue on Lithium-Ion Battery reliability. Energies *6*, 4682–4695.

17. Battery Fires in Air Transportation (2007).

18. Explosion in McMicken Battery Energy Storage System (2020). https://spectrum.ieee.org/dispute-erupts-over-what-sparked-an-explosive-liion-energy-storage-accident.

19. Harris, S.J., and Lu, P. (2013). Effects of inhomogeneities -Nanoscale to mesoscale -on the durability of Li-ion batteries. J. Phys. Chem. C *117*, 6481–6492.

20. Qi, Y., and Harris, S.J. (2010). In situ observation of strains during lithiation of a graphite electrode. J. Electrochem. Soc. *157*, 741–747.

21. Liu, J., Kunz, M., Chen, K., Tamura, N., and Richardson, T.J. (2010). Visualization of charge distribution in a lithium battery electrode. J. Phys. Chem. Lett. *1*, 2120–2123.

22. Thomas-Alyea, K.E., Jung, C., Smith, R.B., and Bazant, M.Z. (2017). In Situ Observation and Mathematical Modeling of Lithium Distribution within Graphite. J. Electrochem. Soc. *164*, E3063–E3072.

23. Chueh, W.C., El Gabaly, F., Sugar, J.D., Bartelt, N.C., McDaniel, A.H., Fenton, K.R., Zavadil, K.R., Tyliszczak, T., Lai, W., and McCarty, K.F. (2013). Intercalation pathway in many-particle LiFePO4 electrode revealed by nanoscale state-of-charge mapping. Nano Lett. *13*, 866–872.

24. Yang, Y., Xu, R., Zhang, K., Lee, S.-J., Mu, L., Liu, P., Waters, C.K., Spence, S., Xu, Z., Wei, C., et al. (2019). Quantification of Heterogeneous Degradation in Li-Ion Batteries. Adv. Energy Mater. *9*, 1900674.

25. Liu, H., Kazemiabnavi, S., Grenier, A., Vaughan, G., Di Michiel, M., Polzin, B.J., Thornton, K., Chapman, K.W., and Chupas, P.J. (2019). Quantifying Reaction and Rate Heterogeneity in Battery Electrodes in 3D through Operando X-ray Diffraction Computed Tomography. ACS Appl. Mater. Interfaces *11*, 18386–18394.

26. Finegan, D.P., Quinn, A., Wragg, D.S., Colclasure, A.M., Lu, X., Tan, C., Heenan, T.M.M., Jervis, R., Brett, D.J.L., Das, S., et al. (2020). Spatial dynamics of lithiation and lithium plating during high-rate operation of graphite electrodes. Energy Environ. Sci. *13*,

2570–2584.

27. Wang, J., Chen-Wiegart, Y.C.K., and Wang, J. (2014). In operando tracking phase transformation evolution of lithium iron phosphate with hard X-ray microscopy. Nat. Commun. *5*, 1–10.

28. Holtz, M.E., Yu, Y., Gunceler, D., Gao, J., Sundararaman, R., Schwarz, K.A., Arias, T.A., Abruña, H.D., and Muller, D.A. (2014). Nanoscale imaging of lithium ion distribution during in situ operation of battery electrode and electrolyte. Nano Lett. *14*, 1453–1459.

29. Gent, W.E., Li, Y., Ahn, S., Lim, J., Liu, Y., Wise, A.M., Gopal, C.B., Mueller, D.N., Davis, R., Weker, J.N., et al. (2016). Persistent State-of-Charge Heterogeneity in Relaxed, Partially Charged Li1−xNi3Co3Mn3O2 Secondary Particles. Adv. Mater. *28*, 6631–6638.

30. Nanda, J., Remillard, J., O'Neill, A., Bernardi, D., Ro, T., Nietering, K.E., Go, J.Y., and Miller, T.J. (2011). Local state-of-charge mapping of lithium-ion battery electrodes. Adv. Funct. Mater. *21*, 3282–3290.

31. Nakamura, T., Watanabe, T., Kimura, Y., Amezawa, K., Nitta, K., Tanida, H., Ohara, K., Uchimoto, Y., and Ogumi, Z. (2017). Visualization of Inhomogeneous Reaction Distribution in the Model LiCoO2 Composite Electrode of Lithium Ion Batteries. J. Phys. Chem. C *121*, 2118–2124.

32. Fang, S., Yan, M., and Hamers, R.J. (2017). Cell design and image analysis for in situ Raman mapping of inhomogeneous state-of-charge profiles in lithium-ion batteries. J. Power Sources *352*, 18–25.

33. Tian, C., Xu, Y., Nordlund, D., Lin, F., Liu, J., Sun, Z., Liu, Y., and Doeff, M. (2018). Charge Heterogeneity and Surface Chemistry in Polycrystalline Cathode Materials. Joule *2*, 464–477.

34. Li, Y., El Gabaly, F., Ferguson, T.R., Smith, R.B., Bartelt, N.C., Sugar, J.D., Fenton, K.R., Cogswell, D.A., Kilcoyne, A.L.D., Tyliszczak, T., et al. (2014). Current-induced transition from particle-by-particle to concurrent intercalation in phase-separating battery electrodes. Nat. Mater. *13*, 1149–1156.

35. Zhang, W., Yu, H.C., Wu, L., Liu, H., Abdellahi, A., Qiu, B., Bai, J., Orvananos, B., Strobridge, F.C., Zhou, X., et al. (2018). Localized concentration reversal of lithium during intercalation into nanoparticles. Sci. Adv. *4*, 1–12.

36. Levi, M.D., Sigalov, S., Salitra, G., Nayak, P., Aurbach, D., Daikhin, L., Perre, E., and Presser, V. (2013). Collective phase transition dynamics in microarray composite Li xFePO4 electrodes tracked by in situ electrochemical quartz crystal admittance. J. Phys. Chem. C *117*, 15505–15514.

37. Park, J., Zhao, H., Kang, S.D., Lim, K., Chen, C.C., Yu, Y.S., Braatz, R.D., Shapiro, D.A., Hong, J., Toney, M.F., et al. (2021). Fictitious phase separation in Li layered oxides driven by electro-autocatalysis. Nat. Mater. *20*, 991–999.

38. Pfaffmann, L., Birkenmaier, C., Müller, M., Bauer, W., Scheiba, F., Mitsch, T., Feinauer, J., Kr, Y., Hintennach, A., Schleid, T., et al. (2016). Investigation of the electrochemically active surface area and lithium diffusion in graphite anodes by a novel OsO 4 staining method. *307*, 762–771.

39. Liu, X., Ren, D., Hsu, H., Feng, X., Xu, G.L., Zhuang, M., Gao, H., Lu, L., Han, X., Chu, Z., et al. (2018). Thermal Runaway of Lithium-Ion Batteries without Internal Short Circuit. Joule *2*, 2047–2064.

40. Finegan, D.P., Vamvakeros, A., Tan, C., Heenan, T.M.M., Daemi, S.R., Seitzman, N., Di Michiel, M., Jacques, S., Beale, A.M., Brett, D.J.L., et al. (2020). Spatial quantification of dynamic inter and intra particle crystallographic heterogeneities within lithium ion electrodes. Nat. Commun. *11*, 1–11.

41. Weppner, W., and Huggins, R.A. (1977). Determination of the Kinetic Parameters of Mixed-Conducting Electrodes and Application to the System Li3Sb. J. Electrochem. Soc. *124*, 1569–1577.

42. Wen, C.J., and Huggins, R.A. (1980). Thermodynamic and mass transport properties of "LiIn." Mater. Res. Bull. *15*, 1225–1234.

43. Nicholson, R.S., and Shain, I. (1964). Theory of Stationary Electrode Polarography: Single Scan and Cyclic Methods Applied to Reversible, Irreversible, and Kinetic Systems. Anal. Chem. *36*, 706–723.

44. Ho, C., Raistrick, I.D., and Huggins, R.A. (1980). Application of A-C Techniques to the Study of Lithium Diffusion in Tungsten Trioxide Thin Films. J. Electrochem. Soc. *127*, 343–350.

45. Zhu, Y., Gao, T., Fan, X., Han, F., and Wang, C. (2017). Electrochemical Techniques for Intercalation Electrode Materials in Rechargeable Batteries. Acc. Chem. Res. *50*, 1022–1031.

46. Takahashi, K., and Srinivasan, V. (2015). Examination of Graphite Particle Cracking as a Failure Mode in Lithium- Ion Batteries : A Model-Experimental Study Examination of Graphite Particle Cracking as a Failure Mode in Lithium-Ion Batteries : A Model-Experimental Study. J. Electrochem. Soc. *162*, A635–A645.

47. Franger, S., Le Cras, F., Bourbon, C., and Rouault, H. (2002). LiFePO4 synthesis routes for enhanced electrochemical performance. Electrochem. Solid-State Lett. *5*, A231–A233.

48. Gao, F., and Tang, Z. (2008). Kinetic behavior of LiFePO4/C cathode material for lithium-ion batteries. Electrochim. Acta *53*, 5071–5075.

49. Yu, D.Y.W., Fietzek, C., Weydanz, W., Donoue, K., Inoue, T., Kurokawa, H., and Fujitani, S. (2007). Study of LiFePO4 by cyclic voltammetry. J. Electrochem. Soc. *154*, 253–257.

50. Xie, J., Imanishi, N., Zhang, T., Hirano, A., Takeda, Y., and Yamamoto, O. (2009). Li-ion

diffusion kinetics in LiFePO4 thin film prepared by radio frequency magnetron sputtering. Electrochim. Acta *54*, 4631–4637.

51. Churikov, A. V., Ivanishchev, A. V., Ivanishcheva, I.A., Sycheva, V.O., Khasanova, N.R., and Antipov, E. V. (2010). Determination of lithium diffusion coefficient in LiFePO4 electrode by galvanostatic and potentiostatic intermittent titration techniques. Electrochim. Acta *55*, 2939–2950.

52. Zhu, Y., and Wang, C. (2010). Galvanostatic intermittent titration technique for phase-transformation electrodes. J. Phys. Chem. C *114*, 2830–2841.

53. Dathar, G.K.P., Sheppard, D., Stevenson, K.J., and Henkelman, G. (2011). Calculations of Li-ion diffusion in olivine phosphates. Chem. Mater. *23*, 4032–4037.

54. Sugiyama, J., Nozaki, H., Harada, M., Kamazawa, K., Ofer, O., Månsson, M., Brewer, J.H., Ansaldo, E.J., Chow, K.H., Ikedo, Y., et al. (2011). Magnetic and diffusive nature of LiFePO4 investigated by muon spin rotation and relaxation. Phys. Rev. B - Condens. Matter Mater. Phys. *84*, 1–9.

55. Santos-Mendoza, I.O., Vázquez-Arenas, J., González, I., Ramos-Sánchez, G., and Castillo-Araiza, C.O. (2019). Revisiting Electrochemical Techniques to Characterize the Solid-State Diffusion Mechanism in Lithium-Ion Batteries. Int. J. Chem. React. Eng. *17*, 1–19.

56. Prosini, P.P., Lisi, M., Zane, D., and Pasquali, M. (2002). Determination of the chemical diffusion coefficient of lithium in LiFePO4. Solid State Ionics *148*, 45–51.

57. Morgan, D., der Ven, A., and Ceder, G. (2004). Li Conductivity in LixMPO4 (M = Mn , Fe , Co , Ni) Olivine Materials. Electrochem. Solid-State Lett. *7*, A30–A32.

58. Yu, P., Popov, B.N., Ritter, J.A., and White, R.E. (1999). Determination of the Lithium Ion Diffusion in Graphite. J. Electrochem. Soc. *146*, 8–14.

59. Umeda, M., Dokko, K., Fujita, Y., Mohamedi, M., Uchida, I., and Selman, J.R. (2001). Electrochemical impedance study of Li-ion insertion into mesocarbon microbead single particle electrode: Part I. Graphitized carbon. Electrochim. Acta *47*, 885–890.

60. Yang, H., Bang, H.J., and Prakash, J. (2004). Evaluation of Electrochemical Interface Area and Lithium Diffusion Coefficient for a Composite Graphite Anode. J. Electrochem. Soc. *151*, A1247.

61. Levi, M.D., and Aurbach, D. (2007). The application of electroanalytical methods to the analysis of phase transitions during intercalation of ions into electrodes. J. Solid State Electrochem. *11*, 1031–1042.

62. Persson, K., Hinuma, Y., Meng, Y.S., Van Der Ven, A., and Ceder, G. (2010). Thermodynamic and kinetic properties of the Li-graphite system from first-principles calculations. Phys. Rev. B - Condens. Matter Mater. Phys. *82*, 125416.

63. Ong, T.S., and Yang, H. (2002). Lithium Intercalation into Mechanically Milled Natural

Graphite Electrochemical and Kinetic Characterization. J. Electrochem. Soc. *149*, A1–A8.

64. Chang, Y., and Sohn, H. (2000). Electrochemical Impedance Analysis for Lithium Ion Intercalation into Graphitized Carbons Electrochemical Impedance Analysis for Lithium Ion Intercalation into Graphitized Carbons. J. Electrochem. Soc. *147*, 50–58.

65. Piao, T., Park, S.M., Doh, C.H., and Moon, S.I. (1999). Intercalation of Lithium Ions into Graphite Electrodes Studied by AC Impedance Measurements Intercalation of Lithium Ions into Graphite Electrodes Studied by AC Impedance Measurements. J. Electrochem. Soc. *146*, 2794–2798.

66. Yang, S., Wang, X., Yang, X., Bai, Y., Liu, Z., Shu, H., and Wei, Q. (2012). Determination of the chemical diffusion coefficient of lithium ions in spherical Li[Ni 0.5Mn 0.3Co 0.2]O 2. Electrochim. Acta *66*, 88–93.

67. Amin, R., and Chiang, Y.M. (2016). Characterization of electronic and ionic transport in Li1-xNi0.33Mn0.33Co0.33O2 (NMC333) and Li1-xNi0.50Mn0.20Co0.30O2 (NMC523) as a function of Li content. J. Electrochem. Soc. *163*, A1512–A1517.

68. Verma, A., Smith, K., Santhanagopalan, S., Abraham, D., Yao, K.P., and Mukherjee, P.P. (2017). Galvanostatic intermittent titration and performance based analysis of LiNi0.5Co0.2Mn0.3O2 cathode. J. Electrochem. Soc. *164*, A3380–A3392.

69. Hemminger, J.C., Sarrao, J., Crabtree, G., Fleming, G., and Ratner, M. (2015). Challenges at the Frontiers of Matter and Energy: Transformative Opportunities for Discovery Science. BESAC Subcomm. Challenges Front. Matter Energy, 1–78.

70. Yang, C., Chen, J., Ji, X., Pollard, T.P., Lü, X., Sun, C.J., Hou, S., Liu, Q., Liu, C., Qing, T., et al. (2019). Aqueous Li-ion battery enabled by halogen conversion–intercalation chemistry in graphite. Nature *569*, 245–250.

71. Li, Y., Lu, Y., Adelhelm, P., Titirici, M.-M., and Hu, Y.-S. (2019). Intercalation chemistry of graphite: alkali metal ions and beyond. Chem. Soc. Rev. *48*, 4655–4687.

72. Maire, P., Evans, A., Kaiser, H., Scheifele, W., and Novák, P. (2008). Colorimetric Determination of Lithium Content in Electrodes of Lithium- Ion Batteries. J. Electrochem. Soc. *155*, A862–A865.

73. Bai, P., and Tian, G. (2013). Statistical kinetics of phase-transforming nanoparticles in LiFePO 4 porous electrodes. Electrochim. Acta *89*, 644–651.

74. A. Pesaran , S.Santhanagopalan, G.K. (2013). Addressing the Impact of Temperature Extremes on Large Format Li-Ion Batteries for Vehicle Applications. 30Th Int. Batter. Semin.

75. Zhang, S.S., Xu, K., and Jow, T.R. (2003). The low temperature performance of Li-ion batteries. J. Power Sources *115*, 137–140.

76. Petzl, M., Kasper, M., and Danzer, M.A. (2015). Lithium plating in a commercial lithium-ion battery - A low-temperature aging study. J. Power Sources *275*, 799–807.

77. Ma, S., Jiang, M., Tao, P., Song, C., Wu, J., Wang, J., Deng, T., and Shang, W. (2018). Temperature effect and thermal impact in lithium-ion batteries: A review. Prog. Nat. Sci. Mater. Int. *28*, 653–666.

78. Bhowmik, A., Castelli, I.E., Garcia-lastra, J.M., Bj, P., Winther, O., and Vegge, T. (2019). A perspective on inverse design of battery interphases using multi-scale modelling , experiments and generative deep learning. *21*, 446–456.

79. Chu, S., Cui, Y., and Liu, N. (2016). The path towards sustainable energy. Nat. Mater. *16*, 16–22.

80. Harris, S.J., Timmons, A., Baker, D.R., and Monroe, C. (2010). Direct in situ measurements of Li transport in Li-ion battery negative electrodes. Chem. Phys. Lett. *485*, 265–274.

81. Etiemble, A., Besnard, N., Bonnin, A., Adrien, J., Douillard, T., Tran-Van, P., Gautier, L., Badot, J.C., Maire, E., and Lestriez, B. (2017). Multiscale morphological characterization of process induced heterogeneities in blended positive electrodes for lithium–ion batteries. J. Mater. Sci. *52*, 3576–3596.

82. Vanpeene, V., Villanova, J., King, A., Lestriez, B., Maire, E., and Roué, L. (2019). Dynamics of the Morphological Degradation of Si-Based Anodes for Li-Ion Batteries Characterized by In Situ Synchrotron X-Ray Tomography. Adv. Energy Mater. *9*, 1–13.

83. Jiang, Z., Li, J., Yang, Y., Mu, L., Wei, C., Yu, X., Pianetta, P., Zhao, K., Cloetens, P., Lin, F., et al. (2020). Machine-learning-revealed statistics of the particle-carbon/binder detachment in lithium-ion battery cathodes. Nat. Commun. *11*.

84. Bard, A.J., and Faulkner, L.F. (2001). Electrochemical Methods: Fundamentals and Applications 2nd ed. (John Wiley & Sons, Inc., New York, NY).

85. Maire, P., Kaiser, H., Scheifele, W., and Novák, P. (2010). Colorimetric determination of lithium-ion mobility in graphite composite electrodes. J. Electroanal. Chem. *644*, 127–131.

86. Guo, Y., Smith, R.B., Zhonghua, Y., Efetov, D.K., Wang, J., Kim, P., Bazant, M.Z., and Brus, L.E. (2016). Li Intercalation into Graphite: Direct Optical Imaging and Cahn−Hilliard Reaction Dynamics. J. Phys. Chem. Lett. *7*, 2151–2156.

87. Fraggedakis, D., Nadkarni, N., Gao, T., Zhou, T., Zhang, Y., Han, Y., Stephens, R.M., Shao-Horn, Y., and Bazant, M.Z. (2020). A scaling law to determine phase morphologies during ion intercalation. Energy Environ. Sci.

88. Avrami, M. (1939). Kinetics of phase change. I: General theory. J. Chem. Phys. *7*, 1103–1112.

89. Avrami, M. (1940). Kinetics of phase change. II Transformation-time relations for random distribution of nuclei. J. Chem. Phys. *8*, 212–224.

90. Tikhomirov, V.M. (2012). Selected Works of AN Kolmogorov: Volume I: Mathematics

and Mechanics. *25*.

91. Hyde, M.E., and Compton, R.G. (2003). A review of the analysis of multiple nucleation with diffusion controlled growth. J. Electroanal. Chem. *549*, 1–12.

92. Li, J., Xiao, X., Yang, F., Verbrugge, M.W., and Cheng, Y.T. (2012). Potentiostatic intermittent titration technique for electrodes governed by diffusion and interfacial reaction. J. Phys. Chem. C *116*, 1472–1478.

93. Tsai, P.C., Wen, B., Wolfman, M., Choe, M.J., Pan, M.S., Su, L., Thornton, K., Cabana, J., and Chiang, Y.M. (2018). Single-particle measurements of electrochemical kinetics in NMC and NCA cathodes for Li-ion batteries. Energy Environ. Sci. *11*, 860–871.

94. Xu, K. (2004). Nonaqueous liquid electrolytes for lithium-based rechargeable batteries. Chem. Rev. *104*, 4303–4417.

95. Single, F., Horstmann, B., and Latz, A. (2019). Theory of Impedance Spectroscopy for Lithium Batteries. J. Phys. Chem. C.

96. Arya, A., and Sharma, A.L. (2018). Effect of salt concentration on dielectric properties of Li-ion conducting blend polymer electrolytes. J. Mater. Sci. Mater. Electron. *29*, 17903–17920.

97. Takami, N., Satoh, A., Hara, M., and Ohsaki, T. (1995). Structural and Kinetic Characterization of Lithium Intercalation into Carbon Anodes for Secondary Lithium Batteries. J. Electrochem. Soc. *142*, 371–379.

98. Flores, E., Novák, P., and Berg, E.J. (2018). In situ and Operando Raman spectroscopy of layered transition metal oxides for Li-ion battery cathodes. Front. Energy Res. *6*, 1–16.

99. De Jesus, L.R., Zhao, Y., Horrocks, G.A., Andrews, J.L., Stein, P., Xu, B.X., and Banerjee, S. (2017). Lithiation across interconnected V2O5 nanoparticle networks. J. Mater. Chem. A *5*, 20141–20152.

100. Massé, R.C., Liu, C., Li, Y., Mai, L., and Cao, G. (2017). Energy storage through intercalation reactions: Electrodes for rechargeable batteries. Natl. Sci. Rev. *4*, 26–53.

101. Nanda, J., Remillard, J., O’Neill, A., Bernardi, D., Ro, T., Nietering, K.E., Go, J.Y., and Miller, T.J. (2011). Local state-of-charge mapping of lithium-ion battery electrodes. Adv. Funct. Mater. *21*, 3282–3290.

102. Rivera-Barrera, J.P., Muñoz-Galeano, N., and Sarmiento-Maldonado, H.O. (2017). Soc estimation for lithium-ion batteries: Review and future challenges.

103. Tran, M.K., and Fowler, M. (2020). A review of lithium-ion battery fault diagnostic algorithms: Current progress and future challenges. Algorithms *13*.

104. Hannan, M.A., Lipu, M.S.H., Hussain, A., and Mohamed, A. (2017). A review of lithium-ion battery state of charge estimation and management system in electric vehicle applications: Challenges and recommendations. Renew. Sustain. Energy Rev. *78*, 834–

854.

105. Tian, C., Xu, Y., Nordlund, D., Lin, F., Liu, J., Sun, Z., Liu, Y., and Doeff, M. (2018). Charge Heterogeneity and Surface Chemistry in Polycrystalline Cathode Materials. Joule *2*, 464–477.

106. Thomas-alyea, K.E., Jung, C., Smith, R.B., and Bazant, M.Z. (2017). In Situ Observation and Mathematical Modeling of Lithium Distribution within Graphite. J. Electrochem. Soc. *164*, E3063–E3072.

107. Qi, Y., and Harris, S.J. (2010). In situ observation of strains during lithiation of a graphite electrode. J. Electrochem. Soc. *157*, 741–747.

108. Merryweather, A.J., Schnedermann, C., Jacquet, Q., Grey, C.P., and Rao, A. (2021). Operando optical tracking of single-particle ion dynamics in batteries. Nature *594*, 522–528.

109. Agrawal, S., and Bai, P. (2021). Operando Electrochemical Kinetics in Particulate Porous Electrodes by Quantifying the Mesoscale Spatiotemporal Heterogeneities. Adv. Energy Mater. *203344*, 1–12.

110. Wang, D.Y., Wei, C.Y., Lin, M.C., Pan, C.J., Chou, H.L., Chen, H.A., Gong, M., Wu, Y., Yuan, C., Angell, M., et al. (2017). Advanced rechargeable aluminium ion battery with a high-quality natural graphite cathode. Nat. Commun. *8*, 1–7.

111. Kravchyk, K. V., and Kovalenko, M. V. (2019). Rechargeable Dual-Ion Batteries with Graphite as a Cathode Key Challenges and Opportunities. Adv. Energy Mater. *9*.

112. Zhang, X., Tang, Y., Zhang, F., and Lee, C.S. (2016). A Novel Aluminum–Graphite Dual-Ion Battery. Adv. Energy Mater. *6*, 1–6.

113. Zhang, M., Song, X., Ou, X., and Tang, Y. (2019). Rechargeable batteries based on anion intercalation graphite cathodes. Energy Storage Mater. *16*, 65–84.

114. Smith, R.B., Khoo, E., and Bazant, M.Z. (2017). Intercalation kinetics in multiphase layered materials. 1–28.

115. Ohzuku, T. (1993). Formation of Lithium-Graphite Intercalation Compounds in Nonaqueous Electrolytes and Their Application as a Negative Electrode for a Lithium Ion (Shuttlecock) Cell. J. Electrochem. Soc. *140*, 2490.

116. Levi, M.D., Levi, E.A., and Aurbach, D. (1997). The mechanism of lithium intercalation in graphite film electrodes in aprotic media. Part 2. Potentiostatic intermittent titration and in situ XRD studies of the solid-state ionic diffusion. J. Electroanal. Chem. *421*, 89–97.

117. Thomas-alyea, K.E., Jung, C., Smith, R.B., and Bazant, M.Z. (2017). In Situ Observation and Mathematical Modeling of Lithium Distribution within Graphite. *164*, E3063.

118. Bai, P., Cogswell, D.A., and Bazant, M.Z. (2011). Suppression of phase separation in LiFePO4 nanoparticles during battery discharge. Nano Lett. *11*, 4890–4896.

119. Li, Y., Chen, H., Lim, K., Deng, H.D., Lim, J., Fraggedakis, D., Attia, P.M., Lee, S.C., Jin, N., Moškon, J., et al. (2018). Fluid-enhanced surface diffusion controls intraparticle phase transformations. Nat. Mater. *17*, 915–922.

120. Cogswell, D.A., and Bazant, M.Z. (2013). Theory of coherent nucleation in phase-separating nanoparticles. Nano Lett. *13*, 3036–3041.

121. Kondo, H., Sasaki, T., Barai, P., and Srinivasan, V. (2018). Comprehensive Study of the Polarization Behavior of LiFePO 4 Electrodes Based on a Many-Particle Model. *165*, A2047.

122. Dreyer, W., Jamnik, J., Guhlke, C., Huth, R., Moškon, J., and Gaberšček, M. (2010). The thermodynamic origin of hysteresis in insertion batteries. Nat. Mater. *9*, 448–453.

123. Lim, J., Li, Y., Alsem, D.H., So, H., Lee, S.C., Bai, P., Cogswell, D.A., Liu, X., Jin, N., Yu, Y.S., et al. (2016). Origin and hysteresis of lithium compositional spatiodynamics within battery primary particles. Science (80-.). *353*, 566–571.

124. Tang, M., Carter, W.C., and Chiang, Y.M. (2010). Electrochemically driven phase transitions in insertion electrodes for lithium-ion batteries: Examples in lithium metal phosphate olivines.

125. Bazant, M.Z. (2013). Theory of chemical kinetics and charge transfer based on nonequilibrium thermodynamics. Acc. Chem. Res. *46*, 1144–1160.

126. Dresselhaus, M.S., and Dresselhaus, G. (2002). Intercalation compounds of graphite. Adv. Phys. *51*, 1–186.

127. Song, X.Y., Kinoshita, K., and Tran, T.D. (1996). Microstructural Characterization of Lithiated Graphite. J. Electrochem. Soc. *143*, L120–L123.

128. Ferguson, T.R., and Bazant, M.Z. (2014). Phase transformation dynamics in porous battery electrodes. Electrochim. Acta *146*, 89–97.

129. Cogswell, D.A., and Bazant, M.Z. (2012). Coherency strain and the kinetics of phase separation in LiFePO 4 nanoparticles. ACS Nano *6*, 2215–2225.

130. Ferguson, T.R., and Bazant, M.Z. (2012). Nonequilibrium thermodynamics of porous electrodes. J. Electrochem. Soc. *159*.

131. Newman, J., and Thomas-alyea, K.E. (2004). Electrochemical Systems (John Wiley & Sons, Inc., New York, NY).

132. Srinivasan, V., and Newman, J. (2004). Discharge model for the lithium iron-phosphate electrode. J. Electrochem. Soc. *151*.

133. Ferguson, T.R., and Bazant, M.Z. (2014). Phase transformation dynamics in porous battery electrodes. Electrochim. Acta *146*, 89–97.

134. Mori, F., Kubouchi, M., and Arao, Y. (2018). Effect of graphite structures on the

productivity and quality of few-layer graphene in liquid-phase exfoliation. J. Mater. Sci. *53*, 12807–12815.

135. Wang, F., Graetz, J., Moreno, M.S., Ma, C., Wu, L., Volkov, V., and Zhu, Y. (2011). Chemical distribution and bonding of lithium in intercalated graphite: Identification with optimized electron energy loss spectroscopy. ACS Nano *5*, 1190–1197.

136. Bazant, M.Z. (2017). Thermodynamic stability of driven open systems and control of phase separation by electro-autocatalysis. Faraday Discuss. *199*, 423–463.

137. Cai, L., An, K., Feng, Z., Liang, C., and Harris, S.J. (2013). In-situ observation of inhomogeneous degradation in large format Li-ion cells by neutron diffraction. *236*, 163–168.

138. Shao, M. (2014). In situ microscopic studies on the structural and chemical behaviors of lithium-ion battery materials. J. Power Sources *270*, 475–486.

139. Agrawal, S., and Bai, P. (2022). Dynamic interplay between phase transformation instabilities and reaction heterogeneities in particulate intercalation electrodes. Cell Reports Phys. Sci. *3*, 1–19.

140. Gilbert, J.A., Maroni, V.A., Cui, Y., Gosztola, D.J., Miller, D.J., and Abraham, D.P. (2018). Composition and Impedance Heterogeneity in Oxide Electrode Cross-Sections Detected by Raman Spectroscopy. *1701447*, 1–9.

141. Wei, Z., Salehi, A., Lin, G., Hu, J., Jin, X., Agar, E., and Liu, F. (2020). Probing Li-ion concentration in an operating lithium ion battery using in situ Raman spectroscopy. J. Power Sources *449*, 227361.

142. Cheng, Q., Wei, L., Liu, Z., Ni, N., Sang, Z., Zhu, B., Xu, W., Chen, M., Miao, Y., Chen, L., et al. Raman scattering microscopy. Nat. Commun., 1–10.

143. Rao, C.V., Soler, J., Katiyar, R., Shojan, J., West, W.C., and Katiyar, R.S. (2014). Investigations on Electrochemical Behavior and Structural Stability Situ Raman Spectroscopy.

144. Liu, W., Oh, P., Liu, X., Lee, M., Cho, W., Chae, S., Kim, Y., and Cho, J. (2015). Nickel-Rich Layered Lithium Transitional-Metal Oxide for High-Energy Lithium-Ion Batteries. Angew. Rev. *54*, 4440–4458.

145. Lu, H., Zhou, H., Mari, A., Fossdal, A., Sheridan, E., Lu, S., and Vullum-bruer, F. (2013). High capacity Li[Ni0.8Co0.1Mn0.1]O2 synthesized by sol–gel and co-precipitation methods as cathode materials for lithium-ion batteries. Solid State Ionics *249–250*, 105–111.

146. Kim, M., Shin, H., Shin, D., and Sun, Y. (2006). Synthesis and electrochemical properties of Li[Ni0.8Co0.1Mn0.1]O2 and Li[Ni0.8Co0.2]O2 via co-precipitation. J. Power Sources *159*, 1328–1333.

147. Inaba, M., Iriyama, Y., Ogumi, Z., Todzuka, Y., and Tasaka, A. (1997). Raman Study of

Layered Rock-Salt LiCoO and Its Electrochemical Lithium Deintercalation 2. *28*, 613–617.

148. Sasaki, T., Ukyo, Y., and Novák, P. (2013). Memory effect in a lithium-ion battery. Nat. Mater. *12*, 569–575.

149. Zhu, G., Wen, K., Lv, W., Zhou, X., Liang, Y., Yang, F., Chen, Z., Zou, M., Li, J., Zhang, Y., et al. (2015). Materials insights into low-temperature performances of lithium-ion batteries. J. Power Sources *300*, 29–40.

150. Pan, C.J., Yuan, C., Zhu, G., Zhang, Q., Huang, C.J., Lin, M.C., Angell, M., Hwang, B.J., Kaghazchi, P., and Dai, H. (2018). An operando X-ray diffraction study of chloroaluminate anion-graphite intercalation in aluminum batteries. Proc. Natl. Acad. Sci. U. S. A. *115*, 5670–5675.

151. Zhang, Y., Liu, S., Ji, Y., Ma, J., and Yu, H. (2018). Emerging Nonaqueous Aluminum-Ion Batteries: Challenges, Status, and Perspectives. Adv. Mater. *30*.

152. Elia, G.A., Marquardt, K., Hoeppner, K., Fantini, S., Lin, R., Knipping, E., Peters, W., Drillet, J.F., Passerini, S., and Hahn, R. (2016). An Overview and Future Perspectives of Aluminum Batteries. Adv. Mater. *28*, 7564–7579.

153. Ambroz, F., Macdonald, T.J., and Nann, T. (2017). Trends in Aluminium-Based Intercalation Batteries. Adv. Energy Mater. *7*.

154. Das, S.K., Mahapatra, S., and Lahan, H. (2017). Aluminium-ion batteries: developments and challenges. J. Mater. Chem. A *5*, 6347–6367.

155. Wei, J., Chen, W., Chen, D., and Yang, K. (2018). An amorphous carbon-graphite composite cathode for long cycle life rechargeable aluminum ion batteries. J. Mater. Sci. Technol. *34*, 983–989.

156. Wang, S., Yu, Z., Tu, J., Wang, J., Tian, D., Liu, Y., and Jiao, S. (2016). A Novel Aluminum-Ion Battery: Al/AlCl3-[EMIm]Cl/Ni3S2@Graphene. Adv. Energy Mater. *6*, 2–11.

157. Gao, Y., Zhu, C., Chen, Z.Z., and Lu, G. (2017). Understanding Ultrafast Rechargeable Aluminum-Ion Battery from First-Principles. J. Phys. Chem. C *121*, 7131–7138.

158. Wu, M.S., Xu, B., Chen, L.Q., and Ouyang, C.Y. (2016). Geometry and fast diffusion of AlCl4 cluster intercalated in graphite. Electrochim. Acta *195*, 158–165.

159. Jung, S.C., Kang, Y.J., Yoo, D.J., Choi, J.W., and Han, Y.K. (2016). Flexible Few-Layered Graphene for the Ultrafast Rechargeable Aluminum-Ion Battery. J. Phys. Chem. C *120*, 13384–13389.

160. Hu, H., Cai, T., Bai, P., Xu, J., Ge, S., Hu, H., Wu, M., Xue, Q., Yan, Z., Gao, X., et al. (2020). Small graphite nanoflakes as an advanced cathode material for aluminum ion batteries. Chem. Commun. *56*, 1593–1596.

161. Reed, L.D., and Menke, E. (2013). The Roles of V 2 O 5 and Stainless Steel in Rechargeable Al–Ion Batteries . J. Electrochem. Soc. *160*, A915–A917.

162. Chiku, M., Takeda, H., Matsumura, S., Higuchi, E., and Inoue, H. (2015). Amorphous Vanadium Oxide/Carbon Composite Positive Electrode for Rechargeable Aluminum Battery. ACS Appl. Mater. Interfaces *7*, 24385–24389.

163. Nakayama, Y., Senda, Y., Kawasaki, H., Koshitani, N., Hosoi, S., Kudo, Y., Morioka, H., and Nagamine, M. (2015). Sulfone-based electrolytes for aluminium rechargeable batteries. Phys. Chem. Chem. Phys. *17*, 5758–5766.

164. Wang, S., Jiao, S., Song, W.L., Chen, H. Sen, Tu, J., Tian, D., Jiao, H., Fu, C., and Fang, D.N. (2018). A novel dual-graphite aluminum-ion battery. Energy Storage Mater. *12*, 119–127.

165. Agrawal, S., and Bai, P. (2021). Interplay between Phase Transformation Instabilities and Spatiotemporal Reaction Heterogeneities in Particulate Intercalation Electrodes. arXiv *2110.13403*.

166. Li, J., Yang, F., Xiao, X., Verbrugge, M.W., and Cheng, Y.T. (2012). Potentiostatic intermittent titration technique (PITT) for spherical particles with finite interfacial kinetics. Electrochim. Acta *75*, 56–61.

167. Ho, C., Raistrick, I.D., and Huggins, R.A. (1980). Application of A-C Techniques to the Study of Lithium Diffusion in Tungsten Trioxide Thin Films. J. Electrochem. Soc. *127*, 343–350.

168. Doyle, M., Fuller, T.F., and Newman, J. (1993). Modeling of Galvanostatic Charge and Discharge of the Lithium/Polymer/Insertion Cell. J. Electrochem. Soc. *140*, 1526–1533.

169. Oldham, K.B. (2008). A Gouy-Chapman-Stern model of the double layer at a (metal)/(ionic liquid) interface. J. Electroanal. Chem. *613*, 131–138.

170. McEldrew, M., Goodwin, Z.A.H., Kornyshev, A.A., and Bazant, M.Z. (2018). Theory of the Double Layer in Water-in-Salt Electrolytes. J. Phys. Chem. Lett. *9*, 5840–5846.

171. Cosby, T., Durkin, D.P., Mantz, R.A., and Trulove, P.C. (2021). Ion Dynamics and Charge Transport in Imidazolium Chloroaluminate Ionic Liquids. ECS Meet. Abstr. *MA2021-01*, 424–424.

172. Biesheuvel, P.M., van Soestbergen, M., and Bazant, M.Z. (2009). Imposed currents in galvanic cells. Electrochim. Acta *54*, 4857–4871.

173. Marcus, R.A. (1956). Electrostatic free energy and other properties of states having nonequilibrium polarization. I. J. Chem. Phys. *24*, 979–989.

174. Bai, P., and Bazant, M.Z. (2014). Charge transfer kinetics at the solid-solid interface in porous electrodes. Nat. Commun. *5*, 1–7.

175. Bangle, R.E., Schneider, J., Piechota, E.J., Troian-Gautier, L., and Meyer, G.J. (2020).

Electron Transfer Reorganization Energies in the Electrode-Electrolyte Double Layer. J. Am. Chem. Soc. *142*, 674–679.

176. Xiao, T., and Song, X. (2013). Reorganization energy of electron transfer processes in ionic fluids: A molecular Debye-Hückel approach. J. Chem. Phys. *138*.

177. Kornyshev, A.A. (2007). Double-layer in ionic liquids: Paradigm change? J. Phys. Chem. B *111*, 5545–5557.

178. Lin, M.C., Gong, M., Lu, B., Wu, Y., Wang, D.Y., Guan, M., Angell, M., Chen, C., Yang, J., Hwang, B.J., et al. (2015). An ultrafast rechargeable aluminium-ion battery. Nature *520*, 325–328.

179. Shinde, P., Ahmed, A.N., Nahian, M.K., Peng, Y., and Reddy, R.G. (2020). Conductivity of 1-Ethyl-3-Methylimidazolium Chloride (EMIC) and Aluminum Chloride (AlCl 3) Ionic Liquids at Different Temperatures and AlCl 3 Mole Fractions . ECS Meet. Abstr. *MA2020-02*, 3006–3006.

180. Canongia Lopes, J.N., Deschamps, J., and Pádua, A.A.H. (2004). Modeling Ionic Liquids Using a Systematic All-Atom Force Field. J. Phys. Chem. B *108*, 2038–2047.

181. Mains, G.J., Nantsis, E.A., and Carper, W.R. (2001). Ab Initio Bonding, Molecular Structure, and Quadrupole Coupling Constants of Aluminum Chlorides. J. Phys. Chem. A *105*, 4371–4378.

182. Jewett, A.I., Stelter, D., Lambert, J., Saladi, S.M., Roscioni, O.M., Ricci, M., Autin, L., Maritan, M., Bashusqeh, S.M., Keyes, T., et al. (2021). Moltemplate: A Tool for Coarse-Grained Modeling of Complex Biological Matter and Soft Condensed Matter Physics. J. Mol. Biol. *433*, 166841.

183. Martinez, L., Andrade, R., Birgin, E.G., and Martinez, J.M. (2009). Packmol: A Package for Building Initial Configurations for Molecular Dynamics Simulations. J. Comput. Chem. *30*, 2157–2164.

184. Humphrey, W., Dalke, A., and Schulten, K. (1996). VMD: Visual Molecular Dynamics. J. Mol. Graph. *14*, 33–38.

185. Persson, K., Hinuma, Y., Meng, Y.S., Van Der Ven, A., and Ceder, G. (2010). Thermodynamic and kinetic properties of the Li-graphite system from first-principles calculations. Phys. Rev. B - Condens. Matter Mater. Phys. *82*, 1–9.

186. Ohzuku, T., Iwakoshi, Y., and Sawai, K. (1993). Formation of Lithium-Graphite Intercalation Compounds in Nonaqueous Electrolytes and Their Application as a Negative Electrode for a Lithium Ion (Shuttlecock) Cell. J. Electrochem. Soc. *140*, 2490–2498.

Appendix A. Supporting Materials for Chapter 2

A.1 Illustration of the *operando* setup

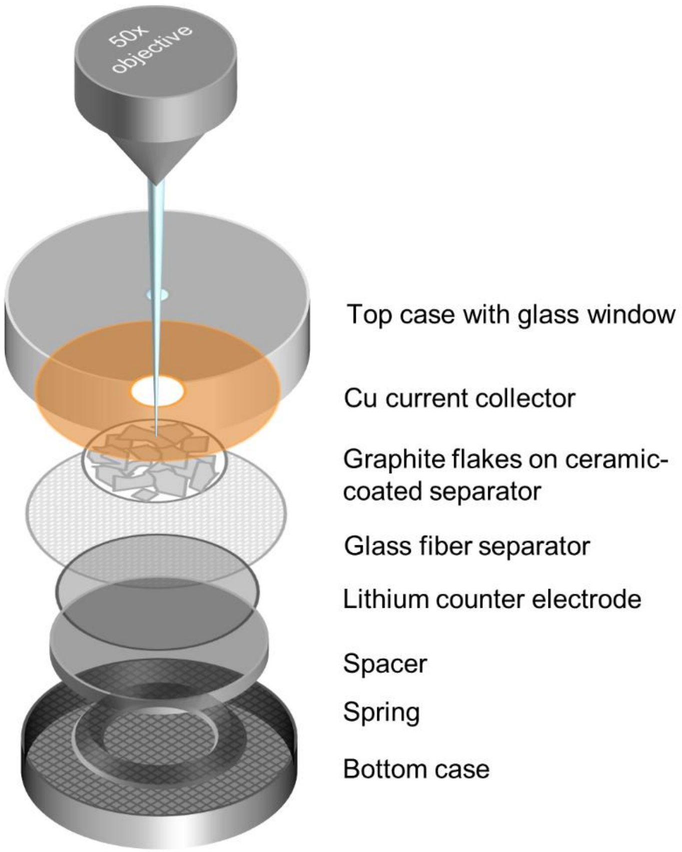

Figure A-1: The *operando* setup to monitor real-time Li^+ ion intercalation into graphite flakes

A.2 Fabrication of thin graphite electrode

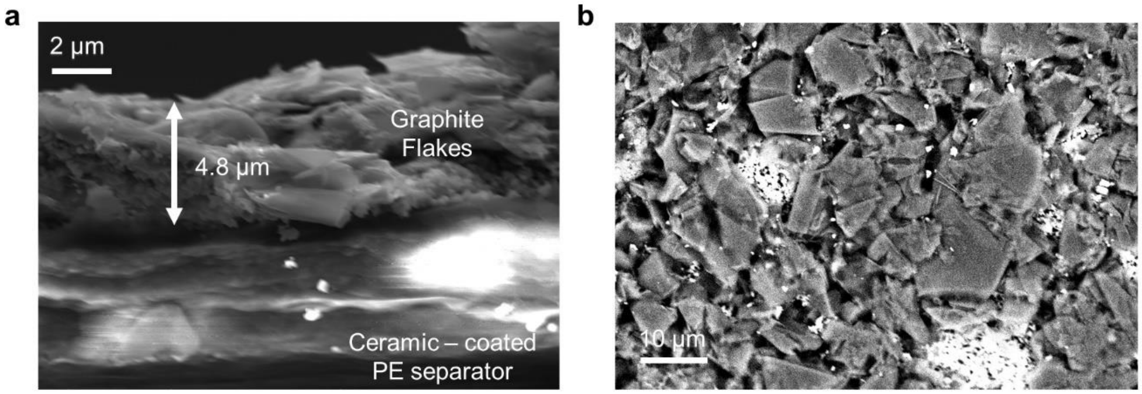

Figure A-2: Thin uniform graphite electrode. (a) Cross-section of the graphite electrode. Flake-type graphite is coated on the commercial ceramic-coated PE separator. (b) Top view of the graphite electrode. The bright white regions are the native ceramic coating (Al_2O_3 particles) of the separator.

A.3 PITT curve

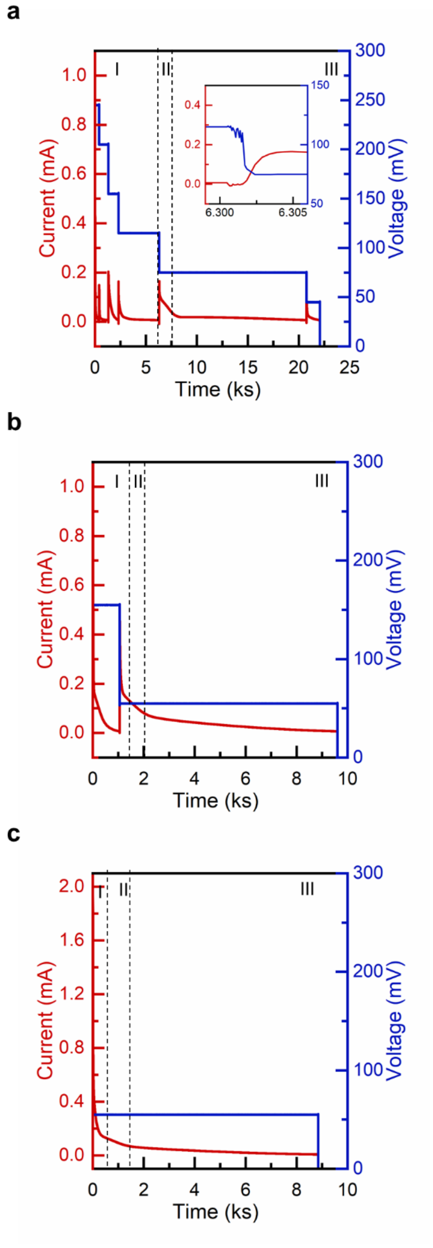

Figure A-3: PITT discharge from 245mV to 5mV. (a) PITT discharge at 10 mV step. Some of the steps are indistinguishable as they reach the threshold current C/20 much faster than the sampling rate of the voltage response (1 second). Inset shows the transition from 125 mV to 75 mV through a series of unrecognizable voltage steps. (b) PITT discharge at 100 mV step. (c) PITT discharge at 200 mV step.

The overall PITT experiment is divided into three segments: Segment (I) is the solid-solution transformation from empty to Stage 3, Segment (II) is the phase transformation from Stage 3 to Stage 2 and Segment (III) is the phase transformation from Stage 2 to Stage 1.

A.4 Phase transformation in graphite

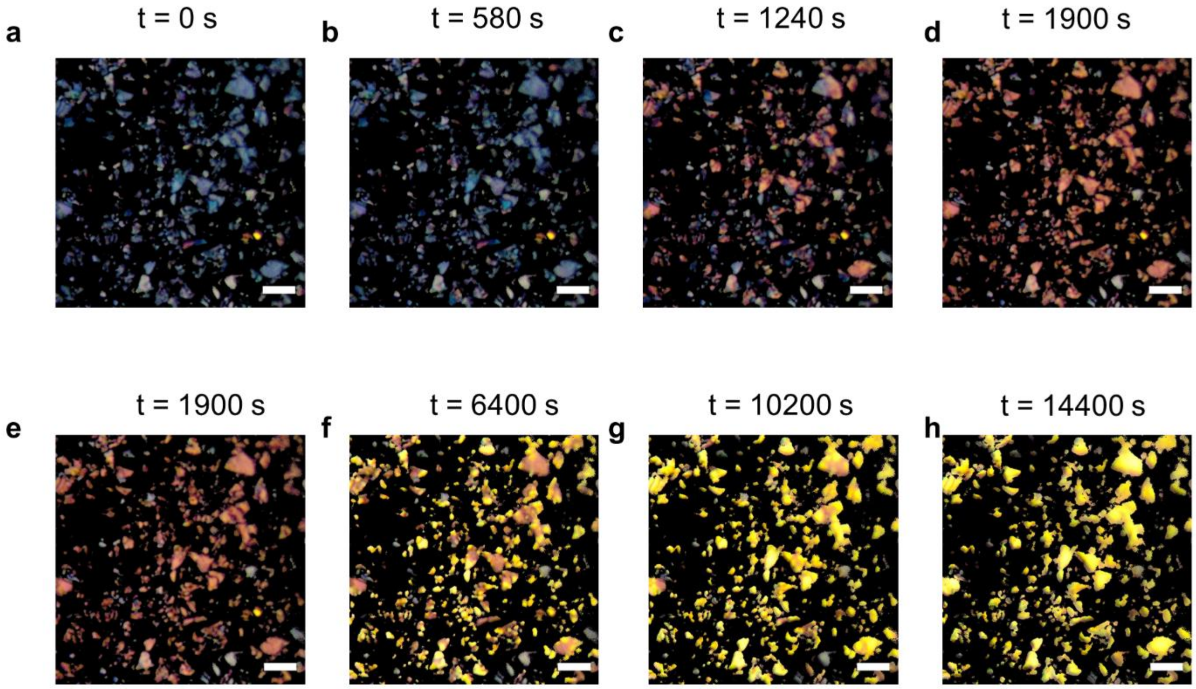

Figure A-4: Phase transformation from Stage 3 to Stage 1 during Li$^+$ ion intercalation in graphite. Particle-by-particle intercalation from (a-d) Stage 3 (blue) to Stage 2 (red), and (e-h) Stage 2 to Stage 1 (gold). Scale bar: 10μm

A.5 Validation of charge conservation

The validity of equation $\sum_i x_i a_i(t) q_o A_T = Q_T(t)$ during the phase transformation confirms that a fixed SOC value (i.e. characteristic filling fraction) can be assigned to the stable phases and that the phenomena in the frame of view can be extrapolated to the entire electrode, as explained in the main text. Figure A-5 shows the comparison between the total charge supplied in the phase transformation regions with the total charge calculated from the above equation. The normalized capacity contributions from each phase were fitted with analytical formulas listed in Table A-1 to ensure that R^2 greater than 0.98 (Figure A-5(a)-(c)). Due to normalization of the capacities, the same parameters can reflect the corresponding evolution of area fractions displayed in Figure 2.1(d) of the main text. These analytical curves were then used to derive the “phase currents” shown in Figure 2.1(e) by taking the first order time derivative. This treatment preserves the charge conservation, and at the same time avoid the excessive noises generated by differentiating the experimental data directly.

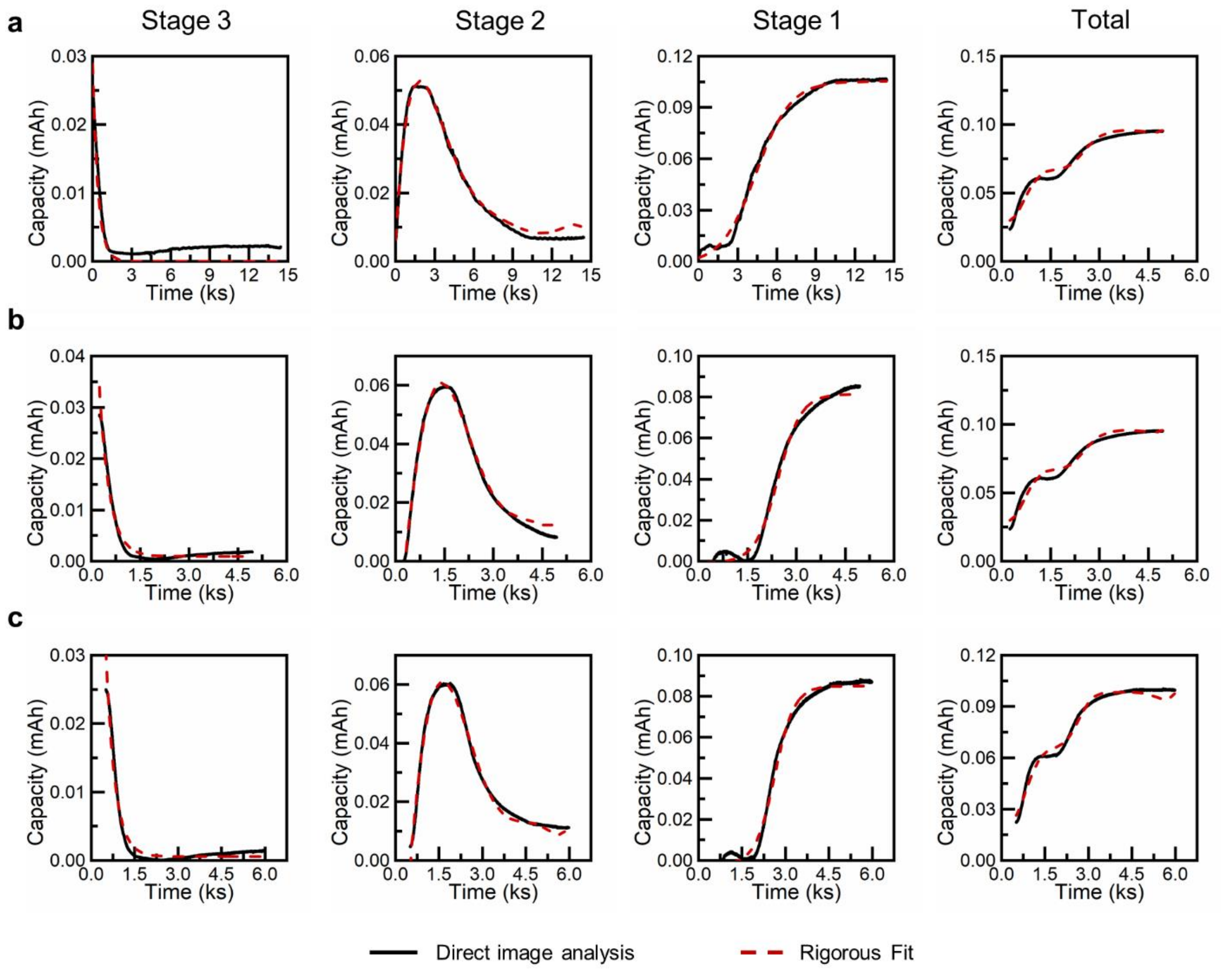

Figure A-5: Validated evolution curves for individual phases (stages) based on global charge conservation. Fitting of individual capacity contribution by Stage 3, Stage 2, Stage 1, and the total capacity in (a) 10 mV, (b) 100 mV, and (c) 200mV, with corresponding analytical formulas shown in **Table A-1**. These analytical expressions were used to calculate the phase currents.

The equations used for fitting the capacity evolutions shown in Figure A-8, along with the fitting parameters are shown in **Table A-1**.

Table A-1: Fitting parameters of the charge contribution by individual stages

	Phase	Stage 3	Stage 2	Stage 1
	Equation	a exp(-bx)+c	$ax^6+bx^5+cx^4+dx^3+ex^2+fx+g$	$\mathbf{a}+\frac{\mathbf{1}}{\mathbf{b+c\,exp(-dx)}}$
10 mV	**a**	1.07	-95.28	-0.02
	b	34.43	337.40	1.00
	c	0.07	-474.60	27.90
	d	-	334.60	10.88
	e	-	-119.90	-
	f	-	17.84	-
	g	-	0.12	-
100 mV	**a**	0.08	5.68	-0.001
	b	15.72	-18.41	8.64
	c	0.001	21.67	9078.00
	d	-	-10.22	14.09
	e	-	0.72	-
	f	-	0.62	-
	g	-	-0.04	-
200 mV	**a**	0.17	7.07	-0.003
	b	19.10	-21.21	8.34
	c	0.0006	22.13	19900
	d	-	-7.82	17.71
	e	-	-1.18	-
	f	-	1.12	-
	g	-	-0.084	-

A.6 Phase evolution during 100 mV and 200 mV PITT

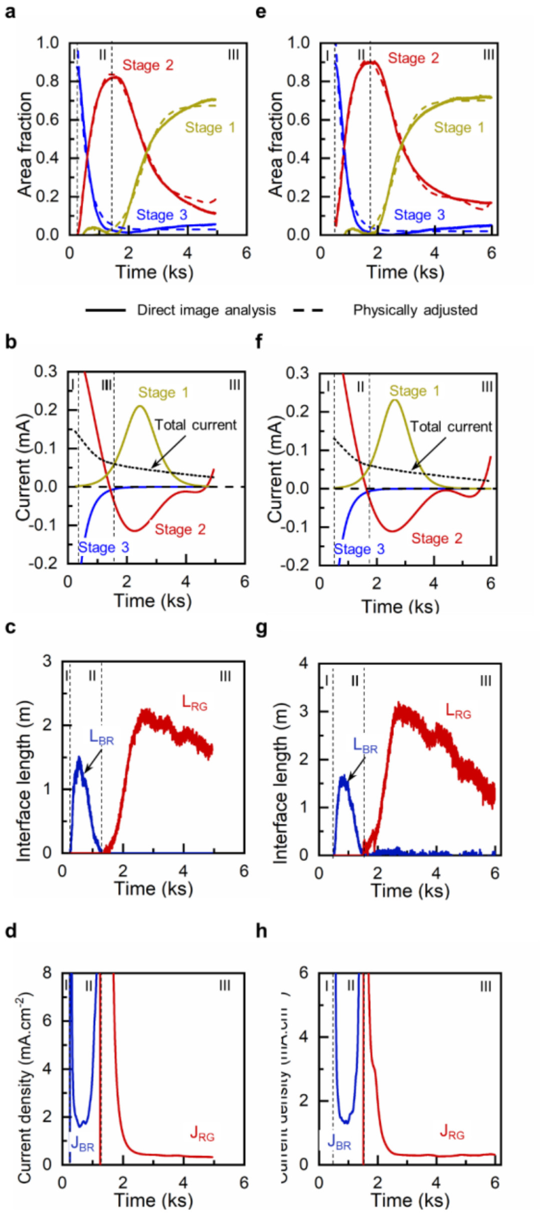

Figure A-6: Phase evolution at 100 mV and 200 mV steps. (a) *Operando* area evolution of Blue, Red and Gold phases, (b) Phase current evolution during phase transformation, (c) Propagation of Blue-Red and Red-Gold interface lengths during phase transformation, and (d) *Operando* interfacial current density during Blue-Red and Red-Gold phase transformations, during 100 mV step experiment. (e) *Operando* area evolution of Blue, Red and Gold phases, (f) Phase current evolution during phase transformation, (g) Propagation of Blue-Red and Red-Gold interface lengths during phase transformation, and (h) *Operando* interfacial current density during Blue-Red and Red-Gold phase transformations, during 200 mV step experiment.

A.7 Particle size distribution

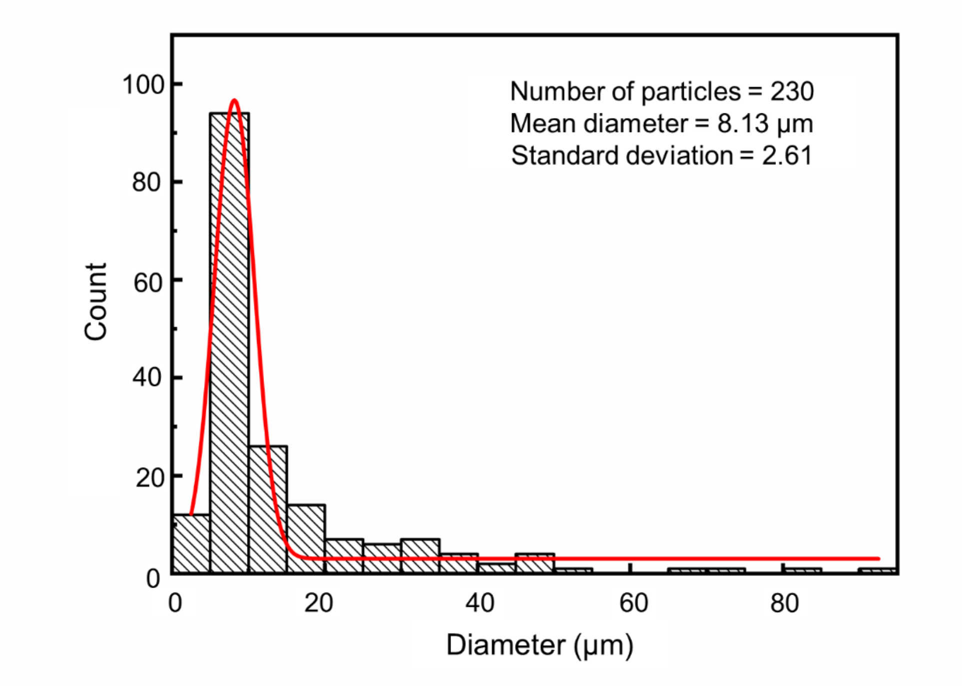

Figure A-7: Lognormal particle size distribution of the graphite particles present in the viewing area under the optical microscope.

A.8 Benchmark images for characteristic SOCs

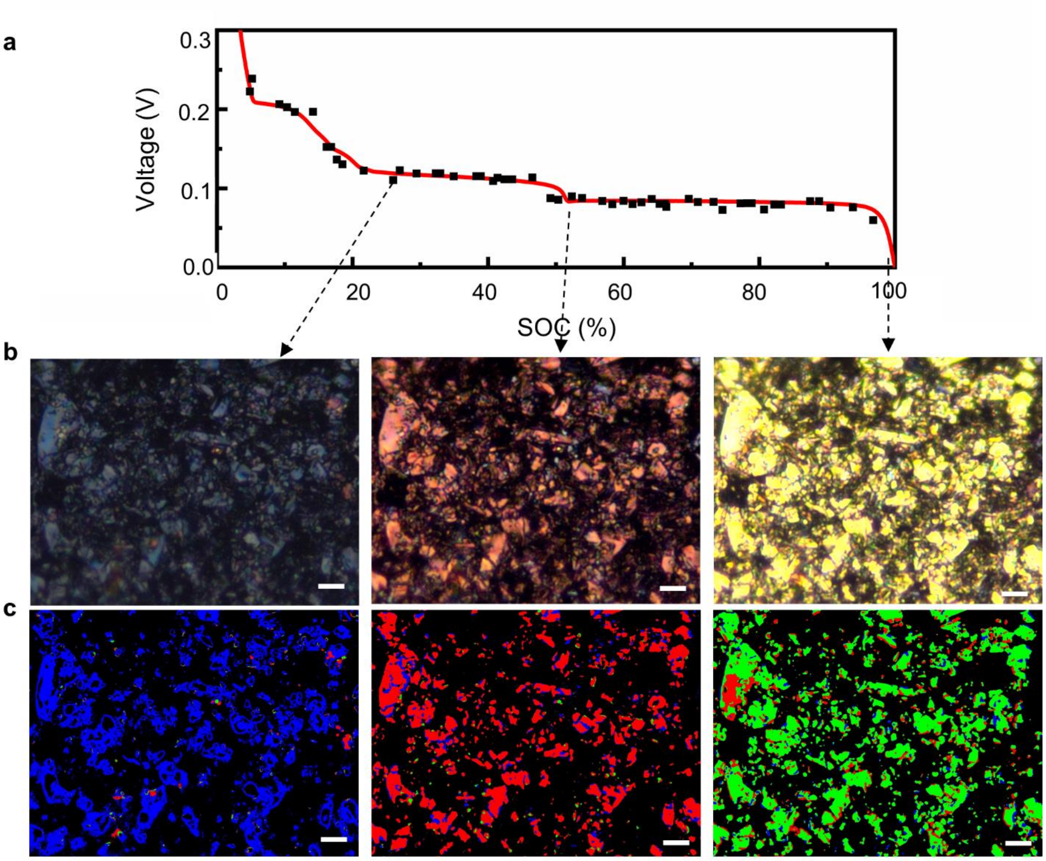

Figure A-8: Benchmark Images at characteristic SOCs of the three stable phases (the blue Stage 3, red Stage 2 and gold Stage 1), along with their transformed standard RGB images. (a) Comparison of OCV curve obtained from Ohzuku et al. (1993) and discharge profile of our lithiated graphite electrode at the current C/72[186]. (b) The digital photos of the graphite electrode at 23% SOC at 115 mV, 55% SOC at 84 mV, and 100% SOC at 0.5 mV, along with their (c) standard RGB transformed images. All the flakes were in Stage 3 (blue) at 23% SOC, Stage 2 (red) at 55% SOC, and Stage 1 (gold) at 100% SOC. The blue, red and gold colors were converted to standard blue, red and green colors respectively using ImageJ. *Scale bar: 10µm*

To avoid system errors that led to the fluctuation of OCV[186], we obtained a quasi-OCV by performing a constant current discharge at C/72. The smooth curve, while perfectly match the OCV by Ohzuku, ensures that no unphysical derivative ($dU/dc \geq 0$) will be introduced to undermine our analysis.

A.9 Calculation of length of Interfaces

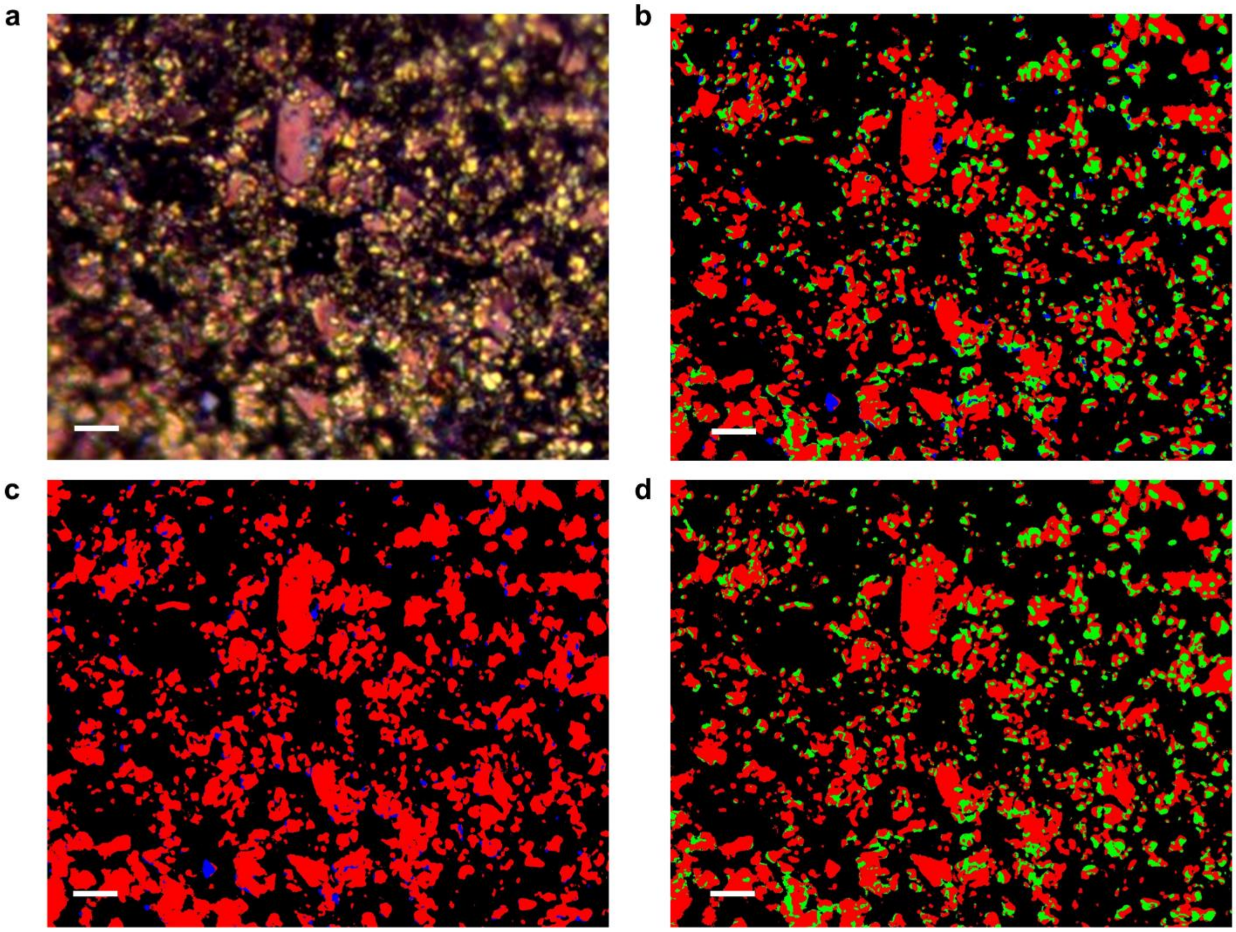

Figure A-9: Image processing to calculate the length of interfaces. (a) Snapshot of graphite electrode at an intermediate SOC. (b) Transformed RGB image of the snapshot in panel (a). (c) Green regions in panel (b) are changed to red to calculate the length of the Blue-Red interface using $\boldsymbol{L_{BR}} = \frac{l_{Blue}+l_{Red}-l_{particles}}{2}$. (d) Blue regions in panel b are changed to red to calculate the length of the Red-Gold interface using $\boldsymbol{L_{RG}} = \frac{l_{Red}+l_{Gold}-l_{particles}}{2}$. Here $\boldsymbol{l_{Blue}}$, $\boldsymbol{l_{Red}}$ and $\boldsymbol{l_{Gold}}$ are the perimeters of the regions covered with Blue, Red and Green regions respectively and $\boldsymbol{l_{particles}}$ is the outer perimeter of all the particles. *Scale bar: 10 µm*

A.10 Kolmogorov-Johnson-Mehl-Avrami (KJMA) theory

Figure 2.3(a) in the main text shows a typical growth of the subsequent stable phase over the earlier phase. If A is the normalized area of the new growth and Aext is the normalized extended area (in case of no impingement), then according to the KJMA theory $dA/dA_{ext} = 1 – A$. It can be solved further as shown below.

$$\frac{dA}{1-A} = A_{ext}$$

$$A = 1 - \exp(-A_{ext}) \qquad (S1)$$

The same relation can be continued to the surrounding length of the new phase l and that of the extended length l_{ext} as follows.

$$\frac{l}{l_{ext}} = 1 - A = \exp(-A_{ext})$$

$$l = l_{ext} \exp(-A_{ext}) \qquad (S2)$$

Assuming k (s^{-1}) is the normalized growth rate of the new phase, if the growth is

two-dimensional, $A_{ext} = \pi(kt)^2$ and $l_{ext} = 2\pi kt$

three-dimensional, $A_{ext} = (4/3)\pi(kt)^3$ and $l_{ext} = 4\pi(kt)^2$

n-dimensional, $A_{ext} = (Skt)^n$ and $l_{ext} = nS(kt)^{n-1} = (1/k)(dA_{ext}/dt)$

The above derivation returns the normalized growth velocity, but the theory needs to be formalized using the correct dimensions to obtain the actual growth velocity. If the growth is n-dimensional, the generalized equation can be written as follows

$$\frac{d\left[A/\left(A_{sys}\right)^{n/2}\right]}{d\left[A_{ext}/\left(A_{sys}\right)^{n/2}\right]}=1-\frac{A}{\left(A_{sys}\right)^{n/2}}$$

where A_{sys} is the total area of the basal plane calculated by extrapolation of the basal area in the viewing plane to the total electrode area. The above equation can be simplified into the following.

$$A=\left(A_{sys}\right)^{\frac{n}{2}}\left[1-\exp\left\{-\frac{S(kt)^n}{\left(A_{sys}\right)^{\frac{n}{2}}}\right\}\right] \qquad (S3)$$

Again, l and l_{ext} can be related in the same manner.

$$\frac{l}{l_{ext}}=1-\frac{A}{\left(A_{sys}\right)^{\frac{n}{2}}}=\exp\left[-\frac{(Skt)^n}{\left(A_{sys}\right)^{\frac{n}{2}}}\right]$$

$$l=nS(kt)^{n-1}\exp\left[-\frac{(Skt)^n}{\left(A_{sys}\right)^{\frac{n}{2}}}\right] \qquad (S4)$$

An important point to note here is that the shape factor S derived from Equation (S4) is a function of A_{sys}. Hence, the shape factor S and dimension of growth n are derived from Equation (S2) while the growth velocity of the interface is estimated from Equation (S4).

If n is fixed at 2, the shape factor S obtained from the KJMA fitting is close to the corresponding value of $\sqrt{\pi}$ as shown in **Table A-2**.

Table A-2: Parameters obtained from fittings the *operando* interface lengths with Equation (2) with n = 2 and the averaged growth velocity calculated from *operando* interfacial current densities

		10 mV	100mV	200 mV
Blue-Red	**n**	2	2	2
	S	1.44	1.34	1.48
	k_{fit} (nm.s^{-1})	13.4	11.6	15.8
	$k_{exp} = \overline{dx/dt}$ (nm.s^{-1})	8.02	14.20	12.10
Red-Gold	**n**	2	2	2
	S	1.50	1.58	1.42
	k_{KJMA} (nm.s^{-1})	0.5	1.5	2.2
	$k_{exp} = \overline{dx/dt}$ (nm.s^{-1})	0.3	1.6	1.2

A.11 Relation between growth velocity and interfacial current density

Figure 2.3(d) represents the process of growth of the interfaces between two stable phases. Mass conservation can be applied at any instant *t* to give the following equation.

$$V(t) = \frac{Q(t)}{F} V_m$$

where *V(t)* is the volume covered by a phase, *Q(t)* is the total charge accumulated in the same phase, V_m is the molar volume of that phase and *F* is the Faraday constant. The above equation can be used as follows.

$$\frac{dV(t)}{A(t)} = dx = \frac{dQ(t)}{A(t)} \frac{V_m}{F} = \frac{I(t)dt}{A(t)} \frac{V_m}{F}$$

Since *I(t)/A(t)* is the *operando* interfacial current density $j_{int}(t)$ and *dx/dt* is the growth velocity of the interface v_{int}, we can write

$$v_{int} = j_{int} \frac{V_m}{F} \qquad (S5)$$

The growth velocity of interface between Blue-Red and Red-Gold can be individually calculated from their respective *operando* interfacial current density obtained from direct image analysis using Equation (S5).

A.12 Modified PITT model

Adopting the method developed by Li et al.,[92] the analytical solution of Li^+ ion diffusion in graphite particles is

$$\frac{C(x,t) - C_0}{C_S - C_0} = 1 - 2B \sum_{n=1}^{\infty} \frac{\cos\left[\lambda_n \left(1 - \frac{x}{l}\right)\right]}{(\lambda_n^2 + B^2 + B)\cos\lambda_n} \exp\left(-\lambda_n^2 \frac{D_{Li^+} t}{l^2}\right) \qquad (S6)$$

where $B = -\frac{l(j_0|_S)(\partial U/\partial C|_S)}{DRT}$ is the dimensionless electrochemical Biot number, a ratio of the diffusion resistance and the resistance due to surface reaction. λ_1 is the 1st positive root of equation $\lambda_1 \tan \lambda_1 = B$. For our systems, the term $(C_S - C_0)$ can be replaced with the total charge transferred in the applied potential step using the Faraday's law as $Q_T = zFV_T(C_S - C_0)$, where V_T is the total particles volume (calculated using active material loading and density of material, 1.2 g.cm^{-3}). Neglecting higher order terms, the transient current can be written as Equation (S7a) for $t << l^2/D_{Li}$ and as Equation (S7b) for $t >> l^2/D_{Li}$

$$J(t) = \frac{I(t)}{S(t)} = \frac{D_{Li} Q}{l V_T} B \exp\left(B^2 \frac{D_{Li} t}{l^2}\right) erfc\left(B \sqrt{\frac{D_{Li} t}{l^2}}\right) \qquad (S7a)$$

$$\ln[J(t)] = -\lambda_1^2 \left(\frac{D_{Li} t}{l^2}\right) + \ln\left[\frac{2Q D_{Li}}{l V_T} \frac{B^2}{(\lambda_1^2 + B^2 + B)}\right] \qquad (S7b)$$

Both B and D_{Li^+} were estimated by fitting the experimental *operando* interfacial current density with the above analytical expressions by minimizing least squares using MATLAB.

As explained in the main text, the mPITT model was applied to the solid-solution regime during the phase transformation (Segment (I)) to extract the D_{Li^+} and B. **Figure A-10** shows a good agreement between *operando* current densities at the significant voltage steps at 10 mV, 100 and 200 mV PITT experiments during solid-solution regimes.

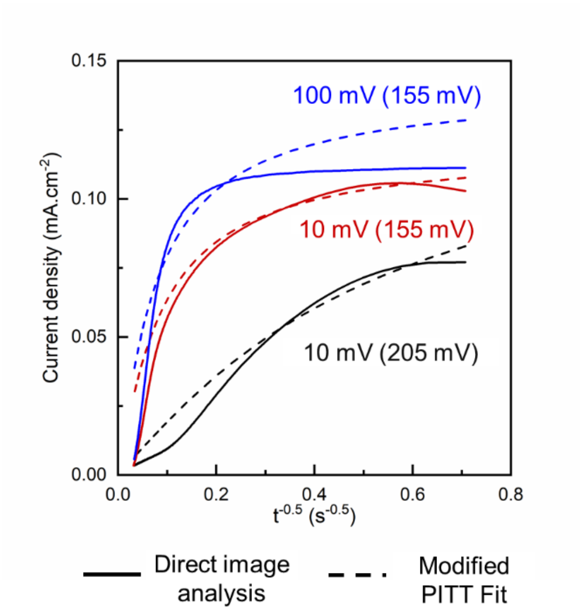

Figure A-10: Fitting of operando interfacial current densities on J vs 1/√t plot obtained from solid-solution intercalation with the mPITT model. The voltage in brackets indicate the voltage step during the corresponding PITT experiments.

A.13 Electrochemical Impedance Spectroscopy (EIS) parameters

The EIS data from 10% - 100% SOCs were fitted with the equivalent circuit model suggested in Figure 2.5(e) in the main text, as shown in Figure A-11. A porous bounded Warburg impedance with admittance W and parameter b has been used for the diffusive component. The parameters obtained from the fitting are shown in **Table A-3**.

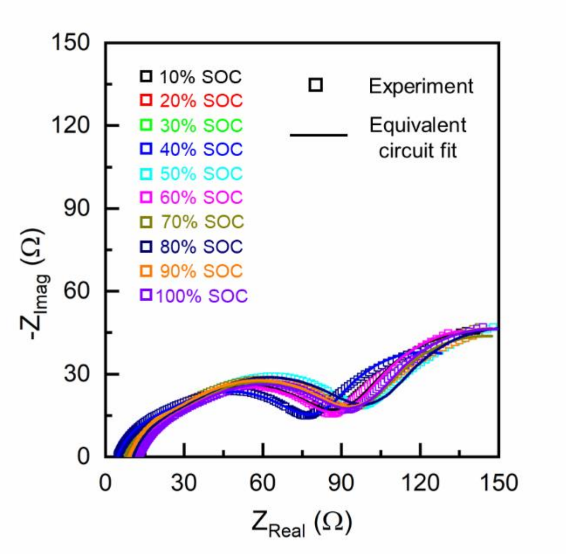

Figure A-11: Nyquist plots from 10% - 100% SOCs during Li$^+$ ion intercalation in graphite. The Nyquist plots are fitted with the equivalent circuit model shown in Figure 2.5(e) in the main text.

Table A-3: Fitting parameters of the equivalent circuit model

SOC	10%	20%	30%	40%	50%	60%	70%	80%	90%	100%
R_{bulk} (Ω)	8.69	12.76	8.748	10.49	10.34	10.37	8.712	4.542	8.701	12.7
R_{CT}^{SEI} (Ω)	38.44	38.30	39.68	40.61	38.91	35.79	39.45	37.18	39.12	38.21
Y_o^{SEI} (F)	1.86E-05	1.84E-05	1.83E-05	1.83E-05	1.83E-05	1.85E-05	1.43E-05	2.00E-05	1.78E-05	1.90E-05
a^{SEI}	0.800	0.800	0.800	0.800	0.800	0.800	0.800	0.796	0.800	0.800
R_{CT}^{SEI} (Ω)	31.97	33.45	36.45	38.48	36.45	33.30	37.45	28.90	32.07	32.40
Y_o^{SEI} (F)	3.59E-05	3.61E-05	3.61E-05	3.68E-05	3.86E-05	3.41E-05	3.91E-05	4.12E-05	3.61E-05	3.69E-05
a^{SEI}	0.882	0.877	0.875	0.874	0.867	0.879	0.905	0.877	0.879	0.821
W ($S.s^{0.5}$)	5.87E-03	5.73E-03	5.86E-03	5.81E-03	6.04E-03	6.32E-03	5.63E-03	6.59E-03	5.81E-03	5.77E-03

b	0.623	0.628	0.646	0.639	0.624	0.692	0.645	0.590	0.621	0.621

The frequency of the peaks of the individual components is found out from the respective semicircles, similar to Figure 2.5(e), to calculate the respective capacitance using $\omega_P = 1/(R_{CT}C)$. They are, then used to estimate the dielectric constant of each layer (assuming thicknesses of SEI as 10 nm and double layer as 1 nm) from $C = \varepsilon\varepsilon_r A_{edge}/d$ as shown in **Table A-4**.

Table A-4: Calculation of dielectric constant from frequency of the peaks

SOC	10%	20%	30%	40%	50%	60%	70%	80%	90%	100%
ω_P^{SEI} (Hz)	1266	1266	1266	1172	1266	1359	1172	1266	1359	1266
ω_P^{dl} (Hz)	146.5	158.4	146.5	135.2	146.5	158.4	135.2	158.4	146.5	135.2
C^{SEI} (F)	2.05E-05	2.06E-05	1.99E-05	2.10E-05	2.03E-05	2.06E-05	2.15E-05	2.12E-05	1.91E-05	2.06E-05
C^{dl} (F)	2.14E-04	1.89E-04	1.87E-04	1.92E-04	1.87E-04	1.90E-04	2.03E-04	2.18E-04	2.14E-04	2.21E-04
ε^{SEI}	161.24	161.83	156.20	164.87	159.29	161.33	168.73	166.71	150.21	161.83
ε^{dl}	167.54	148.09	146.95	150.83	146.95	148.76	159.23	171.41	167.54	173.51

The Li^+ ion diffusion coefficient into graphite particles (D) at different SOCs can be estimated from the admittance of Warburg impedance using the following relation.

$$\frac{1}{\sqrt{2}W} = \frac{RT}{n^2F^2A_i\sqrt{2D}C_{Li}}$$

where A_i is the operando interface area obtained from direct image analysis, C_{Li} is the concentration of Li+ ions within graphite at the respective SOC, R is the gas constant and T is the absolute temperature (298 K). The obtained values of the diffusion coefficient are shown in **Table A-5**.

Table A-5: Estimated diffusion coefficient from Warburg impedance

SOC	W ($S.s^{0.5}$)	A_i (cm^2)	D ($cm^2.s^{-1}$)
10%	5.87E-03	1.459	1.15E-13
20%	5.73E-03	1.459	2.73E-14
30%	5.86E-03	0.085	1.12E-12

40%	5.81E-03	0.134	4.37E-13
50%	6.04E-03	0.189	2.38E-13
60%	6.32E-03	0.161	1.09E-13
70%	5.63E-03	0.266	3.16E-14
80%	6.59E-03	0.294	3.56E-14
90%	5.81E-03	0.289	2.86E-14
100%	5.77E-03	0.309	2.46E-14

A.14 Performance of thin graphite electrode

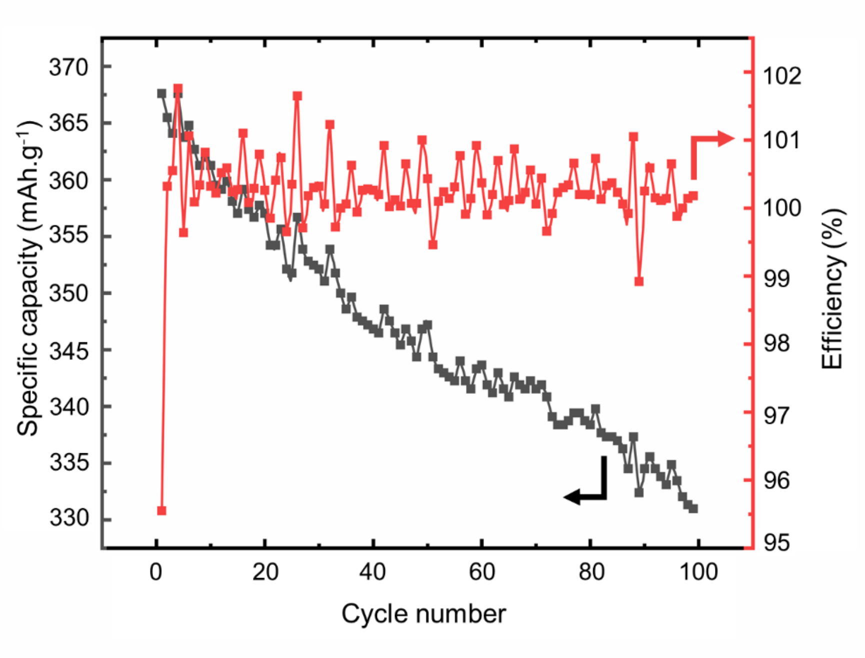

Figure A-12: Performance of the thin graphite electrode. After 100 cycles, the capacity retention is >92% with coulombic efficiency >99%.

A.15 Sensitivity analysis of the phase area fractions

Since the choices of color thresholds are prone to human error, a sensitivity analysis has been performed by varying the color thresholds by ±10%. Figure A-13 shows that such a variation causes only up to ±0% – 5% change in the area fractions of the respective colors.

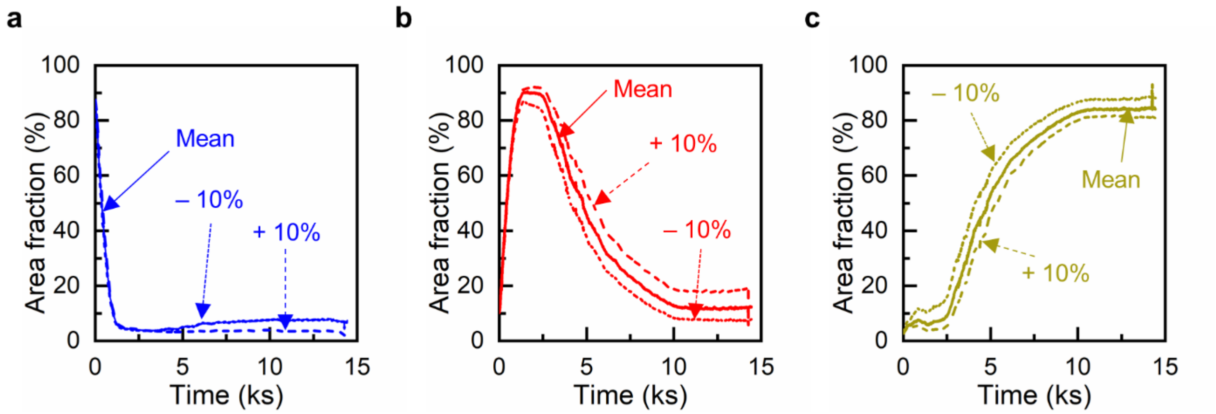

Figure A-13: Sensitivity analysis of the area fractions. A ±10% change in the color thresholds of the (a) blue, (b) red, and (c) gold color results in a small variation in the area fraction of the respective phases.

Appendix B. Supporting Materials for Chapter 3

B.1 Electrochemical performance under constant-current

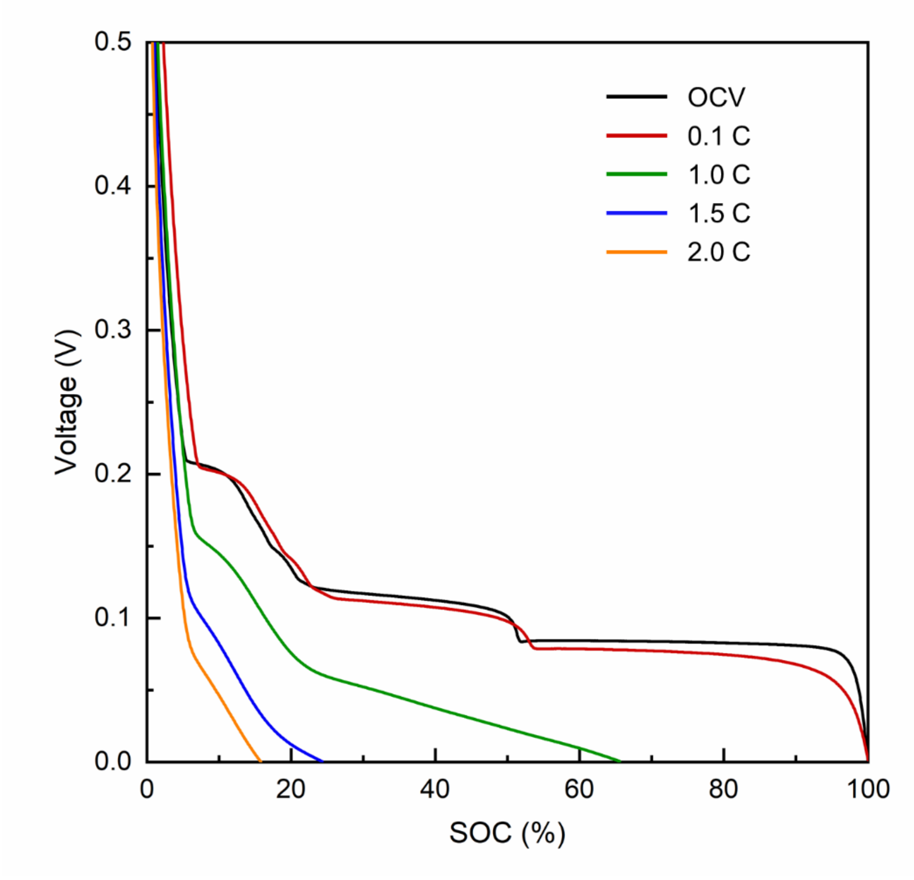

Figure B-1: Voltage profiles during lithiation in graphite under galvanostatic conditions. Discharge voltage profile at 0.1 C, 1 C, 1.5 C, and 2 C currents. The graphite electrode can reach nearly 100% of its theoretical capacity (365 mAh.g^{-1}) at 0.1 C current while can only 65%, 24% and 15% of the theoretical capacity at 1 C, 1.5 C and 2 C currents, respectively. The OCV profile is obtained at very low current (C/72), to maintain near-equilibrium conditions.

B.2 (De)lithiation within Graphite Anodes

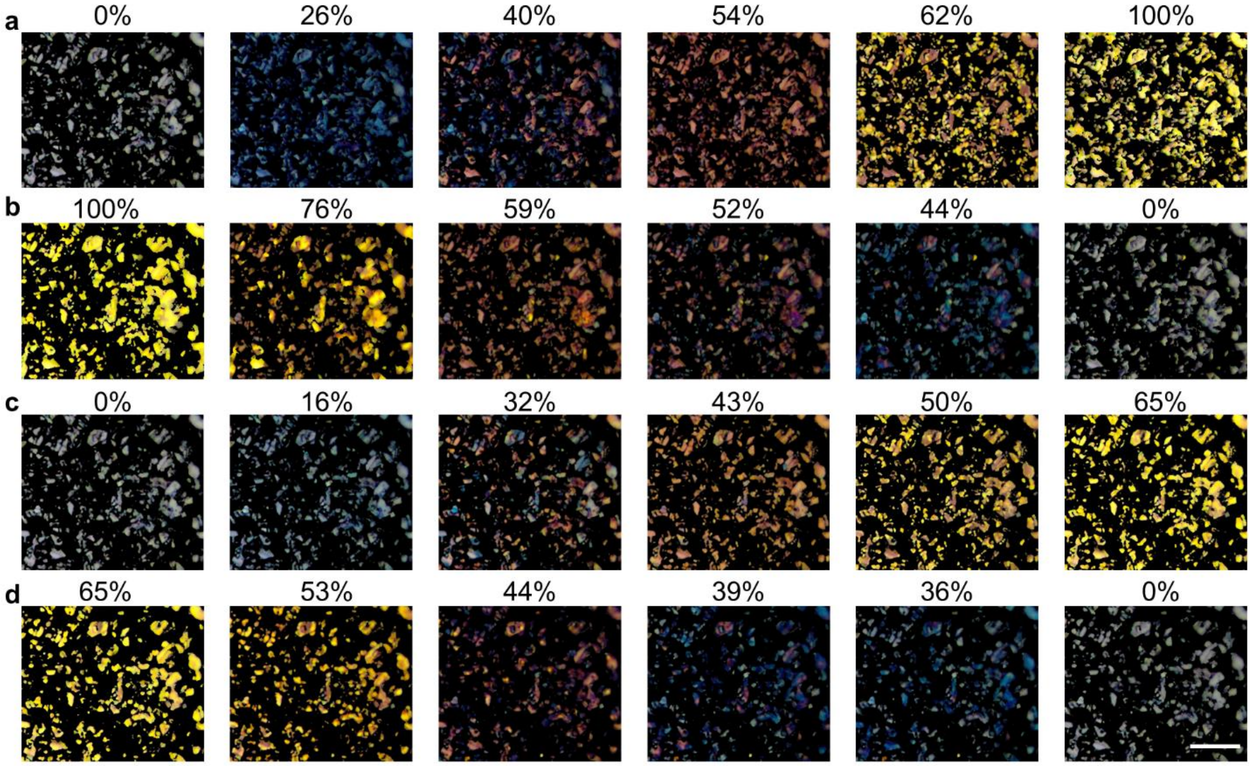

Figure B-2: Snapshots of Li^+ ion (de)intercalation into thin graphite anode under slow and fast galvanostatic conditions. (a) Lithiation at 0.1 C current, (b) Delithiation at 0.1 C current, (c) Lithiation at 1 C current, and (d) Delithiation at 1 C current.

B.3 Phase evolution under galvanostatic conditions

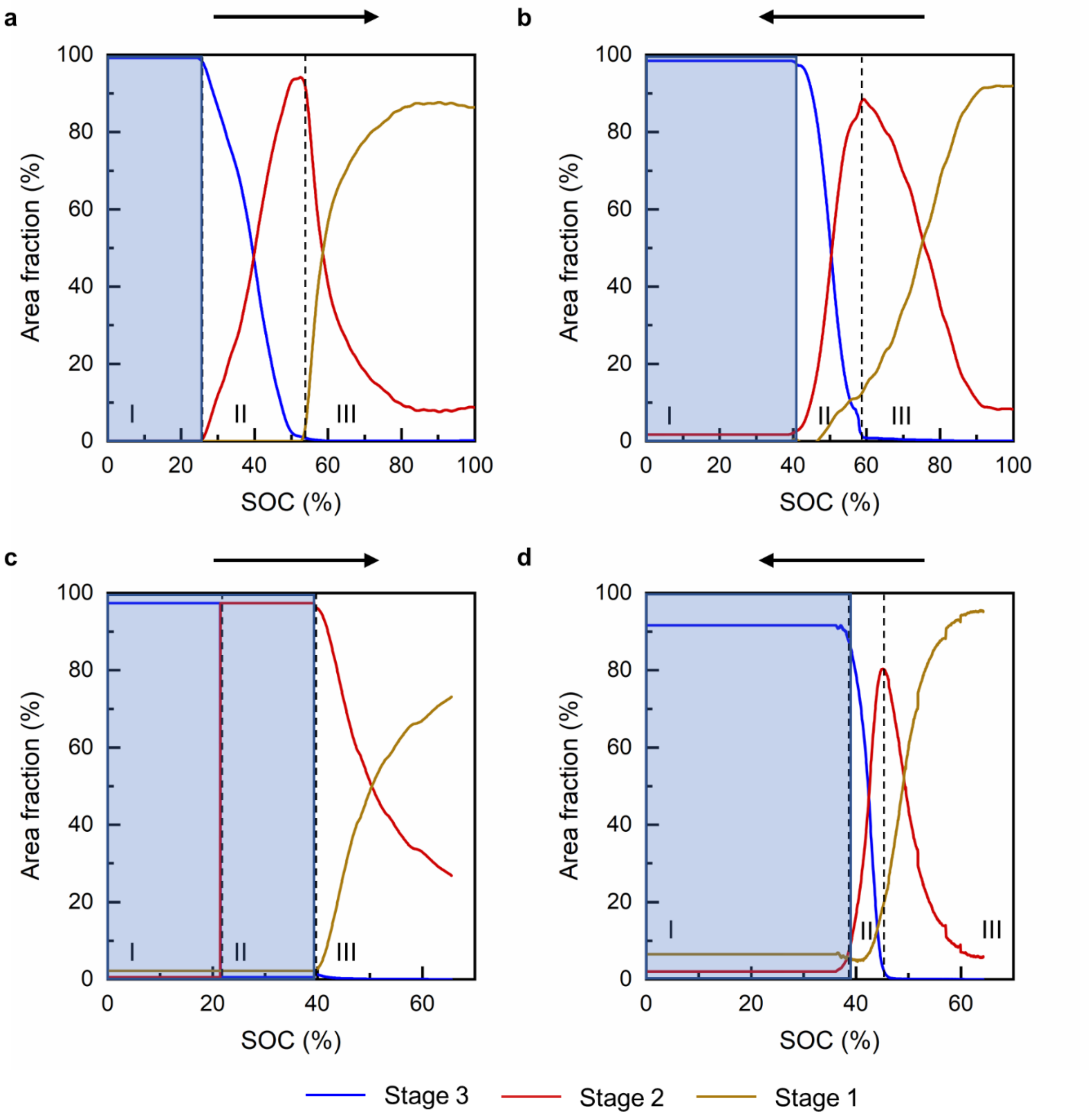

Figure B-3: Evolution of stable phases (stage 3, 2 and 1) during slow and fast galvanostatic conditions. Area fraction during (a) lithiation at 0.1 C current, (b) delithiation at 0.1 C current, (c) lithiation at 1 C current, and (d) delithiation at 1 C current. The entire process is divided into three segments I, II and III corresponding to the phase transformations from empty state to stage 3, stage 3 to stage 2, and stage 2 to stage 1. The blue shaded region represents the solid-solution phase transformation. The direction of the arrow represents the direction of charge transfer in each panel.

B.4 Charge conservation

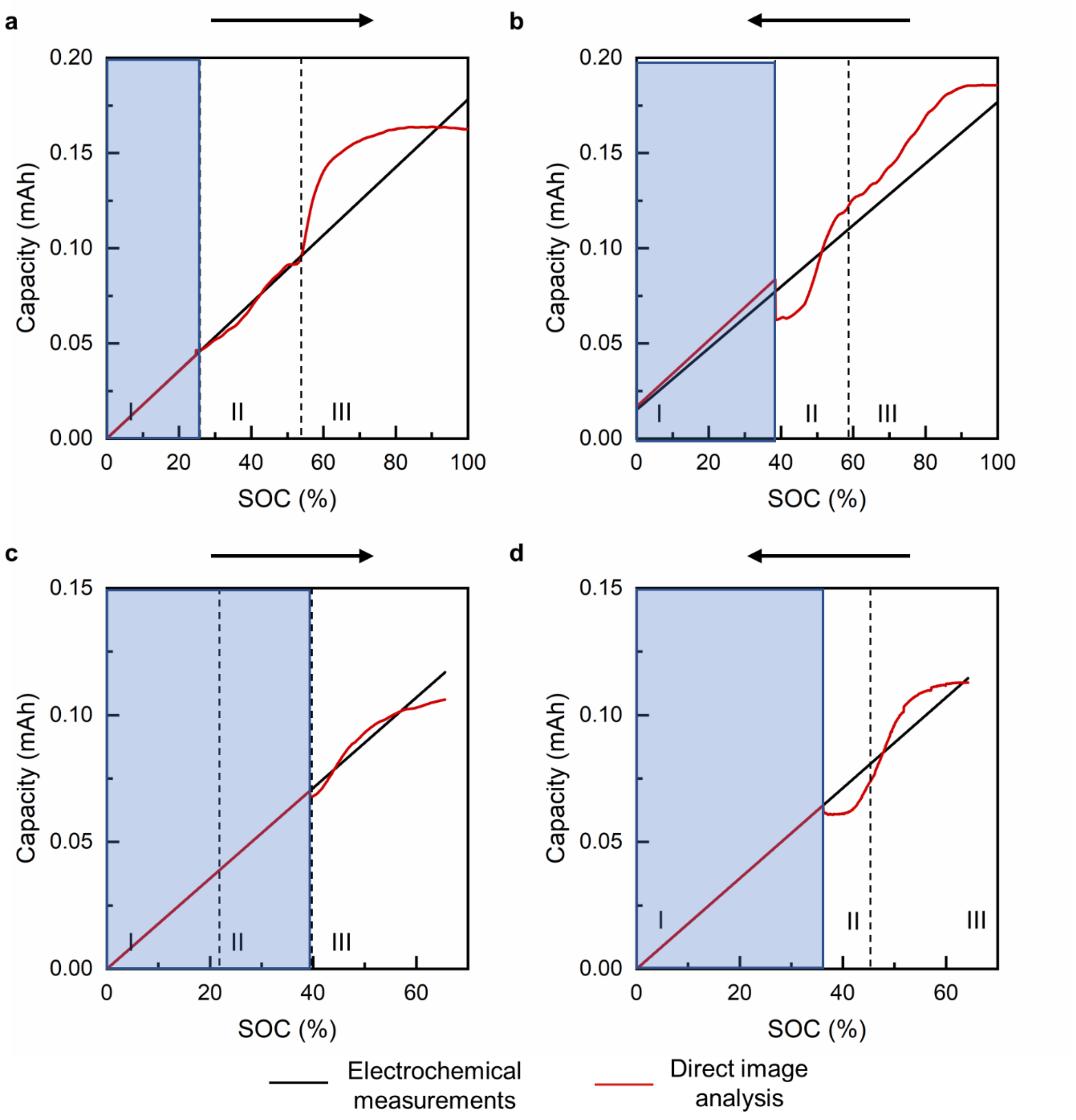

Figure B-4: Comparison of total capacity between experiments and image analysis during slow and fast galvanostatic conditions. Total capacity comparison between experiments and image analysis during (a) lithiation at 0.1 C current, (b) delithiation at 0.1 C current, (c) lithiation at 1 C current, and (d) delithiation at 1 C current. The entire process is divided into three segments I, II and III corresponding to the phase transformations from empty state to stage 3, stage 3 to stage 2, and stage 2 to stage 1. The blue shaded region represents the solid-solution phase transformation. The direction of the arrow represents the direction of charge transfer in each panel.

B.5 Capacity and current evolution within single particle

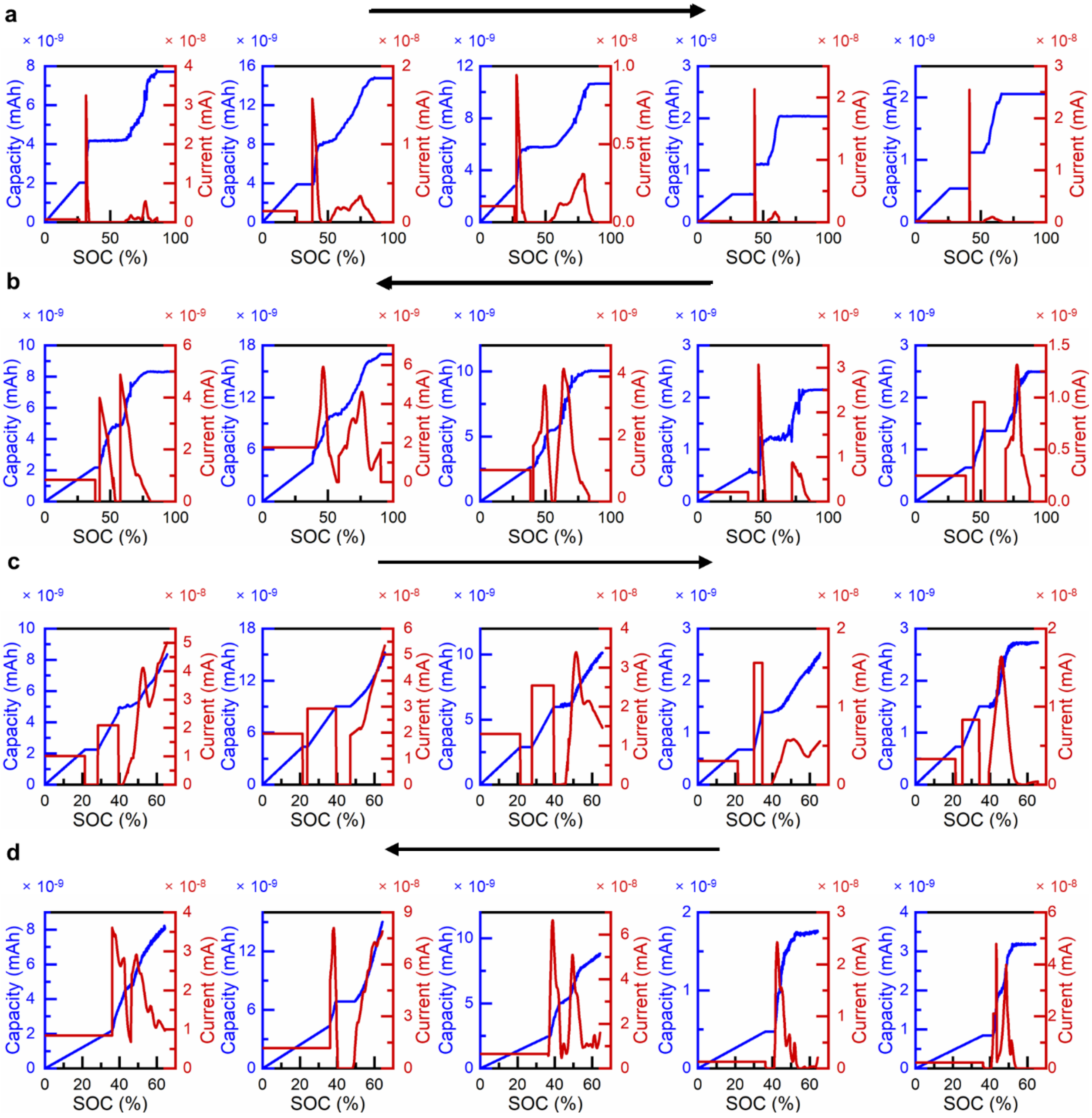

Figure B-5: Single-particle capacity and current evolution. The capacity and current vs global SOC in particles P1 – P5 (left to right) during (a) lithiation at 0.1 C current, (b) delithiation at 0.1 C current, (c) lithiation at 1 C current, and (d) delithiation at 1 C current. The capacity grows linearly while the current remains constant in the solid-solution regimes. The capacity remains constant when the particle is idle which means there is no inherent current. An increase in capacity during phase separation regions results in sharp increase in current which decays as the capacity grows gradually.

B.6 Interface length

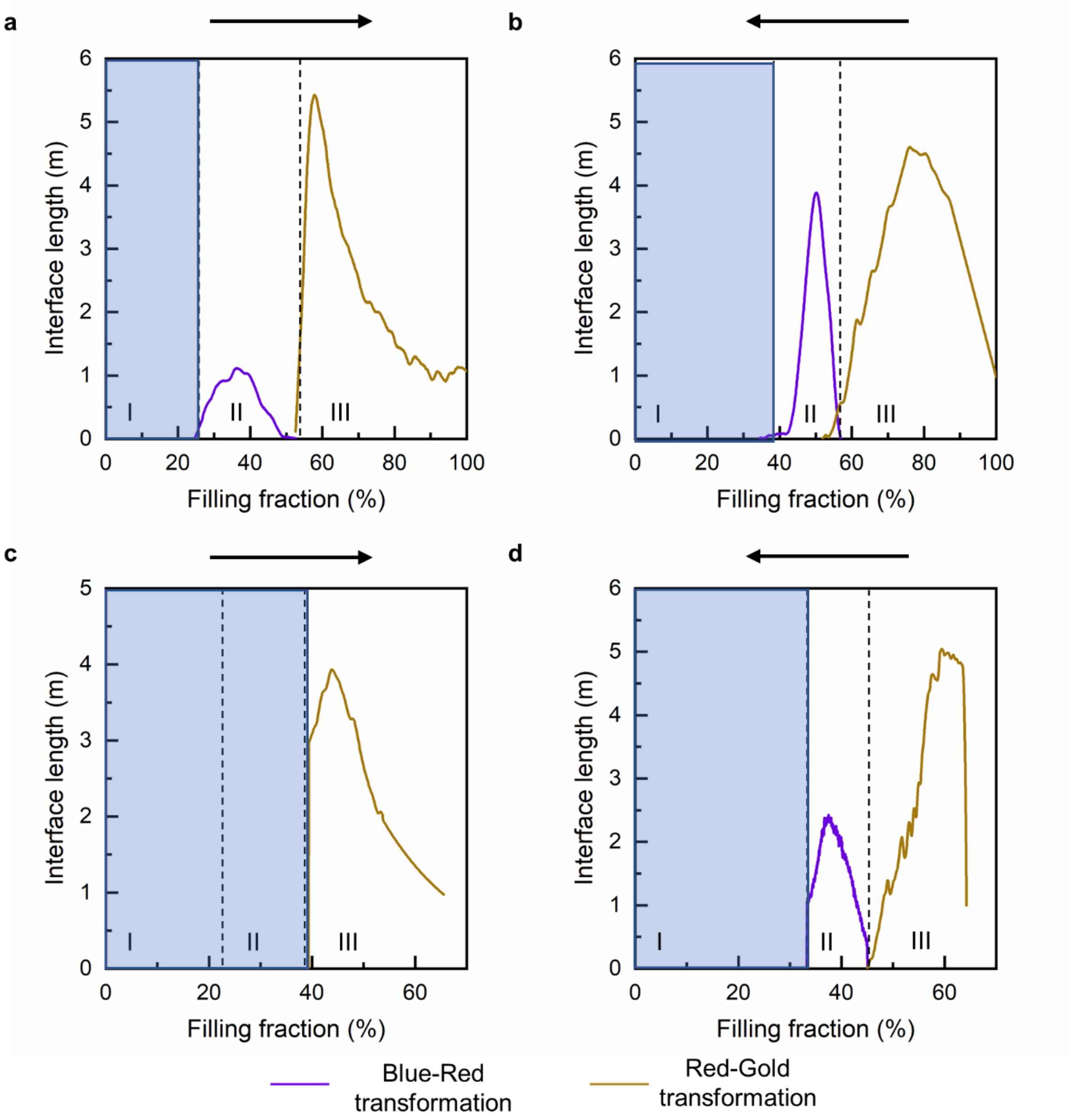

Figure B-6: Total interface length of phase boundaries obtained from image analysis during slow and fast galvanostatic conditions. The total length of phase boundaries during blue-red and red-gold phase transformations obtained from direct image analysis during (a) lithiation at 0.1 C current, (b) delithiation at 0.1 C current, (c) lithiation at 1 C current, and (d) delithiation at 1 C current. The entire process is divided into three segments I, II and III corresponding to the phase transformations from empty state to stage 3, stage 3 to stage 2, and stage 2 to stage 1. The blue shaded region represents the solid-solution phase transformation. The direction of the arrow represents the direction of charge transfer in each panel.

B.7 Linear Stability Analysis

Following the work of Ferguson and Bazant, the Gibbs free energy obtained from the two-layer regular solution for graphite can be written as $g(c_1,c_2) = g(c_1) + g(c_2) + g_{int}(c_1,c_2)$. Here c_1 and c_2 are the Li$^+$ ion filling fractions of adjacent graphite layers, g(ci) is the homogeneous Gibbs free energy of the i^{th} layer, given by $g(c_i) = k_BT[c_i ln(c_i) + (1-c_i)ln(1-c_i)] + \Omega_a c_i(1-c_i)$, and $g_{int}(c_1,c_2) = \Omega_b c_1 c_2 + \Omega_c c_1(1-c_1)c_2(1-c_2)$ is the repulsive interaction Gibbs free energy between the adjacent layers. In the above formulation, $\Omega_a = 3.4k_BT$ is the regular solution parameters for the particles-vacancies interaction within a layer, and $\Omega_c = 20k_BT$ is that for the particles-vacancies cross-plane interactions, $\Omega_b = 1.4k_BT$ is the repulsive interaction between cross-plane, k_B is the Boltzmann constant and T is the room temperature set as 298 K. The average filling fraction is equal to $(c_1 + c_2)/2$. The schematic of the above description is shown in Fig S7 below.

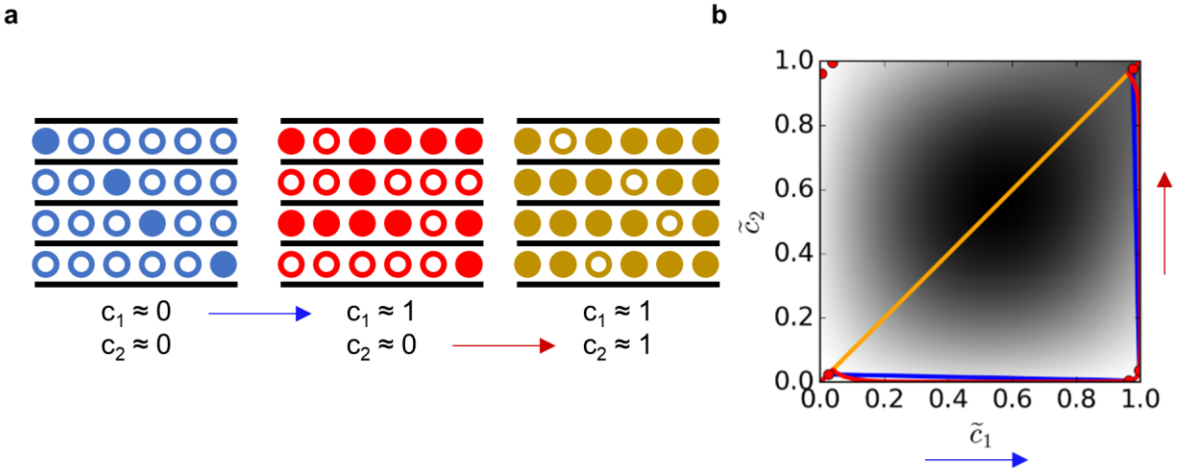

Figure B-7: Schematic of bilayer intercalation and intercalation pathway of Li$^+$ ion into graphite required for simplified two-layer regular solution model. Panel (b) is directly adopted from Smith and Bazant, 2017[114] and shows the free energy density surface map during intercalation pathway into graphite.

It is clear from Fig S7 that the entire phase transformation in graphite can be separated into two sections where only c_1 varies from 0 to 1 during blue-red transformation, with $c_2 = 0$ and only c_2

varies from 0 to 1 during red-gold transformation, with $c_1 = 1$. This assumption leads to an easier representation of the homogeneous chemical potential for each phase transformation[114,133] as

$$\mu_i^h = \frac{\partial g}{\partial c_i} = k_B T \ln\left(\frac{c_i}{1 - c_i}\right) + \Omega_a(1 - 2c_i) + \Omega_b c_j + \Omega_c(1 - 2c_i)c_j(1 - c_j)$$

$$\bar{\mu}_\iota = \frac{\mu_i^h}{k_B T} - \widetilde{\mathrm{K}}\nabla^2 c_i \qquad (S1)$$

where $\widetilde{K} = V_S K / k_B T L^2$, with V_S as volume per intercalation site (can be calculated from the molar volume of graphite), K as the Cahn-Hilliard penalty gradient coefficient, and L as the facet width.

In equation (S1), the subscript $i = 1$ and $j = 2$ during blue-red phase transformation and $i = 2$ and $j = 1$ during red-gold phase transformation.

Hereon, all the variables in the analysis are dimensionless with tilde removed and the bar on the variables represent their homogeneous state.

Assuming $\alpha = 0.5$, the governing equations become

$$\frac{\partial c}{\partial t} = -2F(c)\sinh\left[\frac{\eta(c, \nabla^2 c)}{2}\right] \qquad (S2)$$

$$J_0(c) = k_0 F(c) \qquad (S3)$$

where

$$k_0 = \begin{cases} 8.30\ \mathrm{mA.cm^{-2}} & \text{blue} - \text{red phase transformation} \\ 3\ \mathrm{mA.cm^{-2}} & \text{red} - \text{gold phase transformation} \end{cases}$$

$$F(c) = \begin{cases} 1.73(1 - \mathrm{c})\exp(0.46\mu) & \text{blue} - \text{red phase transformation} \\ 1 & \text{red} - \text{gold phase transformation} \end{cases}$$

$$\eta(c,\nabla^2 c) = \Delta\phi + \mu(c,\nabla^2 c) \qquad (S4)$$

$$J = \int_0^1 \frac{\partial c}{\partial t}\,dx \qquad (S5)$$

Equation S1 is a result of Butler-Volmer equation.

Following the work of Bai, Cogswell and Bazant, Nano Letters (2011),[118] if we allow small perturbations in filling fraction about a homogeneous, constant current density base state,

$$c = c_0 + Jt + \nu \qquad (S6)$$

where c_0 is a constant composition, J is a constant current density, $c_h = c_0 + Jt$ is the homogeneous base state and $v = exp(ikx).exp(st)$ is a small perturbation. The growth factor s of a perturbation wave with wave number k can be determined as the following equation.

$$s(k,c,J) = -[\overline{\mu_h}' + \mathrm{K}k^2]\sqrt{F(c)^2 + \frac{J^2}{4}} + \left[\frac{F'(c)}{F(c)} + \frac{1}{2}\mathrm{K}k^2\right]J \qquad (S7)$$

On calculating the expressions of $\overline{\mu_h}'$, $\overline{J_0}$, and $\overline{J_0}'/\overline{J_0}$ from equations S1 and S3, replacing $\delta = 1 - 2c$ and substituting in equation S7, we get a simplified expression.

$$s_i = \left(2\Omega_a + 2\Omega_c c_j(1-c_j) - \frac{1}{c_i(1-c_i)} - \mathrm{K}k^2\right)\sqrt{\frac{J^2}{4} + F(c_i)^2} + \left(\frac{F'(c_i)}{F(c_i)} + \frac{1}{2}\mathrm{K}k^2\right)J \qquad (S8)$$

For the most unstable mode k = 2π,

$$\bar{s}_i^{max}(c,\bar{J}) = \left(2\Omega_a + 2\Omega_c c_j(1-c_j) - \frac{1}{c_i(1-c_i)} - 4\mathrm{K}\pi^2\right)\sqrt{\frac{J^2}{4} + F(c_i)^2} + \left(\frac{F'(c_i)}{F(c_i)} + 2\mathrm{K}\pi^2\right)\bar{J} \qquad (S9)$$

The constants in the normalized exchange current density function *F(c)* are selected based on available literature[118,123,125] and fitted on the experimental data provided in Agrawal & Bai (2021).[109]

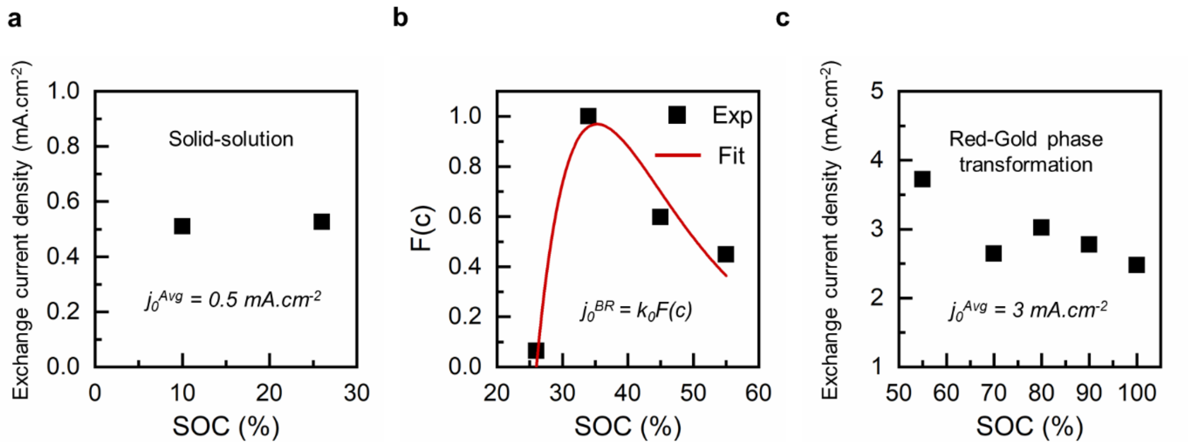

Figure B-8: Concentration-dependent exchange current density. The experimental data of exchange current densities is obtained via an *operando* EIS published in Agrawal & Bai (2021). The exchange current densities are separated based on the (a) Empty to Stage 3, (b) Stage 3 to Stage 2, and (c) Stage 2 to Stage 1 phase transformations. The Empty to Stage 3 and Stage 2 to Stage 2 to Stage 1 phase transformations have almost constant exchange current densities and are thus averaged for calculations. The exchange current density of Stage 3 to Stage 2 phase transformation is dependent on the filling fraction and is fitted with the *F(c)* function for the blue-red phase transformation.

B.8 Electrochemical phase diagram for each particle

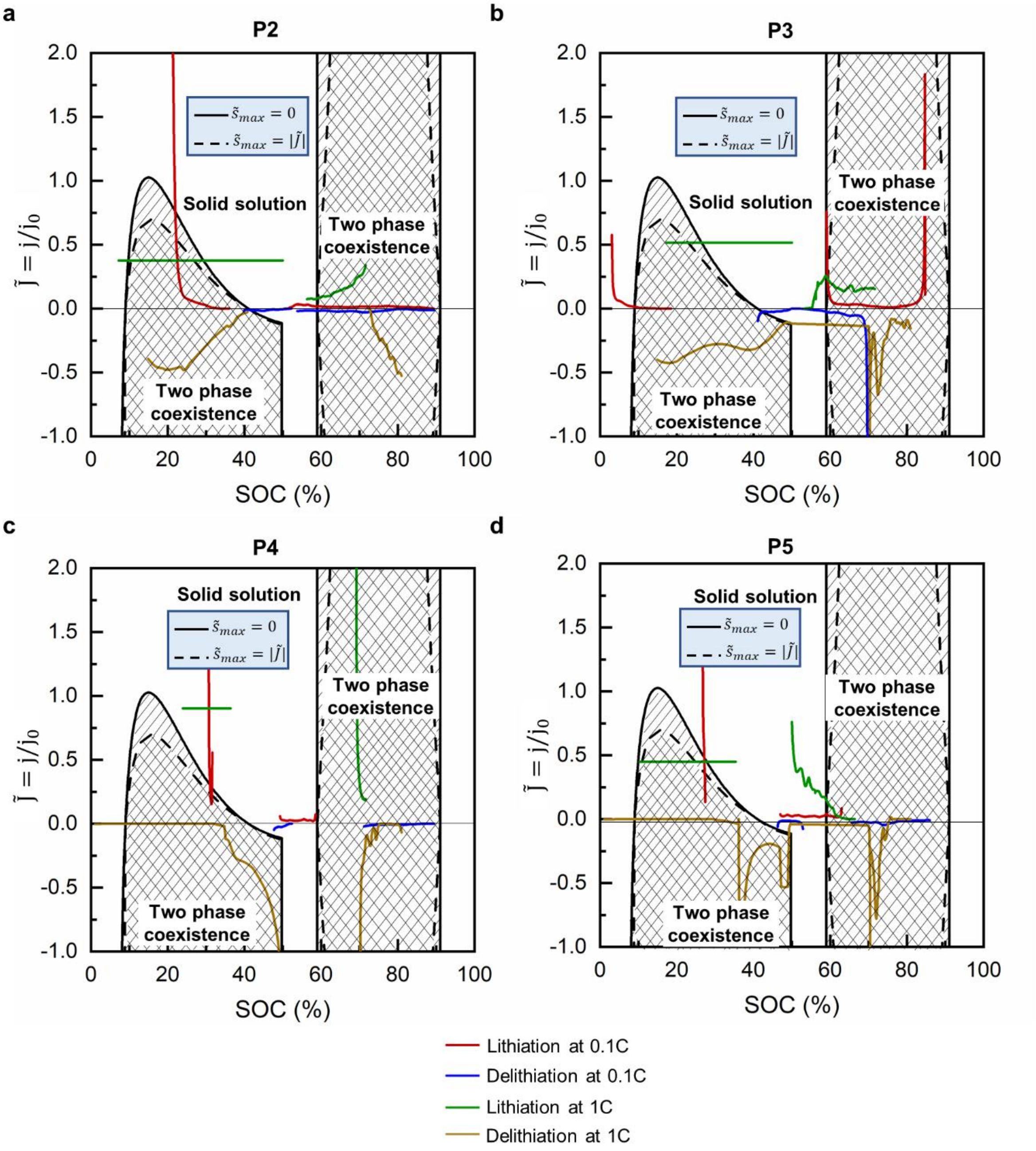

Figure B-9: Linear stability diagram for (de)lithiation in graphite particles in particles (a) P2, (b) P3, (c) P4, and (d) P5. The phase transformation regions in these particles (segments II and III) lie within the domains of two-phase coexistence in all the cases except the blue-red lithiation process at 1 C current. This observation is consistent with the visual examination of the (de)lithiation process.

Table B-1: The SOC ranges of phase transformation under slow and fast galvanostatic conditions obtained from electrochemical observations

Galvanostatic condition	Global SOC (%) at				
	Stage 3		Stage 2		Stage 1
0.1 C Lithiation	26.23	⟶	54.28	⟶	100
0.1 C Delithiation	39.5	⟵	55	⟵	100
1 C Lithiation	21.89	⟶	39.38	⟶	65.57
1 C Delithiation	36.16	⟵	45.18	⟵	65.57

B.9 Multiphase Porous Electrode theory

The MPET developed by Bazant and coworkers,[130] uses the free energy density function as the bilayer regular solution model as explained in the Section 6, Linear Stability Analysis.

The reaction boundary condition based on the intrinsic reaction rate obtained from our operando experiments[109] is applied on both the opposite and active edges (length) of all the rectangular-shaped particles, as formulated below.

$$J = J_0\left(e^{-\frac{\alpha n e \eta}{k_B T}} - e^{-\frac{(1-\alpha) n e \eta}{k_B T}}\right) \qquad (S10)$$

where exchange current density same as Equation (S3).

The simulations are carried out at 0.1 C and 1 C current for both charge and discharge, until the voltage reaches the cut-off values, using the parameters in the Table S2.

Table B-2: Parameters used in the MPET simulations

Parameter	Value	Note
Diffusion coefficient, D_0	9×10^{-8} $cm^2.s^{-1}$	Obtained from Agrawal & Bai, 2021[109]
k_0	8.3 $mA.cm^{-2}$	Obtained from Agrawal & Bai, 2021[109]

I	0.1 C and 1 C	Consistent with experiments
Ω_a	3.4 k_BT	From Smith and Bazant, 2017[114]
Ω_b	1.4 k_BT	
Ω_c	10 k_BT	
K	5×10^{-7}	Gradient penalty parameter
λ	6.26×10^{-20} eV	Reorganization energy
T	298 K	Room temperature

B.10 Phase transformation using MPET

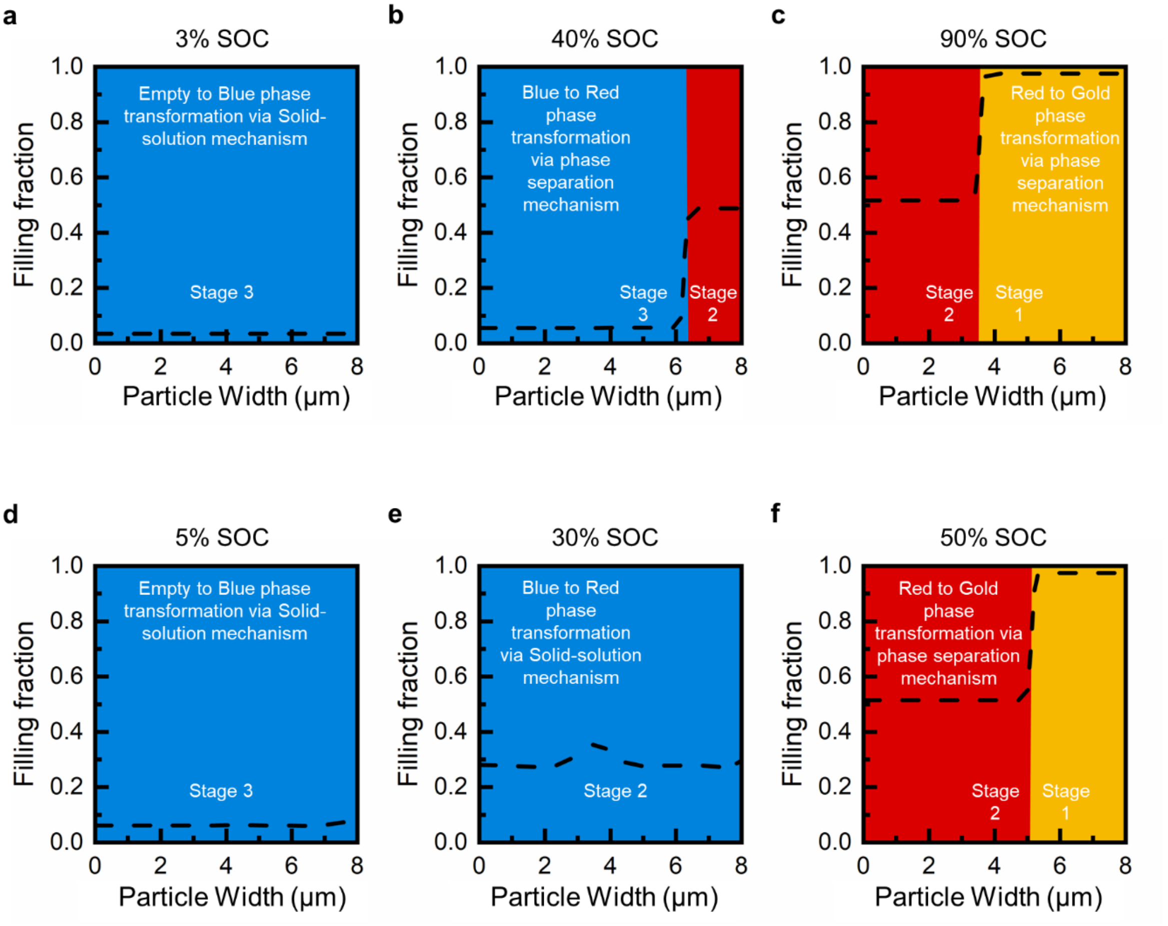

Figure B-10: Calibration of colors in the MPET simulation. Phase transformation during lithiation at (a)-(c) 0.1 C current and (d)-(f) 1 C current. The blue, red and gold colors represent the Stages or the mechanism of phase transformation. The dashed line represents the average filling fraction at each location within a single particle. Here particle with length 7.65 μm (Particle ID #100) is chosen for representation. At 0.1 C, the empty to Stage 3 transformation, panel (a) occurs via solid-solution pathway, so the entire particle appears blue. The Stage 3 to Stage 2 (panel (b)) and Stage 2 to Stage 1 (panel (c)) phase transformations occur via phase-separation. Thus, we can see the respective phase boundaries at the concentration jumps. At 1 C current, both the Empty to Stage 3 and Stage 3 to Stage 2 phase transformations occur via solid-solution mechanism and hence, the entire particle appears blue in panels (d) and (e). The Stage 2 to Stage 1 transformation is similar to that at 0.1 C current.

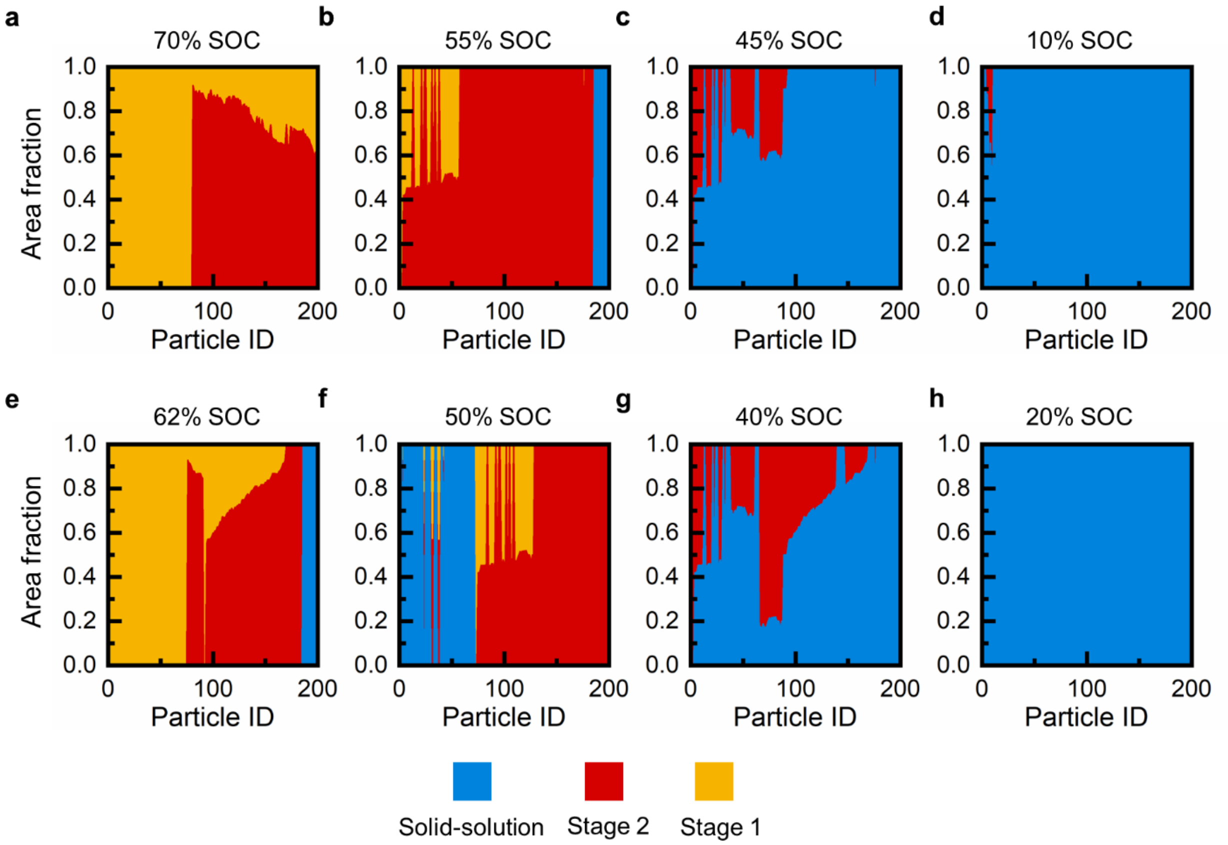

Figure B-11: Theoretical predictions of area fraction of the stable phases using MPET within 200 lognormally distributed particles. Area fraction of stages 3, 2 and 1 at four global SOCs during delithiation process at (a-d) 0.1 C current, and (e-h) 1C current. The increasing particle numbers signifies increasing particle lengths. The red-gold phase boundaries appear initially in smaller particles, and then continue to the larger particles. Once almost all the particles are in stage 2, the blue-red transformation occurs along the phase boundaries at both the currents.

B.11 Interface length using MPET

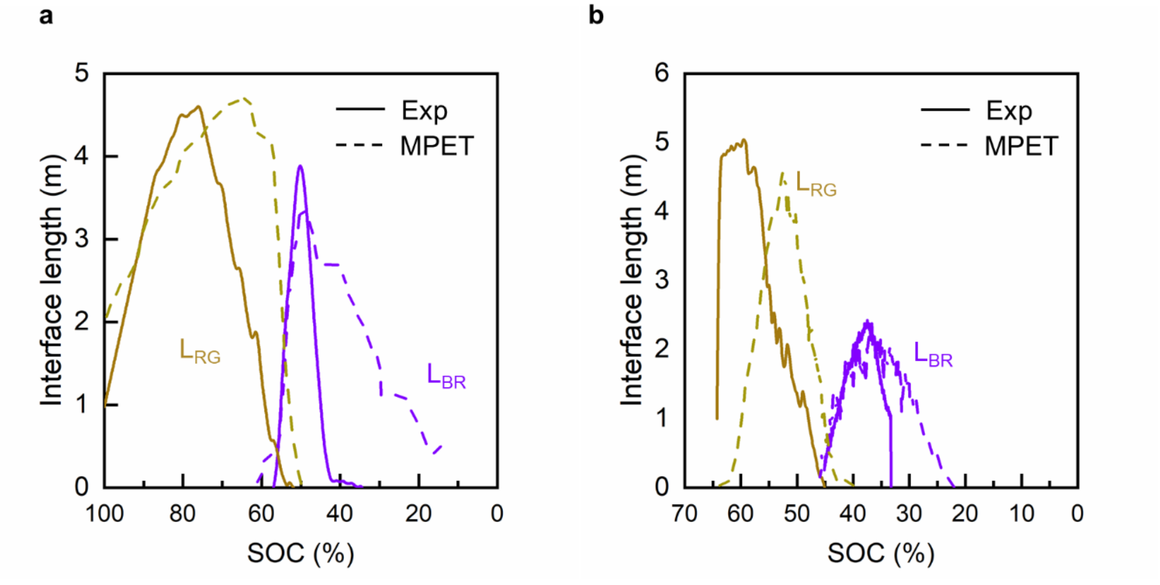

Figure B-12: Length of phase boundaries obtained from operando experiments vs MPET. Comparison between length of phase boundaries during delithiation extracted from direct image analysis (solid lines) and that simulated from MPET (dashed lines) at (a) 0.1 C current, and (b) 1 C current. The delithiation process occurs via phase boundaries for both the phase transformations (blue-red and red-gold) unlike lithiation process. Their lengths can be calculated by the concentration gradient at the phase boundaries.

B.12 Thin Graphite Electrode

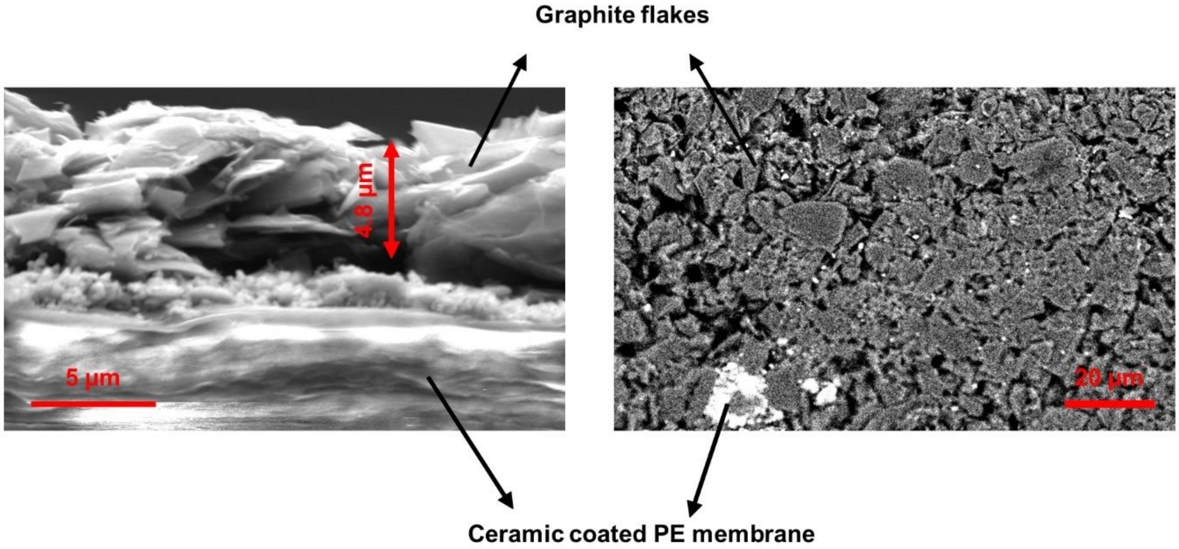

Figure B-13: Scanning Electron Microscope (SEM) of the thin graphite electrode. The graphite slurry is coated on a ceramic-coated PE separator to enable unobstructed view. SEM image of the (a) cross-section shows a ~ 5 µm thick electrode with a uniform coating in the (b) top view. The white patches on the electrode are parts of uncoated separator.

B.13 Stable phases of lithium-intercalated graphite

Table B-3: Colors and State of charges of the stable phases during Li ion intercalation in graphite

Color	**Stable phase**	**SOC**
Grey	Empty	0%
Blue	Stage 3	23%
Red	Stage 2	55%
Gold	Stage 1	100%

B.14 Particle Size Distribution Curve

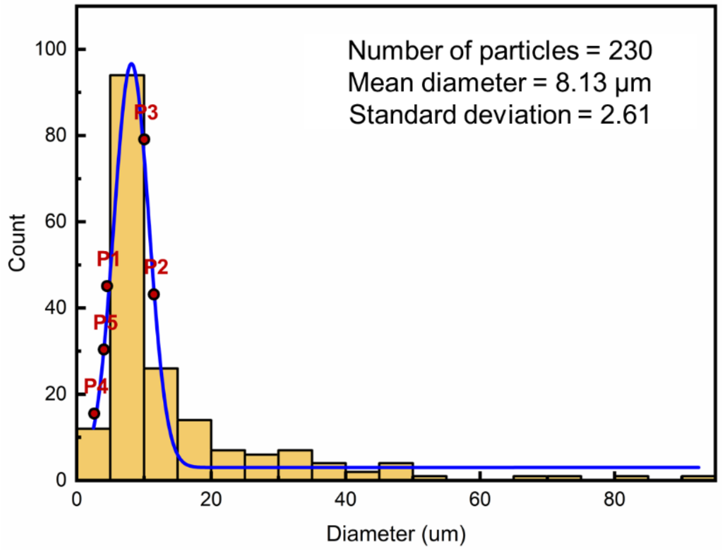

Figure B-14: Particle Size Distribution curve. The particle size distribution has been obtained from scanning the entire view under the microscope. The five particles P1-P5 are randomly selected to represent the entire particle size distribution. The average size of these particles is marked in the figure.

B.15 Image segmentation

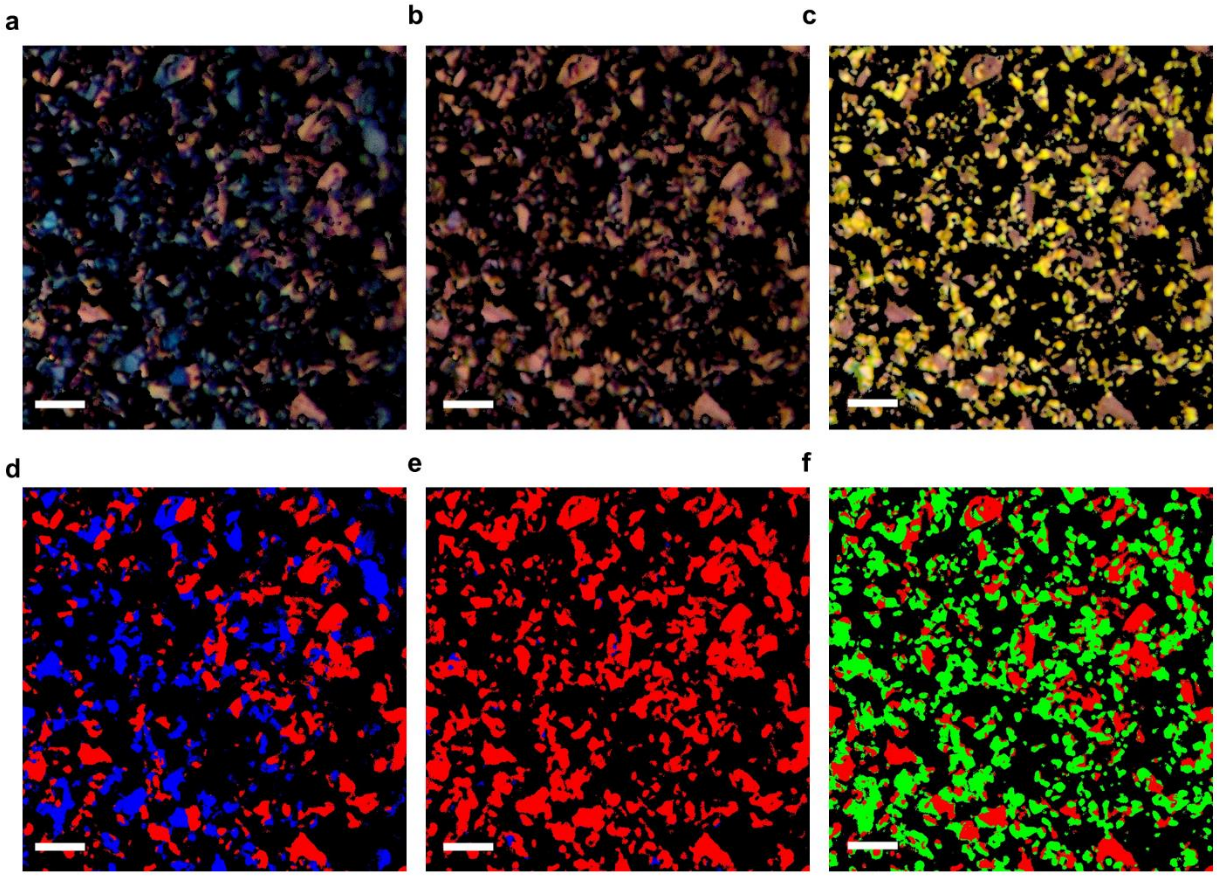

Figure B-15: Conversion of images obtained from optical microscope to RGB colors. (a–c) 3 representative images obtained from optical microscope during phase transformation in graphite. (d – f) Converted RGB images of panels (a–c) respectively. The stage 3 (blue) is converted to standard Blue, stage 2 (red) to standard Red and stage 1 (gold) to standard Green. The remaining regions are converted to Black. The conversions are based on the Hue-Saturation-Brightness thresholds mentioned in Experimental Section.

B.16 Determination of interface length

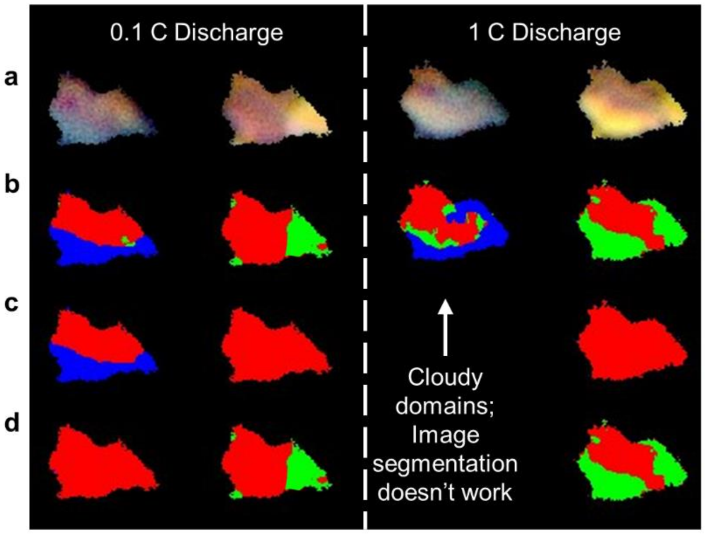

Figure B-16: Criteria to determine interface length within particles. (a) Raw images of particle P1 at two representative SOCs under 0.1 C and 1 C discharge rates. (b) Converted RGB images particle P1 at respective SOCs. At 1 C discharge, the blue-red transformation (Stage 3 to 2) occurs through solid-solution mechanism. Thus, clear phase boundaries are not observed, and the image segmentation protocol fails in sucha cases. (c) All the green regions (Stage 1) are converted to red color to calculate the interface length between Stage 3 and Stage 2 using $L_{BR} = (l_{Blue} + l_{Red} – l_{particle})/2$. (d) All the blue regions (Stage 3) are converted to red color to calculate the interface length between Stage 2 and Stage 1 using $L_{RG} = (l_{Red} + l_{Gold} – l_{particle})/2$. Here L_{BR} and L_{RG} are the lengths of Blue – Red and Red – Gold interfaces respectively, l_{Blue}, l_{Red} and l_{Gold} are the perimeters of the blue, red and gold regions in the corresponding transformed images, and $l_{particle}$ is the outer perimeter of all the particles within the viewing frame.

B.17 Schematic representation of Li ion intercalation into graphite

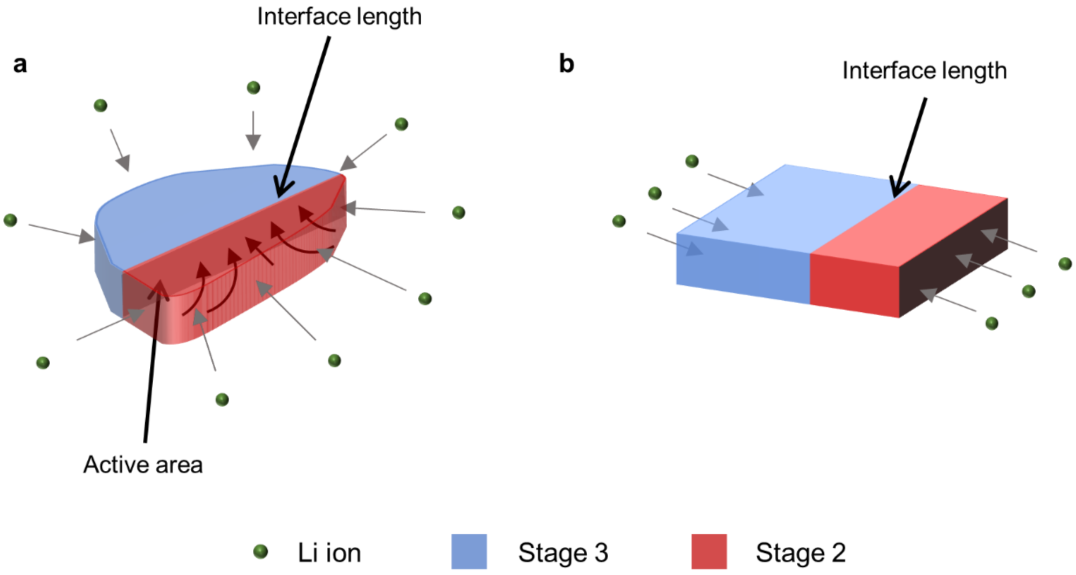

Figure B-17: Schematic representation of Li ion intercalation into graphite in experiments and MPET model. (a) In actual particles, the Li ions enter graphite flakes from the edge planes. During phase separation, the net flux of Li ions concentrates on the interface between the two stable phases, and thus is considered as active area. (b) In MPET simulation, the Li ions enter the square-shaped particles only through the two opposite ends. The remaining two ends are blocked facilitating 1D simulation.

Appendix C. Supporting Materials for Chapter 4

C.1 Thin NMC532 Electrode

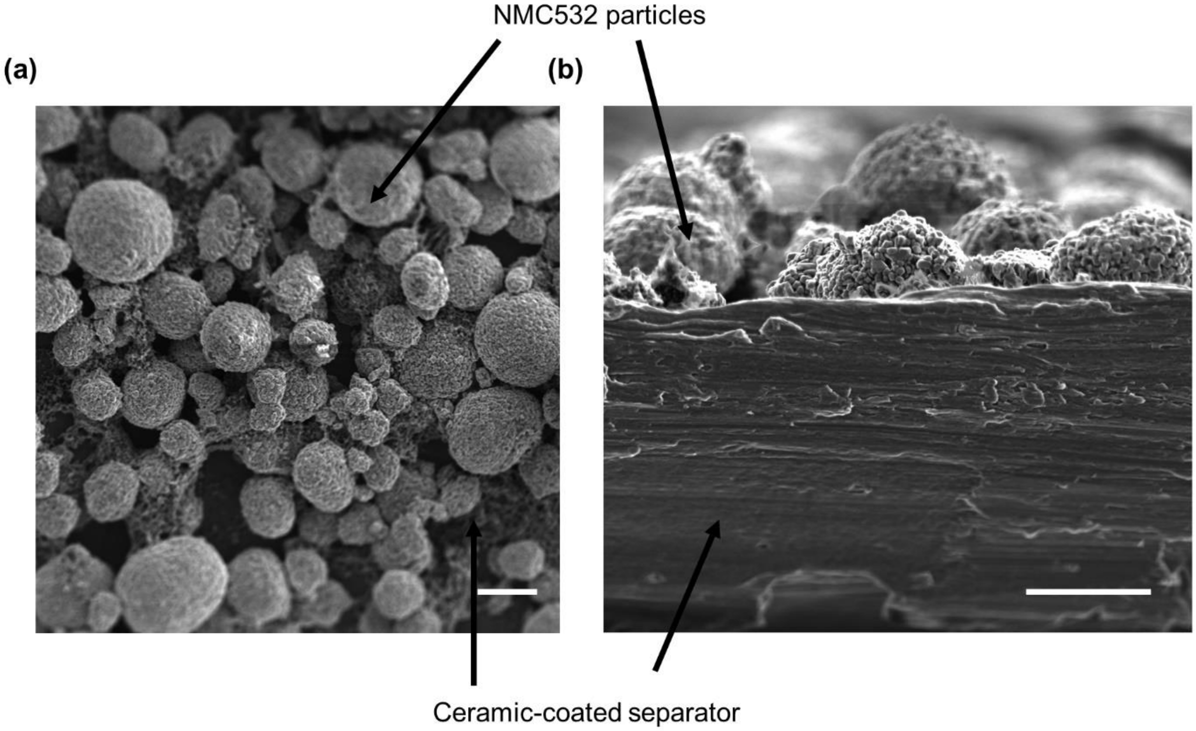

Figure C-1: Scanning Electron Microscope (SEM) of the thin NMC532 electrode. The cathode slurry is coated on a ceramic-coated PE separator to enable unobstructed view. SEM image of the (a) cross-section shows a ~ 10 µm thick electrode with a uniform coating in the (b) top view.

C.2 Cell Performance and Reference Raman Spectra

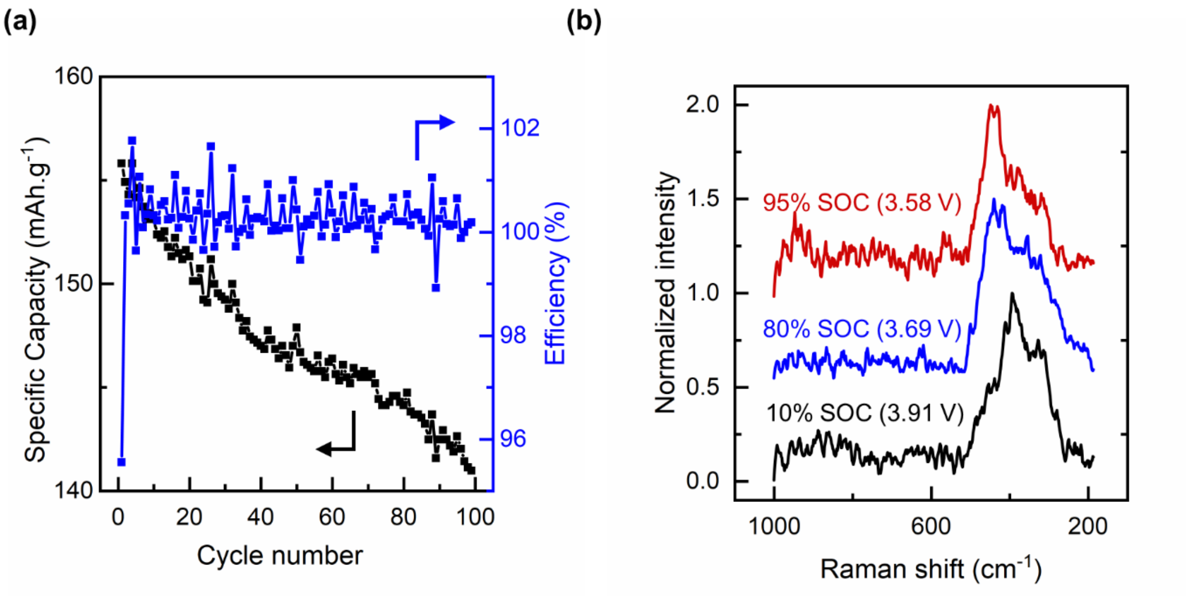

Figure C-2: Cell performance and reference Raman spectra. (a) Coulombic efficiency and Cycle retention of the optical cell. The cells showed ~100% Coulombic efficiency and >90% retention after 100 cycles. (b) Reference Raman spectra at 3 SOCs between 0% and 100% showing sharp A_{1g} and E_g peaks. The A_{1g} peaks at 10%, 80% and 95% SOCs occur at 545.8 cm^{-1}, 591.3 cm^{-1}, and 596.3 cm^{-1} respectively and the E_g peaks occur at 481.4 cm^{-1}, 506.9 cm^{-1}, and 532.3 cm^{-1}.

C.3 Peak Deconvolution

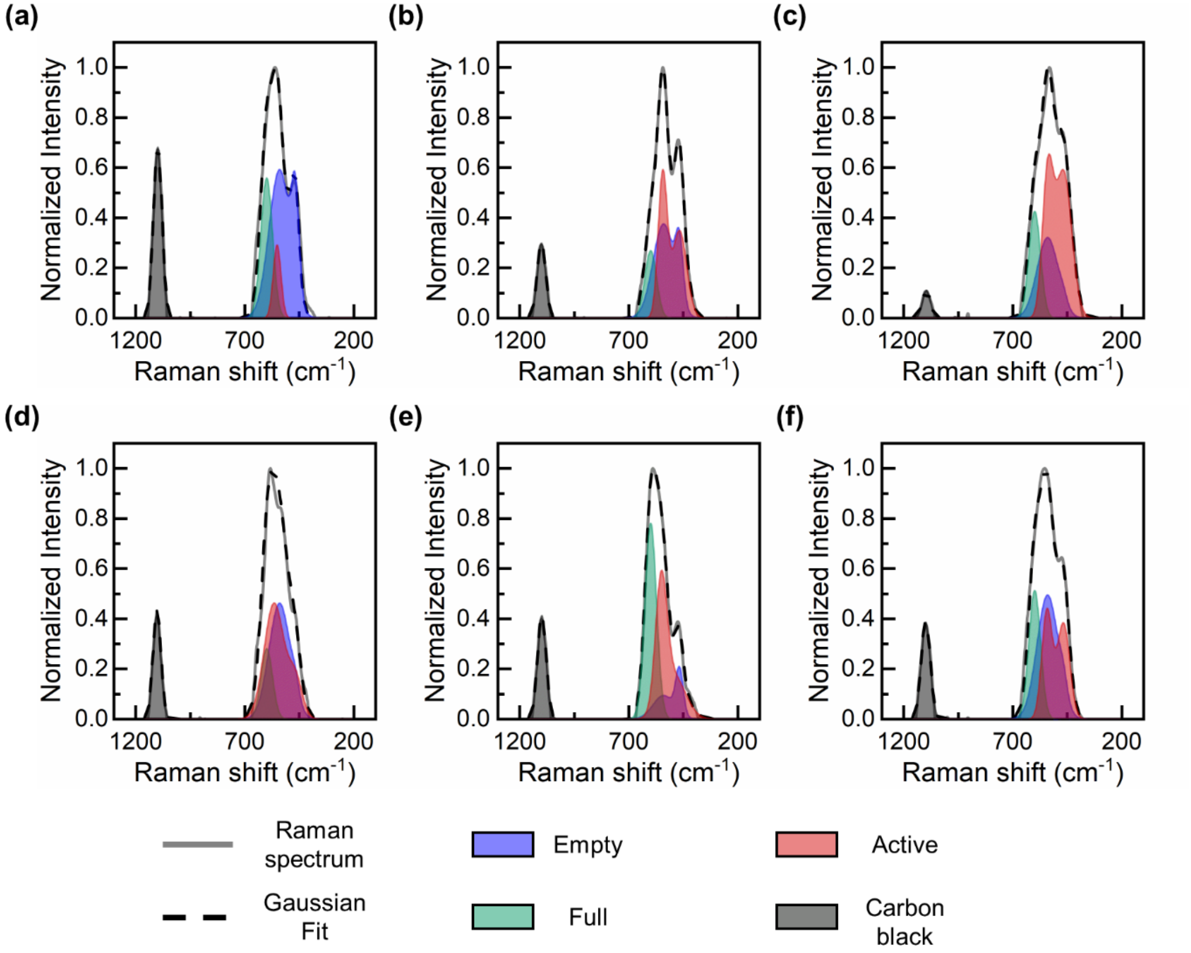

Figure C-3: Deconvolution of Raman spectra. (a)-(f) Examples of deconvolution of 6 random Raman spectra out of more than 600 Raman spectra for the entire analysis. The spectra are deconvoluted into three regions, namely empty, full, and active. All the spectra also show the peak of carbon black at ~1100 cm^{-1}.

C.4 Raman spectra at empty spots

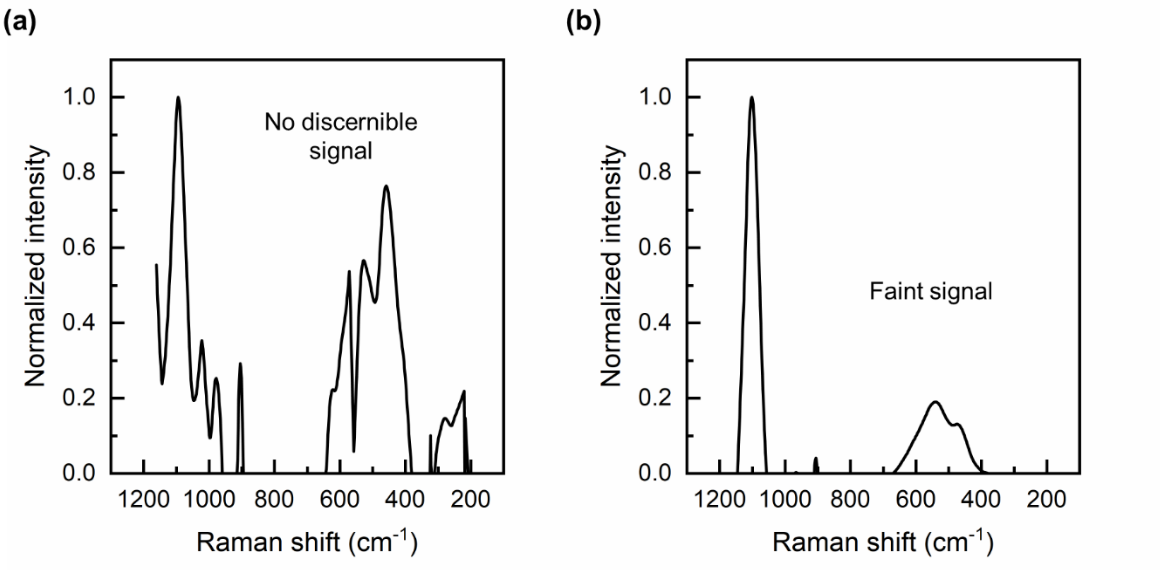

Figure C-4: Raman spectra at points without active material. (a)-(b) The spectra at points with voids either have high noise or faint signals indicating either no or indetectable active material.

Appendix D. Supporting Materials for Chapter 5

D.1 3rd Voltage plateau during charging

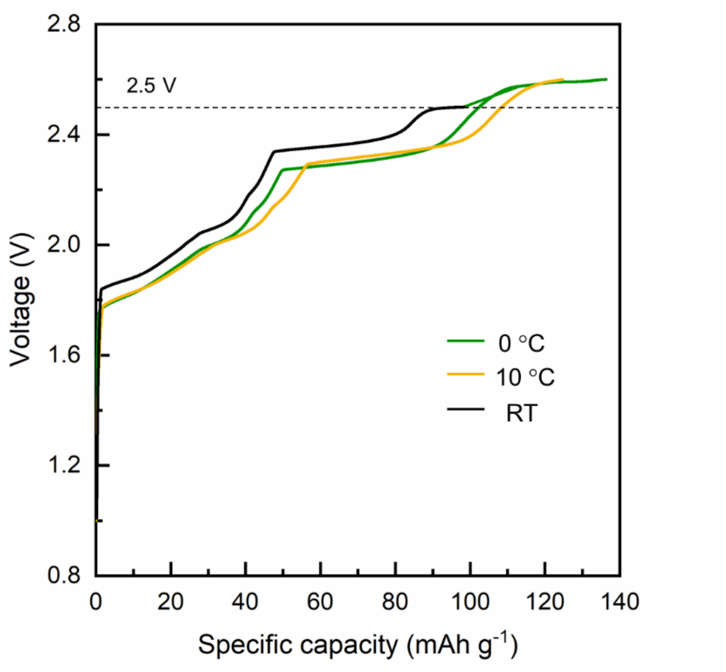

Figure D-1: A 3rd voltage plateau appears during charging at temperatures higher than 0°C. This 3rd plateau may indicate a side reaction with the current collector. The 3rd plateau reduces the Coulombic efficiency of the AIBs.

D.2 Short-time fit during PITT Discharge

D.2.1 -20°C

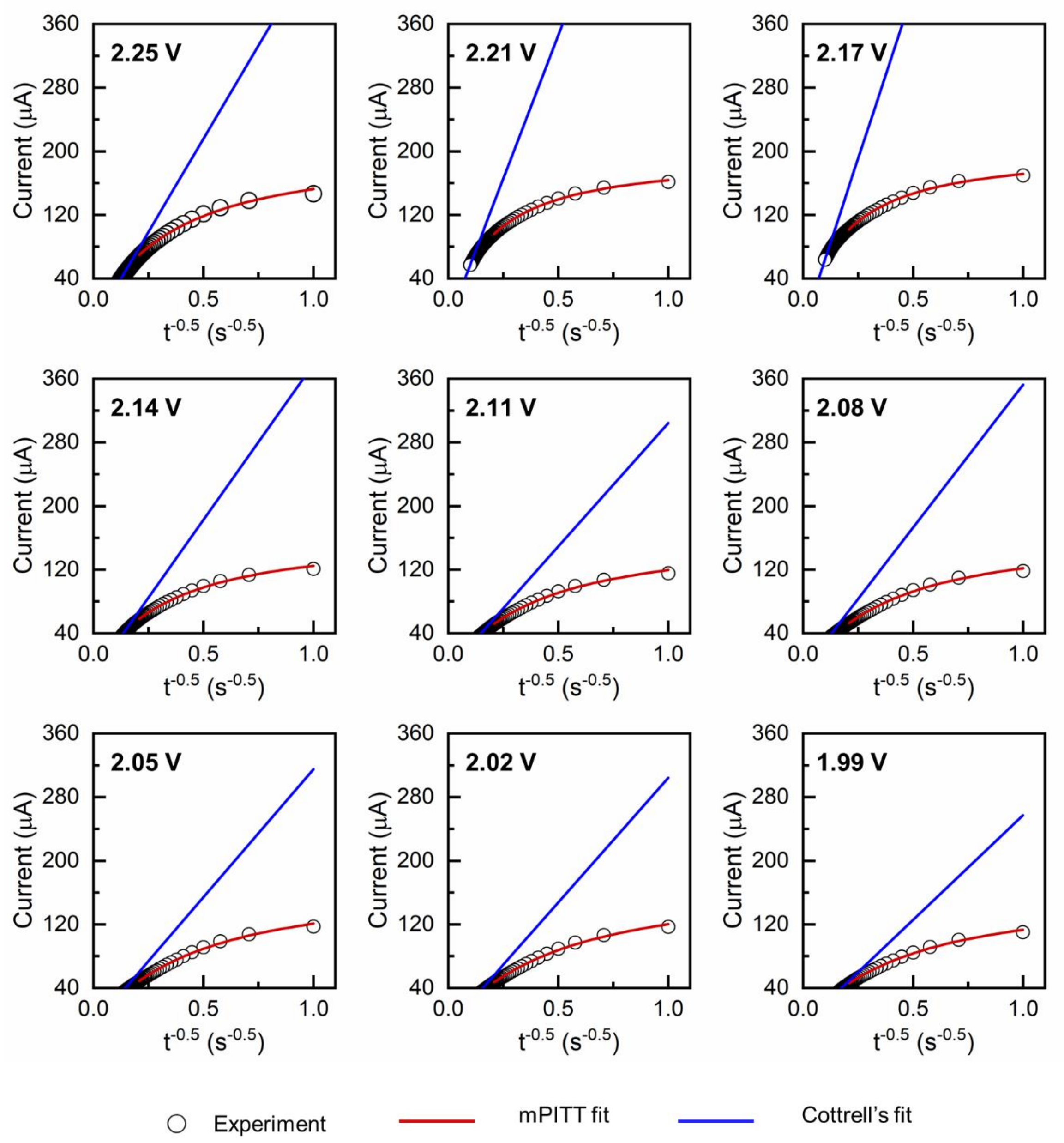

continued

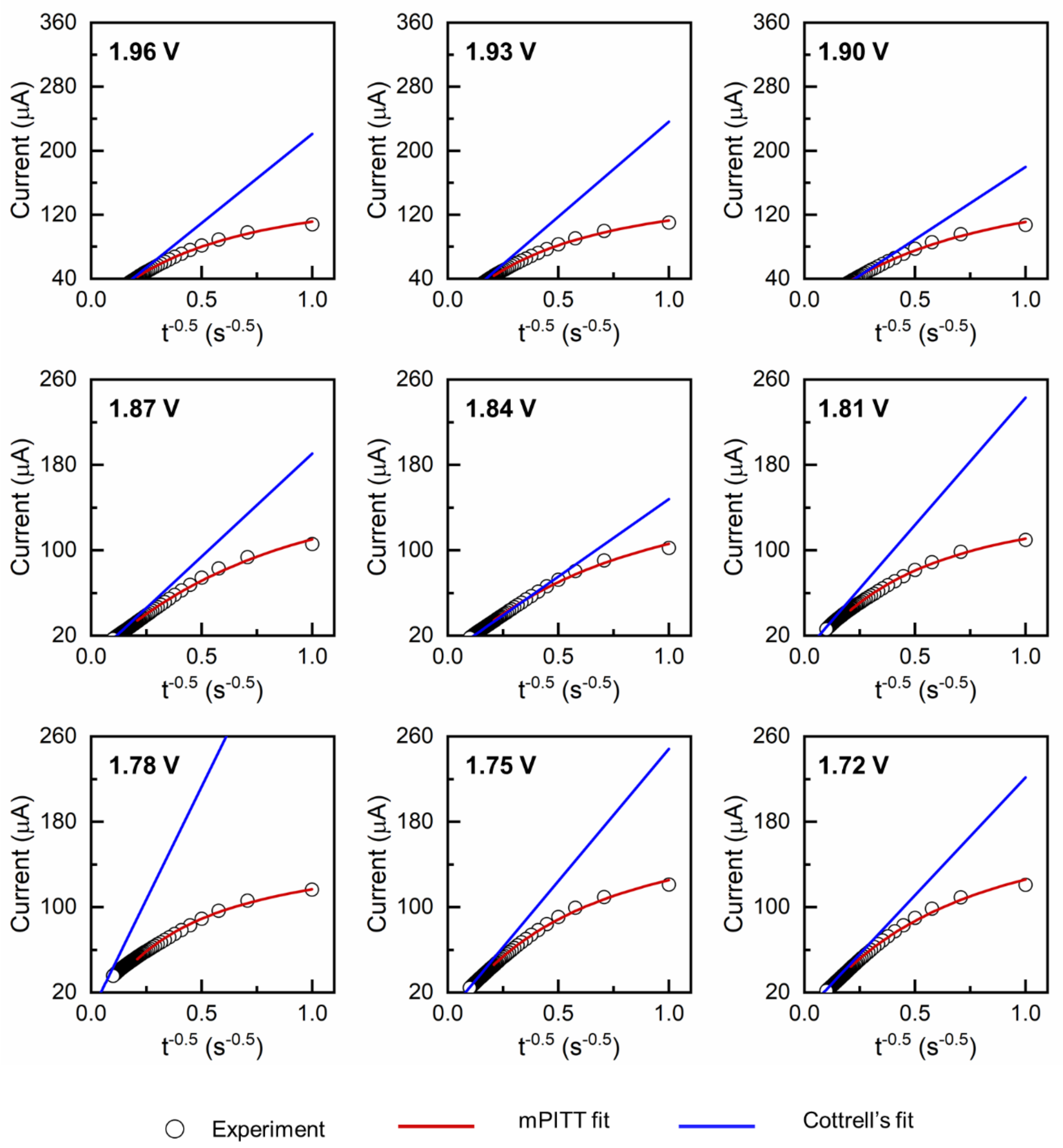
1.96 V
1.93 V
1.90 V
1.87 V
1.84 V
1.81 V
1.78 V
1.75 V
1.72 V
Current (μA)
40
120
200
280
360
20
100
180
260
0.0
0.5
1.0
t^-0.5 (s^-0.5)
Experiment
mPITT fit
Cottrell's fit

continued

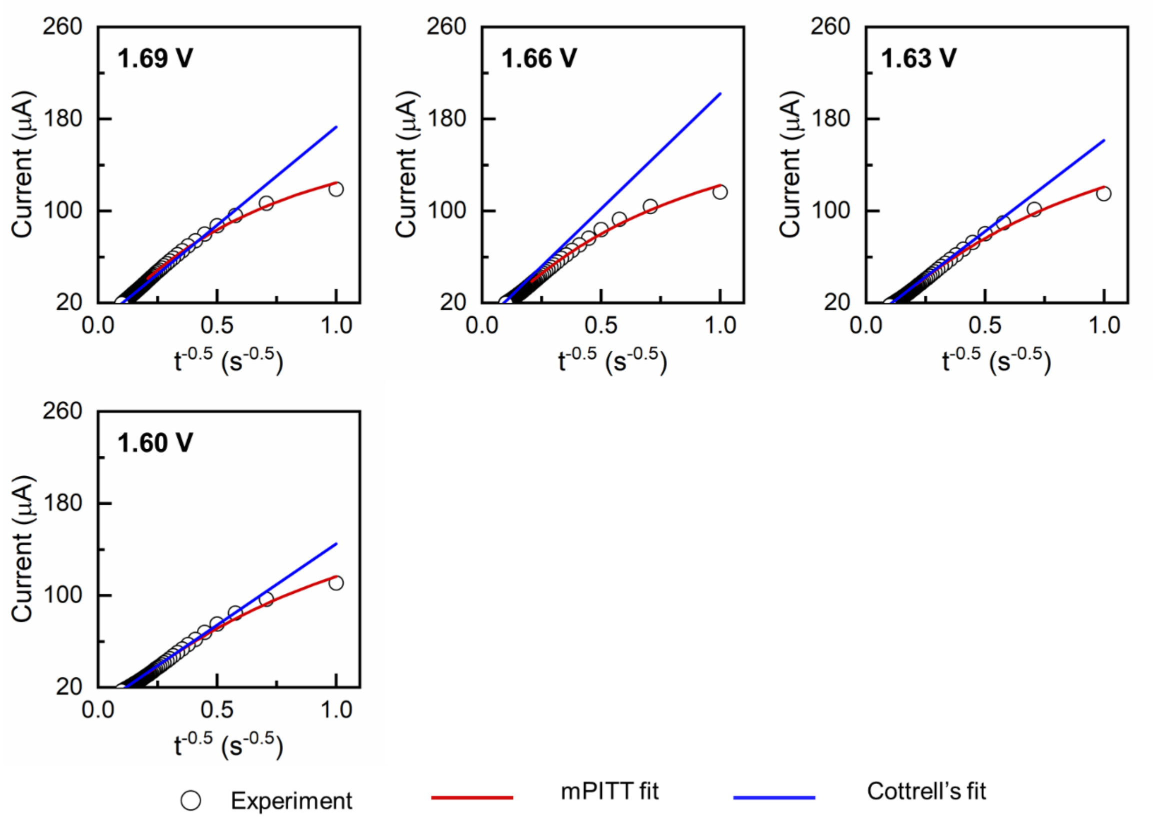

Figure D-2: The fitting of absolute transient currents at the selected voltage steps during PITT discharge at -20°C. Cottrell's method and the mPITT method are used to fit the transient currents in the short-time regime and estimate the diffusion coefficients and Damköhler number.

D.2.2 -10°C

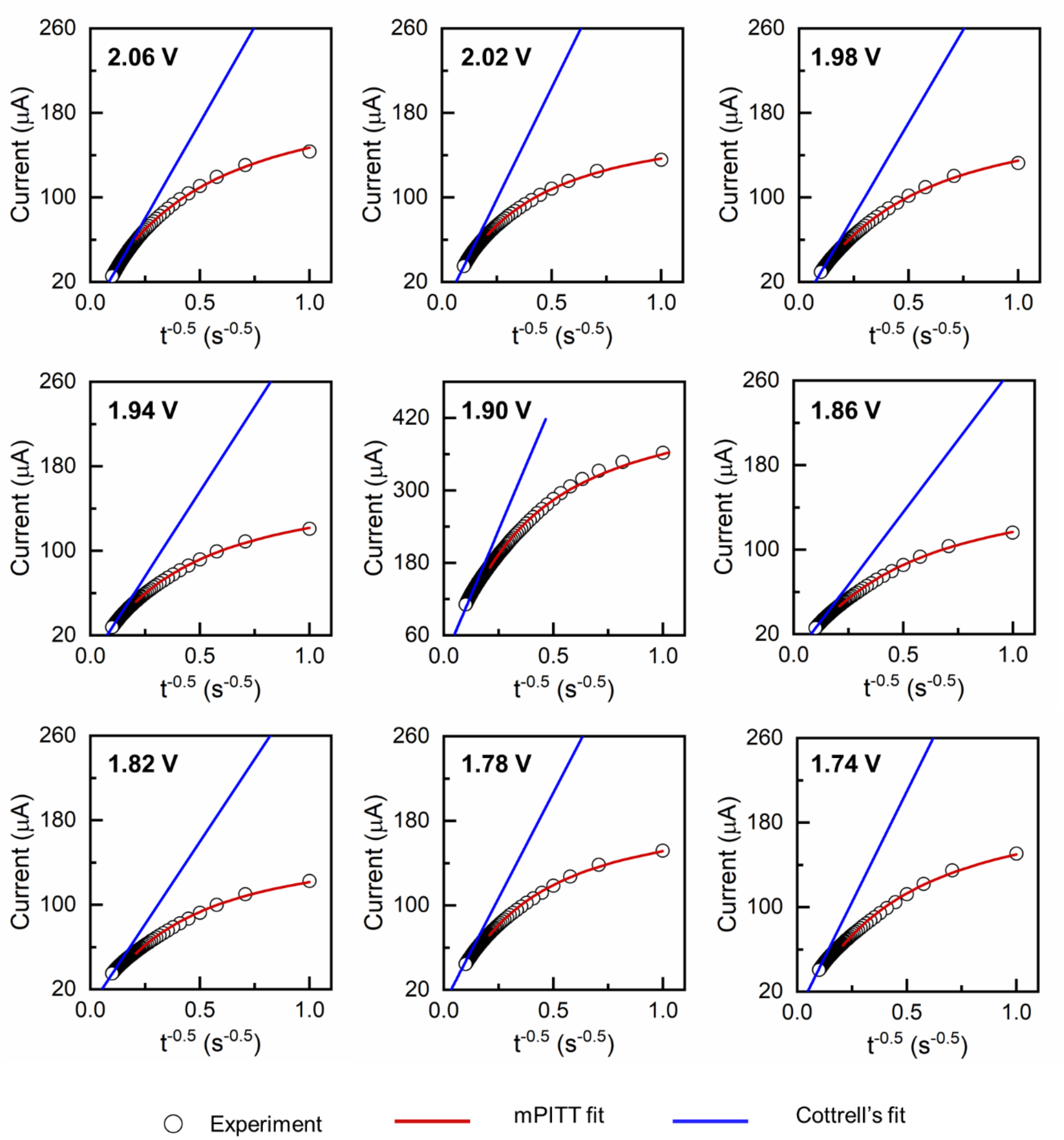

continued

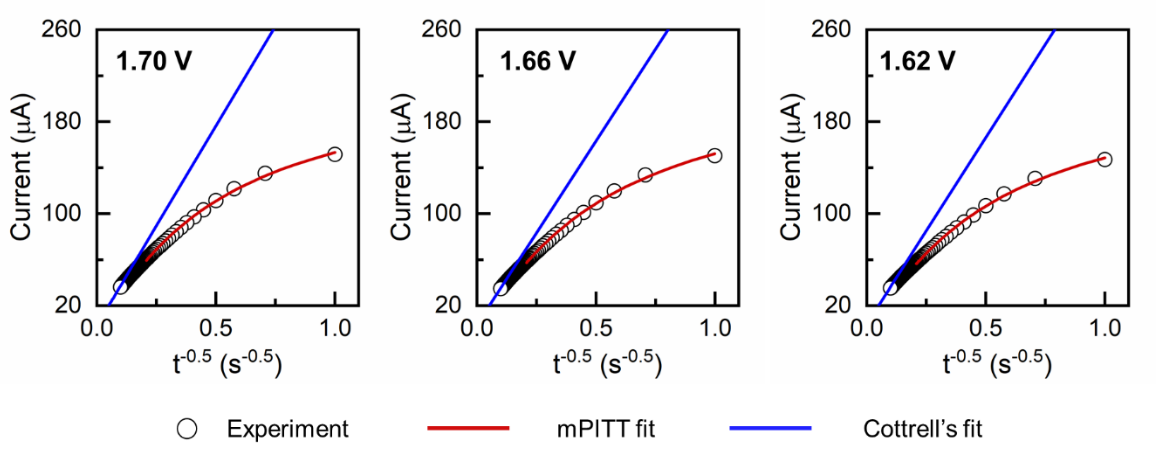

Figure D-3: The fitting of absolute transient currents at the selected voltage steps during PITT discharge at -10°C. Cottrell's method and the mPITT method are used to fit the transient currents in the short-time regime and estimate the diffusion coefficients and Damköhler number.

D.2.3 0°C

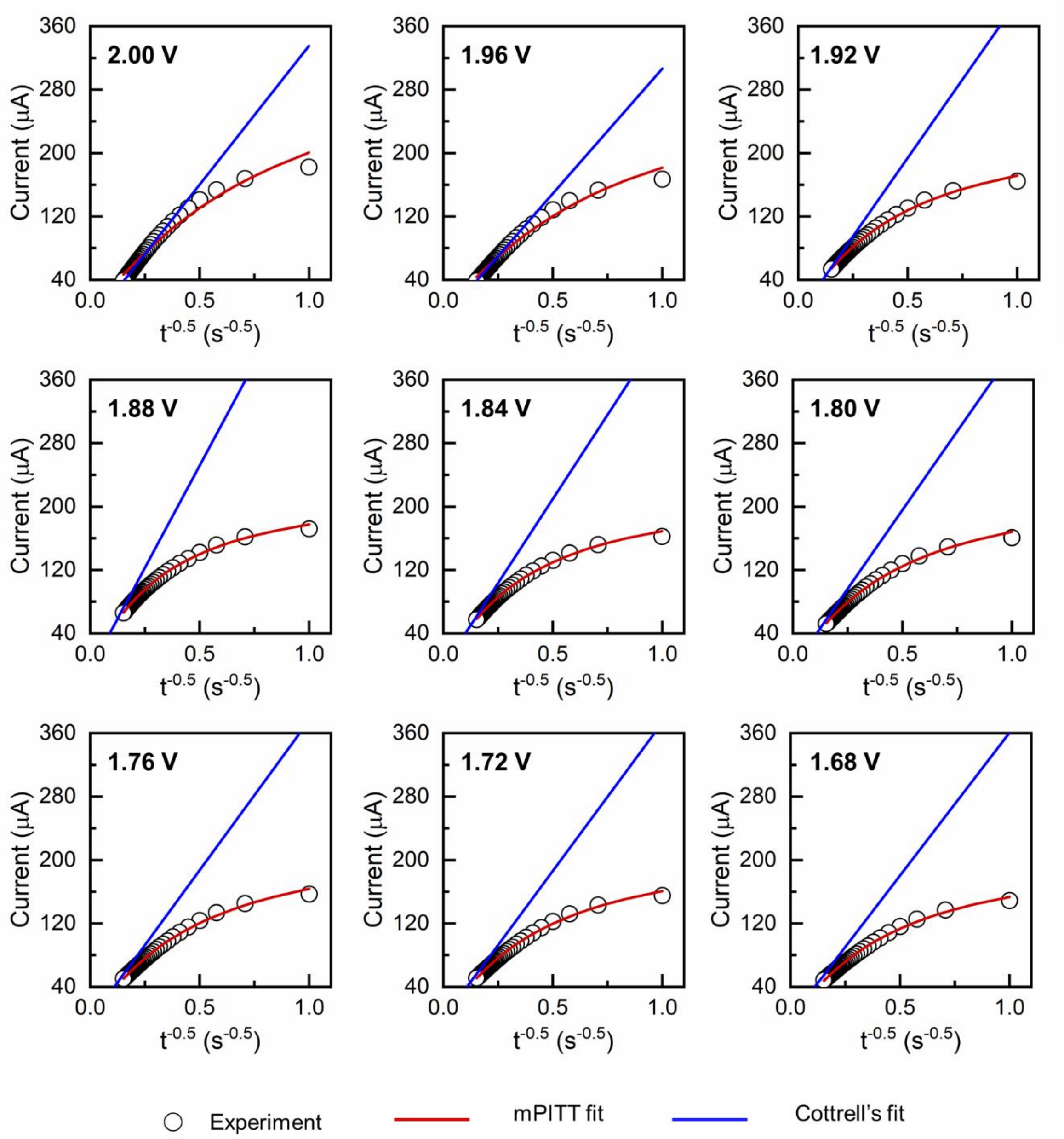

continued

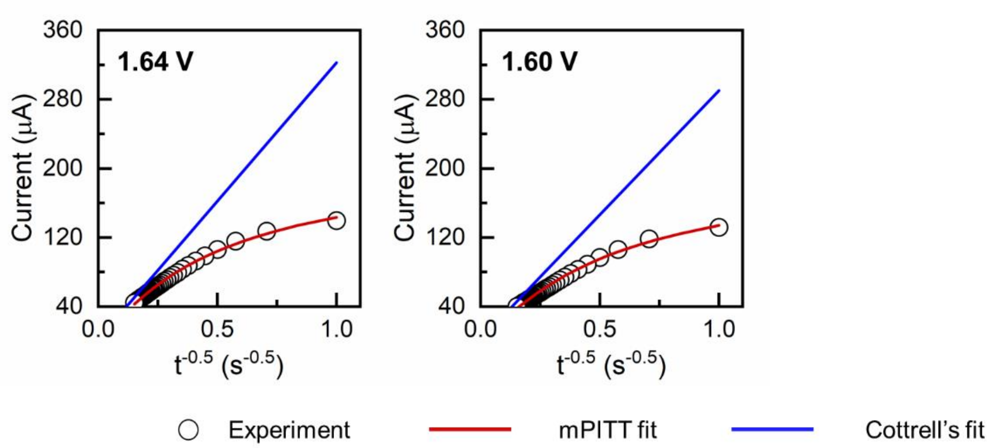

Figure D-4: The fitting of absolute transient currents at the selected voltage steps during PITT discharge at 0°C. Cottrell's method and the mPITT method are used to fit the transient currents in the short-time regime and estimate the diffusion coefficients and Damköhler number.

D.2.4 10°C

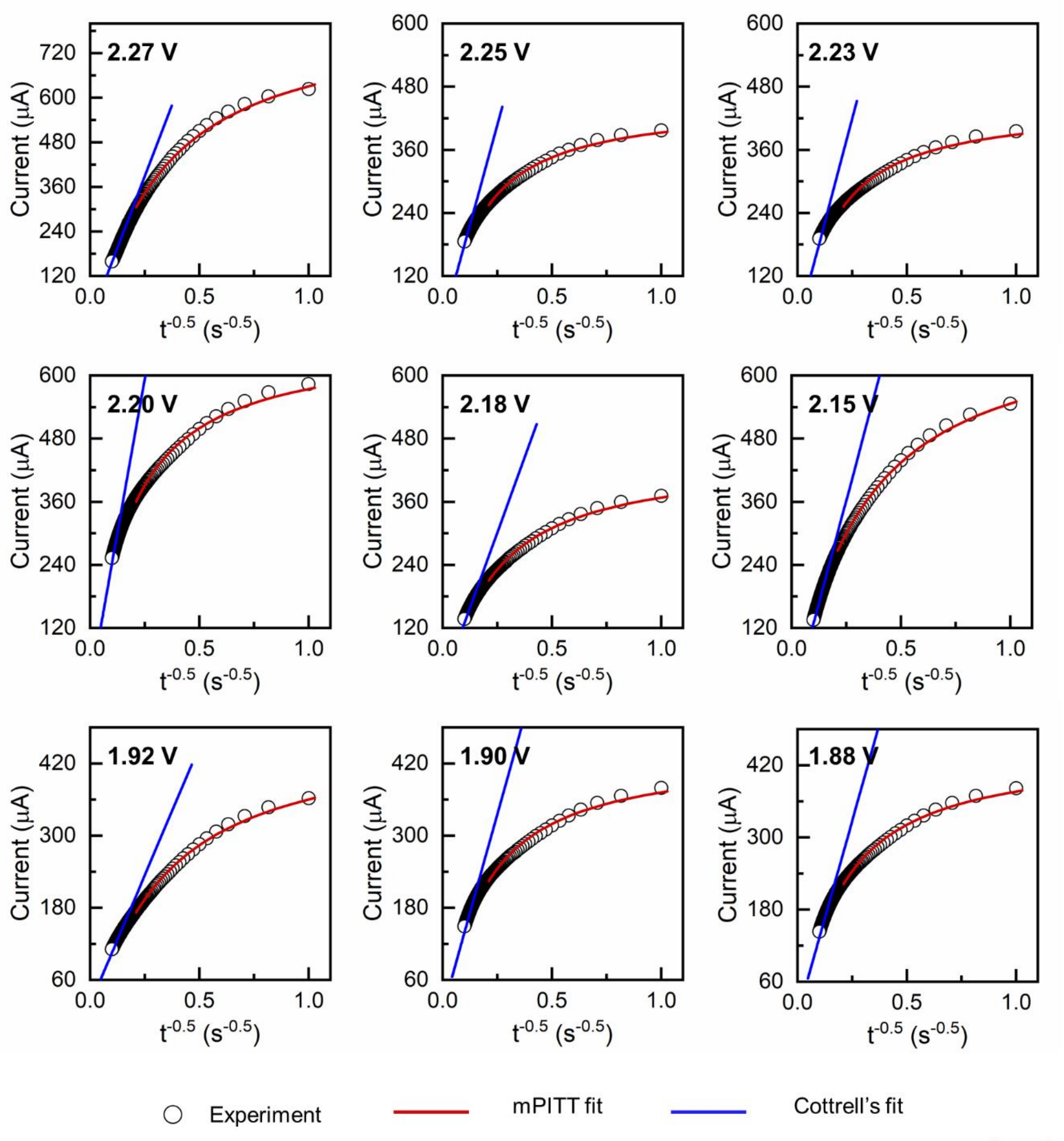

continued

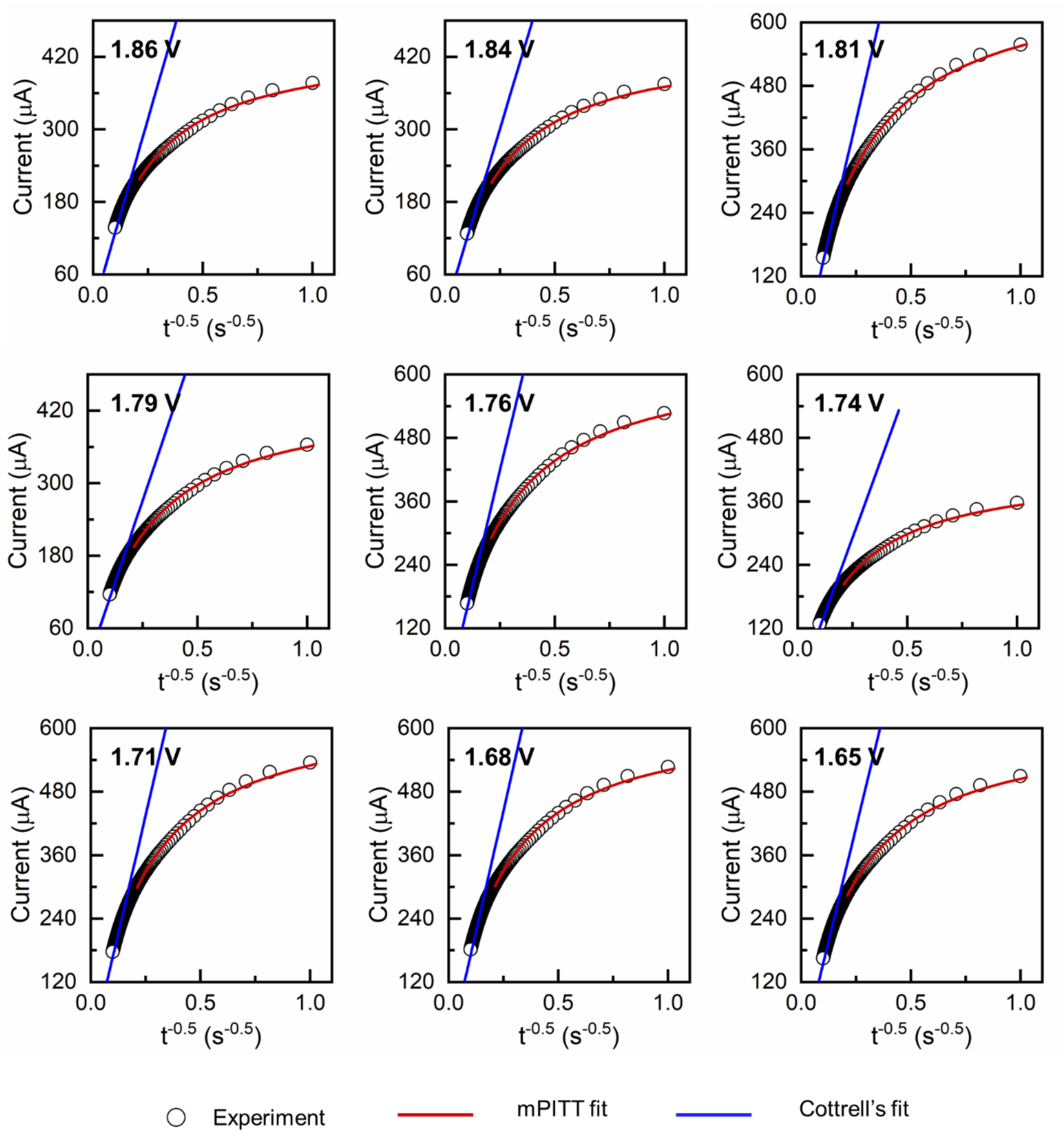
1.86 V
1.84 V
1.81 V
1.79 V
1.76 V
1.74 V
1.71 V
1.68 V
1.65 V
Current (μA)
60
180
300
420
120
240
360
480
600
t$^{-0.5}$ (s$^{-0.5}$)
0.0
0.5
1.0
Experiment
mPITT fit
Cottrell's fit

continued

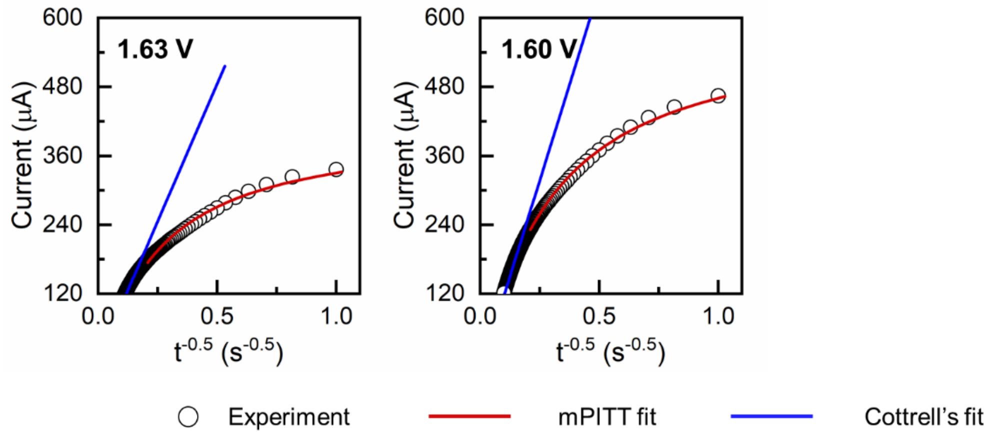

Figure D-5: The fitting of absolute transient currents at the selected voltage steps during PITT discharge at 10°C. Cottrell's method and the mPITT method are used to fit the transient currents in the short-time regime and estimate the diffusion coefficients and Damköhler number.

D.2.5 Room Temperature

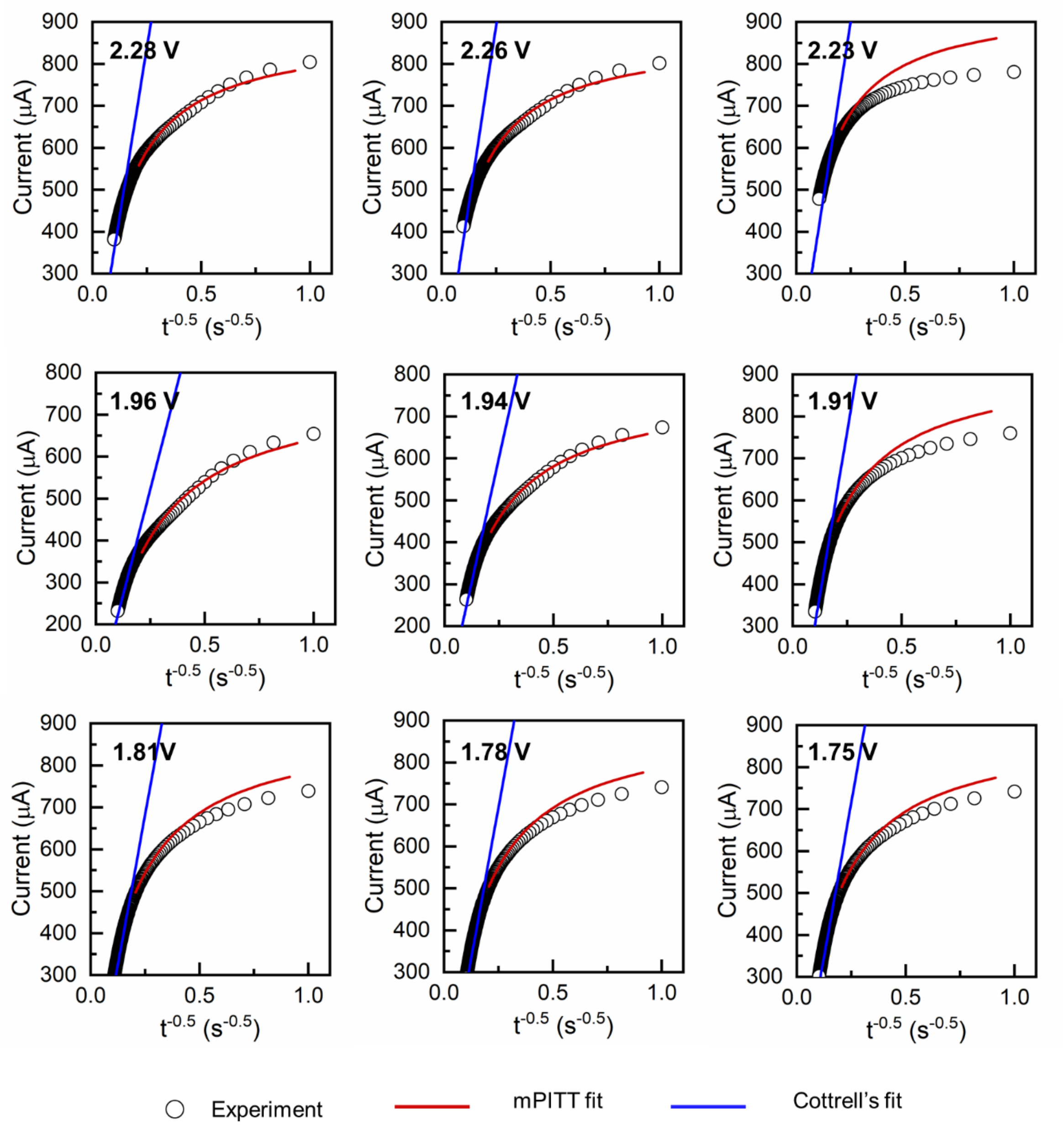

continued

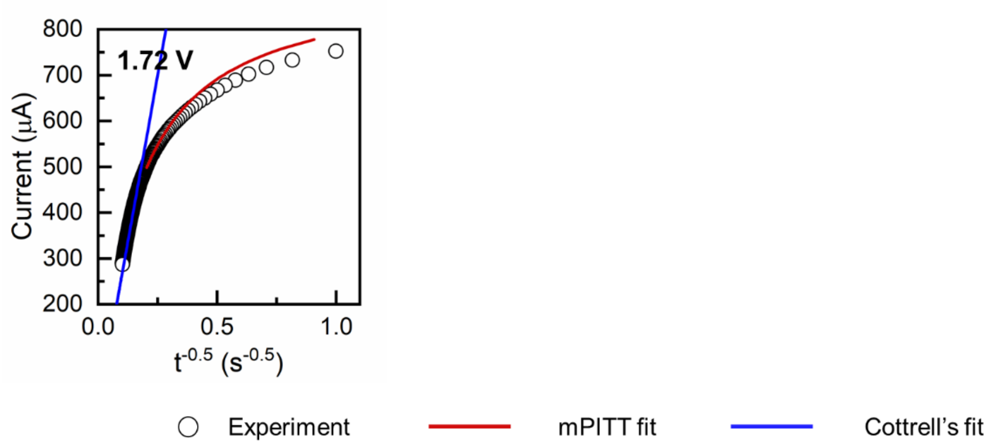

Figure D-6: The fitting of absolute transient currents at the selected voltage steps during PITT discharge at room temperature. Cottrell's method and the mPITT method are used to fit the transient currents in the short-time regime and estimate the diffusion coefficients and Damköhler number.

D.3 Short-time fit during PITT Charge

D.3.1 -20°C

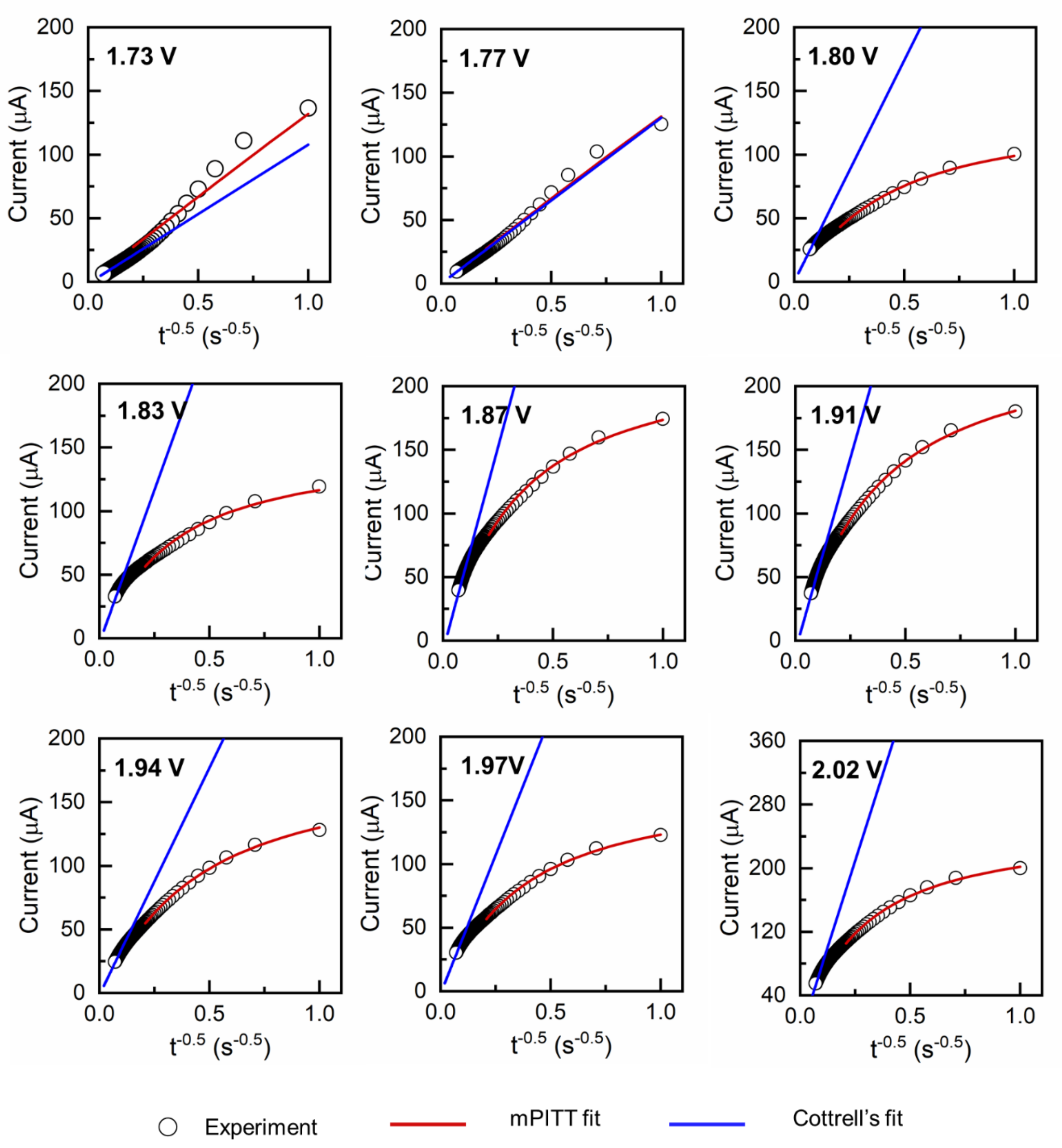

continued

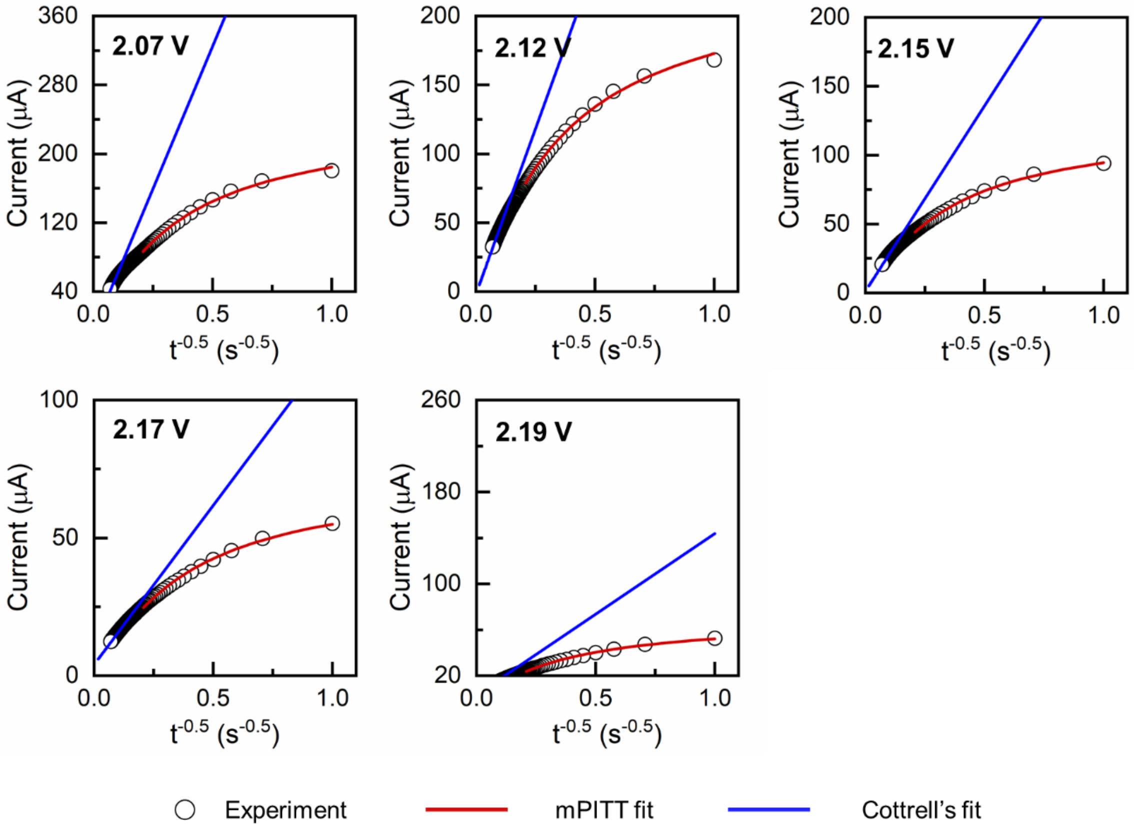

Figure D-7: The fitting of absolute transient currents at the selected voltage steps during PITT charge at -20°C. Cottrell's method and the mPITT method are used to fit the transient currents in the short-time regime and estimate the diffusion coefficients and Damköhler number.

D.3.2 -10°C

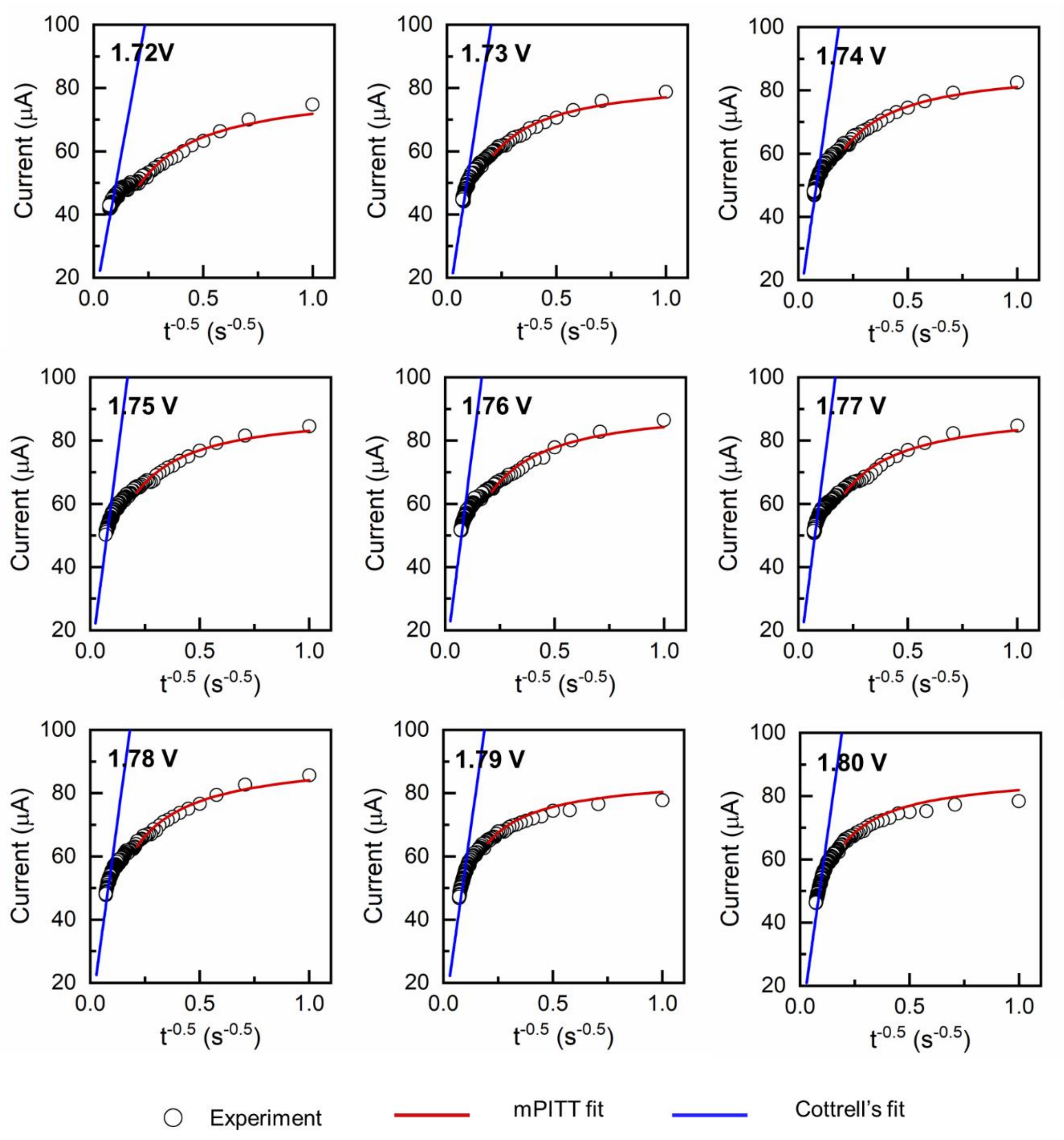
1.72V
1.73 V
1.74 V
1.75 V
1.76 V
1.77 V
1.78 V
1.79 V
1.80 V
Current (μA)
20
40
60
80
100
t^-0.5 (s^-0.5)
0.0
0.5
1.0
Experiment
mPITT fit
Cottrell's fit

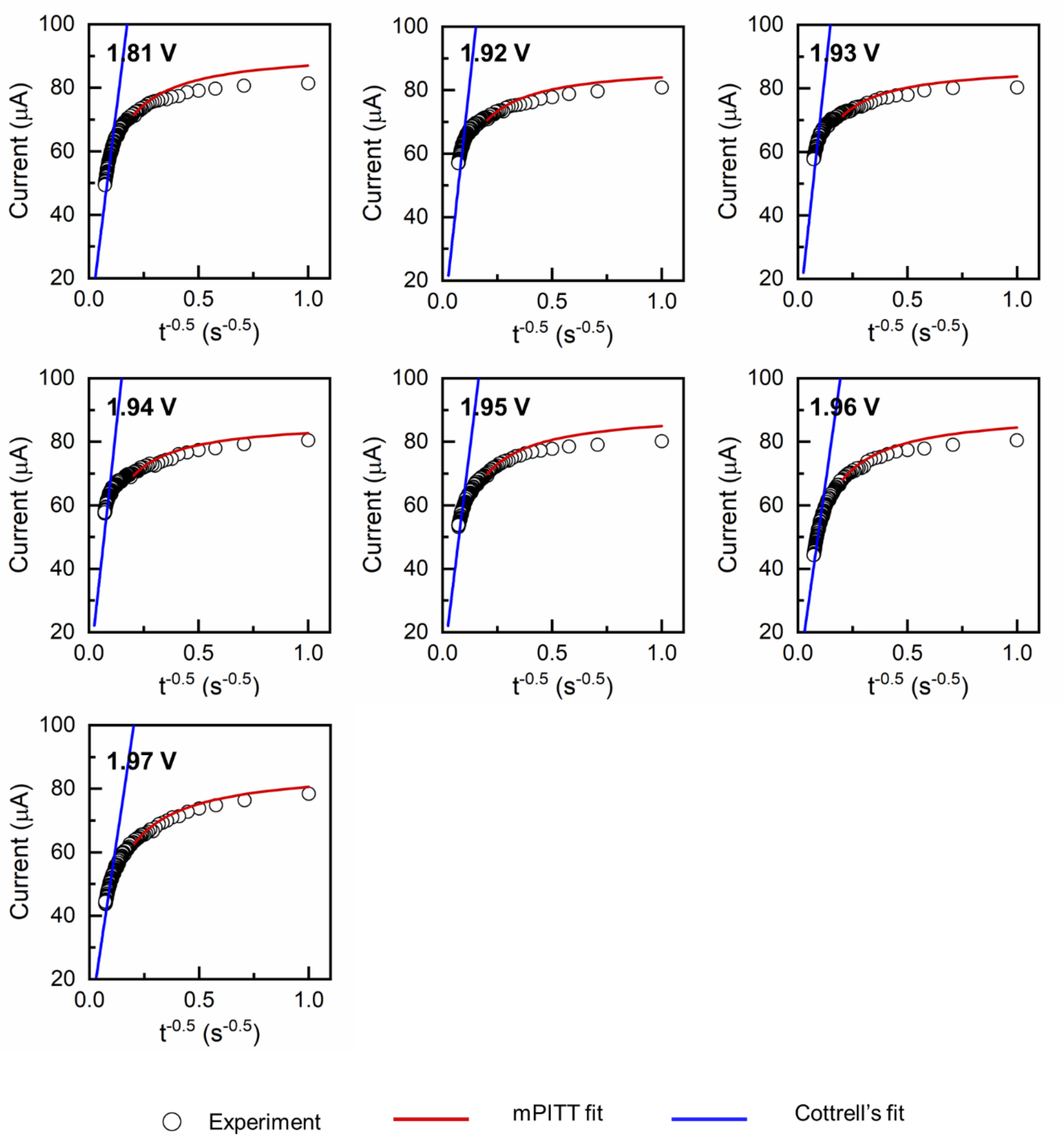

Figure D-8: The fitting of absolute transient currents at the selected voltage steps during PITT charge at -10°C. Cottrell's method and the mPITT method are used to fit the transient currents in the short-time regime and estimate the diffusion coefficients and Damköhler number.

D.3.3 0°C

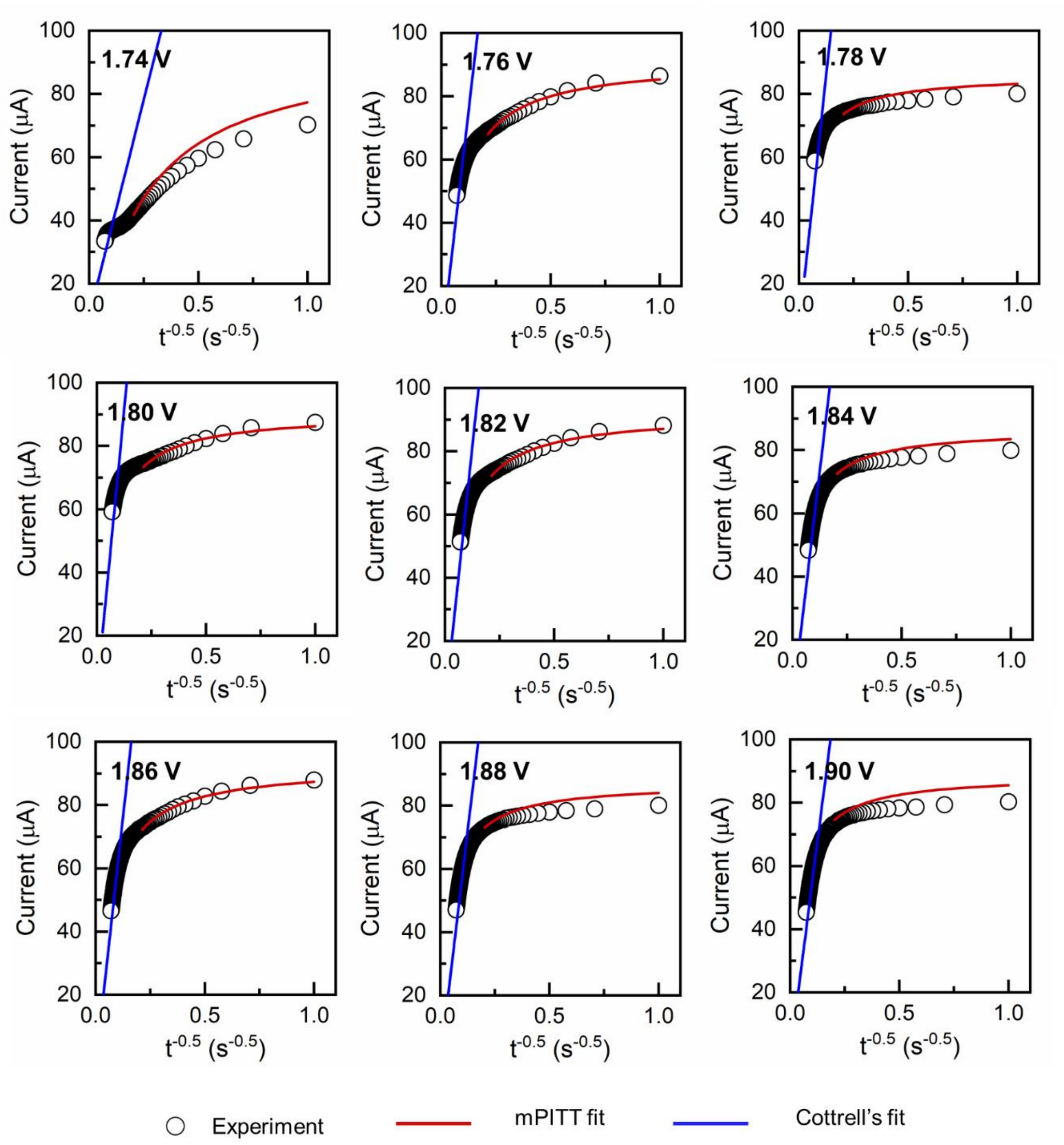

continued

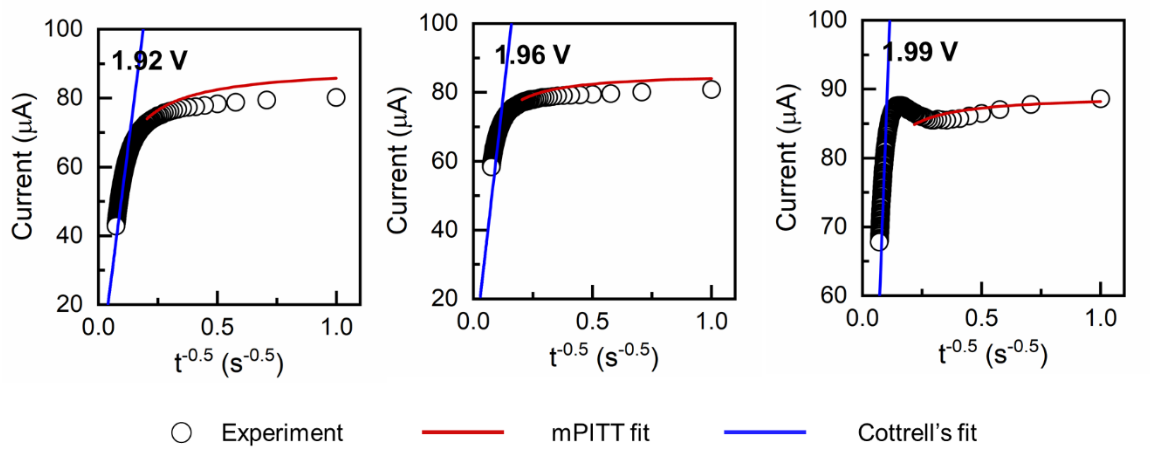

Figure D-9: The fitting of absolute transient currents at the selected voltage steps during PITT charge at 0°C. Cottrell's method and the mPITT method are used to fit the transient currents in the short-time regime and estimate the diffusion coefficients and Damköhler number.

D.3.4 10°C

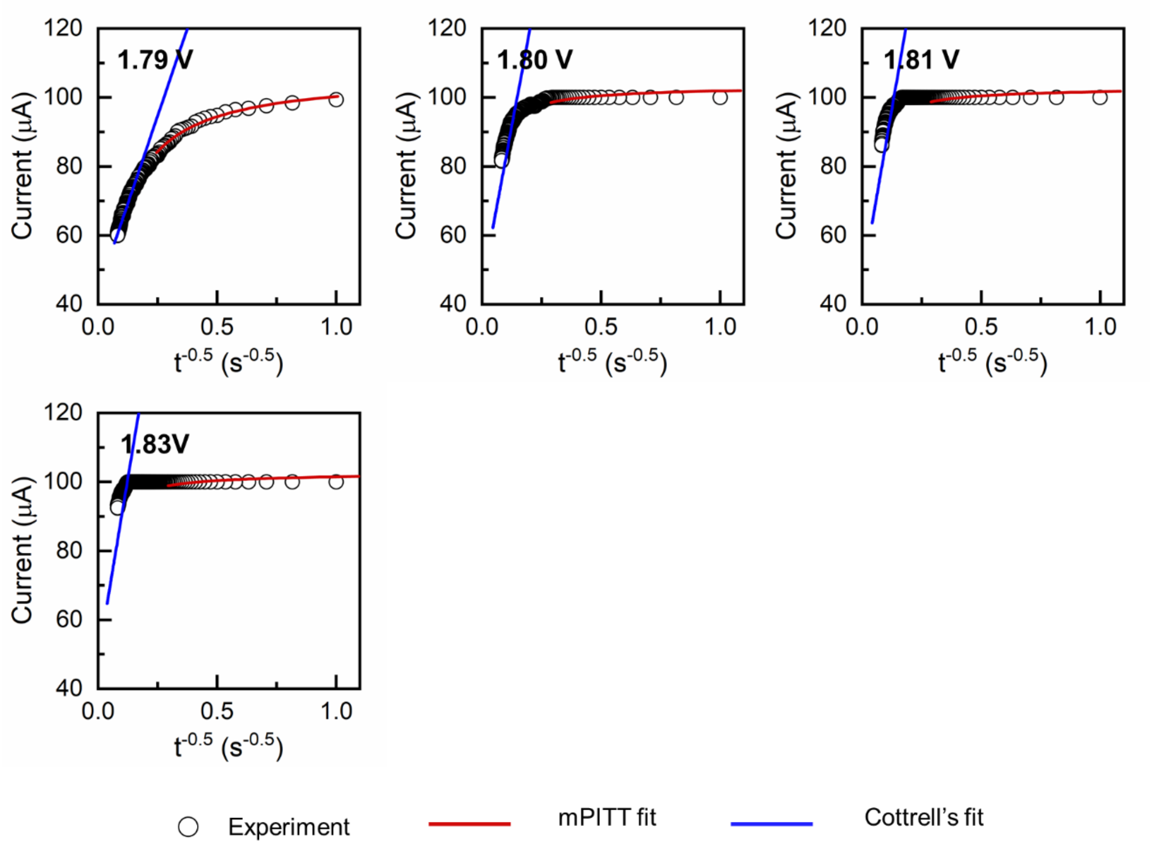

Figure D-10: The fitting of absolute transient currents at the selected voltage steps during PITT charge at 10°C. Cottrell's method and the mPITT method are used to fit the transient currents in the short-time regime and estimate the diffusion coefficients and Damköhler number.

D.3.5 Room Temperature

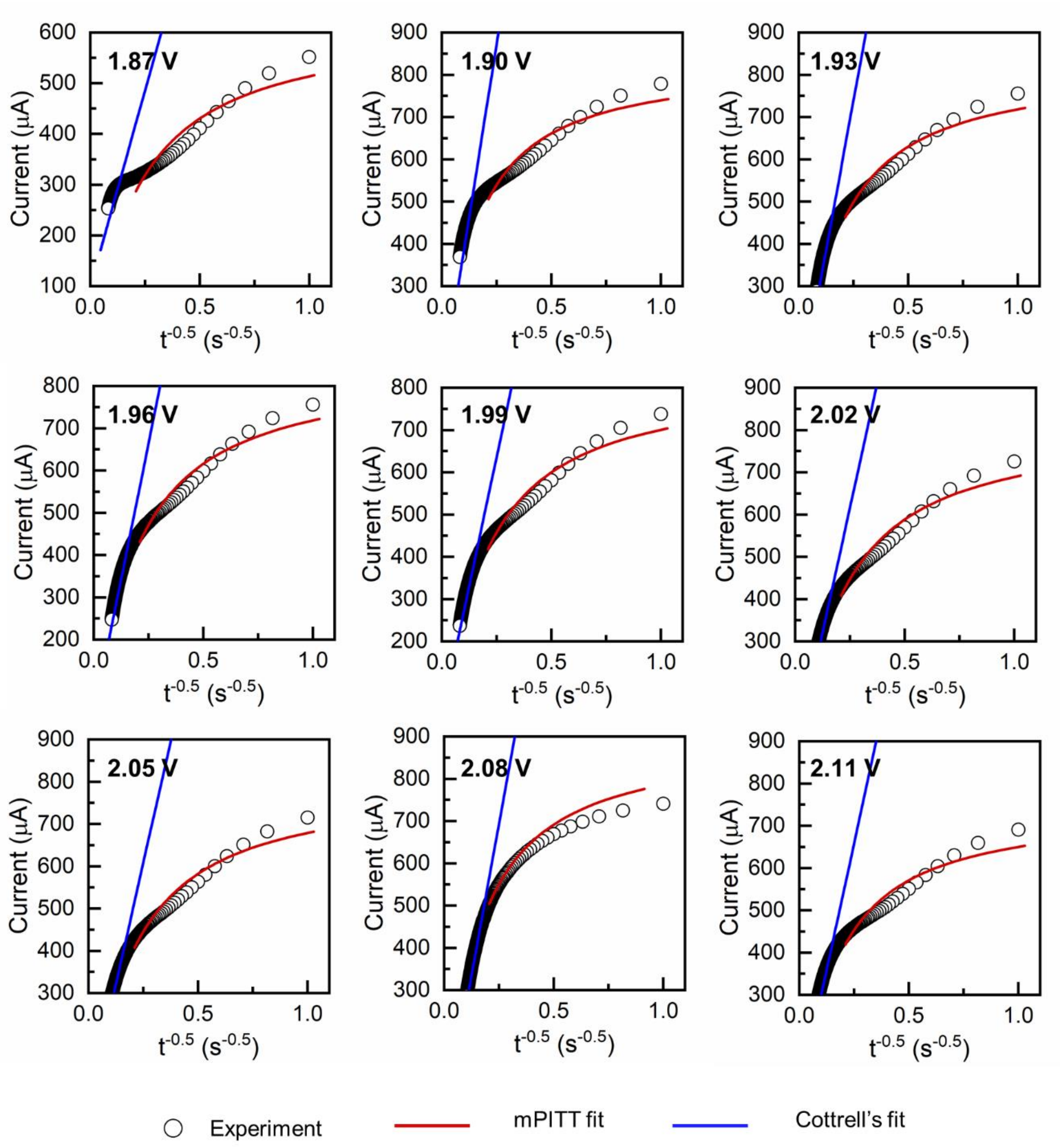

continued

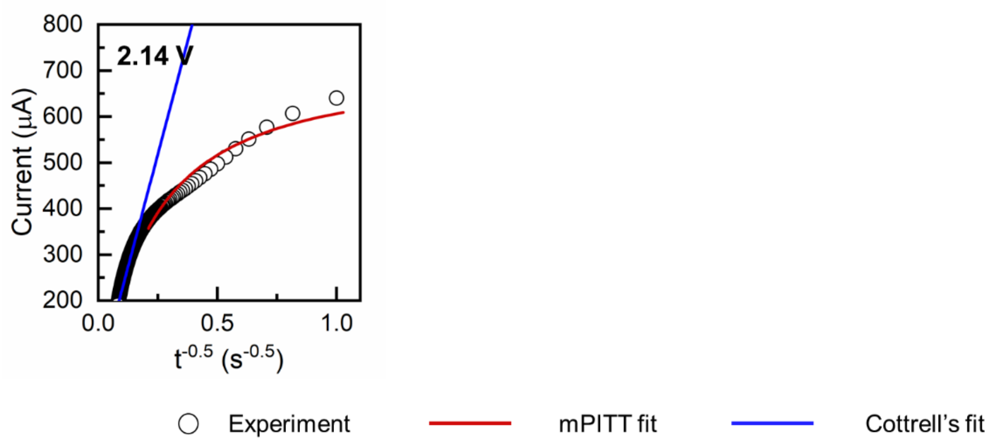

Figure D-11: The fitting of absolute transient currents at the selected voltage steps during PITT charge at room temperature. Cottrell's method and the mPITT method are used to fit the transient currents in the short-time regime and estimate the diffusion coefficients and Damköhler number.

D.4 Long-time fit during PITT Discharge

D.4.1 -20°C

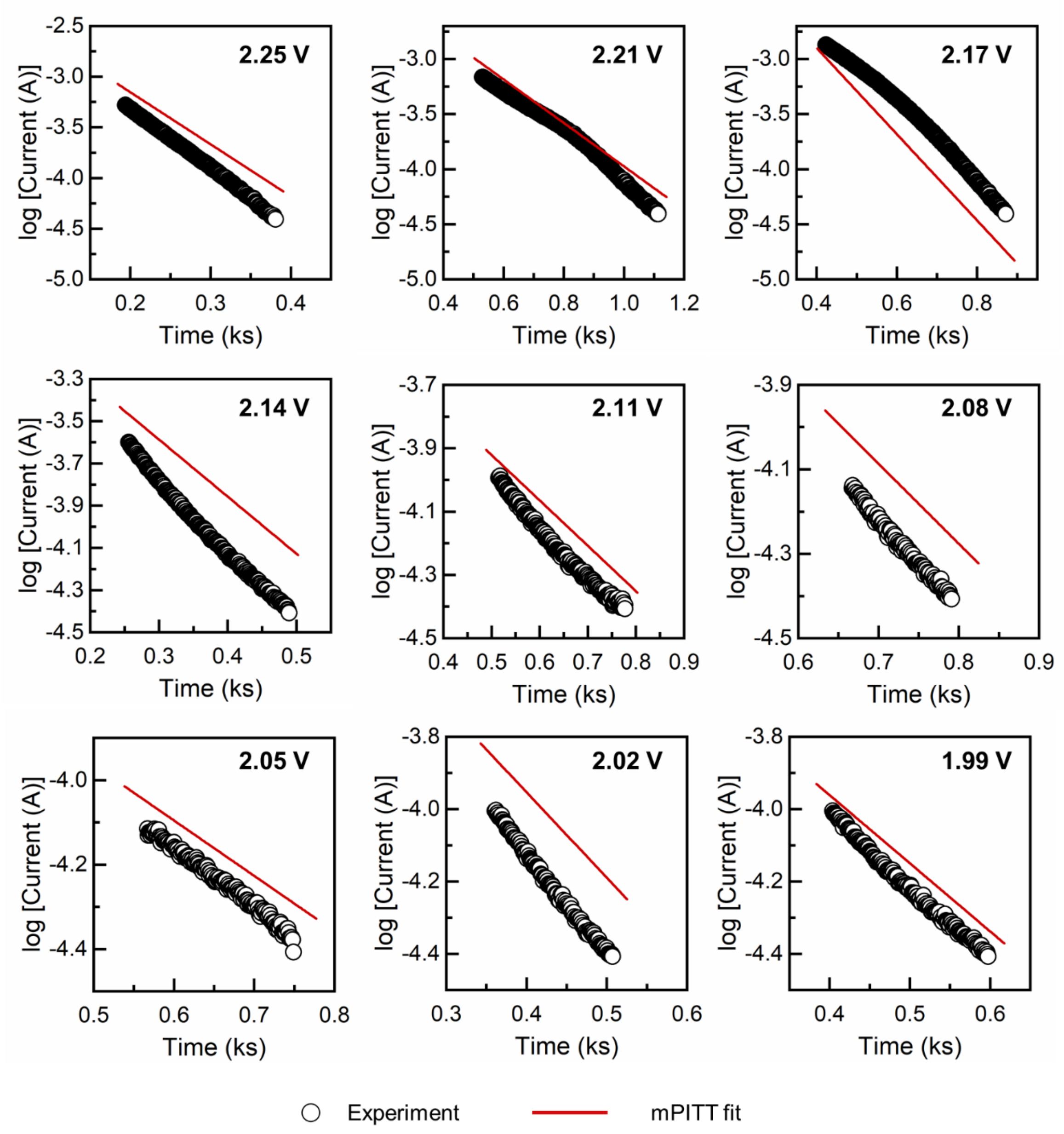

Figure D-12: The fitting of absolute transient currents at the selected voltage steps during PITT discharge at -20°C. Cottrell’s method and the mPITT method are used to fit the transient currents in the long-time regime and estimate the diffusion coefficients and Damköhler number.

D.4.2 -10°C

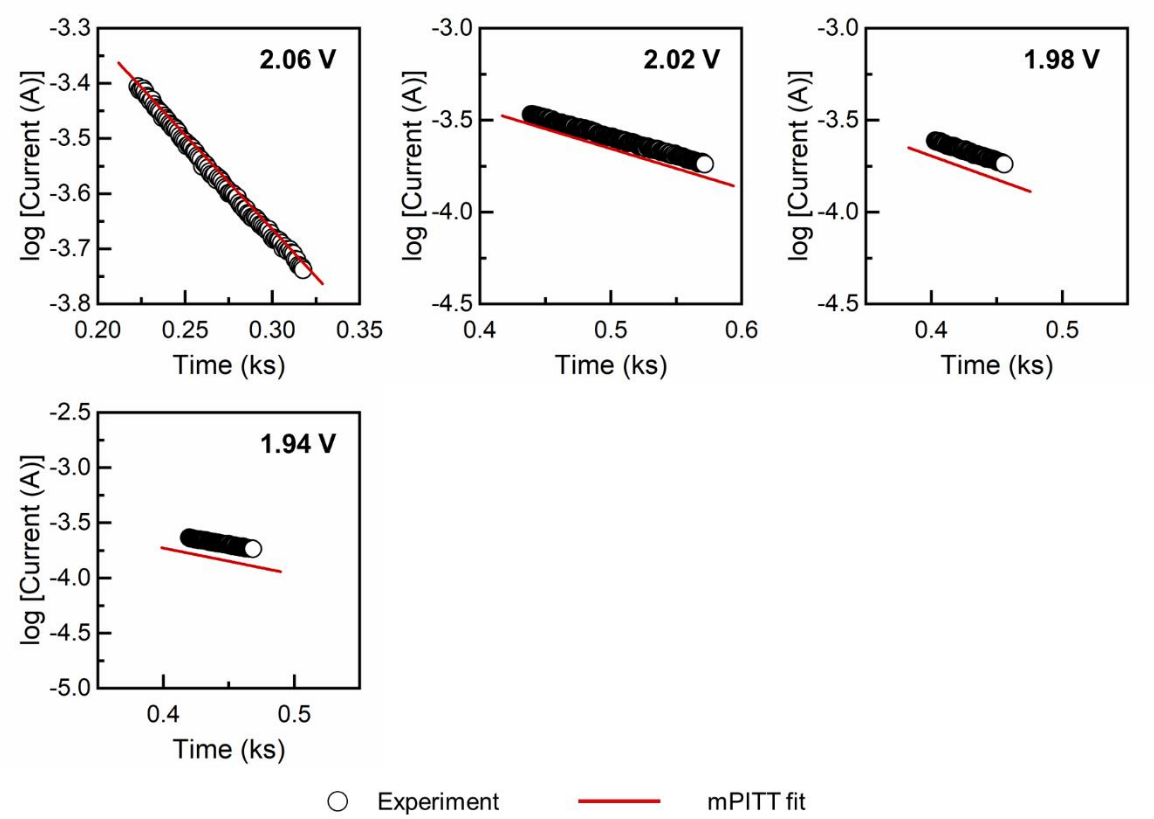

Figure D-13: The fitting of absolute transient currents at the selected voltage steps during PITT discharge at -10°C. Cottrell's method and the mPITT method are used to fit the transient currents in the long-time regime and estimate the diffusion coefficients and Damköhler number.

D.4.3 0°C

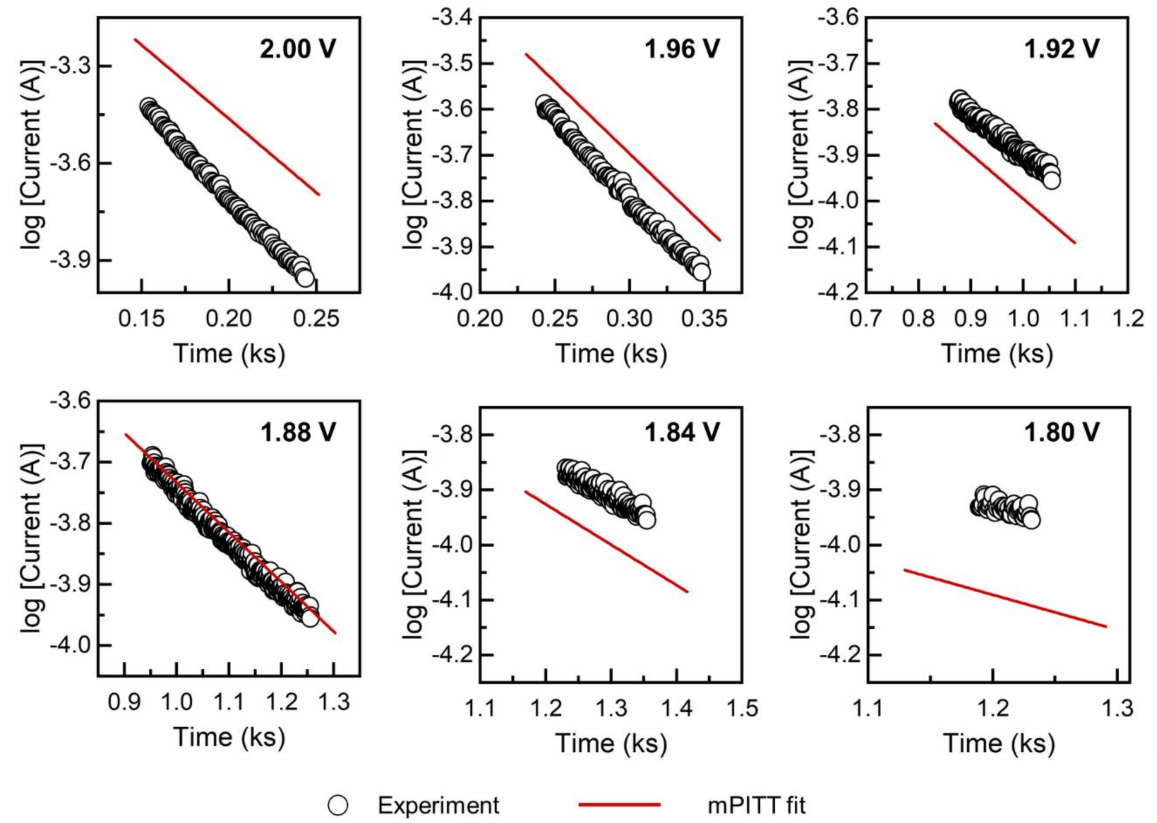

Figure D-14: The fitting of absolute transient currents at the selected voltage steps during PITT discharge at 0°C. Cottrell’s method and the mPITT method are used to fit the transient currents in the long-time regime and estimate the diffusion coefficients and Damköhler number.

D.4.4 10°C

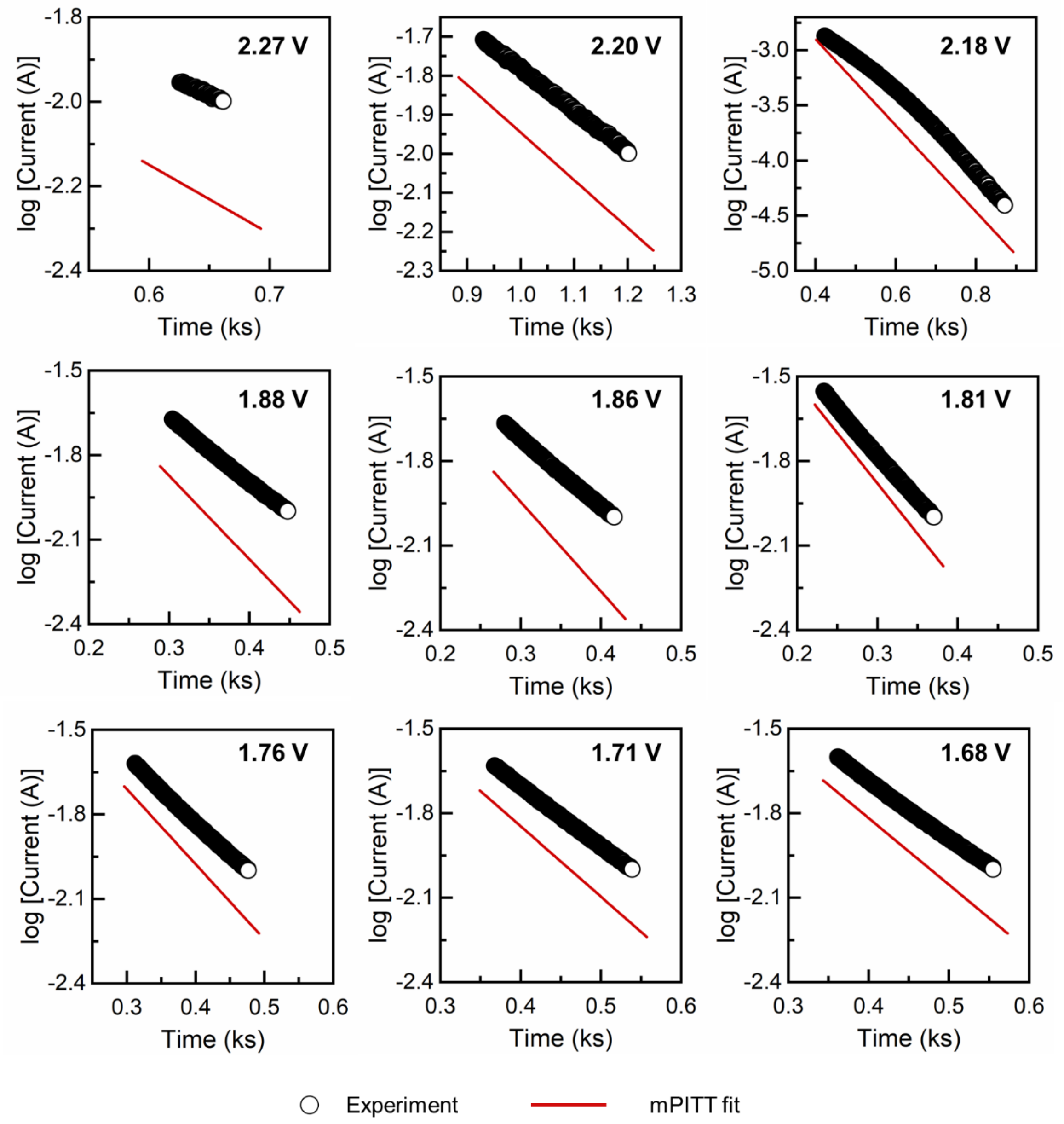

Figure D-15: The fitting of absolute transient currents at the selected voltage steps during PITT discharge at 10°C. Cottrell's method and the mPITT method are used to fit the transient currents in the long-time regime and estimate the diffusion coefficients and Damköhler number.

D.4.5 Room Temperature

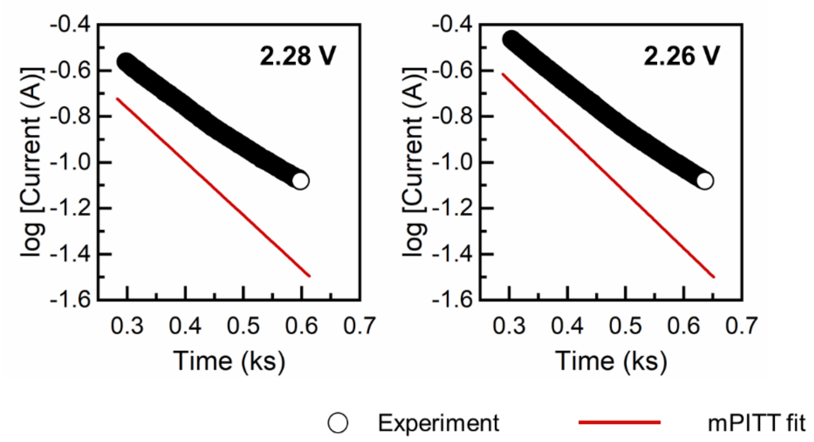

Figure D-16: The fitting of absolute transient currents at the selected voltage steps during PITT discharge at room temperature. Cottrell's method and the mPITT method are used to fit the transient currents in the long-time regime and estimate the diffusion coefficients and Damköhler number.

D.5 Long-time fit during PITT Charge

D.5.1 -20°C

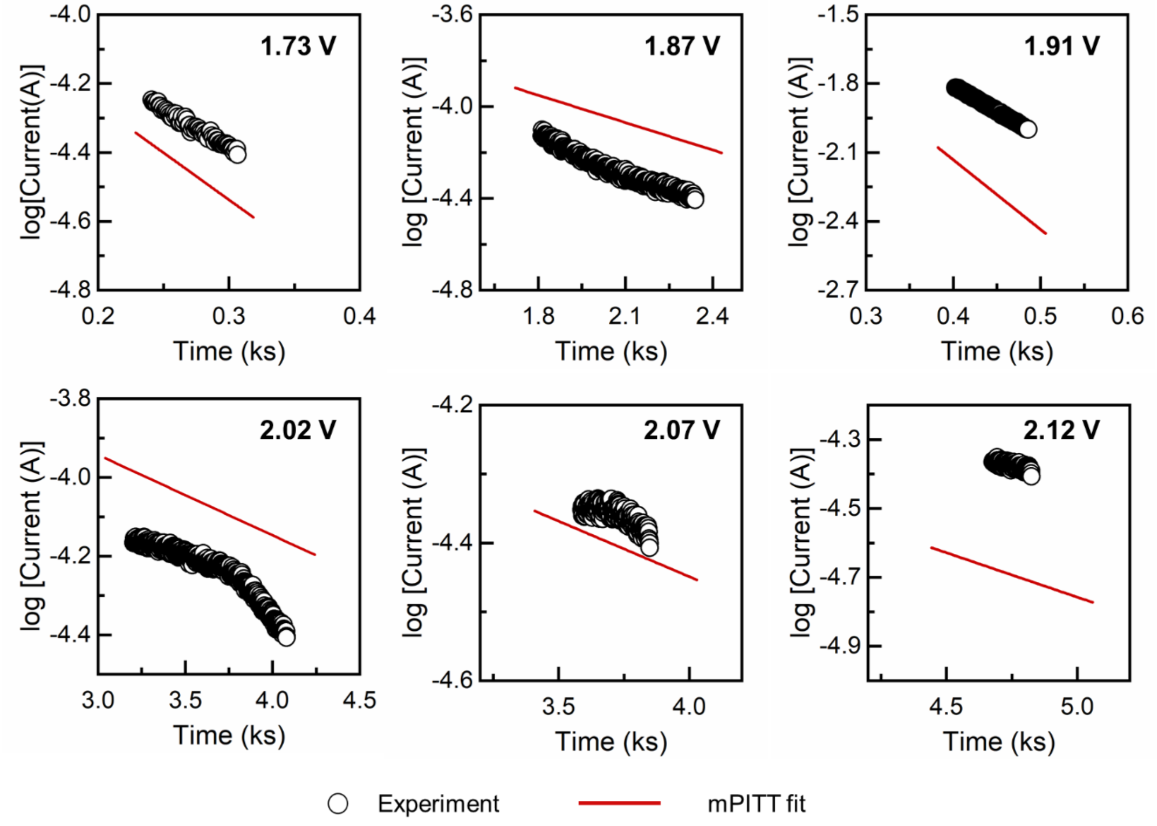

Figure D-17: The fitting of absolute transient currents at the selected voltage steps during PITT charge at -20°C. Cottrell's method and the mPITT method are used to fit the transient currents in the long-time regime and estimate the diffusion coefficients and Damköhler number.

D.5.2 -10°C

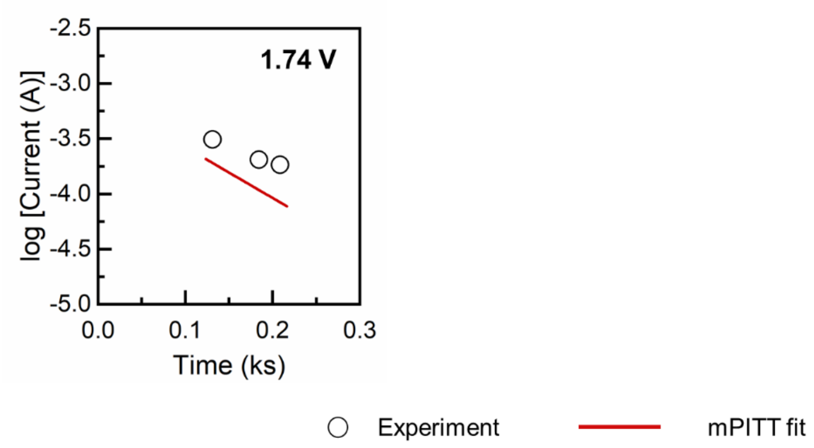

Figure D-18: The fitting of absolute transient currents at the selected voltage steps during PITT charge at -10°C. Cottrell's method and the mPITT method are used to fit the transient currents in the long-time regime and estimate the diffusion coefficients and Damköhler number.

D.5.3 0°C

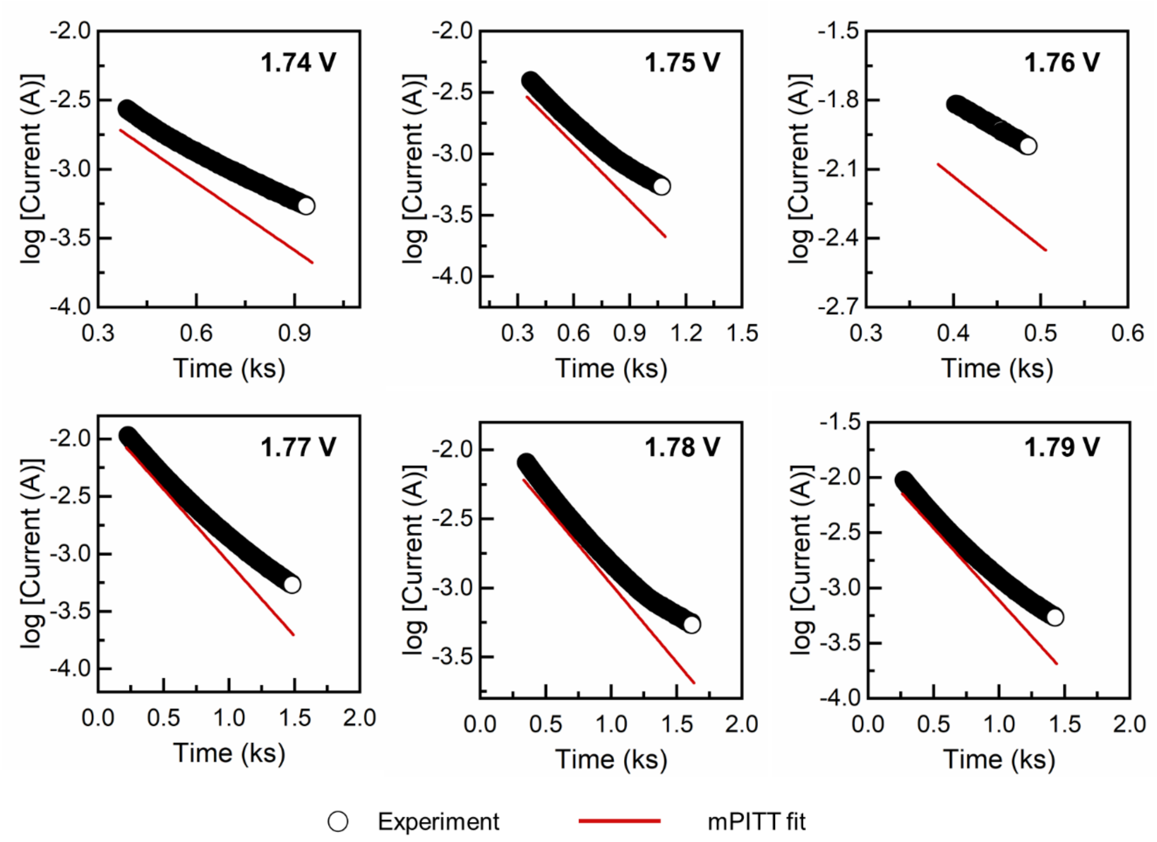

Figure D-19: The fitting of absolute transient currents at the selected voltage steps during PITT charge at 0°C. Cottrell's method and the mPITT method are used to fit the transient currents in the long-time regime and estimate the diffusion coefficients and Damköhler number.

D.5.4 10°C

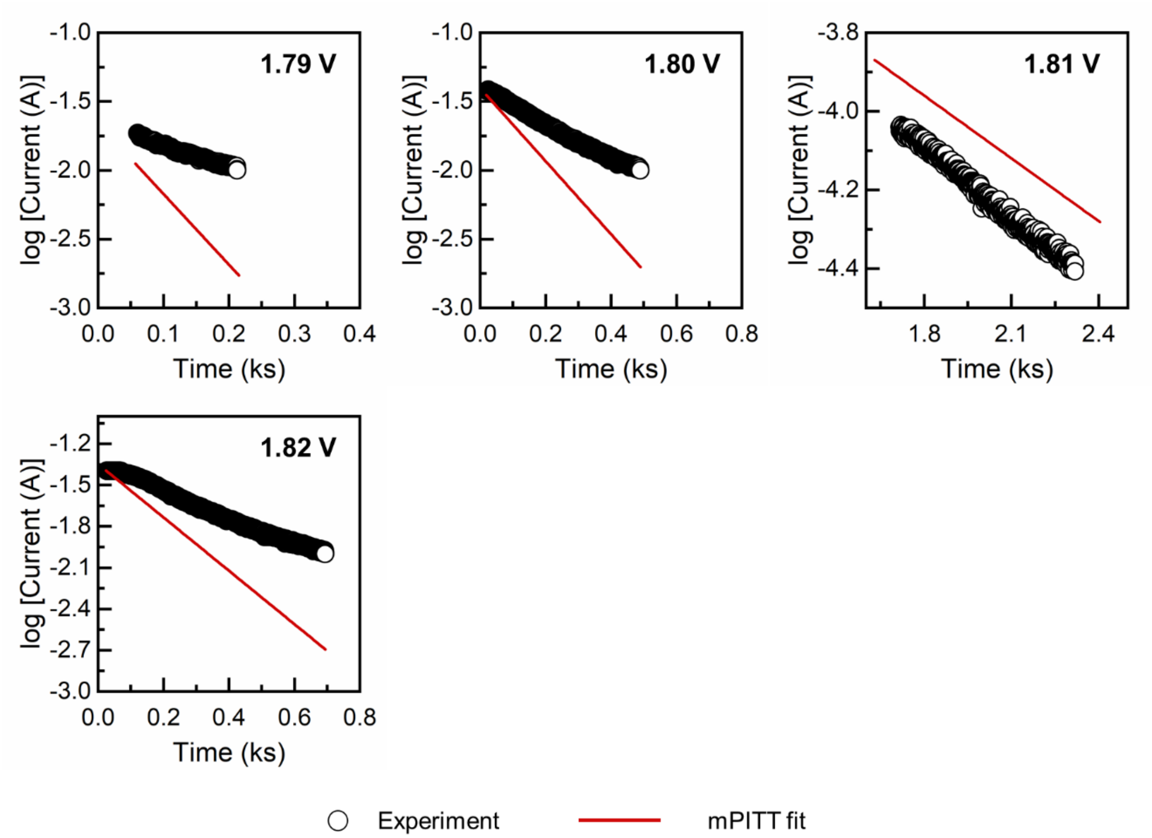

Figure D-20: The fitting of absolute transient currents at the selected voltage steps during PITT charge at 10°C. Cottrell’s method and the mPITT method are used to fit the transient currents in the long-time regime and estimate the diffusion coefficients and Damköhler number.

D.5.5 Room Temperature

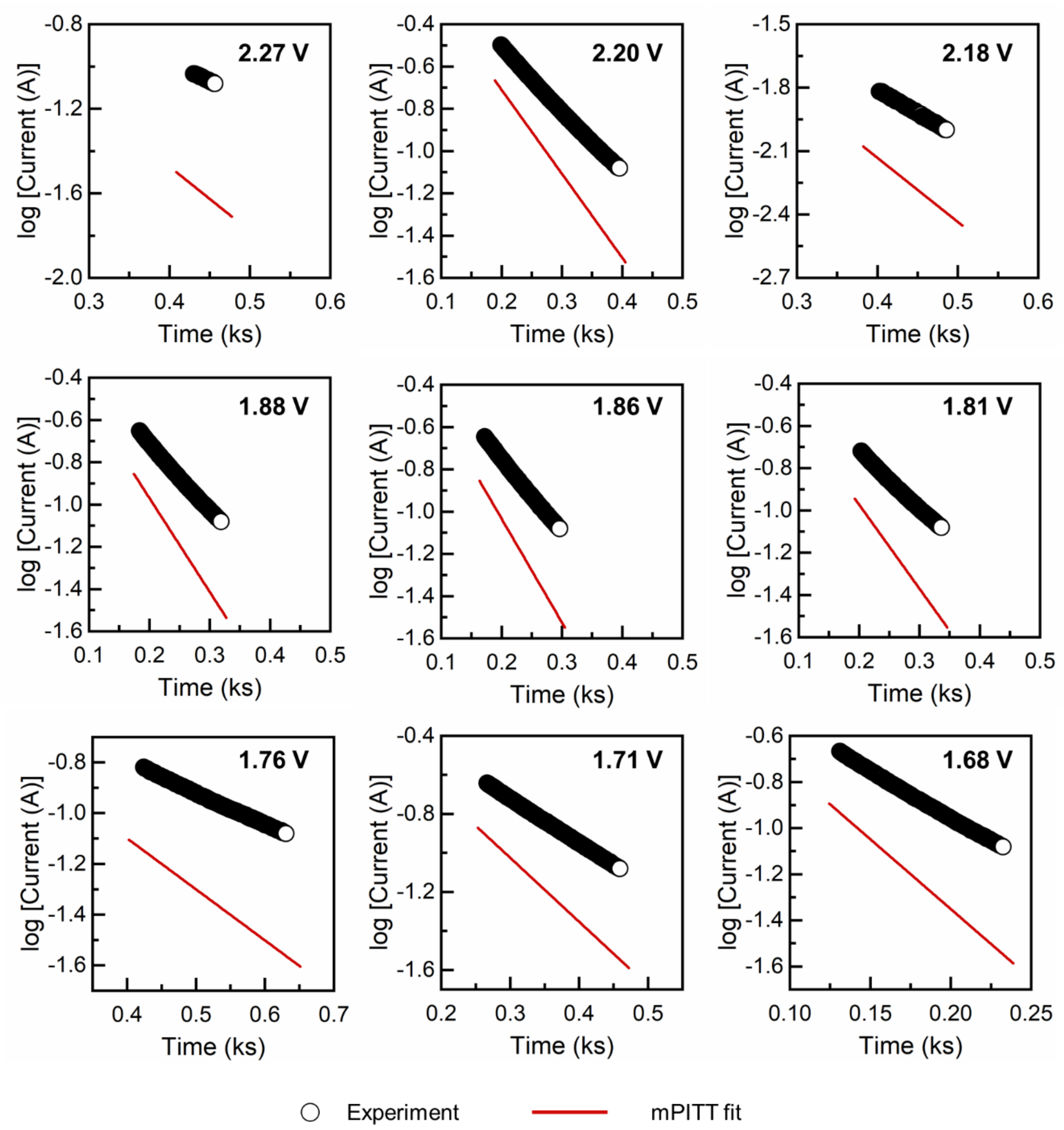

Figure D-21: The fitting of absolute transient currents at the selected voltage steps during PITT charge at room temperature. Cottrell's method and the mPITT method are used to fit the transient currents in the long-time regime and estimate the diffusion coefficients and Damköhler number.

D.6 Electrochemical Impedance Spectroscopy

D.6.1 Equivalent Circuit Fit

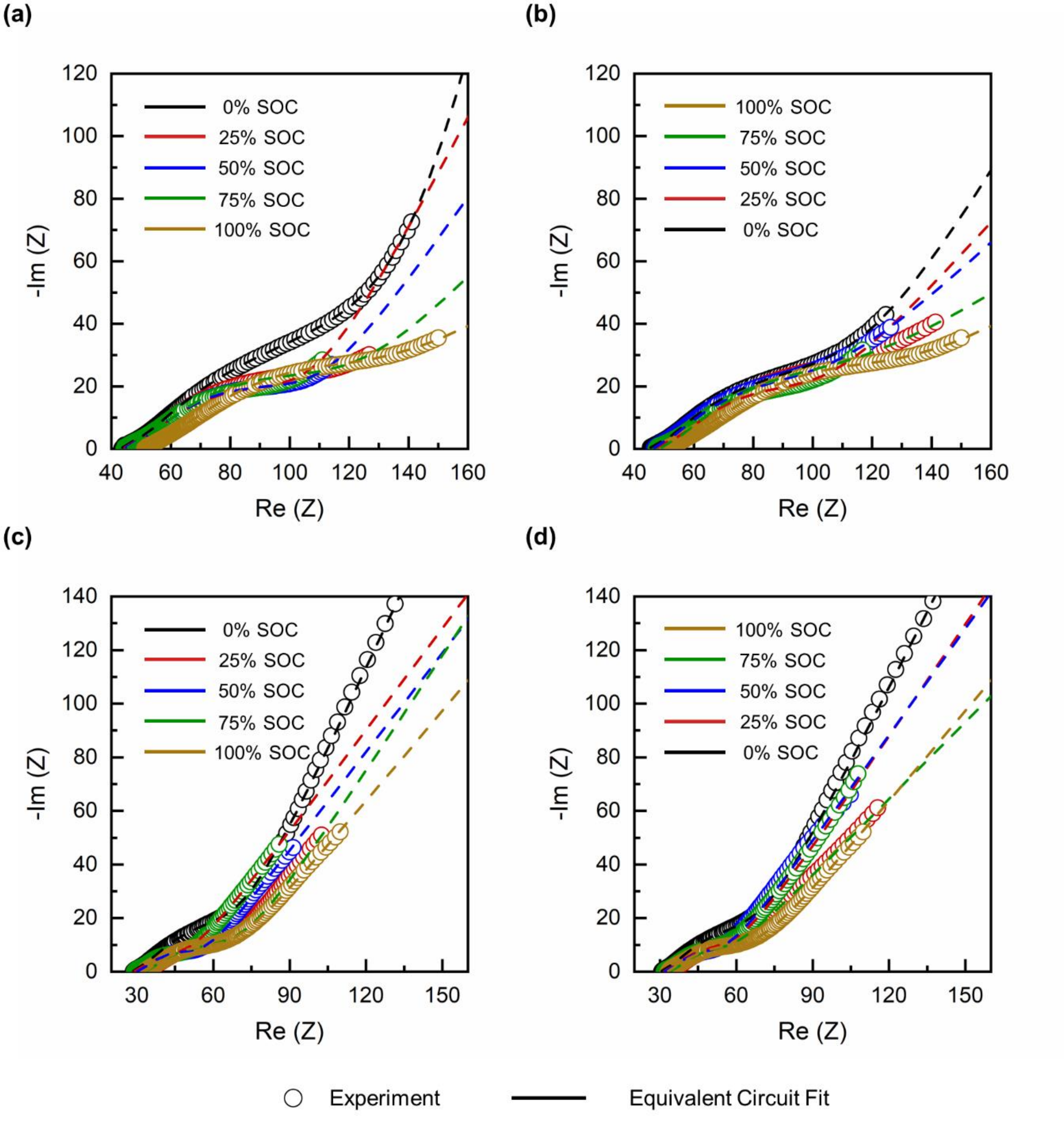

continued

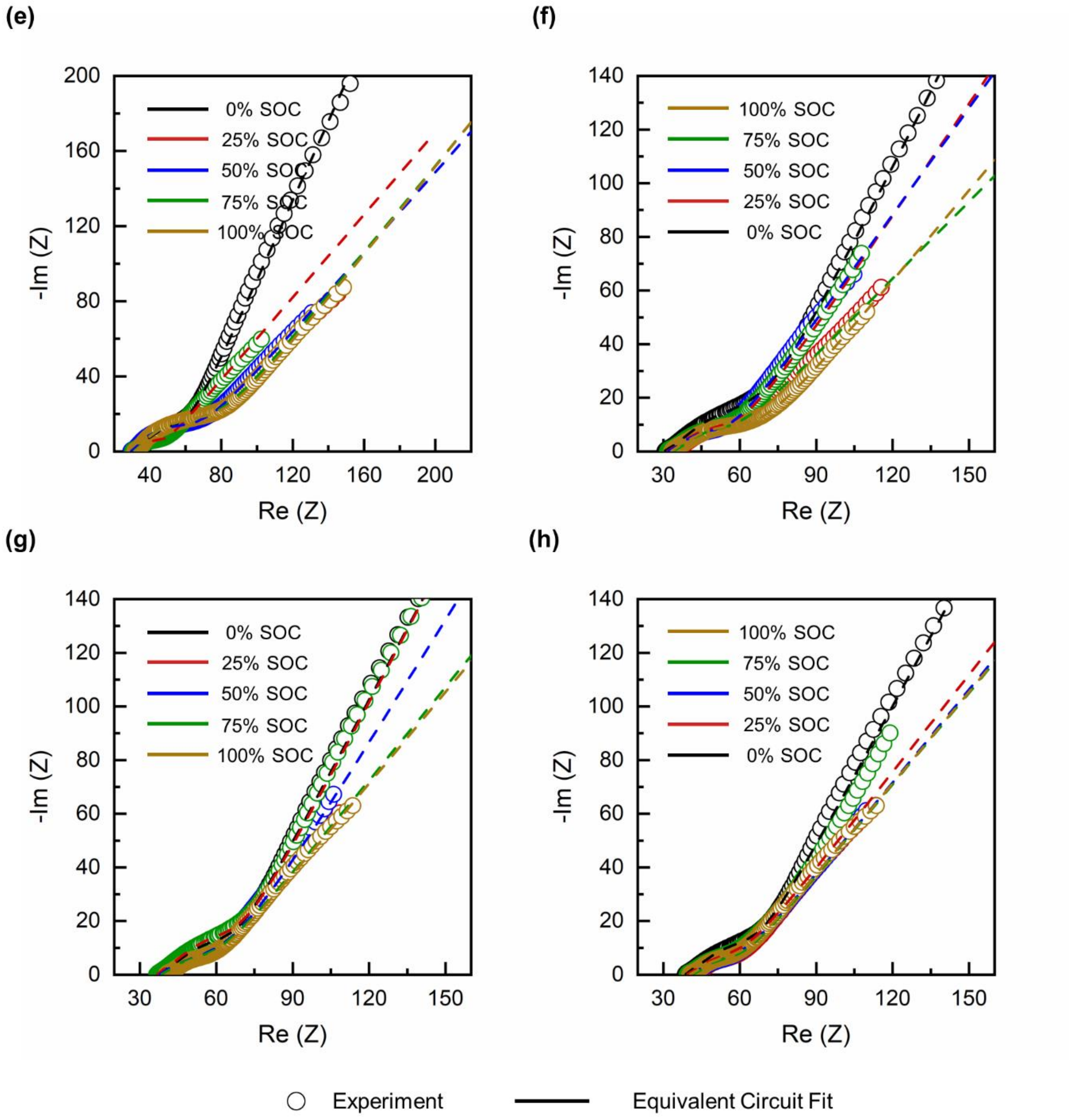
(e)
-Im (Z)
Re (Z)
0% SOC
25% SOC
50% SOC
75% SOC
100% SOC
0
40
80
120
160
200
40
80
120
160
200
(f)
-Im (Z)
Re (Z)
100% SOC
75% SOC
50% SOC
25% SOC
0% SOC
0
20
40
60
80
100
120
140
30
60
90
120
150
(g)
-Im (Z)
Re (Z)
0% SOC
25% SOC
50% SOC
75% SOC
100% SOC
0
20
40
60
80
100
120
140
30
60
90
120
150
(h)
-Im (Z)
Re (Z)
100% SOC
75% SOC
50% SOC
25% SOC
0% SOC
0
20
40
60
80
100
120
140
30
60
90
120
150
○ Experiment
Equivalent Circuit Fit

continued

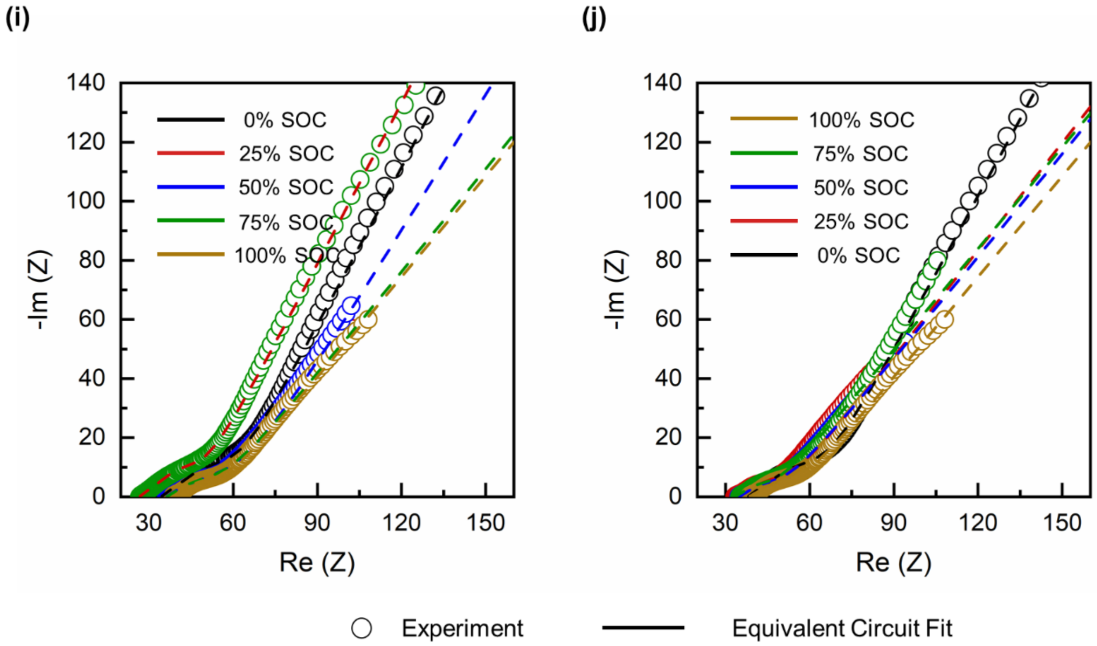

Figure D-22: The fitting of EIS at SOCs ranging from 0% to 100% using the equivalent circuit model shown in the main text at (a, b) -20°C, (c, d) -10°C, (e, f) 0°C, (g, h) 10°C, and (i, j) room temperature. Panels (a, c, e, g, and i) show the spectra during charge while panels (b, d, f, h, and j) show the spectra during discharge.

D.6.2 Fitting data

(a) -20°C

SOC	Charge					Discharge			
	0%	**25%**	**50%**	**75%**	**100%**	**75%**	**50%**	**25%**	**0%**
R_{bulk} (Ω)	43.16	43.89	44.29	45.02	50.97	48.57	46.25	46.85	44.99
R_{CT}^{SEI} (Ω)	8.525	10.60	10.44	9.081	22.69	3.056	7.458	10.87	7.164
Y_o^{SEI} (F)	9.61E-04	1.23E-03	1.25E-03	1.36E-03	5.43E-03	1.38E-03	1.61E-03	1.49E-03	1.10E-03
a^{SEI}	0.46	0.45	0.45	0.45	0.33	0.51	0.45	0.42	0.46
R_{CT}^{dl} (Ω)	99.54	50.83	49.96	58.85	33.77	31.18	37.79	37.77	60.94
Y_o^{dl} (F)	1.16E-03	1.21E-03	1.09E-03	1.12E-03	1.11E-03	1.18E-03	1.18E-03	1.18E-03	1.30E-03
a^{dl}	0.59	0.64	0.65	0.62	0.71	0.69	0.65	0.67	0.60
W ($S.s^{0.5}$)	2.66E-05	8.55E-05	2.57E-04	2.19E-04	9.98E-04	1.43E-05	2.15E-08	2.12E-09	1.17E-07
b	0.44	0.34	0.30	0.26	0.17	0.17	0.24	0.26	0.33

(b) -10°C

SOC	Charge					Discharge			
	0%	**25%**	**50%**	**75%**	**100%**	**75%**	**50%**	**25%**	**0%**
R_{bulk} (Ω)	28.30	28.91	30.08	33.41	33.10	33.87	31.98	31.58	30.32
R_{CT}^{SEI} (Ω)	13.93	2.610	3.200	1.550	3.060	3.740	2.410	2.230	11.97
Y_o^{SEI} (F)	3.23E-03	3.13E-04	4.32E-04	1.19E-04	6.25E-04	1.57E-03	2.51E-04	2.01E-04	4.13E-03
a^{SEI}	0.41	0.63	0.60	0.73	0.58	0.48	0.63	0.65	0.39
R_{CT}^{dl} (Ω)	25.30	18.30	20.84	36.07	28.87	15.63	19.84	24.77	24.01
Y_o^{dl} (F)	1.00E-03	2.28E-03	1.81E-03	2.56E-03	1.96E-03	1.56E-03	2.10E-03	2.31E-03	1.14E-03
a^{dl}	0.76	0.58	0.60	0.49	0.55	0.66	0.59	0.56	0.72
W ($S.s^{0.5}$)	1.54E-12	2.44E-10	6.06E-11	8.75E-12	7.70E-10	1.21144E-08	3.09E-11	2.05E-11	1.28E-12
b	0.36	0.29	0.28	0.31	0.27	0.24	0.29	0.30	0.35

(c) 0°C

SOC	Charge					Discharge			
	0%	**25%**	**50%**	**75%**	**100%**	**75%**	**50%**	**25%**	**0%**
R_{bulk} (Ω)	29.65	29.97	29.34	31	31.45	32.15	32.23	31.19	30.55
R_{CT}^{SEI} (Ω)	10.69	3.058	1.507	1.531	1.484	1.455	1.483	1.157	2.133
Y_o^{SEI} (F)	2.30E-03	8.47E-04	9.73E-05	9.07E-05	7.10E-05	6.82E-05	3.55E-05	2.85E-05	4.79E-04
a^{SEI}	0.47	0.56	0.75	0.75	0.77	0.77	0.81	0.85	0.61

R_{CT}^{dl} (Ω)	17.85	12.42	30.76	37.10	39.39	42.68	50.58	54.46	53.16
Y_o^{dl} (F)	7.78E-04	1.37E-03	1.16E-03	1.12E-03	1.10E-03	1.06E-03	1.18E-03	1.27E-03	1.08E-03
a^{dl}	0.79	0.68	0.66	0.66	0.66	0.67	0.64	0.63	0.65
W ($S.s^{0.5}$)	7.17E-13	1.28E-09	2.58E-09	1.04E-09	4.26E-09	9.36E-08	1.04E-07	7.79E-08	4.99E-08
b	0.36	0.27	0.26	0.27	0.28	0.27	0.27	0.27	0.30

(d) 10°C

SOC	**Charge**					**Discharge**			
	0%	**25%**	**50%**	**75%**	**100%**	**75%**	**50%**	**25%**	**0%**
R_{bulk} (Ω)	37.39	36.69	37.45	38.46	40.49	41.60	40.66	39.40	38.60
R_{CT}^{SEI} (Ω)	11.23	11.88	0.1463	1.069	1.628	1.939	1.011	1.395	11.02
Y_o^{SEI} (F)	1.71E-03	1.73E-03	6.09E-07	1.78E-05	7.80E-05	1.13E-04	1.62E-05	1.11E-04	1.81E-03
a^{SEI}	0.47	0.48	0.75	0.88	0.73	0.70	0.88	0.73	0.47
R_{CT}^{dl} (Ω)	15.49	16.84	30.96	19.67	16.18	14.92	17.81	18.07	14.13
Y_o^{dl} (F)	6.94E-04	6.46E-04	5.05E-03	3.07E-03	2.22E-03	2.09E-03	3.27E-03	2.42E-03	7.53E-04
a^{dl}	0.80	0.81	0.40	0.49	0.56	0.57	0.48	0.54	0.79
W ($S.s^{0.5}$)	1.41E-09	3.69E-09	1.16E-09	2.99E-09	7.45E-09	8.46E-09	7.23E-09	3.47E-09	4.11E-09
b	0.34	0.34	0.32	0.28	0.27	0.27	0.27	0.28	0.34

(e) Room Temperature

SOC	**Charge**					**Discharge**			
	0%	**25%**	**50%**	**75%**	**100%**	**75%**	**50%**	**25%**	**0%**
R_{bulk} (Ω)	34.35	26.62	36.02	36.31	38.56	33.37	34.79	34.95	38.05
R_{CT}^{SEI} (Ω)	10.32	8.621	0.1407	1.009	1.551	1.556	0.8651	1.238	10.86
Y_o^{SEI} (F)	1.57E-03	1.26E-03	5.86E-07	1.68E-05	7.43E-05	9.04E-05	1.39E-05	9.81E-05	1.78E-03
a^{SEI}	0.44	0.35	0.72	0.83	0.70	0.56	0.75	0.64	0.47
R_{CT}^{dl} (Ω)	14.23	12.22	29.78	18.57	15.41	11.97	15.24	16.03	13.93
Y_o^{dl} (F)	6.38E-04	4.69E-04	4.86E-03	2.90E-03	2.12E-03	1.67E-03	2.79E-03	2.15E-03	7.42E-04
a^{dl}	0.73	0.59	0.38	0.47	0.54	0.46	0.41	0.48	0.78
W ($S.s^{0.5}$)	1.30E-09	2.68E-09	1.12E-09	2.83E-09	7.10E-09	6.78E-09	6.19E-09	3.08E-09	4.05E-09
b	0.31	0.25	0.31	0.26	0.26	0.22	0.23	0.25	0.33

D.7 MD Simulation at -20°C

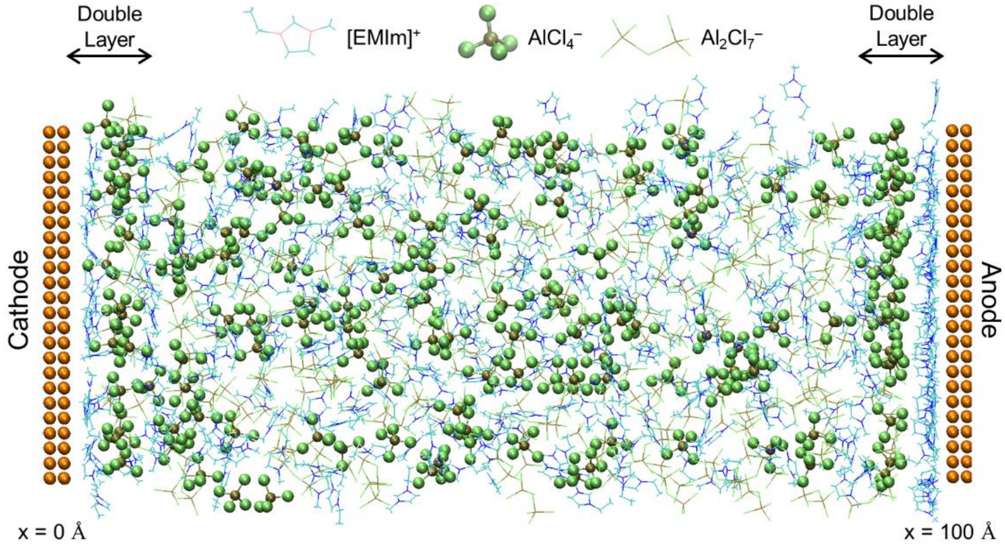

Figure D-23: Structure of the electric double layer near the cathode and anode with surface charge 0.1 C.m^{-2}, along with the bulk at -20°C obtained from MD simulation.